PRODUCTION OF BIO-OIL FROM CATALYTIC PYROLYSIS OF *SIDA RHOMBIFOLIA* (ARROW LEAF) WITH LOW- AND HIGH-DENSITY POLYETHYLENE

BY

Abdullahi, Alhaji Musa

PhD/SEET/2016/938

CHEMICAL ENGINEERING DEPARTMENT

FEDERAL UNIVERSITY OF TECHNOLOGY, MINNA, NIGERIA

OCTOBER, 2023

ABSTRACT

Zeolite Y catalyst was successfully synthesized using Bambu clay for the production of bio-oil from *Sida rhombifolia* (arrow leaf) with Low- and High-Density Polyethylene (LDPE and HDPE). The synthesis of the zeolite Y was via a two-step process: seed gel and feed gel, which were thereafter protonated through ion exchange with ammonium chloride. The catalyst was characterised using X-ray Fluorescence (XRF), X-ray diffraction (XRD), Brunauer-Emmett-Teller (BET), Scanning Electron Microscopy (SEM), Fourier Transform Infrared (FTIR) spectroscopy, Pyridine proof, and X-ray Photoelectron Spectroscopy (XPS). Similarly, the physico-chemical properties of the bio-oil were determined. The characterization results showed that Bambu clay was kaolinite with a Si/Al ratio of 1:8, metakaolinite was 2:11, Synthesis Zeolite Y (SZY) was 2:40, and Synthesis Zeolite Y catalyst (HSZY) was 2:42. The calculated lattice constant indicated that the SZY has a unit cell of a = b ≠ c with a hexagonal crystal system. Micrographs showed that the particles of SZY have regular and bulky shapes with average crystallite sizes of 24.77 nm. The BET analysis revealed that the surface area of SZY was 549.10 m^2 g^{-1} and that it possessed a Lewis acidity type. Prior to the application of the synthesised zeolite Y catalyst (HSZY) for catalytic cracking, three pyrolysis methods for the production of bio-oil were employed; pyrolysis of individual samples of SR, LDPE, and HDPE, co-pyrolysis of SR with LDPE and HDPE; and catalytic co-pyrolysis of SR with LDPE and HDPE. The pyrolysis results showed that the maximum yield of bio-oil obtained from the pyrolysis of SR was 48.10 wt. % though, the co-pyrolysis increases the yield of the bio-oil from 48. 10 wt. % to 76.20 wt. %. The physio-chemical analysis indicated that the bio-oil obtained from the pyrolysis of SR has a low calorific value of 17.01 MJ/kg, a high viscosity of 13.23 cst, a density of 1.0460 kg/m^3, and a moisture content of 4.30 wt.%. However, after co-pyrolysis, the calorific value increases from 17.01 to 27.90 MJ/kg, the viscosity decreases from 13.23 to 6.94 cst, and the moisture content decreases from 4.30 to 2.70 wt.%. Therefore, the co-pyrolysis showed an effective synergy between SR with LDPE and HDPE yet the bio-oil was slightly viscous and waxy. In order to reduce the viscosity and waxiness of the bio-oil, SZY and HSZY were used. The performance test of the SZY indicated that the calorific value increased from 27.90 to 36.26 MJ/kg, the viscosity decreased from 6.94 to 2.23 cst, moisture content decreased from 2.70 to 2.3%. However, the HSZY demonstrated a significant improvement with an increase in calorific value from 36.26 to 36.97 MJ/kg, a decrease in viscosity from 2.23 to 1.02 cst, moisture content from 2.3 % to 1.21 % and a density decreases from 0.8220 to 0.7842 g/cm^3. Aromatic hydrocarbons increased from 16.44 % to 35.0 %. Similarly, the bio-oil obtained from catalytic (HSZY) co-pyrolysis contains carbon ranging from octane (C_8) to Eicosane (C_{20}) which is closer to the range of carbons in kerosene from heptane (C_9) to hexadecane (C_{16}) but lower than the carbon range in diesel oil from nonane (C_9) to dotriacontane (C_{30}) and higher than the range of carbons in gasoline from pentane (C_5) to dodecane (C_{12}). It can, therefore, be concluded that the bio-oil obtained using HSZY by catalytic co-pyrolysis is of high quality and has a carbon range closer to kerosene; hence, the bio-oil can be used for domestic cooking.

TABLE OF CONTENTS

LIST OF TABLES

LIST OF FIGURES

LIST OF PLATES

ABBREVIATION, GLOSSARIES AND SYMBOLS

BET	Brunauer-Emmett-Teller
FTI-R	Fourier Transform Infrared
FUT	Federal University of Technology
FWHM	Full Width at Half Maximum
HRSEM	High Resolution Scanning Electron Microscope
HRTEM	High Resolution Transition Electron Microscope
IUPAC	International Union of Pure and Applied Chemistry
PEG	Polyethylene glycol
S_{BET}	Total surface area
SEDI	Scientific Equipment Development Institute
SEM	Scanning Electron Microscopy
USA	United States of America
v /v	volume per volume
w/w	weight per weight
wt.%	Weight per cent.
XRD	X-Ray Diffraction
XRF	X-Ray Fluorescence
XPS	X-ray Photoelectron Spectroscopy
λ	Wavelength
d	d-spacing in Å
θ	Diffraction angle in radians
β	Full Width at Half Maximum (FWHM)

CHAPTER ONE

1.0   INTRODUCTION

1.1 Background to the Study

The world's consumption of fossil fuels has increased during the last few decades. These resources are referred to as finite natural energy, and the global economy is at risk from both their depletion and price fluctuations. When these fuels are utilized, the atmosphere is exposed to dangerous pollutants (Hwang *et al*., 2019). Actually, burning these fuels releases carbon dioxide into the atmosphere, which is known to cause global warming.

Natural resources that can be replaced after use are known as renewable resources. It can be divided into those that require careful planning and harvesting (such as biomass) and those that are sustainable (such as wind power, solar energy, tides, hydroelectricity, and geothermal power). There are three generations of biomass that can be identified. First-generation biomass is made up of starches and sugars. Many researchers produced fuel (bioethanol) from first-generation biomass, but the process resulted in food shortages and land problems because more land was being used for planting. (Isikgor and Becer, 2015).

Second-generation biomass, as defined by Huber *et al*. (2006) and Agrawal *et al*. (2019), is lingo-cellulosic biomass, which comprises agricultural materials like wood, herbs, non-woody straw, rice husks, and so on. These second-generation lingo-cellulose biomasses cannot be used as food. Algae is regarded as a third-generation biomass with a high lipid content for biofuel production (Conti *et al*., 2016).

In recent times, second-generation biomass, specifically non-woody biomass, has been given attention by researchers to produce bio-oil. *Sida rhombifolia* (SR), known as arrow leaf, is a non-woody biomass that is available across all geographical locations in Nigeria. It's a weed plant that is not grown by human activities but rather by itself in most parts of Nigeria. With all these potentials, the SR has yet to attract attention for bio-oil production as transport fuel in Nigeria.

There are three types of biomass conversion processes: biological, physical, and thermochemical. The physical conversion process involves pelletizing biomass to produce briquettes, fuel pellets, and composite materials (Simone *et al*., 2012). Biological conversion involves the use of microorganisms, bacteria, and yeast to extract bioethanol, biogas, and biofuels from the hemicellulose and cellulose of biomass (Chen *et al*., 2010), and lignin is produced as a by-product (waste). Thermochemical conversion involves the use of heat to decompose the chemical structure of biomass to yield solid char (bio-char), liquid oil (bio-oil), and gases.

Thermochemical conversions are further classified into direct combustion, pyrolysis, and gasification techniques. Among these techniques, only pyrolysis is environmentally friendly, and the end-product is bio-oil. Pyrolysis is a technique that produces bio-oil and solid char from lignocellulose feedstock by heating it to temperatures between 400 ºC and 650 ºC in the absence of oxygen (Foong *et al*., 2020).

Asadullah *et al*. (2007) pyrolysed lignocellulose biomass to obtain bio-oil. It has been shown that the bio-oil has undesirable properties that prevent it from being used as a direct fuel for

transportation. These undesirable properties include high oxygen, high water content, and hydrogen deficiency. Hydrogen-rich LDPE and HDPE can be utilized to make up for the hydrogen deficiency in the bio-oil.

Currently, there has been a rise in environmental concern over plastic waste generation and disposal worldwide, resulting from the rise in population and industrialization. Plastics are materials that are made of a wide range of synthetic and natural compounds. Plastics have become indispensable materials in several countries around the world due to their durability, lightweight, and flexibility. They are utilized in a range of industrial and domestic areas (Khan *et al.*, 2016).

In 2015, global plastics production was about 388 million tones and has reached over 407 million tonnes per annum in recent times, and this figure is estimated to double in the next 20 years. The most common and dominant form of plastic waste in Nigeria is Polyethylene. Polyethylene is produced by converting methane gas into ethylene, and then heat and pressure are applied to form polyethylene (Kumar *et al*., 2011). These products are increasingly needed for domestic utilization, especially in Nigeria. The increase in production of HDPE and LDPE and their utilization have led to a large accumulation of these wastes in the final waste stream, especially in Nigeria, due to their low application after first use.

1.2 Statement of the Research Problem

The adverse characteristics associated with bio-oil involved the presence of oxygen, known as oxygenated organic, which led to bio-oil's low calorific value, high viscosity, high acidity, high density, cetane and octane, flash point, and pour point (Onal *et al*., 2014). Several

researchers have carried out different pyrolysis techniques with the view to reducing the oxygenated organic compounds so as to make the bio-oil stable similar to conventional hydrocarbons, yet the bio-oil contained oxygenated organics. Foong *et al*. (2020) produced bio-oil from the pyrolysis of biomass at temperatures between 400 ºC and 650 ºC, average particle size of 2 – 6 mm and specific heating rate of 20 ^{0}C/min, but they didn't take reaction time into account. Again, Kim *et al*. (2019) produced bio-oil, but the oil is of poor quality due to a low hydrogen/carbon effective ratio (H/C). Some researchers, including Dewangan *et al*. (2016), utilized plastic as a hydrogen donor for increasing the hydrogen/carbon effective ratio (H/C) and reducing the quantity of oxygen in the bio-oil, yet it contained viscosity and waxiness. To reduce the higher viscosity and waxiness of the bio-oil resulting from the utilization of hydrogen donors, zeolite is further needed for cracking. On the other hand, the importation of zeolite is not encouraging to local content and has an adverse effect on Gross Domestic Product (GDP). Importation of the zeolite may not be sustainable because it depends on the foreign market; hence, there is a need for locally sourced zeolite catalysts for cracking the bio-oil.

1.3 Aim and Objectives of the Study

The study aimed at improving the quality of bio-oil obtained from co-pyrolysis of *Sida Rhombifolia* (arrow leaf) with LDPE and HDPE using a synthesized zeolite catalyst. The specific objectives of this research are:

1. Proximate and ultimate analysis of SR, LDPE, and HDPE

2. Study the effect of pyrolysis parameters: temperature, reaction time, and particle size on the pyrolysis of SR.

3. Study the effect of temperature on the pyrolysis of LDPE and HDPE and the co-

pyrolysis of SR with LDPE and HDPE.

4. Synthesis of zeolite catalysts obtained from Bambu clay and characterization

5. Production of bio-oil from catalytic co-pyrolysis of SR with LDPE and HDPE

6. Physical and chemical characterization of bio-oil produced.

1.4 Justification of the Study

The choice of pyrolysis of *Sida Rhombifolia* (SR) for the present research was due to its high volatile matter and very low ash content; it does not compete as a food because it is a weed plant; and the species availability in most parts of Nigeria. The species belong to the non-woody plants that grow on their own without human intervention. They are vigorous enough to quickly regrow even after many harvests and mature in less than four months (Kumar *et al.*, 2011). They grow in areas with low amounts of rainfall and poor or semi-desert land. Despite all these potentials, the SR is yet to attract attention for bio-oil production, which would be utilized as transport fuel in Nigeria.

To improve the quality of the bio-oil produced by the pyrolysis of biomass, the LDPE and HDPE, which are inexpensive and hydrogen-rich materials found in our main stream trash, were utilized to make up the low H/C in the bio-oil obtained from pyrolysis of *sida rhombifolia*. Uzoejinwa *et al*. (2018) also co-fed lingo-cellulosic biomass with plastic in the pyrolyzer and found that the amount of oxygen in the bio-oil significantly decreased and the number of aromatic hydrocarbons increased.

However, Li *et al*. (2013) observed that when co-pyrolysis was carried out without the catalyst, the gas chromatogram analysis revealed that the bio-oil obtained from co-pyrolysis

of cellulose with LDPE indicated low effective synergy between the co-pyrolysis intermediates. Therefore, the study utilized zeolite catalysts to establish a synergy between biomass and plastic. On the other hand, the importation of zeolite is not sustainable because it depends on foreign markets. therefore, zeolite catalyst was locally sourced from raw clay considering the fact that, clay is widespread across each geographical location of Nigeria, easily mined, reasonable cost, almost free to harness, generally non-toxic and environmentally friendly.

Several researchers utilized zeolite catalyst obtained from high chemical impurities with premix pyrolysis technique. Jae *et al*. (2011) who reported that zeolites are widely used for catalytic applications due to their properties: surface area, adequate pore size, and high acidity. Kim *et al*. (2019) used micro-porous zeolites as catalysts for catalytic pyrolysis to study the interaction effect. Shah *et al*. (2019) used a fixed bed at a ratio of 2:3 biomass to plastic; the maximum bio-oil obtained was 48 wt.%. Zheng *et al*. (2018) used a fixed bed to pyrolyze LDPE in the presence of catalyst (HZSM-5), and the result showed a low oil yield with high char. Xue *et al*. (2018) co-pyrolyzed catalyst (HZSM-5) biomass with HDPE in a ratio of 1:1:2, and the maximum oil yield was very low (20.6 %). Therefore, this research study utilized zeolite catalyst obtained from Bambu clay and the premix and non-premix pyrolyses techniques were conducted so as to compare the influence of the technique for production of higher bio-oil (Johansson *et al*., 2018).

1.5   Scope of the Research

In this research work, SR, LDPE, and HDPE from Nasarawa State in the north-central part of Nigeria were characterized for pyrolysis. SR, LDPE, and HDPE underwent pyrolysis as well as catalytic co-pyrolysis. The bio-oil from SR, LDPE, and HDPE produced was further underwent catalytic co-pyrolysis to improve its properties and be used as transport fuel.

CHAPTER TWO

2.0   LITERATURE REVIEW

2.1 Biomass

Biomass is referred to as renewable energy (non-fossilized) and is a biodegradable organic material that obtains its energy from the sun through photosynthesis. Sunlight provides plants with the energy required for the process of converting water and carbon dioxide into oxygen and sugars (carbohydrates). These sugars have different varieties, including sugar, starch, and lignocellulose. Ligno-cellulosic biomass is a complex biopolymer that consists of cellulose, hemicellulose, and lignin. It was confirmed that lingo-cellulosic biomass is made up of 15–30 wt. % hemicellulose, 40 - 50 wt. % cellulose and 15 - 30 wt. % lignin. Lignocellulose biomass feedstock was categorized into dry and wet lignocellulose. The dry lignocellulosic feedstock is utilized for thermochemical conversion (liquefaction, combustion, gasification, and pyrolysis), while the wet lignocellulosic feedstock is utilized for biological conversion (Tumuluru *et al*, 2011).

2.1.1 Type of biomass feedstock

Lignocellulose biomass for energy purposes is divided into three feedstocks: woody biomass (forestry and wood waste), non-woody biomass (weeds such as *sida rhombifolia*, agriculture residues such as straws, bagasse strover and so on), and organic waste (animal waste and sewage sludge) (Tumuluru *et al*., 2011).

2.1.2 Proximate and ultimate analysis

Table 2.1 shows the proximate analysis of both woody and non-woody biomasses. The non-woody biomass feedstock is higher than the woody biomass in terms of calorific value, fixed carbon, and volatiles, which implies that non-woody is a suitable feedstock for producing a higher yield of bio-oil.

Table 2.1: Proximate analysis of woody and non-woody biomass (on dry basic)

Biomass feedstock	Volatile Matter	Ash	Fixed carbon	Calorific value MJ/kg
		Woody biomass		
Woody waste	47.79	2.31	7.90	11.696
Saw dust	51.39	22.67	14.29	18.300
		Non-woody biomass		
Sida rhombofolia	67.03	3.85	29.12	19.167
Rice husk	68.20	16.10	15.70	15.175
Switch grass	69.14	8.09	12.93	16.287
Corn stover	69.74	6.90	15.36	16.282

Source: Tumuluru *et al*. (2011)

2.1.3 Ultimate analysis of biomass

The ultimate analysis is an estimation of the important chemical elements that make up the biomass component: carbon, hydrogen, oxygen, nitrogen, and sulphur (Jenkins *et al*., 1998).

2.2   Thermochemical conversion processes

The thermochemical conversion includes; combustion (800 – 1500 ºC), torrefaction (between 200 - 300 ºC), gasification (above 800 – 1200 ºC) and pyrolysis (350 - 600 ºC) (Bridgwater, 2012).

2.2.1 Combustion

The chemical process of burning organic material to generate heat is called combustion, with an estimated quantity of heat of 20 MJ/kg (Ciolkosz, 2014).

The chemical process for conversion is shown in Equation 2.1.

$$CH_{1.44}O_{0.66} + 1.03O_2 = 0.72H_2O + CO_2 + Heat \tag{2.1}$$

2.2.2   Gasification

Gasification is the process of converting materials in a partial oxidation where there is insufficient oxygen to produce hydrogen, carbon monoxide, and traces of methane (syngas). The syngas has a low heating value, ranging from 4.2 to 5.02 MJ/Nm3 (Reed *et al.*, 1982).

2.2.3   Pyrolysis

In pyrolysis, the organic material is heated to a temperature of 400 ºC to 600 ºC to produce liquid oil, char, and gases in a controlled condition. The absence of oxygen prevents the material from combusting; instead, it undergoes thermal degradation and breaks down into different components. (Ralph and Overland, 2002). Depending on the rate of heating, pyrolysis can be categorized as fast, intermediate, or slow.

The equation describing the pyrolysis reaction of lignocellulose biomass is given in Equation 2.2

$$Biomass \rightarrow Biochar + Volatile\ matter \qquad\qquad (2.2)$$

Slow pyrolysis is carried out at temperatures ranging from 200 ºC – 300 ºC sometimes above 300 ºC. The time taken for a feedstock to spend inside the pyrolyser for thermal decomposition (resident time) is one hour to several hours. The products obtained from slow pyrolysis are 70 – 80 % char and 15 – 20 % gas and minimal volatiles (Bridgwater, 2012). However, intermediate pyrolysis occurs at temperatures ranging from 400 ºC – 500 ºC, with a residence time of about 10 – 30 s. The products obtained from intermediates are bio-char 20–30 %, gas of 10–20 %, and bio-oil of 50–60 %. Fast pyrolysis takes place at temperatures between 400 – 600 ^{0}C, with a high heating rate (20 ^{0}C/min). The time taken in terms of fast pyrolysis is actually shorter with < 2 (Bridgwater 2012).

2.2.4   Properties of bio-oil obtained from pyrolysis of biomass

Physical properties of bio-oil include viscosity, calorific value, flash point, density, water content, pH value, pour points, cetane number, and octane number, while chemical properties include the composition of the hydrocarbons, organics, functional groups, and their bonding.

2.2.4.1 *Calorific value of bio-oil*

The source and content of the biomass utilized in producing the bio-oil can affect the calorific value of the product. Bio-oil typically has a low calorific value of 15 to 25 MJ/kg and contains high oxygen. According to Mohanty (2011), when oxygen is present in substantial amounts, the water content increases and the number of hydrocarbons decreases. Generally,

lignocellulosic biomass has a calorific value between 16 and 19 MJ/kg, and gasoline has a calorific value between 40 and 50 MJ/kg (Kumar, 2010).

2.2.4.2 *Water content of bio-oil*

Bio-oil typically contains 10 % to 30 % by weight of water, which is a significant amount. The moisture content of the feedstock, the pyrolysis temperature and residence time, and the effectiveness of the separation procedures during the synthesis of the bio-oil can all have an impact on this percentage. As a result of its high-water content, bio-oil may need further processing or drying to increase its energy density and stability. This might make it difficult to utilize as a fuel (Bardalai *et al*., 2015).

2.2.4.3 *Viscosity of bio-oil*

The viscosity of bio-oil is the property that determines the characteristics of flow quality of bio liquid. The inherent bio-oil viscosity obtained from biomasses does not depend largely on the type of reactor rather on other parameters. The parameters include: biomass feedstock, ageing of bio-oil, temperature, condensation, electrostatic precipitator (ESP) and water content (Bardalai *et al*., 2015).

Biomass feedstock refers to a smaller size of biomass, and the smaller size gives a highly viscous oil. When bio-oil is kept or stored for a certain period of time, its quality changes due to this ageing effect. The viscosity significantly increases continuously with the increase in storage duration because, during storage, the volatile substance and the water present in the bio-oil get the opportunity to evaporate, and thus the liquid becomes more viscous.

Viscosity also increases by condensing the vapour at a very low temperature, such as -5 ^{0}C. The installation of electrostatic precipitation (ESP) is to improve the quality of bio-oil in terms of calorific value, but it seriously affects the viscosity by increasing the viscosity content to a high value (Yin and Liu, 2013).

Several methods were applied to reduce the viscosity of bio-oil; for instance, the addition of polar solvents like methanol or acetone reduces the viscosity of bio-oil but, at the same time, exerts influence on other bio-oil properties. The use of a hot vapor filter is another technique for reducing the viscosity of the pyrolysis oil. The effect of temperature occurs when the temperature increases and the viscosity continuously reduces. For example, a viscosity of 0.0132 N·s m^{-2} measured at a temperature of 40 ^{0}C continuously decreases to 0.002 N·s m^{-2} when the temperature rises to 90 ^{0}C.

2.2.4.4 *Acidity of bio-oil*

The pH level or quantity of acidic chemicals in bio-oil are both considered indicators of the oil's acidity. The pH scale, which spans from acidic to neutral, is commonly used to gauge the acidity of bio-oil. While pH readings below 7 imply acidity and those above 7 suggest alkalinity, pH 7 is regarded as neutral. Depending on the type of feedstock utilized and the particular pyrolysis circumstances, the pH of bio-oil can change. The presence of organic acids and other acidic chemicals, which are created during the thermal degradation of biomass, affects the acidity of bio-oil. Acetic acid, formic acid, levulinic acid, and other acids are examples of these acidic substances (Park, 2004).

2.2.4.5 *Density of bio-oil*

The density of bio-oil could be explained as the degree of compactness of a substance in a specific amount in the oil. The degree of compactness of a substance in the oil affects the energy value of the oil; for example, two different oils could have the same heating value but different energy quantities as a result of variations in density. The density of bio-oil always decreases with an increase in temperature and increases by condensing at low temperatures (García-Parez, 2002).

Unlike other bio-oil properties such as acidity, pH, heating value, and so on, the density of bio-oil is always found to remain the same within some definite range of value. For instance, the density of 1100 kg/m^3 remains the same regardless of the installation of the hot vapour filter, but by using the ESP, the density of the bio-oil increases to a higher value.

2.2.5 Application of bio-oil obtained from biomass

Asadullah *et al*. (2007) state that the use of bio-oil refers to the conversion of bio-oil into energy such as heating oil to power turbines, boilers, and other machinery as well as to produce electricity. It is also used as automotive fuels, bio-refineries, and chemicals as a substitute for heavy fuel oil (Freel *et al*., 1996).

Bio-oil is now not economically viable in Europe and the US because of the cheap price of natural gas, but Brazil uses more bio-oil than any other country in the world due to its abundant biomass, low cost, and expensive natural gas. Again, subsidies for the utilization of bio-oil are currently being introduced to encourage the patronage of bio-oil (Muggen, 2015).

2.3 Plastics

Plastics are synthetic materials composed of various organic polymers, such as polyethylene, nylon, and so on. Plastics are a diverse group of materials with various properties and applications.

2.3.1 Pyrolysis of plastic

Plastic materials are heated to high temperatures between 300^0C and 600^0C during the thermal degradation process known as pyrolysis. Pyrolysis is one of the methods used to recycle or manage plastic waste, offering potential environmental benefits and resource recovery (Sharuddin *et al.*, 2016).

2.3.2   Co-pyrolysis

Co-pyrolysis is the decomposition of more than one material feedstock in a pyrolyser in order to produce an improved pyrolysis oil or bio-oil (Abnisa *et al.*, 2014; Hassan *et al.*, 2016). Co-pyrolysis of a blend of two or more biomass and plastic feedstocks generally produces bio-oils of higher quality and yield than pyrolysis of biomass alone (Sun *et al.*, 2013).

2.3.3 Pyrolysis parameters

Pyrolysis parameters include temperature, reaction time, heating rate, and particle sizes.

2.3.3.1 *Effect of pyrolysis parameters*

The temperature provides the heat of decomposition of a material during the pyrolysis process

(Aktar and Amin, 2012). It was confirmed that low temperatures favor the formation of heavy solid char products, whereas high temperatures usually increase the yield of bio-oils though (Montoya *et al*., 2015). However, for plastics, their decomposition temperature is slightly higher than that of most biomass. The optimum temperature for plastic is in the range of 450 ºC to 650 ºC, (Miandad *et al*., 2016 and Xue *et al*., 2015).

2.3.3.2 *Effect of heating rate*

Heating Rate is an essential parameter in pyrolysis because it can significantly influence the pyrolysis reactions and product distribution. Different heating rates can lead to varying yields of gases, liquids, oil, and solid char. High heating rates result in rapid thermal degradation of the feedstock, leading to shorter reaction times and higher yields. On the other hand, lower heating rates allow for a more gradual and controlled decomposition, which can favor the formation of higher molecular weight products, such as biochar or heavy hydrocarbons. Some researchers have investigated the effect of heating rate on pyrolysis. Montoya *et al*. (2015) reported that slow pyrolysis typically has HR between 1^0C/s and $100\,^0$C/s, while fast pyrolysis requires heating rates above 1000 ºC/s.

2.3.3.3 *Effect of reaction time*

Pyrolysis reaction time refers to the period for which the feedstock, such as plastic waste, biomass, or other organic materials, is subjected to the pyrolysis process. It is the time taken for the thermal degradation and decomposition of the feedstock to produce the desired pyrolysis products, such as gases, liquids, and solids. It is a critical parameter in the pyrolysis process, as it directly influences the extent of thermal degradation and the yield of different products. Longer reaction times generally lead to more complete pyrolysis and a higher

conversion of the feedstock into valuable products. Conversely, shorter reaction times may result in incomplete pyrolysis and lower product yields (Montoya *et al*., 2015).

There are two fundamentals in reaction time: fast and slow pyrolysis. In fast pyrolysis, which is conducted at higher temperatures and rapid heating rates, the reaction time is relatively short, typically on the order of seconds to a few minutes (Montoya *et al*., 2015).

2.3.3.4 *Effect of blending ratio biomass and plastic*

The blending ratio refers to the proportion of biomass and plastic in the feedstock mixture. The blending ratio directly affects the composition of the pyrolysis products. Biomass and plastic have different chemical structures and thermal behaviors, leading to varying product distributions. Higher biomass content typically results in increased production of bio-oil and char, while higher plastic content leads to more hydrocarbon gases. By adjusting the biomass-to-plastic ratio through co-pyrolysis, it improves the quality of bio-oil (Dewangan *et al*., 2016). It was reported by supermoon *et al*. (2015) that co-blending maximizes bio-oil.

2.3.3.5 *Effect of particle size on pyrolysis*

The particle size of the feedstock can influence the distribution of pyrolysis products. Smaller particles may favor the production of more volatile compounds, such as gases and liquid oils, while larger particles may favor the production of char and heavier hydrocarbons. This is due to incomplete decomposition and average particle size, favors quality and quantity of bio-oil (Montoya *et al*., 2015).

2.4 Clay minerals

Clay minerals are a group of naturally occurring minerals that are characterized by their fine particle size and layered structure. They are classified as phylosillicates, which are a type of sheet silicate mineral. Clay minerals are abundant in nature and are commonly found in soils, sediments, and rocks (Holtz and Kovacs, 2010). The basic building block of clay minerals is a sheet-like structure composed of two-dimensional layers. Each layer consists of a stack of tetrahedra and octahedra. In the tetrahedral layer, silicon (Si) atoms are surrounded by four oxygen (O) atoms, forming a tetrahedral arrangement. In the octahedral layer, aluminum (Al) or magnesium (Mg) atoms are surrounded by six hydroxide (OH) groups, forming an octahedral arrangement. The layers are held together by weak electrostatic forces, allowing them to slide past each other (Holtz and Kovacs, 2010). The most common types of clay minerals include kaolinite with a sheet-like structure of 1:1 (Holtz and Kovacs, 2010), illite of 2:1 (Uddin, 2008), and bentonite of 1:2 (ref). Each clay mineral has unique characteristics and properties. For example, kaolinite is known for its low shrink-swell capacity and is used in ceramics and paper production. Bentonite clays are highly expandable clays, and they are used in various applications, including drilling fluids, and as a binder in foundry molds.

2.5 Zeolite

 Zeolites are crystalline aluminosilicate minerals that have a porous structure with well-defined channels and cavities. They are widely used in various industrial applications, including catalysts, adsorbents, ion-exchange materials, and molecular sieves. The production of zeolites typically starts with silica (SiO_2) and alumina (Al_2O_3). These raw materials can be derived from natural sources like clays and volcanic ash or synthesized from chemicals (David, 2007).

2.5.1 Zeolite production

Zeolites are crystalline aluminosilicate minerals that have a porous structure with well-defined channels and cavities. They are widely used in various industrial applications, including catalysts, adsorbents, ion-exchange materials, and molecular sieves. The production of zeolites typically starts with silica (SiO_2) and alumina (Al_2O_3). These raw materials can be derived from natural sources like clays and volcanic ash or synthesized from chemicals.

Hydrothermal production: Hydrothermal production is the most widely employed method for producing zeolites. It involves mixing a source of silica, alumina, and other required components with water or a solvent to form a gel. The gel is then subjected to hydrothermal conditions, typically at elevated temperatures of 90 – 180 ºC, and pressures of 15 bars, in an autoclave or reactor. The reaction conditions promote the growth of zeolite crystals in the gel. The choice of reactants, reaction conditions, and the addition of structure-directing agents or templates can influence the specific type of zeolite formed.

Sol-Gel Production: The sol-gel method is another common technique for zeolite production. The sol is prepared by hydrolyzing alkoxides or metal salts in a suitable solvent. The resulting gel is then aged and dried to remove the solvent, followed by calcination to form the zeolite crystals (Cejka and Zone, 2010).

Ion-Exchange and Template Methods: Zeolites can also be synthesized through ion-exchange or template methods. The exchange of cations takes place, resulting in the desired zeolite with the desired cation composition. Template methods involve using organic molecules or

surfactants as structure-directing agents to control the formation and structure of zeolites. The organic molecules or surfactants form micelles or templates around which the zeolite crystals grow, allowing for control over the pore structure and shape of the zeolite (Cejka and Zone, 2010).

The selectivity of a zeolite catalyst refers to its ability to favor specific reactions or produce desired products while minimizing unwanted side effects. Zeolites have well-defined pore structures with different sizes and shapes. The pore size determines the size of molecules that can enter and interact with the catalyst. Smaller pores may restrict the access of larger molecules, leading to higher selectivity for smaller reactants. Zeolites contain active sites, either Bronsted or Lewis sites, on their surfaces where catalytic reactions occur. The nature and strength of these active sites, such as acid or base sites, influence the selectivity. Different active sites can promote specific reactions or favor certain intermediates, leading to higher selectivity towards desired products (Anderson *et al*., 1979). The silicon-to-aluminum ratio (Si/Al ratio) in zeolites affects their acidity and catalytic behavior. Higher Si/Al ratios result in lower acidity and can influence the selectivity of reactions.

2.5.2 Zeolite classification

Zeolites are classified based on various criteria, including their composition, structure, and application.

1. **Composition-based classification:**
   a. Aluminosilicate zeolites: These zeolites contain aluminum (Al) and silicon (Si) in their framework structure. They are the most common type of zeolites.

b. non-aluminosilicate zeolites: These zeolites substitute aluminum with other elements like boron (B), gallium (Ga), iron (Fe), or titanium (Ti) in their framework structure.

2. **Structure-based classification:**

a. Zeolite framework type (zeolite code): Zeolites are assigned a unique three-letter code, known as the International Zeolite Association (IZA) code, based on their framework structure. For example, ZSM-5, FAU, MOR.

b. Pore size and shape: zeolites can be classified based on their pore sizes and shapes, such as microporous (pores less than 2 nm), macroporous (pores larger than 50 nm), or mesoporous (pores in the range of 2 to 50 nm) (Ruren *et al*., 2007).

3. **Application-based classification:**

a. Catalytic zeolites: zeolites are utilized as catalysts in a variety of industrial processes, including chemical synthesis, petrochemical refining, and environmental applications.

b. Adsorbent zeolites: zeolites employed for gas separation, adsorption of molecules, and purification processes.

c. Ion-Exchange zeolites: zeolites with ion-exchange properties used for water softening, purification, and ion separation applications.

d. Molecular Sieves: zeolites with well-defined pore sizes used for molecular sieving and selective adsorption of specific molecules.

4. **Based on acidity (Si/Al ratio)**

   Low silica: Si/Al ratio of 1.0 to 1.5, as an illustration in zeolite X intermediate silica, for instance, has a Si/Al ratio of 2.0 to 5.0. Y zeolite Si/Al ratio of 10 to 250 indicates high silica, as in zeolite ZSM5. Extreme cases of pure-silica zeolites, such as silicate-1, have also been found (Xu *et al.,* 2007).

2.5.3 Application of zeolite

Zeolites unique characteristics and adaptability make them suitable for a variety of uses.

1. Catalysis: zeolites are extensively used as catalysts in various chemical reactions. Their porous structure and active sites facilitate molecular adsorption and catalytic transformations. They find applications in petrochemical refining, synthesis of fine chemicals, isomerization, cracking, alkylation, and selective oxidation reactions (Cejka and Zone, 2010).

2. Adsorption and separation: zeolites have excellent adsorption properties, making them effective for gas and liquid separation processes. They can selectively adsorb and separate molecules based on their size, shape, and polarity. zeolites are used in gas purification, air separation, natural gas dehydration, removal of volatile organic compounds (VOCs), and water treatment processes (Cejka and Zone, 2010).

3. Ion Exchange: zeolites possess ion-exchange capabilities, allowing them to selectively remove or exchange ions in solution. They are used in water softening processes to remove calcium and magnesium ions, as well as in heavy metal removal from industrial

wastewater. zeolites are also employed for nutrient management in agriculture, acting as slow-release fertilizers (Auerbach *et al*., 2003).

4. Molecular sieves, zeolites with clearly defined pore diameters are used. Depending on the size and structure of the molecules, they can selectively adsorb and separate them. Molecular sieves find applications in the drying of gases, removal of moisture from liquids, and selective adsorption of specific molecules in industries such as petrochemicals and pharmaceuticals (Mravec *et al*., 2005).

5. Environmental Applications: Zeolites have several environmental applications. They are used in adsorption-based technologies for air purification and control of odors, volatile organic compounds (VOCs), and hazardous pollutants. Zeolites are also employed in wastewater treatment processes to remove heavy metals, ammonia, and other contaminants (New York Times, 2011).

6. Construction Materials: Zeolites are incorporated into construction materials such as concrete and asphalt to enhance their properties. They improve the strength, durability, and resistance to chemical attack of these materials. Zeolite-based concrete is used in road construction, building foundations, and infrastructure projects (Andrej, 2012).

7. Personal Care and Cosmetics: Zeolites are utilized in personal care products and cosmetics for their adsorption and moisture control properties. They are found in deodorants, antiperspirants, skin creams, and oral care products (Dyer, 1988).

8. Agriculture and Animal Husbandry: Zeolites are used in agriculture as soil amendments and growth enhancers. They improve water retention, nutrient availability, and cation exchange capacity of soils. Zeolites are also employed in animal husbandry for odor control, ammonia reduction, and as feed additives (Fukushima, 1980).

2.5.4 Nature of acid sites

Acid sites, also known as acid centers or acidic sites, refer to specific chemical entities or locations that can donate protons (H+) or accept pairs of electrons (Lewis's acid sites) during chemical reactions. These acid sites play a crucial role in various chemical processes, including catalysis, adsorption, and acid-base reactions.

There are two main categories of acid sites: Bronsted acid sites and Lewis's acid sites. Brønsted acid sites are named after the Danish chemist Johannes Nicolaus Brønsted. These sites are characterized by their ability to donate protons (H+ ions) to other chemical species. The acidity arises from the presence of acidic protons (H+) attached to certain atoms, such as oxygen, nitrogen, or sulfur, on the surface of the material. Typical examples of Brønsted acid sites include -OH groups on metal oxides and zeolites (Lercher and Jentys, 2002). While Lewis acid sites are named after the American chemist Gilbert N. Lewis. These sites can accept electron pairs from other chemical species, acting as electron pair acceptors. Unlike Brønsted acid sites, which involve proton transfer, Lewis's acid sites involve coordination of electron pairs to a vacant orbital on the acidic site. Common examples of Lewis acid sites include metal cations, such as Al^{3+} or Fe^{3+}, on metal oxide surfaces (Lercher and Jentys, 2002).

2.6 Summary of Literature and Research Gaps

Methods of biomass pyrolysis for producing bio-oil have been enumerated and described. The biomass used in the research was second generation biomass, which does not compete in terms of food availability, shortages, or environmental problems (Isikgor and Becer, 2015). The second-generation biomass, especially the non-woody *Sida Rhombifolia* (SR), was the choice in the research because it is not obtainable as food and is mainly referred to as lingo-cellulosic biomasses (Huber *et al*., 2006: Agrawal *et al*., 2019).

The challenges with bio-oil are oxygenated organic hydrocarbons with hydrogen deficiency. Hydrogen-rich materials can be used to supplement the deficiency. Again, there had been a rise in environmental concern over plastic waste generation and disposal worldwide, resulting from the rise in population and industrialization. Plastics are materials that are made of a wide range of synthetic and natural compounds. Plastics have become indispensable materials in several countries around the world due to their durability, lightweight, and flexibility. They are utilized in a range of industrial and domestic areas (Khan *et al.*, 2016).

Many researchers utilized plastic as a hydrogen donor to reduce oxygen in bio-oil. It was clearly confirmed that as a result of pyrolysis with hydrogen-rich hydrogen, the physicochemical properties of bio-oil have improved, though the oil still contains a small amount of moisture content and is waxy; hence, the oil needs to further crack to remove moisture and waxiness emanating from plastic; therefore, a zeolite catalyst is needed in the research (Sun *et al*., 2013).

Zeolite as a catalyst was used for cracking oil, adsorbents for drying, purification of gases, and bulk separation, among others. In this study, zeolite was required to crack bio-oil, just as it was for conventional hydrocarbons. This zeolite is expensive, and the supply may not be sustainable because it depends on the foreign market. On the other hand, clay is abundant in Nigeria and can be found in all the geographical zones of Nigeria. Available information in the literature does not adequately capture the synthesis of zeolite Y catalyst from locally sourced clay in Nigeria for cracking bio-oil to obtain higher quality fuel.

Zhaol *et al*. (2009) revealed the synergetic effect of catalytic co-pyrolysis of cellulose and polyethylene (PE) over HZSM-5. The study showed that catalytic co-pyrolysis of cellulose and PE improves the quality of bio-oil by decreasing the proportion of oxygenate from 92.8 to 28.3 wt. %. The zeolite catalyst used in the research of Iftikhar *et al*. (2019) and Zhao1 *et al*. (2009) was not locally sourced but rather purchased from higher chemical purity preparations. Therefore, using locally sourced zeolite catalyst from clay for catalytic co-pyrolysis of biomass with plastic is hereby advocated for.

Zhao *et al*. (2009) research demonstrated that the catalytic co-pyrolysis of cellulose and polyethylene (PE) had a synergistic effect over HZSM-5. The study showed that decreasing the proportion of oxygenate in bio-oil from 92.8 to 28.3 wt. % using catalytic co-pyrolysis of cellulose and PE, improves the quality of the oil. The zeolite catalyst used in the studies by Iftikhar *et al*. (2019) and Zhao *et al*. (2009) was not sourced locally but rather was purchased from a preparation with a higher level of chemical purity. Therefore, it is suggested here to use clay-derived zeolite catalysts from local sources for the catalytic co-pyrolysis of biomass and plastic.

Consequently, the research gaps that have been filled in this research work include:

1. Literature on *Sida rhombifolia* for bio-oil production was successfully established.

2. Literature on Bambu clay as a potential source for zeolite synthesis is currently available and being developed.

3. The production of aluminium hydroxide and sodium silicate from Bambu clay was achieved.

4. Zeolite Y-type was successfully produced from Bambu clay using a split concept.

5. Bio-oil was successfully produced from the catalytic pyrolysis of SR with LDPE and HDPE for domestic utilization.

3.0   MATERIAL AND METHOD

3.1   Material

The major material used for this research work are

I. The clay sample obtained from the clay deposit in Wamba Local Government Area (LGA), *Sida rhombifolia*, LDPE and HDPE in Lafia LGA of Nasarawa State were presented in Figure 3.1

Figure 3.1: Location of SR, LDPE, HDPE and Clay in Nigeria and Nasarawa State Map

II. Table 3.1 present the analytical grade chemical and reagents used in the study.

Table 3.1: Chemical and Reagents

s/n	Materials	Source
1	Distilled water and deionized water	Laboratory of National Cereals Research Institute (NCRI) Badeggi, Nigeria.
2	Ice block	Laboratory National Crereals Research Institute (NCRI) Badeggi, Nigeria.
3	Concentrated sulfuric acid	Sigma-Aldrich, GLobal Chemie, 98%
4	Sodium hydroxide pellets	Sigma-Aldrich, Lobal Chemie,$\geq$ 98%
5	Barium chloride	Chem. Light California, USA
	Ammonium Chloride	Chem. Light California, USA
6	Commercial Zeolite Y	Kaduna Refinery and Petrochemical Company (KRPC)/
7	Nitrogen gas	Badeggi, Nigeria

3.1.1 Equipment

The major equipment used for this study are: Pyrolyser, Improvise Pyrolyser Reactor, Fourier Transform Infrared Spectroscopy (FTIR), X-Ray Diffractormeter (XRD), X-Ray Flourescence (XRF), Muffle Furnace, Brunauer-Emmett-Teller (BET) Nitrogen Absorption Analyser, Orbital Shaker, Scanning Electron Microscopy (SEM) are presented in Table 3.2.

Table 3.2: List of Equipment, uses and location

S/n	Equipment (Model and Manufacturer)	Uses	Location
1	Gallenkamp Pyrolyser reactor, (9735 LMF 3 EER -2)	For pyrolysis of *sida rhombifolia*, LDPE and HDPE	National Cereals Research Institute (NCRI), Badeggi. Nigeria
2	Improvised pyrolysis reactor	For catalytic co-pyrolysis of Sida *rhombifolia* with LDPE and HDPE	Kaduna Polytechnic, Kaduna State
3	Stainless Steel reactor	length 150mm, internal diameter 41mm, external diameter 45mm	locally constructed (AZ blacksmith)
4	Mufle Furnace Zhong (Xingwelye Instrument Co. LTD).	Heating of materials at high temperatures greater than 200 ^{o}C	Isa Mustapha Agwai Polytechnic, Lafia. Nasarawa State.
5	Laboratory Oven (TF-9023A Techinel & Technel USA).	For calcination of materials at higher temperature up 1500^0C	Isa Mustapha Agwai Polytechnic, Lafia. Nasarawa State.
6	Miller, (Thomas model 4 Wiley mills)	Reducing the size of samples	NCRI Badeggi. Nigeria
7	Weighing balance	Measuring sample weight	Isa Mustapha Agwai Polytechnic, Lafia. Nasarawa State
8	Stop watch	monitoring time	NCRI Badagery, Mustapha Agwai Polytechnic, lafia and Federal Polytechnic Kaduna.
9	Nitrogen cylinder		

Table 3.2: List of Equipment, uses and location

S/n	Equipment (Model and Manufacturer)	Uses	Location
10	X-ray diffraction machine (XRD)	(i) Determination of structures, phases minerals, crystallinity in samples of the minerals.	National Geological Science Research laboratory Kaduna State
11	X-ray fluorescence machine (XRF)	Chemical analyses of materials	Geological Laboratory Kaduna State
12	Hot plate with magnetic stirrer, (AMTAST, MS300)	For heating the samples while stirring.	Isa Mustapha Agwai Polytechnic, Lafia. Nasarawa State
13	Brunauer-Emmett-Teller (BET) Machine. (QUANTACHROME, NOVA4200e Made in USA)	Surface area and pore size measurements and analysis of materials	Centre for Genetic Engineering and Biotechnology, FUT Minna.
14	Fourier Transformed Infrared Radiation (FTIR)	Determination of functional groups and bonding systems in materials	Geological Laboratory Kaduna State
15	Scanning Electron Microscope (SEM)		Sultanate Qaboose University (SQU). Oman
16	Thermo-gravimetric Analyzer. (PerkinElmer TGA 4000 Made in Netherlands)	(i) Determining materials thermal stability	Biotechnology, FUT Minna.
17	Gas Chromatograph Mass Spectroscopy (GCMS). (Agilent-Technologies USA).	GC-MS was used to; Separate complex mixtures, identify the components at a molecular level, unknown peaks and determine trace levels of contamination.	Chemistry Multi-purpose lab ABU Zaria
18	Laboratory Thermometer (Mercury-Free Celsius Scale Spirit Thermometer)	Temperature Measurements	Isa Mustapha Agwai Polytechnic, Lafia. Nasarawa State
19	Heating mantle with voltage regulator (500mL capacity),		Isa Mustapha Agwai Polytechnic, Lafia. Nasarawa State
20	List of apparatus: Beakers, Measuring cylinders, Conical	For synthesis of zeolite catalyst from raw bamboo clay	Isa Mustapha Agwai Polytechnic, Lafia. Nasarawa State
21	Gass Chromatography and Mass Spectroscopy	For analysis of bio-oil from zeolite catalyst	Afe Babalola University Ekiti

3.2 Method

The experimental procedures employed for this research are presented as follows:

3.2.1   Preparation of *Sida Rhombifolia* (SR)

Sida rhombifolia (SR) was collected from Shabu along Jos Road in Lafia, Nasarawa State. The SR are presented as shown in Plate I. Prior to pyrolysis, SR was sun-dried, and all adhering dirt was removed and milled to smaller particle sizes ranging from 0.1–8.0 mm so as to investigate the effect of pyrolysis parameters. The *sida rhombifolia* from the growing site in Nasarawa State is presented in Plate I (a) and Plate I (b) as dry *sida rhombifolia*.
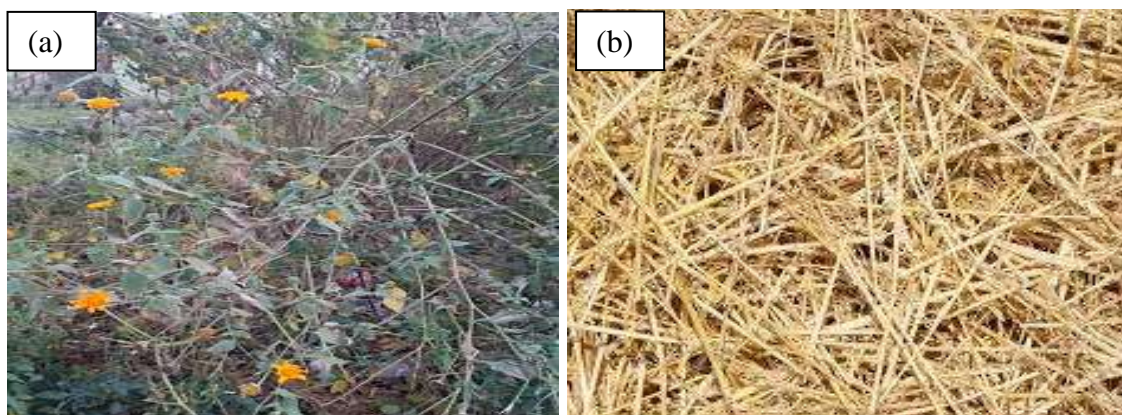
Plate 1 (a) Wet *Sida Rhombifolia*   **(b)** Dry *Sida Rhombifolia*

3.2.2 Proximate and Ultimate analysis of SR, LDPE and HDPE

3.2.2.1 *Proximate analysis of SR, LDPE and HDPE*

Proximate and ultimate analyses provide valuable information about the energy content and elemental composition of the samples.

Moisture content determination: The moisture content analysis was carried out by weighing an empty, clean, and dry crucible (W_1). The samples of materials (SR, LDPE, and HDPE) were added to the crucible of a drying oven at a specified temperature of 1100 °C for a period of 3 hours, and the combined weight (W_2) was recorded. After the drying, the crucible was removed and allowed to cool in a desiccator to avoid moisture uptake from the atmosphere. Thereafter, the crucible with the dried sample was weighed as (W_3). The moisture content was calculated of the using the formula as

$$\text{Moisture content (\%)} \quad MC = \left(\frac{(W2-W1)}{W2-W3}\right) \times 100 \tag{3.1}$$

Ash content determination: The ash content was determined by weighing an empty, clean, and dry crucible (W_1). The sample of materials was added to the crucible and inserted in a muffle furnace, set at a high temperature of 550 °C for 4 hours, and the combined weight (W_2). After the ashing process is completed, the crucible is allowed to cool in a desiccator, and the crucible is weighed with the ashed sample (W_3). The calculation of the ash content was done using the formula:

$$\text{Ash Content (\%)} = AC = \left(\frac{(W2-W1)}{W2-W3}\right) \times 100 \tag{3.2}$$

Volatile matter determination: The ash content was determined by weighing an empty, clean, and dry crucible (W_1). The sample of materials was added to the crucible and placed in a Bunsen burner at 950 °C under a controlled flow of air so as to remove the volatile matter and record the combined weight (W_2). After the process is completed, the crucible is allowed to cool in a desiccator, and the crucible is weighed with the matter (W_3). The calculation of the ash content was done using the formula:

$$\text{Volatile Matter (\%)} = VM = \left(\frac{(W2-W1)}{W2-W3}\right) \times 100 \tag{3.3}$$

Fixed carbon determination: The calculation of the fixed carbon content was carried out using the formula:

$$\text{Fixed carbon (\%)} = 100 - \text{Moisture Content} - \text{Ash Content} - \text{Volatile Matter} \quad (3.4)$$

3.2.2.2 *Ultimate analysis of SR, LDPE and HDPE*

The ultimate analysis provides information about carbon, hydrogen, nitrogen, sulfur, oxygen, and other elements available in the SR. The analysis involves combustion or chemical methods to convert the elements to their respective compounds, which are then measured using various instruments.

3.2.3   Thermogravimetric analysis (TGA) of SR, LDPE and HDPE

In order to study the thermal characteristics of the SR, LDPE and HDPE samples, TGA of Perkin Elmer 4000 was used. Prior to the analysis, the samples were ground into a fine, homogeneous powder and properly labeled for easy identification. 10 mg of each sample was weighed using an analytical balance. The TGA instrument was turned on and allowed to stabilize at the desired temperature range of 110 ^{o}C. Thereafter, the weighed sample was loaded into the crucible and covered the bottom of the crucible for the analysis to begin. The crucible with the sample was placed in the TGA instrument and closed in order to maintain the desired atmosphere condition. The TGA analyzer with the measurement of 10 mg of sample was heated to a temperature of 110 ^{o}C at the heating rate of 10 ^{o}C/min using Nitrogen (N_2) at mass flowing of 100 ml/min. As the TGA set-up begins heating and these samples undergo thermal decomposition, it simultaneously begins to record the temperature. Once this recording analysis is complete, the data are exported to a computer for further analysis. The data on the computer displayed the TGA analysis curves, which would be used to

identify key points such as onset temperature, peak temperature, and weight loss profiles. After the analysis, the crucible was carefully removed from the TGA setup and allowed to cool to room temperature.

3.2.4 Pyrolysis of SR

Hundred grams (100 g) of the SR was inputted inside the tubing reactor. The experiment was conducted at atmospheric pressure, temperature of 350 to 550 $^{\circ}$C and in absence of oxygen. As the temperature begins to increase, volatile vapor was equally beginning to produce. The volatiles from the reactor flows through the flexible tube and passed through condenser containing ice bath and thereby form liquid refer to as bio-oil. The oil was collected in the bottle flasks that was fitted via condenser. The parameters for pyrolysis of SR were equally investigated. These parameters are temperature, reaction time and particle size. The temperature was varied from 350 $^{\circ}$C to 600 $^{\circ}$C, reaction time from 30 to 90 minutes, average particle sizes within 1mm to 8 mm. This implies that as one parameter was varied, all others remain constant. The equation for calculation of bio-oil yield are as follows:

$$\% \text{ yield of Bio-oil} = \frac{Volume \ of \ bio \ oil \ (ml)}{Starting \ weight \ of \ SR} \qquad (3.5)$$

$$\% \text{ yield of Bio-char} = \frac{Weight \ of \ solid \ Char \ (g)}{Starting \ weight \ of \ SR} \qquad (3.6)$$

$$\% \text{ yield of gas} = 100\% - (\% \text{ bio oil} + \% \text{ Solid}) \qquad (3.7)$$

The overall pyrolysis setup was presented in Figure 3.3. With this setup as presented in the Figure, SR was pyrolyzed, co-pyrolyzed with LDPE and HDPE, and catalytically co-pyrolyzed with LDPE and HDPE.
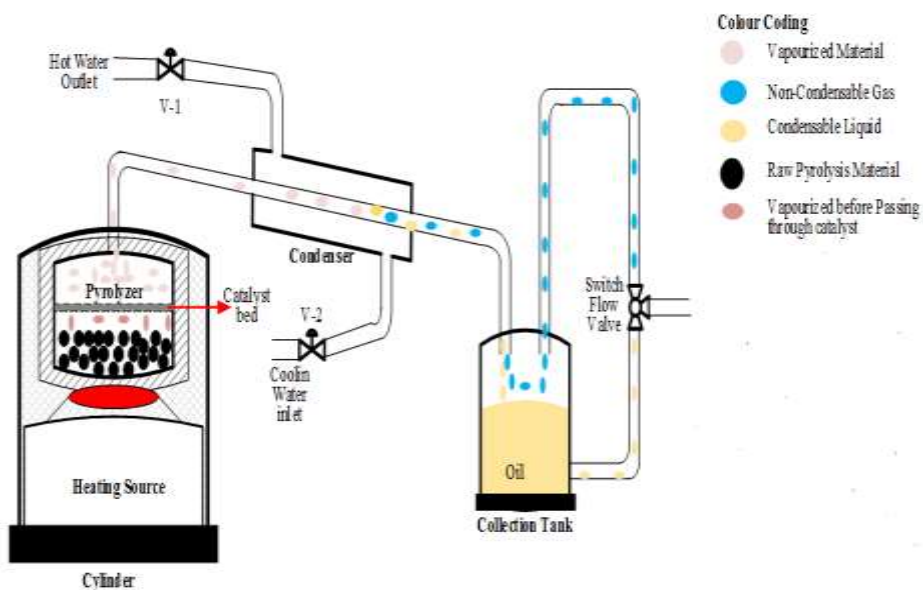
Figure 3.2: Pyrolysis set-up

3.2.6   Plastic preparation

The LDPE and HDPE are sourced from the waste. Prior to the pyrolysis of LDPE, it was collected from plastic dump site in Lafia LGA of Nasarawa State (8.5060°N', 8.5227°E'). The Low- and High-Density Polyethylene from waste dump site in Nasarawa State are presented in Plate II.

Plate II: (a) LDPE   **(b)** HDPE

Step 1: Pretreatment of LDPE and HDPE

The waste LDPE and HDPE was pre-treated by removing all the surface dirt and expose under the sun for one day. It was further washed thoroughly using distilled water and dried under the sun for three days to ensure free from water. The samples were then shredded with the aid of a scissors down to an average size. The shredded sample was sun dried for 7 days to remove any residual liquid that is adhered to the surface of the sample. The dried and shredded was milled 1- 2, 2-4, 4-6, 6-8 mm average particle sizes.

Step 2: Pyrolysis of LDPE and HDPE

The pyrolysis reactor used for SR was the same pyrolyser used for pyrolysis of LDPE and HDPE. 100 g of each run were fed into pyrolysis reactor. The volatile vapor from the pyrolysis reactor was allowed to pass through condenser and thereby condense and collected in the bottle flask that was fitted in to the condenser. The effect of temperatures for pyrolysis of LDPE and HDPE was investigated. The temperature was varied from 350 ºC, 400 ºC, 450 ºC, 500 ºC, 550 ºC, 600 ºC, 650 ºC at constant time of 60-minute interval throughout while the particle size was at 1- 2, 2-4, 4-6, 6-8 mm and heating rate 20 ºC/min for each sample of either LDPE or HDPE. The equations for the calculation of the yield are as follows:

$$\% \text{ yield of Bio-oil} = \frac{Volume\ of\ oil\ (ml)}{Starting\ weight\ of\ LDPE/HDEP} \qquad (3.4)$$

$$\% \text{ yield of Bio-char} = \frac{Weight\ of\ solid\ Char\ (g)}{Starting\ weight\ of\ LDPE/HDEP} \qquad (3.5)$$

$$\% \text{ yield of gas} = 100\% - (\% \text{ bio oil} + \% \text{ Solid}) \qquad (3.6)$$

3.2.7 Co-pyrolysis of SR with LDPE and HDPE

Co-pyrolysis was carried out in the same reactor that was utilized for the individual pyrolysis of SR, LDPE, and HDPE. The three samples are co-fed into the reactor for pyrolysis. The samples were varying at different blend ratio to ascertain the samples' synergistic effects. The ratio varies from 1:1, 1:2, 1:3, 1:4, 1:5 to 1:6 at temperature of 600 $^\circ$C.

Figure 3.1 presented the concept of pyrolysis of *Sida Rhombifolia* with Low- and High-Density Polyethylene and characterization of the pyrolysis oil.
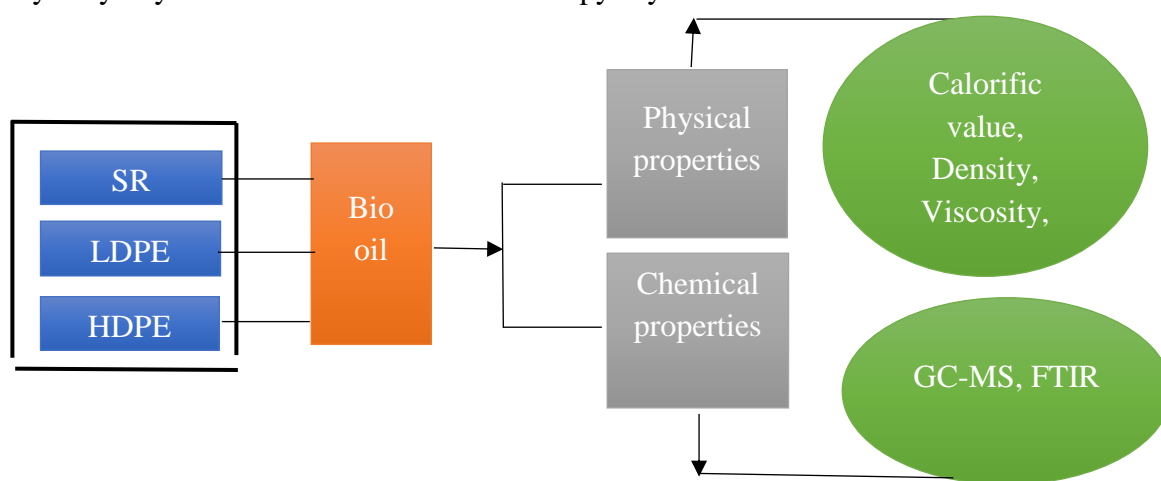
Figure 3.3: Flow chart of pyrolysis and co-pyrolysis for bio-oil production

3.2.8 Catalyst preparation

3.2.8.1 *Collection and preparation of raw clay*

Bambu clay sample was collected from the clay deposits in Wamba LGA at a depth interval of 1.0-1.5 m with the aid of a shovel and digger. The sample was sorted out by hand to minimize the possibility of contamination with sand. 50 kg of the sample was collected for the study and placed in polythene bags. For this study, a sub-sample of 10 kg was subjected to preliminary treatment involving the removal of all the dirt associated with clay and sun-

dried for one week to ensure the water in the clay had completely evaporated. The dried clay was further grinded to smaller particles for characterization so as to determine the suitability as raw materials for synthesis zeolite.

3.2.8.2 *Beneficiation of clay*

The Bambu clay was beneficiated by sedimentation technique to produce clay free from impurities. The beneficiation was conducted at clay to water ratio 100 g: 1 liter   with optimum settling time of 24 hours (Nurudeen, 2015) then vigorously stirring at 200 rpm for 3 hours. The slurries were further allowed to settle overnight as presented in Plate III.

Plate III: Beneficiation of raw Bambu clay

After settle overnight, the sample formed three clear layers; bottom coarse, middle fine and top supernatant water layers. The layers were separated by decantation, while only the middle fine layer was further processed to obtained cake. This cake was further split into smaller sizes and open dried for 3 days. The dried cake was grinded using a laboratory porcelain pestle and mortar then sieved through a 145 µm sieve.

3.2.8.3 *Metakaolinization of clay*

The meta-kaolinization was carried out at 750 °C for 4 hours in a chamber furnace for processing into metakaolin. Equation (3.9) represent the calcination process.

$$Al_2O_3 \bullet 2SiO_2 \bullet 2H_2O \xrightarrow{\text{750 °C/4h}} Al_2O_3 \bullet 2SiO_2 + 2H_2O \qquad (3.9)$$

Through complete dealumination, the metakaolin was totally divided into its silica and alumina components. Dealumination of the metakaolim was achieved by leaching out the structural alumina with sulphuric acid as presented in Plate IV.

Plate IV: Dealumination of metakaolim

3.2.8.4 *Preparation of zeolite catalyst using Bambu clay*

The zeolite catalyst was prepared from bambu clay. First and foremost, the clay underwent beneficiation, metakalonization and split method by dealumination. The product from dealumination alum and silica are further process so as to obtain a desire zeolite. The conceptual approach for synthesis zeolite was presented in Figure 3.2
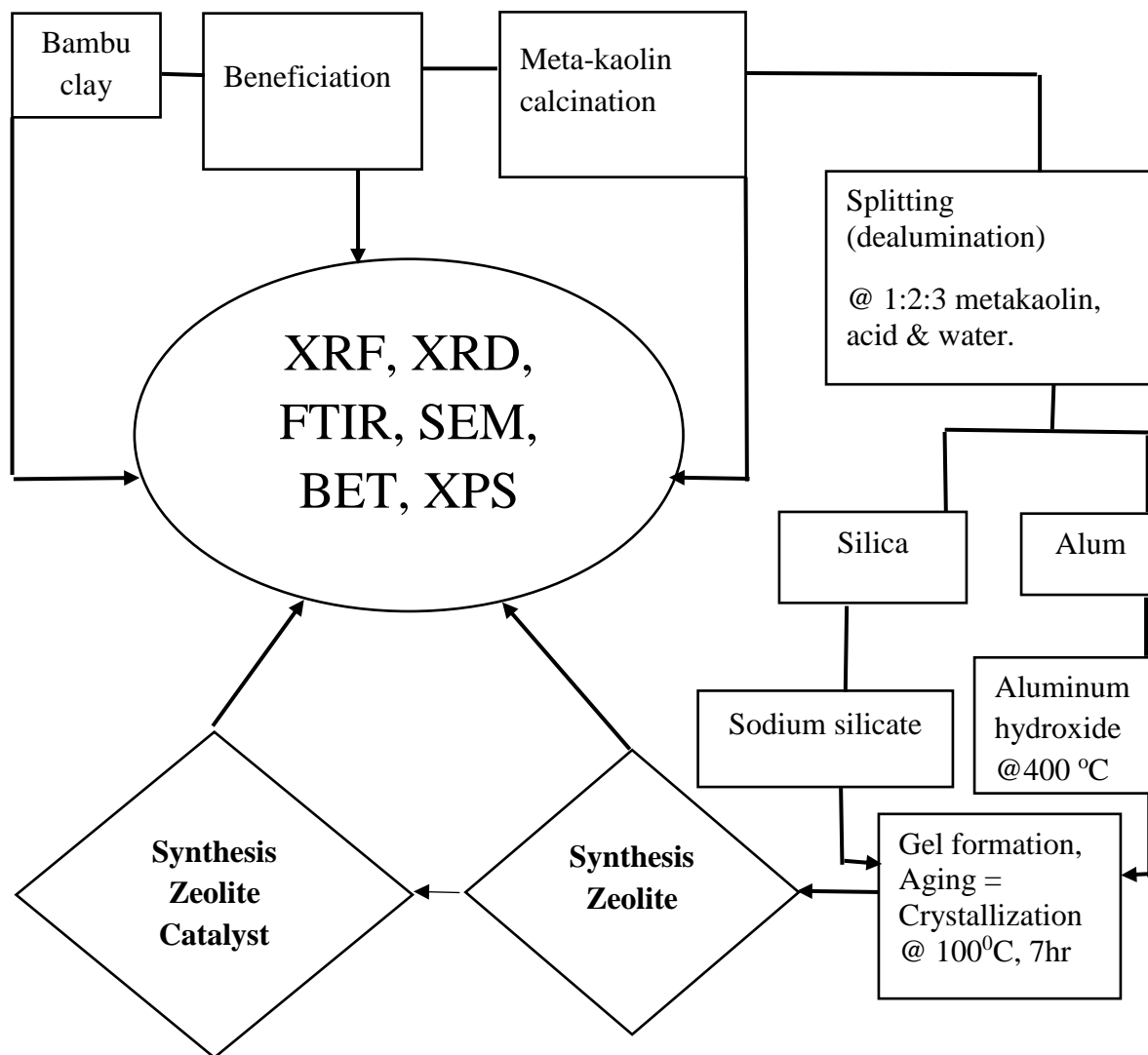
Figure 3.4: Synthesis of zeolite catalyst flow diagram from Bambu clay

3.2.8.5 *Production of aluminium hydroxide from the solution of alum*

The alum obtained from the metakaolin and sulfuric acid solution was further process to obtain aluminium hydroxide $Al(OH)_3$ as shown in Equation 3.10. The alum was titrated by 50 wt. % sodium hydroxide solution against the alum solution at room temperature with continuous stirring as presented in Plate V. The precipitated aluminium hydroxide was

further washed and dried at 110 °C for 7hr, after which the dried aluminium hydroxide was ground using ceramic mortal, then calcined at temperatures of 300 - 600 °C.

$$Al_2(SO_4)_3 + 6NaOH \longrightarrow 2Al(OH)_3 + 3Na_2SO_4 \tag{3.10}$$
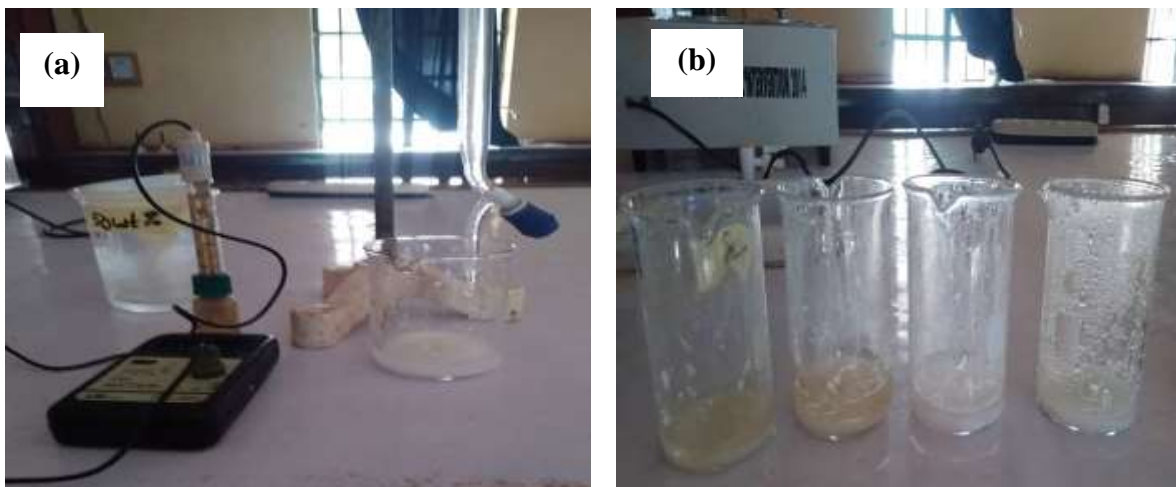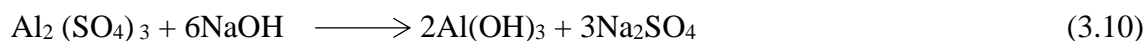
Plate V: Production of aluminium hydroxide from the solution of alum (a) titration by 50% wt. % sodium hydroxide (b) precipitation of aluminium hydroxide

3.2.8.6 *Production of sodium silicate from residue of silica*

The silica residue obtained from the initial splitting of alum and silica was also further processed to produce sodium silicate. The production of sodium silicate was achieved by leaching silica residue in a 500 ml of 2.5 M sodium hydroxide solution. The mixture was maintained at 100 °C for three hours with continuous stirring. Then the mixture was filtered to produce the sodium silicate needed for synthesis of Zeolite.

3.2.8.7 *Synthesis of zeolite Y*

The aluminium hydroxide and sodium silicate produced from Bambu clay was further used to synthesis zeolite in two steps; Seed gel and feed gel. In contrast to the feed gel, which was

prepared using a similar technique to the seed gel but with a different composition of $14Na_2O$: Al_2O_3: $14SiO_2$: $93H_2O$ and was used immediately after preparation without ageing, the seed gel was made by adding Na_2SiO_3 solution dropwise to $NaAlO_2$, $NaOH$, and H_2O to form a composition $15Na_2O$: Al_2O_3: $12SiO_2$: $173H_2O$ then aged for 24 hours at room temperature.

3.2.8.8 *Crystallization of zeolite Y*

The aged overall prepared gel was further crystallized at temperature of 100 ^oC for 7hours. The resulting zeolite was crystallized, filtered, and rinsed with deionized water. It was then dried for a day at 60 °C (Khatrin *et al*., 2020).

3.2.8.9 *Protonation of the synthesized zeolite Y*

To produce zeolite HY, the resulting zeolite underwent further protonation through ion exchange reaction. This was achieved by preparing a M solution of NH_4Cl at 80 ^oC, 20 minutes were spent stirring a solution with a 10 ml solution to 1 g solid ratio. The slurry was completely washed with distilled water after the exchange reaction had place, and a pump was used to suction filter the material. Then, it was dried for six hours at 110 ^oC and NH_4Y zeolite was obtained then calcined at 650 ^oC for two hours as the final zeolite HY. Similarly, the commercial zeolite Y was also undergoing protonation as zeolite Y catalyst for comparison in-terms of the same application.

3.2.8.10 *Characterization of clay, metakaolin and synthesis zeolite*

The clay, metakaolin, synthesis zeolite, zeolite catalyst and commercial zeolite would be characterized using the following equipment;

X-ray Diffraction (XRD): Empyrean Panalytical Multi-Purpose Research X-Ray Diffractometer (XRD) machine as presented in Plate VI was used in the study. The parameter for XRD operation such as voltage, and current were set-up for the analysis. The XRD machine was set up with computer software at copper's 1.5406 nm wavelength (Cu K-alpha). A 2.0g sample was ground, sieved to a size of 75 μm, and then powdered, in order to prepare for analysis. The machine was calibrated by pure silicon standard where the sample is loaded for scanning. The diffraction patterns were captured at 25 °C with a scanning rate of 0.05 °/s and a range of 3 - 90° on the 2-theta scale. The 2θ values was used for calculation of d-spacing for each peak and Equation 3.11 (Braggs law). This was compared between the d-spacing of known and unknown materials using usual matching of search and routine.

$$n\lambda = 2d\ sin\theta \qquad (3.11)$$

Equation 3.11 was the Scherer's equation as presented in Equation 3.12 was used for calculation of average crystallize size of the bambu clay.

$$D = \frac{k\lambda}{\beta cos\theta} \qquad (3.12)$$

Where β =full width at half maximum, θ = diffraction angle, λ = wavelength of x-ray, k = Scherer's constant.

Plate VI: Empyrean Multi-Purpose Research X-ray Diffractometer

X-ray Fluorescence (XRF) : The ARL QUANT'X EDXRF Spectrometer from Thermo-Scientific was used to determine the chemical compositions of the raw clays, beneficiated clay, and meta-kaolin, as shown in Plate VII.

The XRF machine was calibrated by measuring known reference samples with known elemental compositions to establish the instrument's response and calibration curves. The Montona soil SRM 2710 used as the Thermo-Fisher Scientific standard for reference is the accepted procedure. The sample was prepared by grinding the material into a fine powder, ensuring homogeneity, and sometimes pelletizing the powder into a solid sample. The setting of the measurement parameters such as voltage, current, and measurement time was done.

Sample Mounting: Place the prepared sample onto the sample holder or sample stage of the XRF machine. Ensure proper positioning and alignment of the sample to achieve accurate and representative analysis results. Measurement Configuration: Define the measurement

conditions based on the analysis objectives. This involves specifying the elements of interest to be analyzed, the measurement mode (e.g., wavelength-dispersive spectroscopy or energy-dispersive spectroscopy), and other parameters such as measurement time and X-ray tube settings.

Data Collection: Initiate the data collection process by starting the measurement. The XRF machine will generate X-rays, which excite the sample, causing it to emit characteristic X-ray fluorescence. The detector in the XRF machine measures the emitted X-rays, and the resulting spectrum is recorded.

Interpretation and Reporting: Interpret the XRF data to derive meaningful insights about the sample's elemental composition. Summarize the findings in a report, including the identified elements, their concentrations, and any additional analysis or interpretations. Some XRF machines may also provide elemental mapping capabilities for spatial analysis. Weighing the two grams of each sample, we then put it into a sample holder and covered it with cotton wool to stop it from spraying. To remove oxygen and moisture before putting the sample holders carrying the samples into the equipment for chemical analysis, a vacuum pump was used to run them in a vacuum for 10 minutes. The XRF machine will run the samples for a total of 10 minutes before the findings are obtained.

Plate VII: X-ray Fluorescence (XRF) for studies of sample

Brunauer Emmett Teller (BET) C : The nitrogen absorption method for BET was used to measure the surface area and pore data of samples; raw bamboo clay, beneficiated clay, metakaolin, synthesised zeolite catalyst and commercial zeolite Y. The sample of 0.5g was placed at NOVA 4200e model machine and degassed at 273 K (25 °C) for 3hrs. The instrument injected a predetermined volume of nitrogen gas into the tube while measuring the nitrogen relative pressure (P/Po) (P = equilibrium gas pressure and Po = saturation gas pressure). A plot of the specific volume against relative pressure was made by the machine using the Equation 3.13.

$$V = \frac{V_m \; x \; C_p}{(P_o - P_i)[1+(c-1)\frac{P}{P_o}]} \tag{3.13}$$

Where V is the volume of the adsorbed gas, and Vm is the volume of the adsorbed monolayer, and P is the equilibrium gas pressure, Po is the saturation gas pressure, and c is the BET constant. The equation is linearized is given in Equation 3.14.

$$\frac{1}{V[(\frac{P}{P_o})-1]} = \frac{c-1}{V_m c}\left(\frac{P}{P_o}\right) + \frac{1}{V_m c} \tag{3.14}$$

This function's slope and intercept were used to calculate the constants c and V_m, respectively: c = slope/(intercept + 1) and V_m = slope/(intercept + 1). After that, the precise surface area was determined using equation 3.15.

$$S = \frac{V_m (N \times A)}{22,400 \times m} \tag{3.15}$$

Where S = surface area, Vm A = Avogadro's number, m = mass of nanomaterial being analysed and Standard Temperature and Pressure (STP) volume of one mole of gas = 22,400.

Fourier transform infrared (FTIR) spectroscopy: Fourier Transform Infrared (FTIR) Spectroscopy analysis was conducted using the Agilent Cary 630 FTIR machine. Sample weighed 0.005 g was placed directly under FTIR probe for scanning. The Scanning was done between the wavelength 4000 – 400 cm^{-1} and the matching spectra for each sample were recorded as raw data in Excel format.

Plate VIII: Fourier Transform Infrared (FTIR) Spectroscopy for studies of sample

3.2.8.11 *Catalytic co-pyrolysis of SR with LDPE and HDPE*

Catalytic co-pyrolysis of SR with LDPE and HDPE was conducted at temperature 600 ^{0}C, reaction time 60 min, average particle sizes 2- 4 mm and optimum materials ratio of 1:1:4 (SR:LDPE:HDPE) using an improvise pyrolysis reactor. The volatile obtained from the reactor flows through the flexible tube and passed through condenser containing ice bath for condensationBambu clay, metakaolin, synthesis zeolite and commercial zeolite are used for catalytic co-pyrolysis. Table 3.4 presents the catalytic co-pyrolysis process as Raw Clay (RC), Metakaolin (M), Synthesis Zeolite (SZ) and Commercial Zeolite (CZ) respectively.

Table 3.3: Catalytic co-pyrolysis of SR with LDPE and HDPE

S/n	Samples
1	RC,
2	M
3	SZ
4	CZ
5	SZC
6	CZC

The calculations were made for products produced by the catalytic co-pyrolysis of SR with LDPE and HDPE.

$$\% \text{ yield of Bio-oil} = \frac{Volume \; of \; bio \; oil \; (ml)}{Starting \; weight \; of \; the \; blend} \tag{3.16}$$

$$\% \text{ yield of Bio-char} = \frac{Weight \; of \; solid \; Char \; (g)}{Starting \; weight \; of \; the \; blend} \tag{3.17}$$

$$\% \text{ yield of gas} = 100\% - (\% \text{ bio oil} + \% \text{ Solid}) \tag{3.18}$$

Furthermore, the optimum condition of catalytic co-pyrolysis obtained in Table 3.5 was further utilized to study the other pyrolysis techniques. These techniques are premix, non-premix and oil upgrading. The premix involves blend zeolite with *SR*, LDPE and HDPE that

is four materials are fed into pyrolyzer. Non-premix involves separating zeolite from the mixed *SR* with LDPE and HDPE that is three materials are co-fed while zeolite is placed on the bed inside the pyrolyzer. The pyrolysis of SR with LDPE and HDPE was carried out at temperature of 550 ℃, blending ratio of 1:1:4, reaction time 60 min, particle size 2- 4 mm. Table presents catalytic co-pyrolysis of samples Premix (P_1), Non-Premix (NP_1) and fuel upgrading (FU_1) respectively.

Table 3.4: Catalytic co-pyrolysis of samples P1, NP1 and FU1

s/n	Samples
1	P_1
2	NP_1
3	FU_1

3.2.8.12 *Physical properties of the bio-oil*

(i) Calorific value

The calorific value of oil was determined using the Parr 6100 Calorimeter. It was achieved by placing a crucible containing 1 ml of oil sample within a calorimeter that had been filled with oxygen and then ignited. The temperature fluctuations were noted, and the calorific value was calculated.

(ii) Viscosity

Viscosity was measured by introducing the oil sample in a glass capillary viscometer. The temperature in the capillary was maintained at 40 and 100 ℃ and the interval of time needed for a particular amount of oil sample to pass through the capillary tube was recorded.

(iii) Moisture content

The amount of water or moisture in the oil was quantified using a Karl Fischer MKS-500

Moisture Titrator. The sample of oil was inserted into titration vessel. The sample was dispersed in solvents medium containing chloro-ethanol and chloroform for formed a solution. The solution is then titrated with the iodine reagent until the water is completely removed. Since the interaction of water and iodine is on a mole-to-mole basis, therefore, the calculation was conducted by simply deducting the water content of the oil from the oil sample's initial weight.

(iv)   Flash point

A strong heat resistance glass cup and a heating mantle were used for determining the flash points of oil sample. The resistance glass cup containing oil sample was placed on the top of heating mantle. The cup was gradually heated and continuously stirring to ensure equal heat distribution inside the cup while the temperature was monitored with a thermometer. The cup was exposed to an open flame at regular temperature intervals. The temperature at which the fuel gives off a flame which does not promote combustion is recorded and the sample's flash point. The amount of temperature at which fuel ignites (promotes combustion) was recorded to indicate the ignition point of the sample.

(v)   Pour point

Pour point was determined by adding a specific quantity of oil sample to a test tube, a thermometer was inserted and sealed. The seal test tube was inserted in a freezer and monitored at regularly intervals. The pour point was observed when some traces of a cloudy suspension appeared in the test tube and the temperatures of theses appearances were recorded. Therefore, pour point is the temperature at which the oil sample freezes or solidifies.

3.2.8.13 *Chemical properties of the fuel*

(i)   Gas Chromatograph and Mass Spectroscopy (GC-MS) analysis

Gas Chromatograph and Mass Spectroscopy (GC-MS) is a technique that was employed to establish organic chemical species**.**

(ii)   Fourier transform infrared (FT-IR) spectroscopy studies of samples

FT-IR studies were conducted using the Perkin Elmer 100 FT-IR spectrometer model "two". The FT-IR probe was cleaned with ethanol and then baseline run to avoid interference. 0.005 g of sample was used for each analysis. The sample was placed directly under the probe and the scanning done. The corresponding spectra for each sample were obtained as raw data in Excel format.

3.2.8.14 *Experimental Design*

Three independent variables (factors); for the purpose of optimizing the bio-oil, pyrolysis temperature, particle size, and reaction time are taken into account. Full factorial design of experiment method was used for the optimization in-order to determine the effect of independent variables to dependent variables response that is response (bio-oil yield). The effect of the selected factors was studied using full factorial design. The levels of the factors were selected based on preliminary study. The uncoded levels of the factors are presented in Table 3,7 and Table 3.8.

Table 3.4: Uncoded level of the independent variable

Factors	Type	Level	
Pyrolysis Temperature (^{0}C)	Numeric	350	550
Particle size (mm)	Numeric	1	8
Reaction time (min)	Numeric		

Table 3.5: Uncoded level of the independent variables for catalytic co-pyrolysis

Factors	Type	Level	
A			
Pyrolysis Temperature (^{0}C)	Numeric	350	550
Blends (catalytic)	Numeric	1:1:1	1:4:6

The relationship between the selected factors and responses product yield was defined using full factorial method. Design Expert 10.0.1 software package was used for the implementation of the relationship between factors and product yield. The result of the design of experiment is presented in Table 3.9 and Table 3.10

Table 3.6: Design of Experimental of the factors in uncoded values pyrolysis

	Factor 1	Factor 2	Factor 3	Response 1
Run	**A:Temp**	**B: Time**	**C: Av. particle size**	**Yield**
	^{0}C	**Min**	**Mm**	**%**
1	600	120	4	
2	600	60	4	
3	600	60	0.5	
4	550	90	2.25	
5	600	120	0.5	
6	500	120	4	
7	500	60	4	
8	500	120	0.5	
9	550	90	2.25	
10	500	60	0.5	

Table 3.7: Design of Experimental of the factors in uncoded values for catalytic co-pyrolysis

Run	Factors			Response
	Pyrolysis Temp. (^{0}C)	**B: (C:SR:LDPE &HDPE) Ratio**	**Heating Rate (^{0}C/min)**	**Yield (%)**
1	425.00	0.20	13.75	
2	500.00	0.07	20.00	
3	500.00	0.33	7.50	
4	350.00	0.33	7.50	
5	500.00	0.33	20.00	
6	425.00	0.20	13.75	
7	350.00	0.07	20.00	
8	350.00	0.07	7.50	
9	350.00	0.33	20.00	
10	500.00	0.07	7.50	

CHAPTER FOUR

4.0   RESULTS AND DISCUSSION

The results of the research study for the production of bio-oil using locally sourced zeolite

catalyst are presented as follows;

4.1 Characterization of *Sida Rhombifolia* (SR)

The SR underwent preliminary, proximate, and ultimate analysis in order to study its

potential for bio-oil production. The analyses are presented in Tables 4.1 and 4.2.

4.1.1 Proximate analysis of SR

The proximate analysis was carried out to gather data on *Sida Rhombifolia's* potential for

producing bio-oil. As shown in Table 4.1, the analysis comprises ash, volatile matter,

moisture content, and fixed carbon. As determined by the proximate analysis, the volatile

matter was 73.50 wt. %. The volatile matters as presented in the Table were high compared

with volatile matters of other non-woody biomass, such as rice husk (68.20 wt. %) and

switchgrass (69.14 wt. %), as reported by Kumar *et al.* (2011).

The fixed carbon 23.10 wt. % which refers to the amount of carbon available in the SR. The

moisture content was 1.30 wt. % though this amount was within the acceptable limit of 15%

recommended for the production of bio-oil from biomass (Wilaipon, 2008). The ash content

of 2.10 wt. % appears to be low, which is the amount of impurity that resists burning during

and after combustion. Higher ash content in a fuel generally tend to lower calorific value of

the material.

Table 4.1: Proximate analysis of SR

Composition	Amount wt. %
Volatile matter	73.50
Fixed carbon	23.10
Moisture content	1.30
Ash content	2.10

4.1.2 Ultimate analysis of SR

Ultimate analysis provides the estimate of essential chemical elements that made up the SR. The elements are carbon, hydrogen, oxygen, nitrogen and sulphur. Table 4.2 present the ultimate analysis of SR.

The analysis shows that the carbon content was 60.00 wt. % which was higher than other non-woody biomass; rise husk (47.60 wt. %), switch grass (31.77 wt. %) as reported by Kumar *et al*. (2011). Hydrogen 5.00 wt. % and oxygen 33.98% wt. % as presented are relatively the same with other non-woods (rice husk and switchgrass). Nitrogen is 1.0 wt. % and sulphur are 0.02 wt. %. The low amount of nitrogen and sulphur indicates an environmentally friendly type of biomass, which was also explained by Enweremadu, *et al*., (2004).

Table 4.2: Ultimate analysis of SR

Elements	Amount wt %
Carbon	60.00
Hydrogen	5.00
Oxygen	33.98
Nitrogen	1.00
Sulphur	0.02

It can be concluded that the result of proximate analysis of SR indicated higher volatile content with low ash content than other non-woody biomasses such as rise husk and switch grass. The ultimate analysis also indicated SR has a high amount of carbon content, which is higher than other non-woody biomass, Hydrogen shows an equal percent with another non-woody biomass. Therefore, SR has good potential for bio-oil production.

4.1.3 Thermo-gravimetric analysis of SR

Thermo-Gravimetric Analysis (TGA) of SR was employed to study how SR responds to changes in physical and chemical properties.

The TGA analysis as presented in Figure 4.1 shows that SR responded to the temperature increase, which caused weight loss. The Figure clearly shows that the curve pattern was split into three phases. Phase one involved decomposition, which occurred between the temperatures of 49 ^{o}C - 246.57 ^{o}C. This implies that, there was gradual weight loss and that moisture was released. The second phase involved the removal of volatile components, known as degradation, as presented in the Figure. The degradation occurred within the temperature range of 240 ^{o}C to 370 ^{o}C. It was observed that degradation occurred at a temperature of 362.15 ^{o}C. As the temperature rises from 362.15 ^{o}C to 500 ^{o}C, the internal constituents of SR (hemicellulose) break more quickly, with an approximate weight loss of 72 wt.%. In fact, at this temperature, the major weight loss occurred, that is the most significant complex organic compounds, including partial lignin, were breaking down for more removal of volatile substances. The last phase occurred at temperatures above 500 ^{o}C which shows continuous removal of volatile substances from SR.

The TGA analysis guided how laboratory pyrolysis of SR could be conducted at a maximum temperature of 500 °C to obtain a high yield. Above the maximum temperature, the volatile component could decrease and consequently favor solid char. This explanation corroborated other research by Dewangan, (2014) who reported that biomass involves three main stages; elimination of moisture, decomposition of bio-polymers, and continuous volatilization.
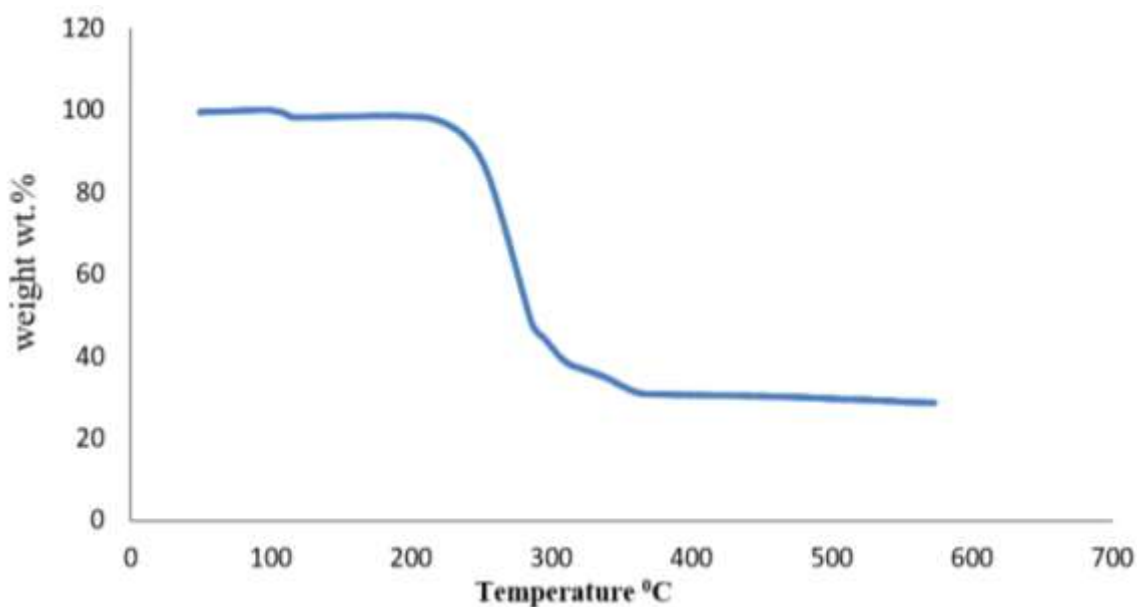
Figure 4.:1 Thermo-gravimetric analysis (TGA) of SR

4.1.4 Differential thermal analysis of SR

The Differential Thermal Analysis of SR was conducted to further detect the reaction pattern that occurred due to the difference in temperature between the constituents of SR (cellulose, hemicelluloses, and lignin) and the reference temperature. The result of DTA was presented in Figure 4.2.

It can be seen from the DTA curve presented in Figure 4.2, the decomposition of cellulose, hemicelluloses, and lignin was assigned to corresponding temperature peaks and reaction

times as presented in Figure 4.2. At 256.0 ^{o}C, endothermic reaction occurred, that is, heat absorbed by the SR resulted in the decomposition of hemicelluloses, and CO_2 and CH_2 were released. A temperature of 283.03 ^{o}C appears to be the highest temperature that was assigned to the time when the maximum decomposition rates of celluloses reached. At temperature of 380 ^{o}C corresponds to the time when the maximum decomposition rate of lignin is reached. Above 380 ^{o}C corresponds to the time when volatilisation begins up to a temperature of 500 ^{0}C as presented in the Figure. The DTA analysis of SR was slightly different from the research work presented by Bu et al. (2014).
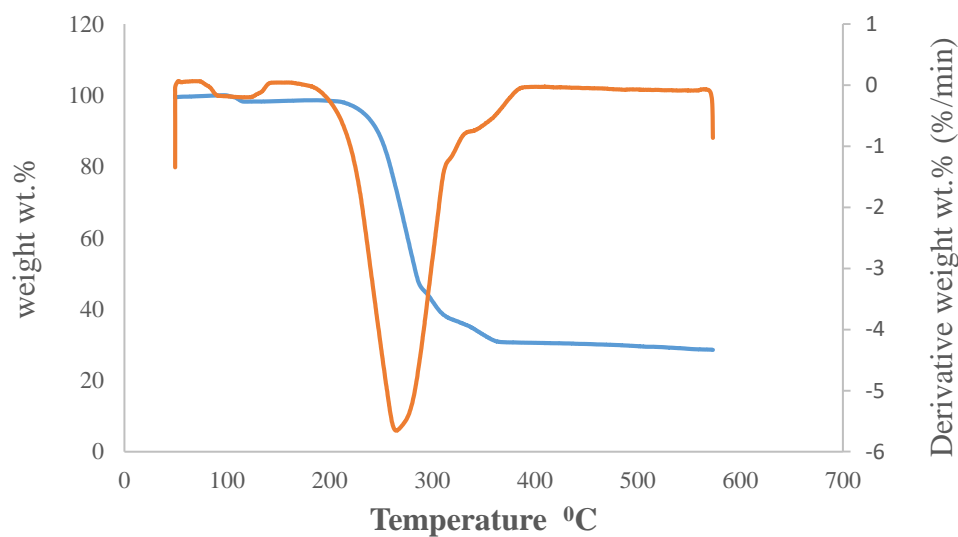
Figure 4.2: Derivative thermal analysis (DTA) of SR

4.1.5 Pyrolysis of SR

The research used the pyrolysis process to produce bio-oil from SR. The pyrolysis parameters for production of the bio-oil were investigated. The parameters in question are: heating rate, temperature, reaction time, and particle size. The results of the parameters are presented in Appendix A.1.

4.1.5.1 *Effect of temperature on pyrolysis of SR*

Figure 4.3 further illustrates the impact of temperature on the pyrolysis of SR to produce bio-oil. The figure shows that at 350 °C, the biochar yield was 49.7 wt. % and the bio-oil yield was 30.04 wt. %. This suggests that the production of bio-oil was lower than that of bio-char. A possible explanation for the low yield of bio-oil at temperatures below 400 °C, is the inadequate heat to causes the decomposition so as to generate more condensable vapor which leads to a higher yield of bio-oil. This explanation supported the TGA analysis of SR as presented in Figure 4.1 Dewangan, (2014) reported a similar assertion that low temperatures gave bio-oil a low yield.

As the temperature increases from 400 °C to 500 °C, the yield increases from 30.04 wt. % to 48.10 wt. % as the highest yield. This highest yield was due to the influence of heat that diffuses into the internal constituent of SR, which results in the rapid production of a more condensable vapor fraction. A sudden decrease in bio-oil yield from 48.1 wt. % to 46.9 wt. % as temperature increased from 500 °C to 550 °C and further decreases as temperature increased to 600 °C. Though the temperature range between 450 °C to 550 °C could be achieved depending on the nature of biomass as either woody or non-woody.

Furthermore, it was observed from the Figure that the curve shows the solid bio-char continuing to decrease from 49.7 wt. % to 29.5 wt. % between temperatures 350 °C – 500 °C due to char gasification.
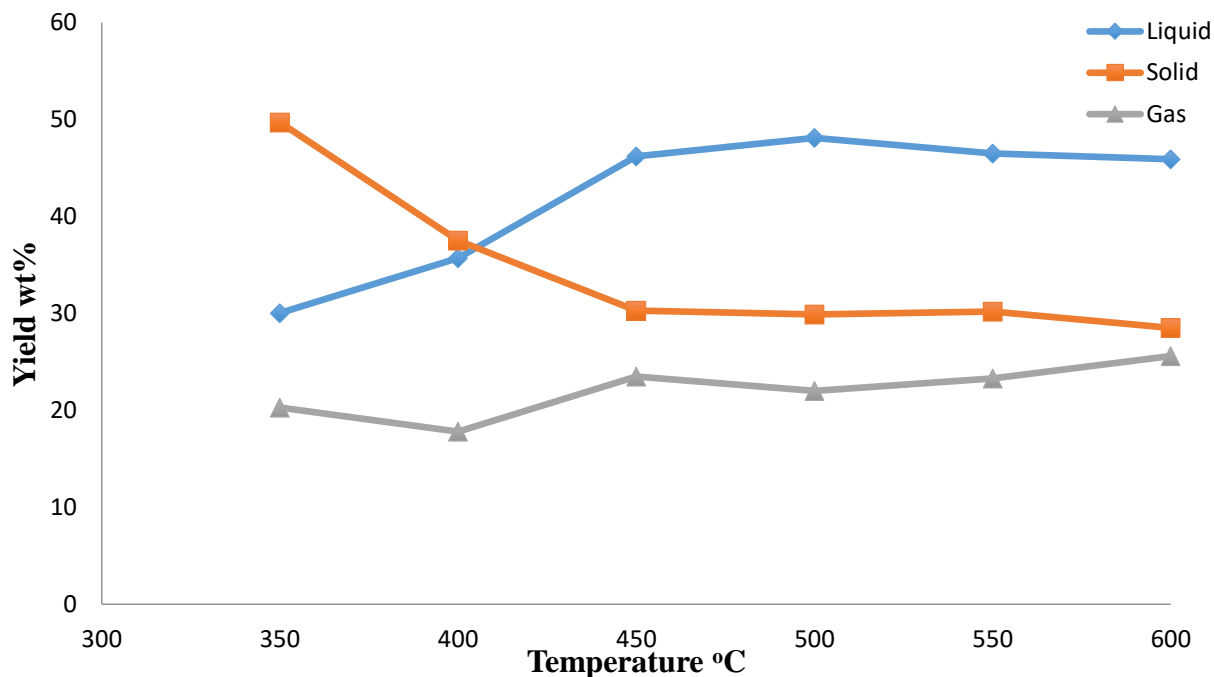
Figure 4.3: Effect of temperature on pyrolysis of SR

4.1.5.2 *Effect of reaction time on pyrolysis of SR*

The effect of reaction time was studied to understand how long SR responds to decomposition at a given temperature. The result obtained from the effect was presented in Appendix A.1 and demonstrated in Figure 4.4.

Figure 4.4 shows that the yield of bio-oil increased linearly from 33.10 wt. % to 48.30 wt. % when reaction time increased from 30 minutes to 60 minutes. Similarly, the yield of bio-oil decreased from 48.30 wt. % to 46.70 wt. % as reaction time reached 70 minutes. The yield further decreases above 70 minutes of reaction time. Therefore, it was observed that the highest yield was at peak 60 min of reaction time. At this peak, the decomposition was completed, meaning the total degradation of the SR particles had reached its maximum.

Furthermore, it was observed that as the reaction time further increases, bio-char slightly decreases and the gaseous product fluctuates. (Dewangan, 2014).
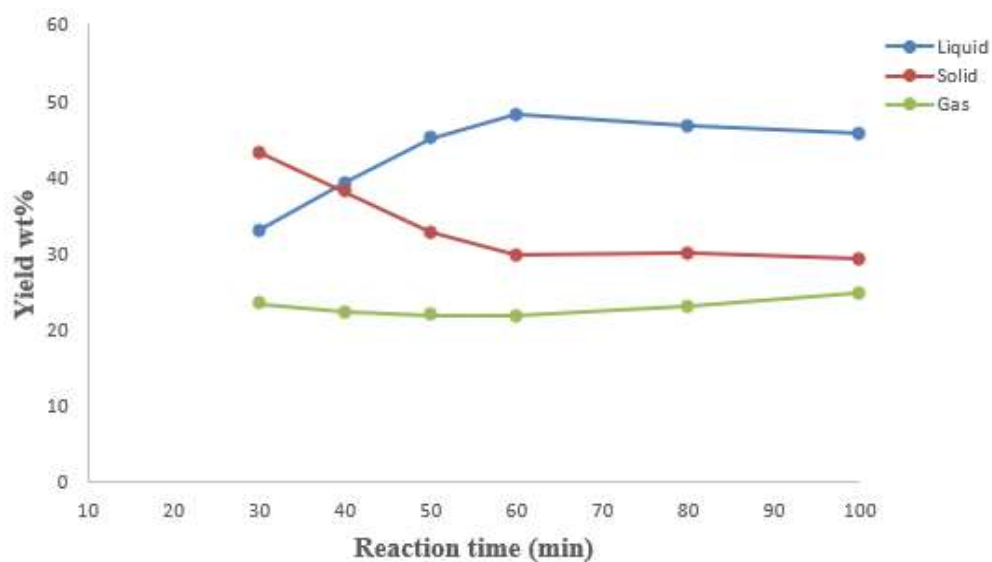
Figure 4.4: Effect of reaction time on pyrolysis at 500 °C

4.1.5.3 *Effect of particle size on pyrolysis of SR*

To comprehend the impact of various particle sizes, a study was conducted on the influence of particle size on the pyrolysis of SR, and the results are presented in Appendix A.1. The result was further demonstrated in Figure 4.5. The curve in the Figure shows that there was a corresponding increase in bio-oil from 35.2 wt. % to 50.55 wt. % when the particle size increased from 0.1 mm to 4.0 mm. It was observed that the influence of particle sizes showed a higher yield than the influence of temperature and reaction time, as presented in Figures 4.3 and 4.4. This higher yield might be explained by the influence of heat penetration at the desired range of particle sizes of SR, which favour the decomposition of the average sizes between 2 mm to 4 mm. This result also corroborated the research work of Zanzi *et al*., (2002)

who demonstrated how the nature of the biomass could influence the impact of particle size on the yield of bio-oil components, either woody or non-woody (cellulose, hemicellulose, and lignin). As particle size increases from 4.0 mm to 8.0 mm, the bio-oil yield decreases. The decrease could be attributed to the large particle size above 4 mm that resulted in less influence of heat penetration inside SR, which does not favour breakdown of large molecules (primary cracking).

The result shows that solid char decreases linearly with increasing particle size, as presented in Figure 4.5. The decrease demonstrated an inverse relationship between bio-oil and solid char. They reported that smaller particle sizes tend to produce less solid char than large particle sizes with less gaseous product. Also, Dewangan *et al*. (2016) reported that the influence of average particle sizes on the pyrolysis of biomass for decomposition in the shortest time.
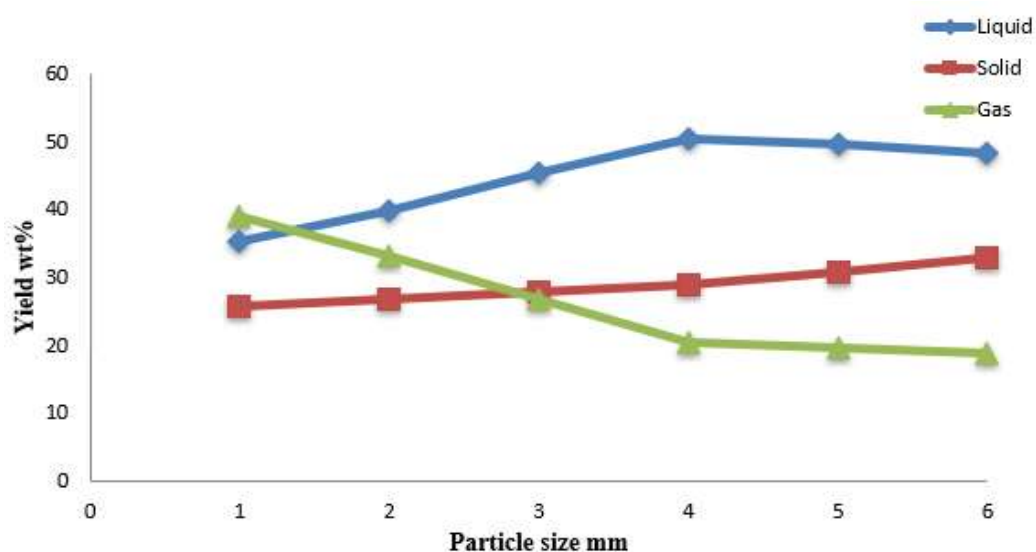
Figure 4.5: Effect of reaction time on pyrolysis of SR at 500 ^{0}C and 60 min.

It can be inferred from the effect of pyrolysis parameters that the highest temperature established for pyrolysis of SR was 500 ^{0}C, reaction time 60 min, particle size 2-4 mm, and heating rate 20 ^{0}C/min. The parameters obtained in this study were compared to those from other studies by different authors, including Dewangan, (2014) on the effects of temperature and reaction time, as well as Dewangan *et al*. (2016) on the effects of particle size. As a result, the yield of bio-oil achieved in this research effort was relatively higher than the authors' provided bio-oil yield of 47.15 wt. %.

4.2 Characterization of LDPE and HDPE

Proximate and ultimate analysis of LDPE and HDPE was conducted and presented in Table 4.3 and 4.4

4.2.1 Proximate and ultimate analysis of LDPE

Table 4.3 presents the results of the proximate and ultimate analyses of LDPE. The Table clearly shows that LDPE has a very good volatile content of 99.53 wt. %. The proximate analysis was supported by the ultimate analysis, which indicated high carbon and hydrogen correspond to 83.63 wt. % and 15.37 wt. % respectively, as presented in the Table. The amount of volatile content, carbon, and hydrogen present in the LDPE is higher than the amount present in the SR, as presented in Table 4.1. Table 4.3 indicated minimum fixed carbon of 0.84 wt. %, which implies that after pyrolysis, there will be far less solid char depending on the pyrolyser since char is a function of fixed carbon in a given sample. It was observed that LDPE was a good material for producing fuel with a higher yield.

Table 4.3: present proximate and ultimate analysis of LDPE

Proximate	Value (wt. %)	Ultimate	Value (wt. %)
Moisture content	1.24	Carbon	83.63
Volatile Content	97.39	Hydrogen	15.37
Fixed Carbon	0.84	Oxygen	0.34
Ash Content	0.53	Nitrogen	0.66
		Sulphur	0.00
Total	100		100

4.2.2 Proximate and ultimate analysis of HDPE

Table 4.4 presents the results of the HDPE's proximate and ultimate analyses. The Table shows that the HDPE has a good volatile content of 92.86 wt. %, moisture content of 1.32 wt. %, fixed carbon content of 2.14 wt. %, and an ash content of 3.68 wt. %. The ultimate analysis indicated that high carbon and hydrogen correspond to 84.63 and 15.37 wt. % while oxygen and nitrogen correspond to 0.34 wt. % and 0.66 wt. % respectively, as presented in the Table. From the Table the volatile content of HDPE was slightly lower than the volatile matter of LDPE, though higher than SR, as presented in Table 4.1. Similarly, the carbon and hydrogen contents are higher than the SR. It was indicated that HDPE was a good material for producing fuel.

Table 4.4: Proximate and ultimate analyses of HDPE

Proximate	Value (wt. %)	Ultimate	Value (wt. %)
Moisture content	1.32	Carbon	84.63
Volatile matter	92.86	Hydrogen	14.37
Fixed carbon	2.14	Oxygen	0.44
Ash content	3.68	Nitrogen	0.56
		Sulphur	0.00
	100		100

It can be concluded that the results of proximate and ultimate analyses of LDPE and HDPE have higher volatile contents as well as high carbon and hydrogen contents. LDPE and HDPE

have the potential for higher fuel yields and could be used as hydrogen donors to the oxygenated organics associated with bio-oil produced from SR.

4.2.3 Thermo-gravimetric and differential thermal analysis of LDPE and HDPE

Thermo-gravimetric analysis (TGA) was also employed to investigate how LDPE and HDPE respond to changes in their physical and chemical states. The results of TGA for LDPE and HDPE are presented in Figure 4.6. Similarly, Figure 4.7 presents the result of Differential Thermal Analysis (DTA) of LDPE and HDPE.

4.2.3.1 *Thermo-gravimetric analysis of LDPE and HDPE*

Thermo-gravimetry (TG) was used as a technique to measure the mass of LDPE and HDPE as a function of temperature or time, where temperature is a variable.

The thermal degradation of LDPE and HDPE could be described in three stages, as presented in the Figure. The first stage corresponds to moisture loss as presented in the Figure. The temperature range of the first stage started from an ambient temperature of 25 ^{o}C to about 300 ^{o}C though it was observed that there were slight changes in the mass of LDPE and HDPE at a temperature of 135 ^{o}C. This temperature of 135 ^{o}C could mark the beginning of the melting points of LDPE and HDPE. It was observed from the Figure that, at this stage of temperature, the thermal degradation curves for LDPE and HDPE were similar. In the second stage, the mass loss occurred from a temperature of 300 ^{o}C to about 500 ^{o}C where a significant drop was observed. This mass loss in the second stage was caused by the thermal decomposition of the short and long chains of hydrocarbon atoms in LDPE and HDPE. As

the temperature increased from 500 $^{\circ}$C, the mass loss was continuing at a steady thermal decomposition of the LDPE and HDPE.
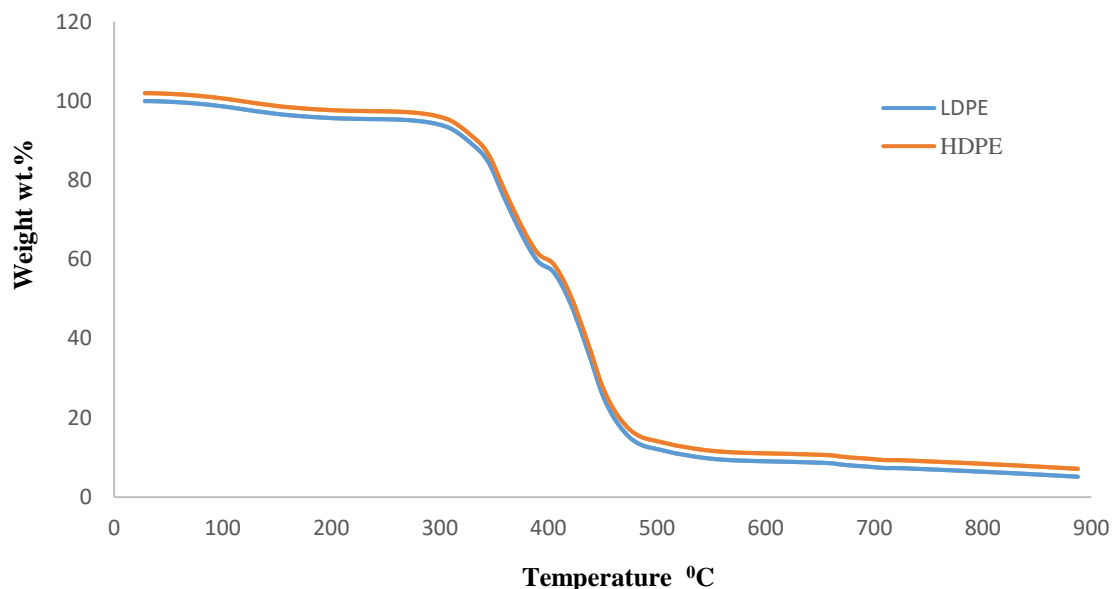
Figure 4.6: Thermo-gravimetric analysis of LDPE and HDPE

4.2.3.2 *Differential thermal analysis of LDPE and HDPE*

Differential Thermal Analysis, (DTA) was utilized to further identify the reaction pattern, whether physical or chemical, that occurred in LDPE and HDPE. The result of DTA was presented in Figure 4.7.

It can be seen from the DTA curve as presented in Figure 4.9 that the decomposition of short-chain hydrocarbons of LDPE and long-chain hydrocarbons of HDPE was assigned to corresponding temperature peaks and reaction times as presented in the Figure. At a temperature of 285 $^{\circ}$C endothermic reaction occurs, that is, LDEP and HDPE begin to absorb heat, which could result in the decomposition of hydrocarbons, though the decomposition of

LDPE started before the HDPE. At a temperature of 400 ^{o}C there appear to be the highest peaks in the thermograph, which were assigned to the time when the maximum decomposition rates of LDPE and HDPE occurred. The decomposition process continues until the temperature reaches 550 ^{o}C. It was observed that the complete decomposition of LDPE and HDPE was achieved at a final temperature of 600 ^{o}C as presented in the Figure. This explanation of the thermal decomposition of LDPE and HDPE was corroborated with the research work of Garba *et. al*., (2017).
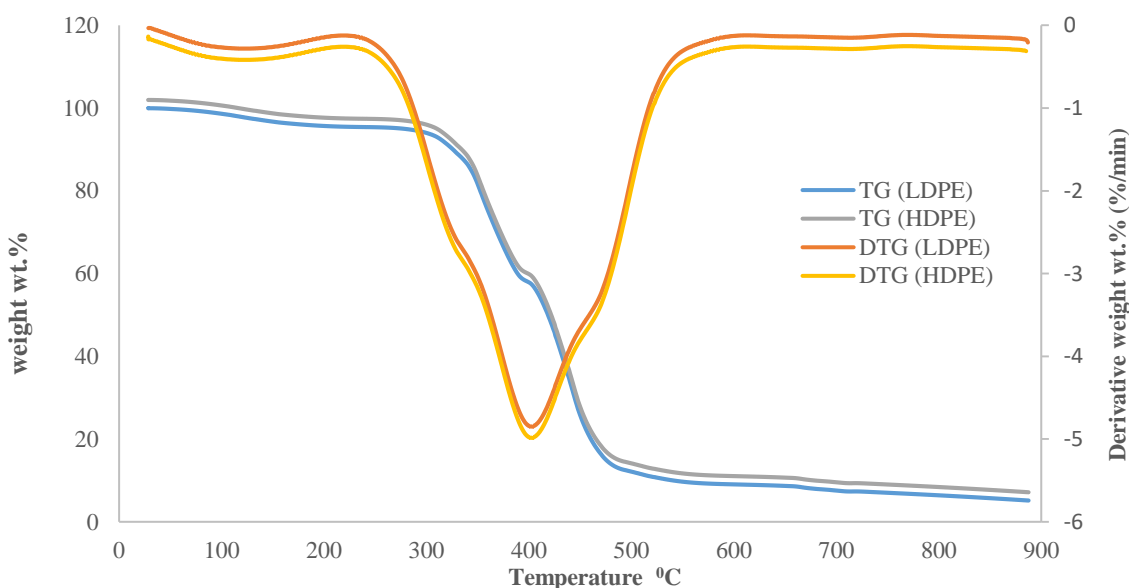
Figure 4.7: Derivative thermal analysis (DTA) of LDPE and HDPE

4.2.4 Pyrolysis of LDPE and HDPE

Pyrolysis of LDPE and HDPE were carried out so as to study the pyrolysis parameters for fuel production.

4.2.4.1 *Pyrolysis of LDPE*

The pyrolysis of LDPE was carried out between temperatures of 350 °C to 600 °C at constant reaction times of 60 minutes and particle sizes. The result of the pyrolysis of LDPE was presented in Appendix B and was further demonstrated in Figure 4.8. The result indicated that as the temperature increased from 350 °C to 550 °C, there were corresponding increases in oil yield up to 78.6 wt. %. The char decreases with corresponding increases in temperature, whereas the gaseous product increases with corresponding increases in temperature. As the temperature increases above 550 °C the yield of oil decreases, while the yield of char also decreases, but the gases increase.

The maximum yield of liquid oil found to be 78.6 wt. % at a temperature of 550 °C could be attributed to the influence of temperature that degrades the LDPE structural chain, which contains short and long chains. As the temperature increases from 550 °C to 600 °C, the liquid oil's yield suddenly decreases from 78.6 wt. % - 74.1 wt. %. The decrease could be attributed to the excessive influence of temperature on LDPE, which absorbs more heat and causes excessive degradation of the structural chain, which produces more gaseous products than liquid oil. Sogancioglu *et al*. (2017) made a similar observation that the production of liquid oil from LDPE at 550^0C and above it, decreases. The solid char decreases linearly from 11.8 wt. % to 11.10 wt. % as the temperature increases, while the gas decreases from 12.68 wt. % to 8.9 wt. % as the temperature increases from 350 °C to 600 °C.
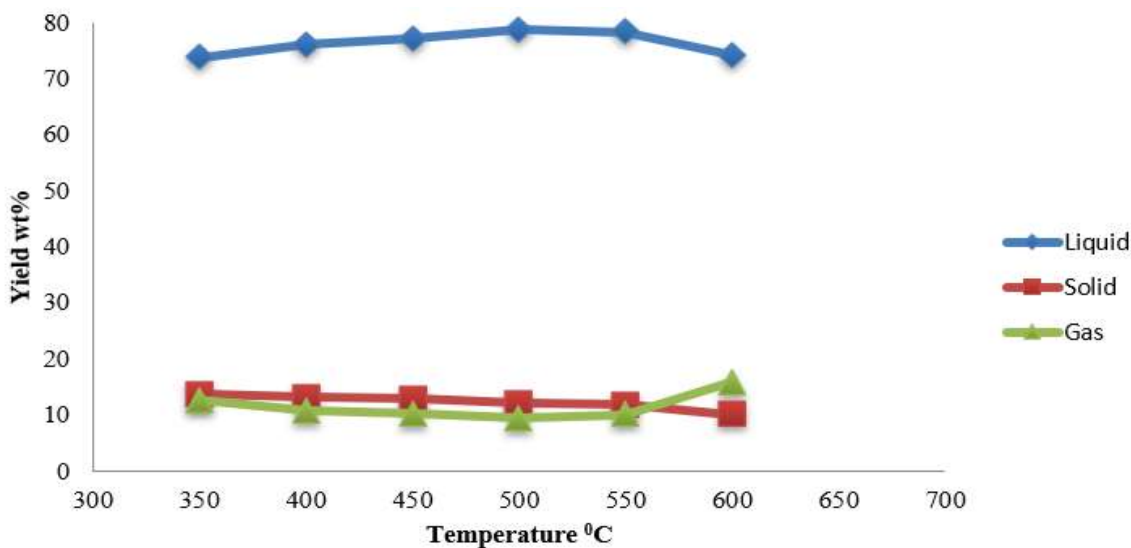
Figure 4.8: Pyrolysis of LDPE at 350-600 $^{\circ}$C

4.2.4.2 *Pyrolysis of HDPE*

The pyrolysis of HDPE was also carried out and the result of pyrolysis was presented in Figure 4.9. The curve in Figure 4.9 demonstrates that as temperature increases from 350 $^{\circ}$C to 550 $^{\circ}$C, there are corresponding increases in liquid oil yield from 70.35 wt. % to 75.20 wt. % as the highest yield. This highest yield of oil could be attributed to the influence of temperature, which degrades the structural chain of HDPE. As the temperature increases from 550 $^{\circ}$C to 600 $^{\circ}$C the oil yield decreases. As the temperature increases from 350 $^{\circ}$C to 600 $^{\circ}$C, the solid char gradually decreases as the gas increases. However, in this study, the oil yield from pyrolysis of HDPE corroborated the research work of Sogancioglu *et al*. (2017).
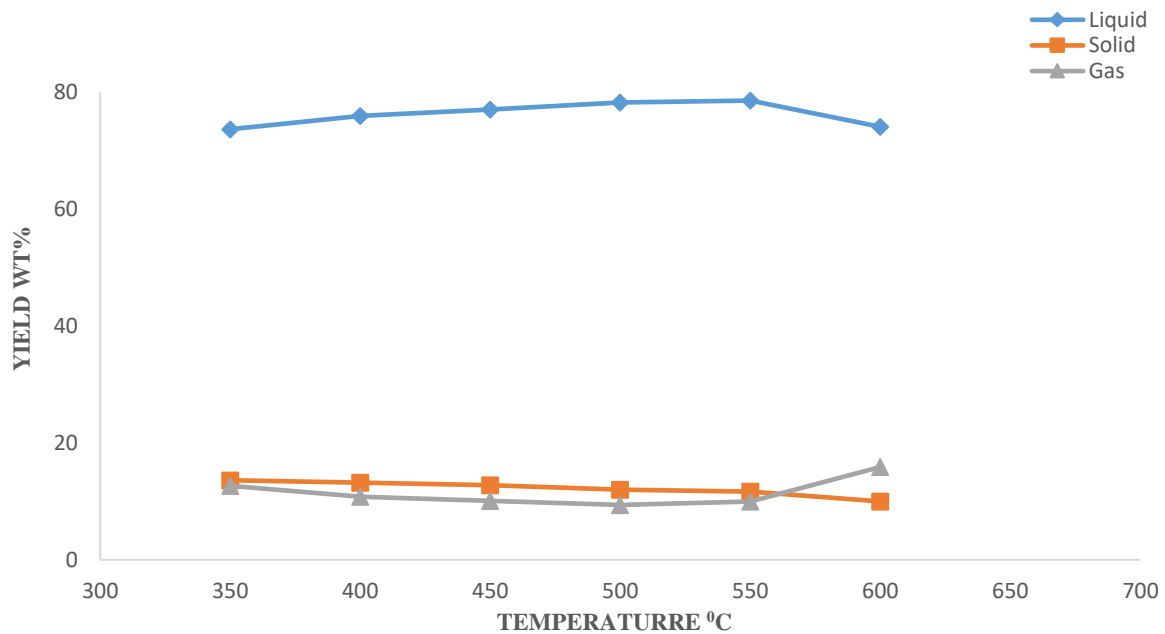
Figure 4.9: Pyrolysis of HDPE at 350 - 600 ºC

4.2.5 Co-pyrolysis SR with LDPE

The co-pyrolysis of SR with LDPE was employed to study the effective synergy between them. In-order to achieve this, different blending ratios of 1:1, 1:2, 1:3, 1:4, and 1:5 SR with LDPE were conducted. The result of the ratio SR:LDPE was presented in Appendix B. Figure 4.10 presents the co-pyrolysis of SR with LDPE.

The Figure indicates that when the blending ratio increases from 1:1 to 1:3 there was corresponding increase in liquid oil yield from 57.2 wt. % to 68.4 wt. % while the solid char increases from blend 1:1 to 1:2 corresponds to 29.1 wt. % to 31.6 wt. % though a shaft decrease was observed from 31.6 wt. % to 10.1 wt. %. The shaft decrease could be attributed to the great interaction between the major volatile components of SR and the hydrogen molecule from LPDE. In other words, the free radicals from LDPE were fully interacting

with the radicals from SR, which favor high formation of primary products (volatile). The curve also showed that the gas yield continued to increase as the blending ratio increased, which could be attributed to the presence of LDPE in the co-pyrolysis. It has been shown in the figure that gaseous products continue to increase as temperature increases.

It was observed that as the blending ratio increases from 1:3 to 1:4, the curve shows that the liquid oil slightly decreases from 68.5 wt. % to 68.4 wt. %. Similarly, slight decreases were also observed in the yield of solid char. This slight decrease implies that the interaction between the SR and LDPE begins to decrease. The curve shows that the maximum yield of the fuel obtained from the interaction between them was found to be 68.5 wt. % which was higher compare with the pyrolysis of SR alone. This was due to an increase in H/C ratio from the LDPE structural chains (short and long chains) that allowed the transfer of more hydrogen to oxygenated organics associated with bio-oil from SR
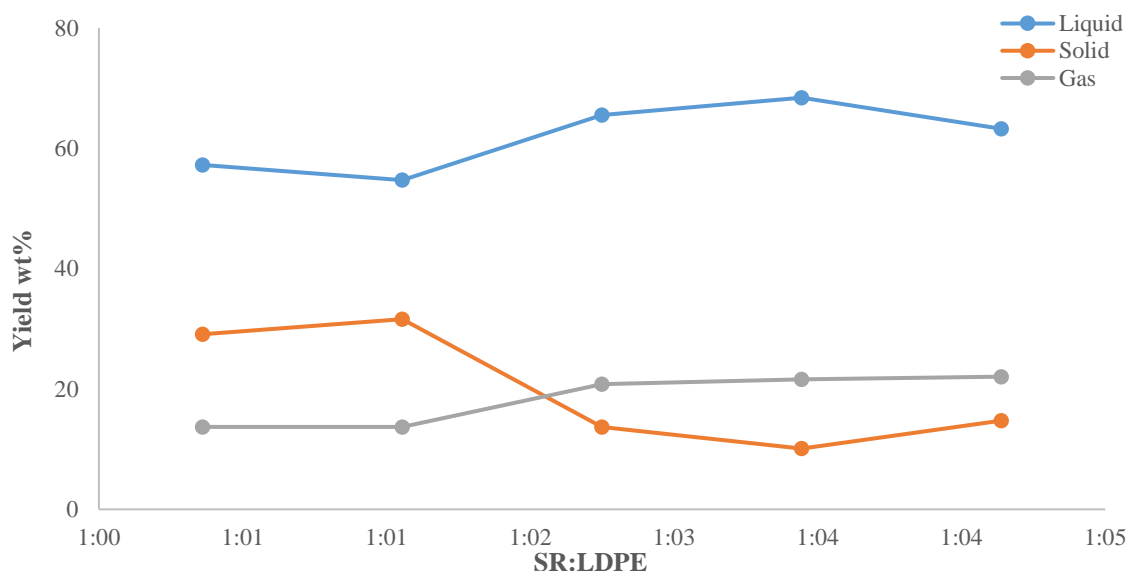
Figure 4.10: Co-pyrolysis SR with LDPE at 500 ºC

4.2.6 Co-pyrolysis of SR with HDPE

Co-pyrolysis of SR with HDPE was equally employed in the study to understand the synergy between them and the influence of HDPE on the transfer of hydrogen to bio-oil from SR. The blending ratios of 1:1, 1:2, 1:3, 1:4, and 1:5 was also carried out on co-pyrolysis of SR with HDPE. The result of co-pyrolysis of SR with HDPE was presented in Appendix B-1. Figure 4.11 presents the co-pyrolysis of SR with HDPE.

The maximum yield of liquid oil from the pyrolysis of HDPE was 64.5 wt. % was a bit lower than the maximum yield of liquid oil from the co-pyrolysis of SR with LDPE. The curve also shows that the highest yield was at the peak of blending ratio of 1:3. While the highest yield of solid char was at a peak of 1:1. The gaseous product indicates fluctuation as the blending ratio increases from 1:1 to 1:4.
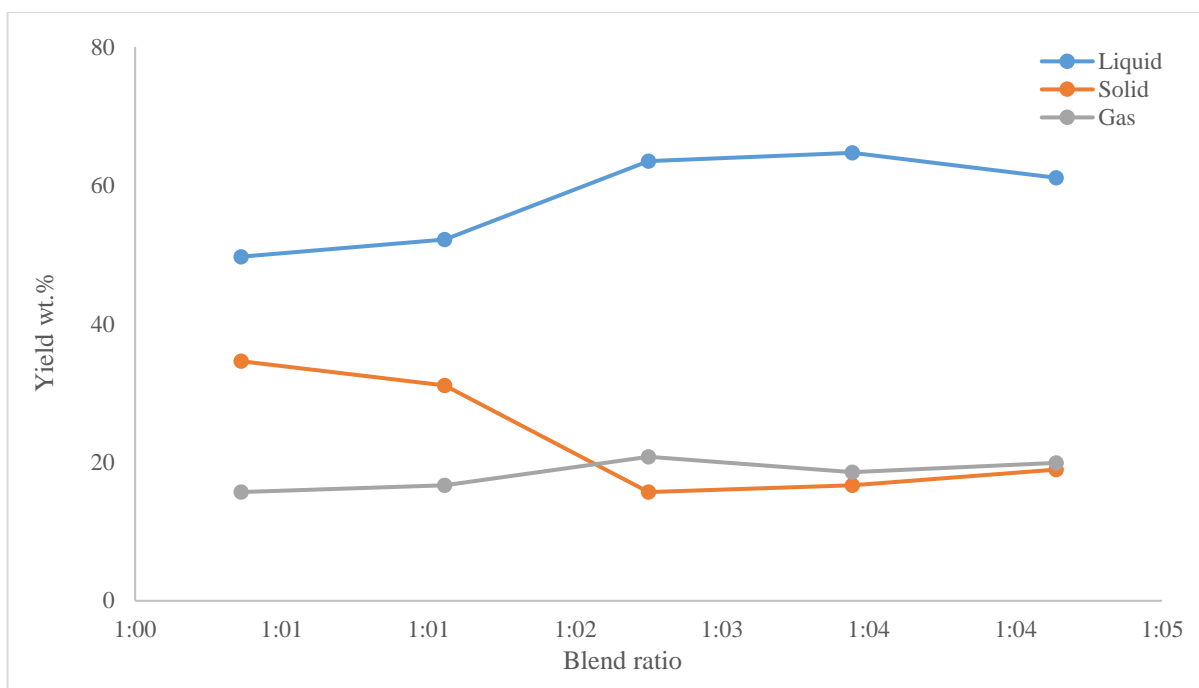
Figure 4.11: Co-pyrolysis of SR with HDPE at 500 ºC

The two pyrolysis results show that the LDPE has a higher yield and effective synergy with SR than the HDPE though both indicate synergy with SR. This was due to the fact that LDPE generates more free radicals in linear molecules of long and short branch chains than HDPE, consequently donates more hydrogen to reduce organic compounds in the bio-oil. In fact, the hydrogen molecules in HDPE are packed together, resulting in greater intermolecular forces than in LDPE. In other words, the free radicals generated from HDPE that would be used to influence interaction with free radicals from SR and thereby produce more primary products (volatiles) were lower than the free radicals from LDPE (Sun *et al*., 2013).

Additionally, LDPE has a high degree of branching in both the short and long chains, preventing the chains from aggregating into a larger agglomerate during pyrolysis in a pyrolyzer. The chain is easier to degrade at a given temperature than HDPE; hence, LDPE is making a greater quantity of bio-oil than HDPE. On the other hand, it was observed that the solid char from HDPE was higher than that from LDPE. This was earlier demonstrated in Tables 4.3 and 4.4, where the LDPE has low fixed carbon while the HDPE has 2.14 wt. %. Again, HDPE has a long chain with little branches. It implies that the chains do aggregate into a larger agglomerate and therefore become harder and cloudier than in LDPE, even though the HDPE chains are degradable similarly to LDPE at a given temperature during pyrolysis.

Finally, the bio-oil yield from co-pyrolysis of SR with either LDPE or HDPE was higher than the yield from pyrolysis of SR. This clearly confirmed that there was effective synergy and interaction between the free radicals of SR with LDPE and HDPE

4.3 Physicochemical Characterization of Bio-oil

The Physiochemical characterization of bio-oil was conducted in order to the study bio-oil.

4.3.1 Physical properties of bio-oil

The physical characteristics of the bio-oil from the pyrolysis of SR, LDPE, and HDPE and the co-pyrolysis of SR with LDPE and HDPE are presented in Table 4.5. The result was compared against conventional diesel and gasoline fuel.

Table 4.5: Physical properties of bio-oil obtained from pyrolysis and co-pyrolysis

Sample description	pH value	Viscosity $(kgm^{-1}s^{-1})$	Density (Kg/m^3)	Moisture content (Wt. %)	Caloric value (MJ/kg)	Flash point (^0C)	Pour point (^0C)
SR	5.97	13.23	1.0460	4.30	17.01	36	−32
LDPE	6.96	5.06	0.7801	2.01	35.04	54	-21
HDPE	6.89	5.73	0.7806	2.14	34.02	53	-21
4:1(SR:LDPE /HDPE)	6.00	11.19	1.0102	4.00	17.89	39	-26
1:1(SR:LDPE /HDPE)	6.12	9.67	0.9311	3.27	18.02	42	-27
1:2 (SR:LDPE /HDPE)	6.33	8.10	0.8651	3.14	19.20	45	-29
1:3 (SR:LDPE /HDPE)	6.51	7.94	0.7893	2.95	22.17	48	-30
1:4 (SR:LDPE /HDPE)	6.65	6.01	0.7887	2.70	28.00	51	-30
Diesel fuel	-	2- 4.5	0.8450	0	42.60	60	-40
Gasoline	-	0.006	0.7197	-	43.71	-43	-57

The Table showed that the calorific value of the bio-oil produced by the pyrolysis of SR is it 17.01 MJ/kg less than the calorific values of petrol and diesel, which were 42.60 MJ/kg and 43.71 MJ/kg, respectively (Mohanty, 2011). The calorific value of the oil after LDPE and HDPE were pyrolyzed is 35.04 MJ/kg and 34.02 MJ/kg, respectively. The co-pyrolysis at blend ratios of 4:1, 1:1, 1:2, 1:3, and 1:4 of co-pyrolysis corresponds to calorific values of 17.01, 17.89, 18.02, 19.20, and 28.00 MJ/Kg. The increase may be a result of the SR free radicals' efficient interaction with LDPE and HDPE (Martinez *et al*., 2014).

The viscosity of the oil obtained from individual pyrolysis was 13.23 cst while LDPE and

HDPE are 5.06 and 6.13 cst. This clearly reveals that the viscosity of LDPE and HDPE was much closer to the viscosity of diesel but far from the viscosity of gasoline, as presented in the Table 4.5. The viscosities of bio-oils from blending (4:1, 1:1, 1:2, 1:3 and 1:4) are 11.19, 9.67, 8.01, 7.94, and 6.10.0 cst respectively. The decrease in viscosity was due to the influence of hydrogen donors from LDPE and HDPE during co-pyrolysis and condensing at ice block temperature Bardalai, (2015). The moisture content from the pyrolysis of SR was 4.20 % while LDPE and HDPE were 2.01 and 2.14 %. However, bio-oil produced through co-pyrolysis has moisture content from blending (4:1, 1:1, 1:2, 1:3, and 1:4) of 4.00, 3.27, 3.14, 2.95 and 2.70%. In fact, co-pyrolysis shows a significant reduction in moisture content. This reduction is corroborated by other researchers, such as Abnisa *et al*. (2014) where co-pyrolysis can significantly reduce the inherent moisture in the bio-oil.

The density of oil obtained from SR was 1.0460 kg/m3, while LDPE and HDPE are 0.7801 and 0.7806 kg/m^3, respectively. It was observed that the density of the oil obtained from LDPE and HDPE was very close to the density of gasoline. The densities from blending (4:1, 1:1, 1:2, 1:3 and 1:4) are 1.0102, 0.9311, 0.8651, 0.7893, and 0.7887 kg/m^3 respectively. This implies that there is an influence of LDPE or HDPE. This assertion was similarly reported by Bardalai, (2015). The pH of the oil for SR was 5.97, while LDPE and HDPE were 6.96 and 6.89, respectively. Though the major contributory factor for high pH was acidic compounds, which include carboxylic acid (Bardalai, 2015), The pH from blending (4:1, 1:1, 1:2, 1:3, and 1:4) are 6.00, 6.12, 6.33, 6.51, and 6.65, respectively.

The flash point of the oil from pyrolysis was 36 ^{0}C while LDPE and HDPE are 54 ^{0}C and 53 ^{0}C. The flash points from blending (4:1, 1:1, 1:2, 1:3 and 1:4) are 39, 42, 45, 48 and 5 ^{0}C

respectively. It was observed that the flash point of the blend was close to the flash point of diesel at 60 ^{0}C but by far not close to the flash point of gasoline at -43 as reported by George and Avelino, (2015). The pour point of bio-oil from the pyrolysis of SR was -32 ^{o}C while LDPE and HDPE were -23 and -21 ^{o}C. The pour points from blending (4:1, 1:1, 1:2, 1:3, and 1:4) are -26, -27, -29, -30 and -32 ^{o}C respectively. It was observed that the co-pyrolysis does not improve the pour point of the bio-oil significantly as compared to the pour point of gasoline.

4.3.2 Chemical properties of pyrolysis oil

In order to study the bio-oil produced from the pyrolysis of SR, LDPE, and HDPE and the co-pyrolysis of SR with LDPE and HDPE, chromatography and mass spectrometry (GC-MS) were used.

4.3.2.1 *GC-MS analysis of bio-oil obtained from pyrolysis of SR*

Figure 4.12 presents the GC-MS analysis of the bio-oil obtained from the pyrolysis of SR, and Appendix C illustrates the library. The result indicates that the bio-oil possesses lower and higher molecular weight species with carbon numbers ranging from C_9-C_{24} and a high concentration of C_9-C_{16}. The lower molecular weight could be attributed to the fact that the major chemical constituent of SR was degraded and cracked during pyrolysis.

The GC-MS analysis presented in Figure 4.12 shows the highest peak was assigned to the phenol compound in peak nine. The first peak at retention time 3.443 was assigned to Propanoic acid ($C_8H_{14}O_3$), retention time 4.842 compound is Oxirane (C_4H_8O), retention time 5.37 compound is Acetamide (CH_3CONH_2), retention time 7.508 compound is Butane

(C_4H_{10}), retention time 8.551 compound is 1,2-Ethanediol (C_5H_6O), retention time 9.553 compound is phenol (C_6H_5OH), retention time 9.767 compound is 3-Penten-2-one (C_5H_8O), retention time 9.917 compound is (Propanoic acid), retention time 12.633 compound is 2-Propanol (C_3H_8O), retention time 14.473 compound is Decane. These peaks as detected are assigned to various abundance compounds and were match under a class of organics compound as phenol, acids, ketones, aldehydes, furans, pyrazoles, and aliphatic compound.
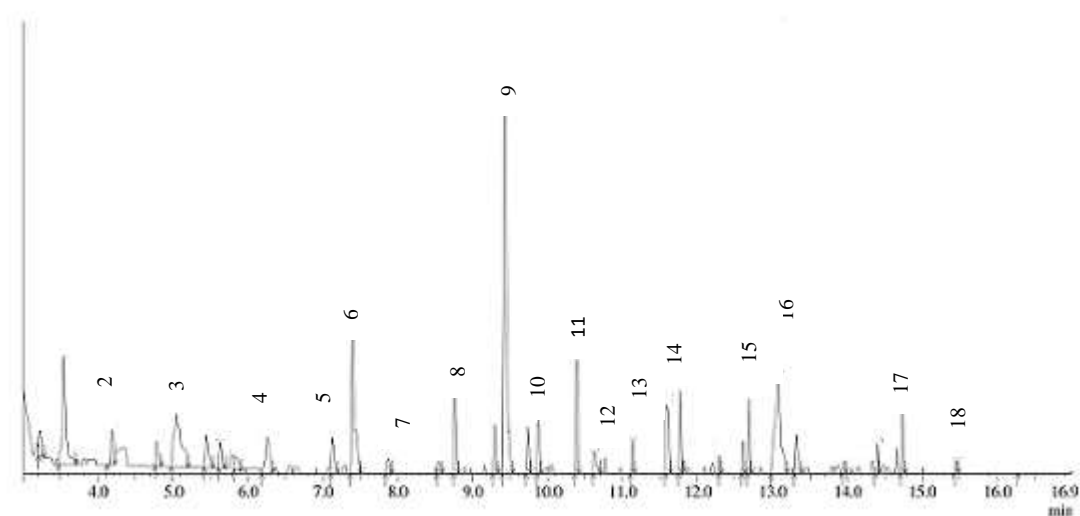
Figure 4.12: GC-MS of bio-oil at temperature 500 °C

It can be deduced that the GC-MS analysis of bio-oil obtained from pyrolysis of SR indicated 77.77 % are oxygenated organic hydrocarbons, while 22.23 % are aliphatic.

4.3.2.2 *GC-MS analysis of bio-oil obtained from pyrolysis of LDPE*

GC-MS was used to analyse the oil obtained from the pyrolysis of LDPE, and the GC-MS library was presented in Appendix C. The library was used to identify the hydrocarbons present in the oil. Figure 4.13 presents the analysis of fuel from the pyrolysis of LDPE. It can

be seen from the analysis that the majority of hydrocarbon compounds are both lower and heavy hydrocarbons, comprising aliphatic and aromatic compounds with carbon numbers ranging from C_6-C_{24} and high concentrations of C_9-C_{15}. This indicated that the fuel contains a typical homologous series of saturated and unsaturated hydrocarbons in LDPE. The first compound identified from the analysis of the oil was 1-hexene (C_6H_{12}) at a retention time of 1.91 minutes, and the last compound identified was Tetracosane ($C_{24}H_{50}$) at a retention time of 2.26 minutes. It also shows that the hydrocarbon compounds are straight-chain as well as branch-chain hydrocarbon compounds, this is because long-chain hydrocarbons were broken down to form shorter ones, thus generating a new substance during the thermal degradation of LDPE. Therefore, the list of compounds identified from this analysis is dominated by alkane and alkene compounds.
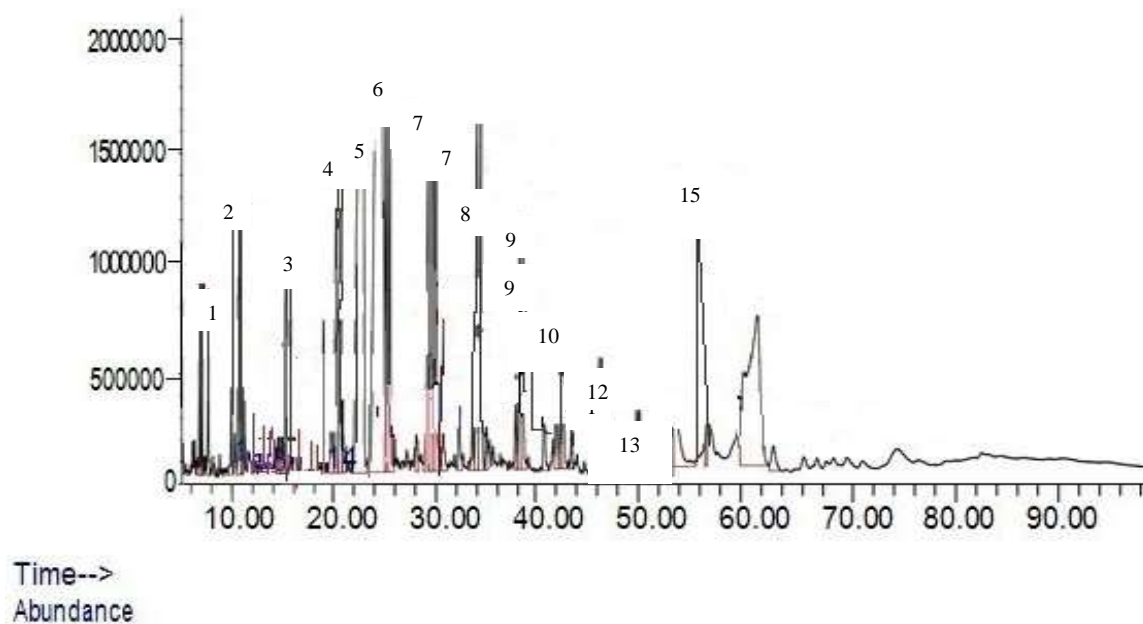
Figure 4.13: GC-MS analysis of oil obtained from pyrolysis of LDPE at 550 °C

4.3.2.3 *GC-MS analysis of oil obtained from pyrolysis of HDPE*

The GC-MS analysis of oil obtained from the pyrolysis of HDPE was also conducted so as to verify the individual chemical components available in the liquid oil. The GC-MS library was presented in Appendix C. Figure 4.14 presents the GC-MMS analysis of fuel from HDPE. It can be seen from the analysis that the hydrocarbon compounds comprise aliphatic and aromatic compounds with carbon numbers C_6 - C_{28} and high concentrations of C_9-C_{15}. The initial carbon number of oil from HDPE was a little higher than the range of heavier hydrocarbons from fuel from LDPE. The first compound identified from the analysis of the fuel was Nonene (C_9H_{28}) at a retention time of 3.062 minutes, and the last compound identified was Tetracosane ($C_{28}H_{58}$) at a retention time of 28.45 minutes. Similarly, the figure shows that the majority of hydrocarbon compounds are straight chains as well as some branch chains. These long chain hydrocarbon compounds were broken down to form smaller ones during the pyrolysis of HDPE.
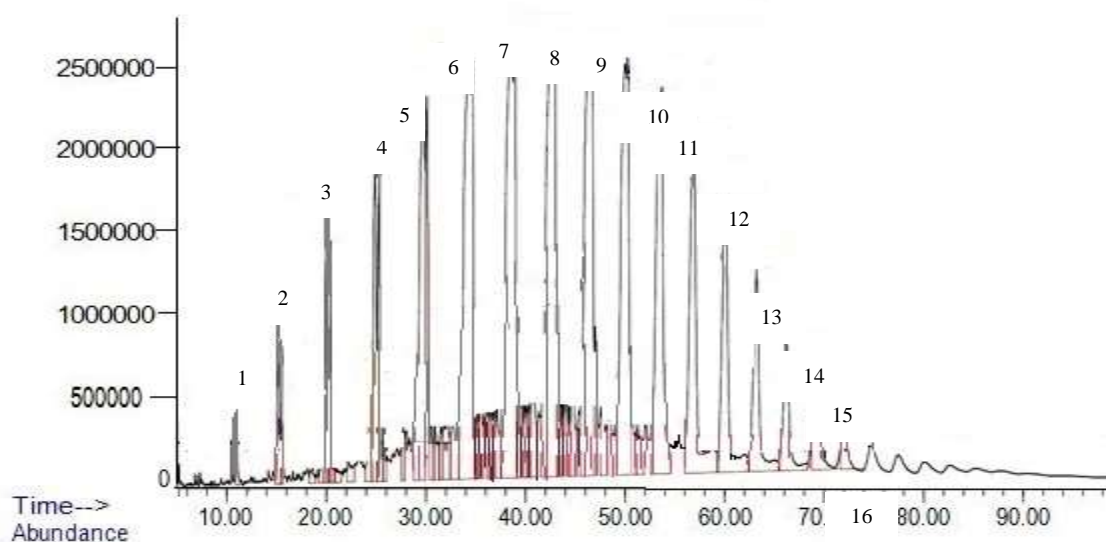
Figure 4.14: GC-MS analysis of oil obtained from pyrolysis of HDPE at 550 °C

4.3.2.4 *GC-MS analysis of bio-oil obtained from co-pyrolysis of SR with LDPE and*

HDPE

The GC-MS analysis of bio-oil obtained from co-pyrolysis of SR with LDPE and HDPE at blend ratio 1:1 was performed in order to understand the effective synergy between SR with LDPE and HDPE. The GC-MS library was presented in Appendix C, while the chromatograph analysis was presented in Figure 4.15. The Figure shows the peaks with various retention times that will be used to assign various hydrocarbon compounds from the GC-MS library. The analysis shows that the hydrocarbon compounds are also lower and heavier hydrocarbons, which contain more aliphatic, aromatic, and little oxygenated compounds with carbon numbers C_6-C_{25}. It also shows that as a result of the blend ratio of SR with LDPE and HDPE, most of the hydrocarbon compounds associated with oxygen emanating from SR begin to disappear, as indicated by the retention time of the analysis. This disappearing could be attributed to the effect of LDPE and HDPE donating hydrogen; consequently, other oxygenated compounds such as esters, ethers, aldehydes, and ketones began to reduce. It was observed from the library, as demonstrated in the Figure, that saturated and unsaturated aliphatic and aromatic hydrocarbons increase while oxygenated organics reduce by 60%.
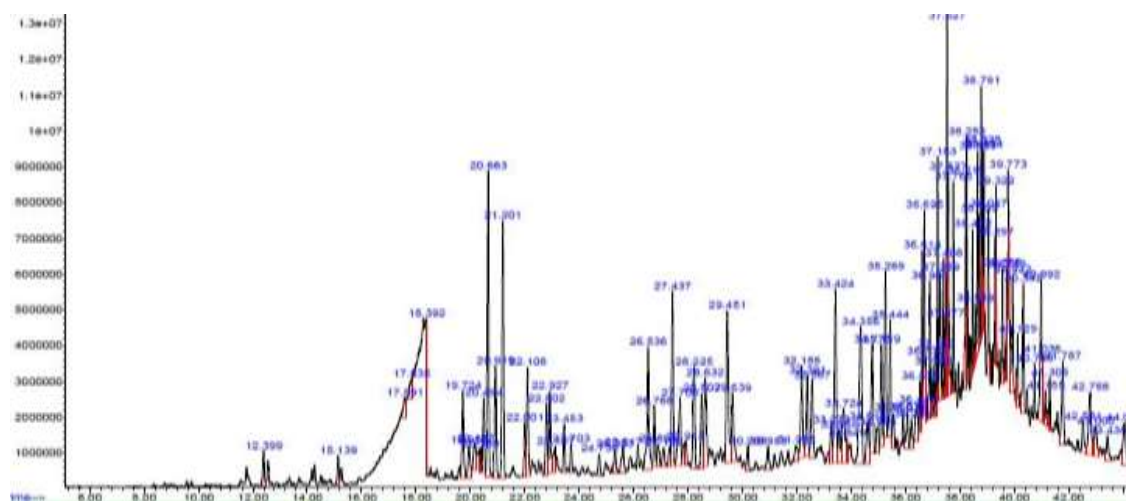
Figure 4.15: GC-MS analysis of bio-oil obtained from co-pyrolysis of SR with LDPE and HDPE

The GC-MS analysis of bio-oil at blend ratio 1:4 was conducted in order to understand the effective influence and synergy between SR with LDPE and HDPE. The GC-MS library was presented in Appendix C. The library was used to identify hydrocarbons present in the bio-oil, while Figure 4.16 presents the GC-MS analysis of the bio-oil. The Figure as presented also shows the peaks with various retention times that will be used to assign various hydrocarbon compounds from the GC-MS library. It can be seen from the analysis that the hydrocarbon compounds contain lower and heavier hydrocarbons as aliphatic, aromatic, and little oxygenated compounds with carbon numbers ranging from C_6-C_{27}. It shows that as a result of the blend ratio of SR to LDPE and HDPE most of the hydrocarbon compounds associated with oxygen that emanate from SR also reduce significantly, as indicated by the retention time of the analysis. It was observed from the library in Appendix C-1 that saturated and unsaturated aliphatic and aromatic hydrocarbons increase while oxygenated organics decrease by 80%.
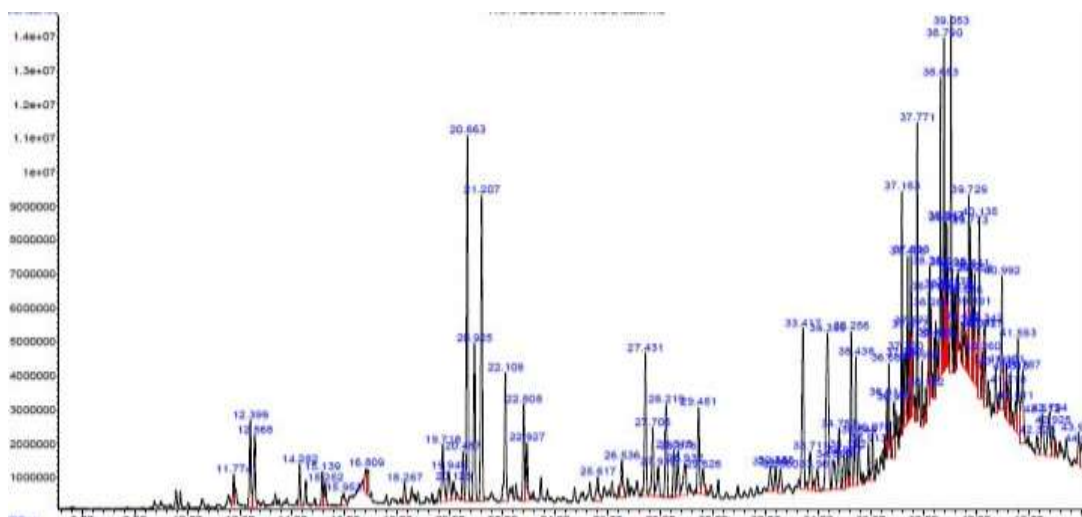
Figure 4.16: GC-MS analysis of pyrolysis oil from ratio 1:4 SR with LDPE and HDPE

The actual composition of oxygenated organics, aromatic and aliphatic, present in the bio-oil produced from pyrolysis of SR and co-pyrolysis of SR with LDPE and HDPE was calculated and presented in Table 4.6.

Table 4.6: Percent composition of hydrocarbons in the bio-oil from the pyrolysis and co-pyrolysis

Functional groups	SR	LDPE	HDPE	4:1 (SR:LDPE/ HDPE)	1:4 (SR:LDPE/ HDPE)	Gasoline (literature)
Oxygenated %	-		-		-	-
Ester	5.57	-	-	5.89	-	-
Ether	5.57	-	-	-	-	-
Aldehyde	20.20	-	-	2.94	-	-
Ketone	5.57	-	-	2.94	5.32	-
Carboxylic	16.66	-	-	6.76	-	-
Amine	**24.20**	-	-	-	-	-
Phenol		-		2.52		-
Aliphatic %	16.66	63.16	59.26		61.54	**43.12**
Alkane	5.57	36.84	40.74	29.41	23.08	**33.03**
Alkene		-	-	41.18	3.86	
Alkyne				2.94		
Aromatic %	-	-	-	5.42	6.20	**16.53**
Benzene	-	-	-	-	-	**3.66**
Toluene	-	-	-	-	-	**3.66**
m.o.p-xylene						

4.3.2.5 *FTIR Spectroscopy of the bio-oil obtained pyrolysis of SR*

To further study the compound identified by GC-MS analysis, the FTIR was used to determine the functional group as well as verify the compound names identified by GC-MS analysis. Figure 4.17 presents the results of an FTIR analysis of bio-oil obtained from SR. The absorption bands of 725.25, 923.86, 1103.32, 1282, 1410.80, 1603.82, 1705.12,

3063.061, 3456.55, and 3842.04 cm^{-1} correspond to functional groups: CH, CH-CH2, C=O, C-O-C, C=C, COO, CH-CH, OH, N-H, O-H, and O-H.

The hydrocarbon C-H shows an absorption band at 725.25 cm^{-1} with the compound name mono alkyl, while alkane corresponds to 923.86 cm^{-1} and 2847.49 cm^{-1}, as seen in the Figure. The absorption bands 1103.32, 1282, 1410.80, 1603.82, and 1705.12 cm^{-1} indicated the presence of C=O, C-C, C-O-C, C-O and COO functional groups, which correspond to light compounds; Ketones, Esters, Ethers, aromatic compounds, and carboxylic acid. Furthermore, the peaks 3063.061-3842.04 cm^{-1} of the absorption bands indicated the presence of O-H which corresponds to alcohol. Furthermore, the weak peaks could be attributed to the presence of moisture and alcohol, which appear at peak 3063.061 cm^{-1}. This result of the FTIR analysis corroborated with the FTIR analysis of bio-oil described by Zhang *et al.* (2016) that the spectrum revealed the appearance of peaks at 3964-3500 cm^{-1} indicating the presence of water, peaks at 1846-1710cm^{-1} indicating the presence of light compounds like acids, peaks at 3050-2800cm^{-1} indicating the presence of alcohols and peaks at 1400–1107cm^{-1} indicating the presence of ketones.

In a similar perspective, the absorption bands assigned to the peaks at 725.25, 923.86 and 2847.62 cm^{-1} represent the C-H-CH bending, which indicates the characteristic of aliphatic hydrocarbons. The C=O, C-O-C, COO stretched at absorption bands 1103.32, 1282 and 1705.12 cm^{-1} while the C-O bends at absorption band 1410.80, which were the characteristics of oxygenated organics (Ketones, Esters, Ethers, aromatic compounds, and carboxylic acid) hydrocarbons. Furthermore, the aromatic C=C stretching at 1603.82 cm^{-1} has medium intensity; the alcohol OH bends at 3063.061 has weak intensity; and the water O-H stretching

at 3842.04 has broad weak intensity. The absorption band at wavelength 3345.25 cm^{-1} whose intensity was strong, is characteristic of amines (N-H stretch).

Therefore, according to the analyses of GC-MS and FTIR as presented in Figures 4.12 and 4.17, the bio-oil contains oxygenated organics that require removal.
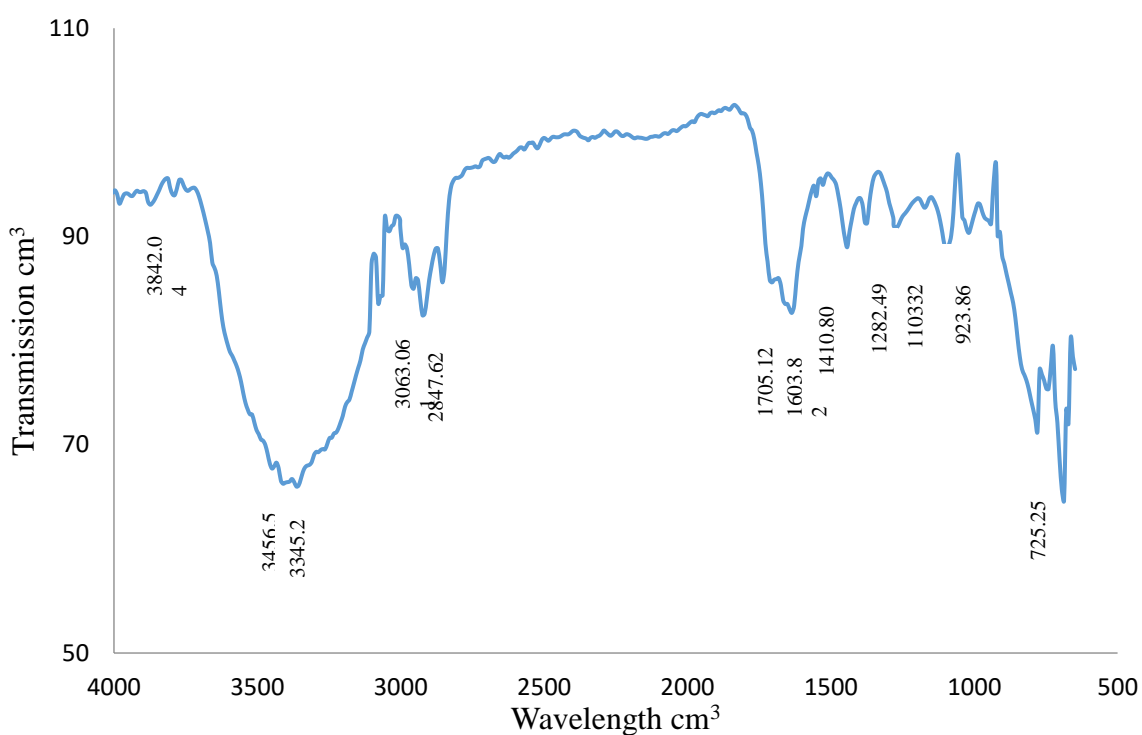
Figure 4.17: FTIR analysis of bio-oil obtained from pyrolysis of SR

4.3.2.6 *FTIR analysis of bio-oil obtained from pyrolysis of LDPE*

The FTIR analysis of bio-oil obtained from the pyrolysis of LDPE was presented in Figure 4.18. The analysis shows that the spectrum exhibits various peaks of wavenumbers 725.25, 964.44, 902.72, 1473.44, 1604.20, 2731.29, 2729.30, and 2939.61 cm^{-1} which correspond to

the assigned functional groups CH=CH, -CH=CH (trans), -CH$_3$, -C-CH$_3$-C-CH$_3$, and -C-CH$_3$. The Figure shows more single- and double bond hydrocarbons. This characteristic of fuel having more double-bonded hydrocarbons could lead to quicker and more efficient burning. It was observed that the FTIR analysis of fuel from LDPE confirmed the result of the GC-MS analysis as presented in Figure 4.13. Furthermore, it appears that some functional groups, such as C–CH$_3$ were repeated, this could be due to the fact that their wavenumbers were also repeated. This analysis was also explained in the research of Moinuddin *et al.,* (2011) who highlighted that some hydrocarbons are closely bonded together while some functional groups are repeated.
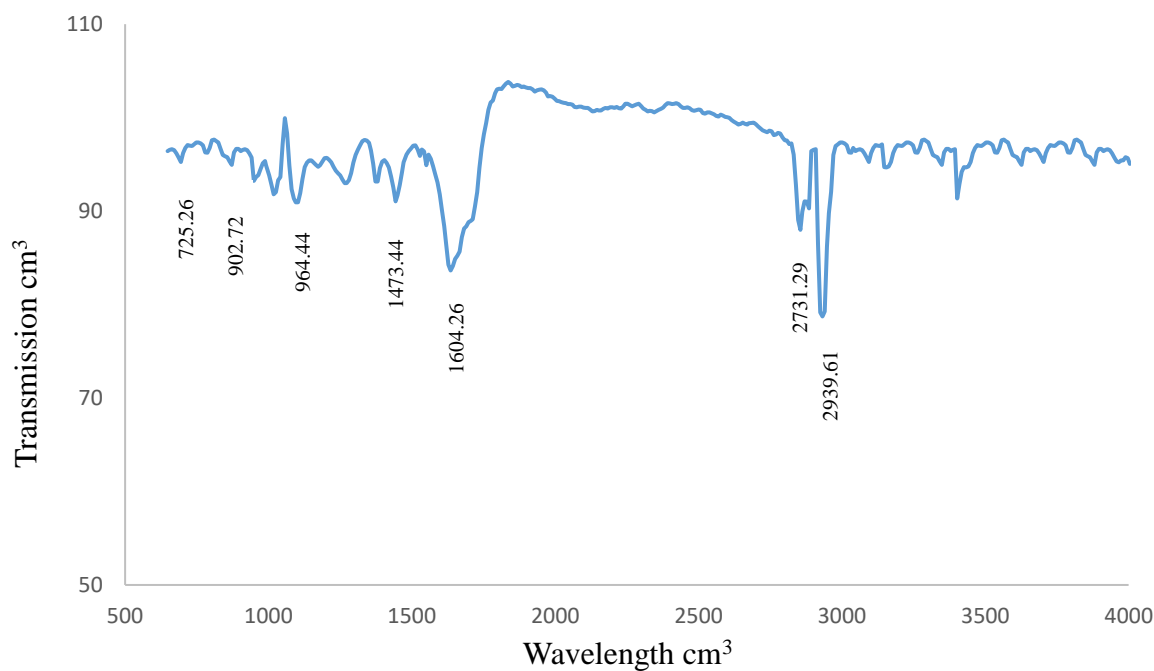
Figure 4.18: FTIR analysis of bio-oil obtained from pyrolysis of LDPE

4.3.2.6 *FTIR analysis of bio-oil obtained from pyrolysis of HDPE*

The FTIR analysis of bio-oil obtained from the pyrolysis of HDPE was also presented in Figure 4.19. The analysis shows that the spectrum exhibits various peaks at wavenumbers 887.28, 991.23, 1226.77, 1465.94, 1604.26, 2731.29, 2729.30 and 3616.58 cm^{-1} as presented in the Figure. These peaks correspond to the assigned functional groups CH=CH, -CH=CH (trans), -CH$_3$, -C-CH$_3$-C-CH$_3$, and -C-CH$_3$ respectively. This FTIR confirmed the analysis of GC- MS as presented in Figure 4.14. The Figure shows that the FTIR analysis of fuel oil obtained from HDPE shows single and double bonds, which also indicate quicker and more efficient burning. These wavenumbers exhibit similar characteristics as demonstrated by the research work of Sachin and Sink, (2011) which indicated the presence of alkanes and alkenes.
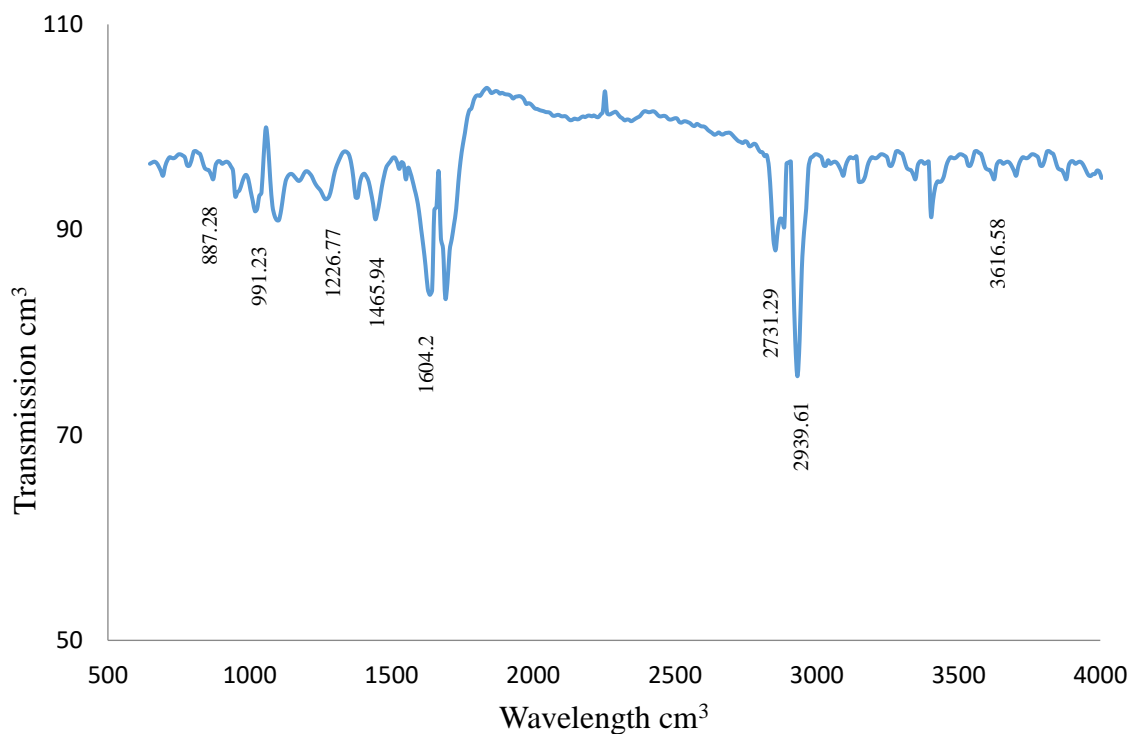
Figure 4.19: FTIR analysis of fuel from pyrolysis of HDPE

4.4 Characterization of raw Bambu clay

The study targeted using locally sourced clay for zeolite synthesis. Prior to catalytic pyrolysis, raw clay samples were collected for analysis so as to check for suitability for this research work.

4.4.1 X-ray fluorescence analysis of Bambu clay

The X-Ray Fluorescence analysis provides the chemical composition of Bambu clay. XRF results usually show the predominant oxide compositions are SiO_2 and AlO_3. Table 4.7 provides full information about the XRF analysis and the oxide's composition. The analysis indicated that Bambu clay has a good silica to alumina ratio, with a value of approximately 1.85, which is corroborated with an ideal kaolinite from literature as exactly 1.8 as presented in the Table hence, the clay was suspected to be kaolinite clay. This clearly reveals that the clay has potential for the synthesis of zeolite. Furthermore, the structure of the Bambu clay consists of one tetrahedral sheet of silica inserting a central octahedral sheet of alumina in the structure (AlO_3). Also, the analysis shows that Bambu clay contains a reddish colour, which indicated the presence of iron oxide.

The Bambu clay contained silica + alumina + water (SiO_2 + Al_2O_3 + H_2O) and some impurities such as iron, potassium, and so on. The clay is made up of 52.30% SiO_2, 29.20% Al_2O_3. Potassium oxide (1.07%), iron III oxide (4.20%) and titanium dioxide (1.64%) are among the major impurities found in the clay samples. The percentages of other oxides such as calcium oxide (0.038%), magnesium oxide (0.007%), manganese oxide (0.081%) and sodium oxide (0.80%) are lower than those of aluminium and silicon.

Table 4.7: XRF analysis of raw Bambu clay

Compound	Raw clay (Bambu)
SiO_2	54.40
Al_2O_3	29.30
Fe_2O_3	4.20
CaO	0.41
V_2O_5	0.029
K_2O	1.76
MnO	0.081
NaO_2	0.80
TiO_2	1.64
P_2O_3	ND
SO_3	ND
CuO	0.028
MgO	0.007
NiO	-
CuO	-
ZnO	0.019
Ga_2O_3	0.012
Ta_2O_5	-
Cl	-
LOI (1000^0C)	7.31
Si/Al ratio	**1.85**

LOI = Loss on ignition

Not display = Nd

4.4.2 X-ray diffractor of Bambu clay

The X-Ray Diffractor (XRD) of Bambu clay was extensively used for the investigation of clay mineralogy, phase identification, and crystallinity. Figure 4.20 presents the XRD of Bambu clay. The Figure shows that the Bambu clay has four minerals: Kaolin, Quartz, Illite, and Albite. The peaks obtained from the study of Bambu clay were compared with The International Centre for Diffraction Data's Powder Diffraction File (PDF) (2015), which uses diffraction patterns to provide a qualitative characterization of the Bambu clays.

Figure 4.20 indicates that the Bambu clay contains various peaks with various diffraction angles and intensities. The first peak, which has an illite mineral feature and is present in potassium bentonite, was at 8.93^0 on the 2-theta scale. Also, the result of XRF analysis, as presented in Table 4.7, shows the presence of potassium oxide (K_2O) in Bambu clay. The second peak was at 12.50^0 and was characterised as kaolinite. While the fourth peak was characteristic of albite, which belongs to the Feldspar group, an isomorphous solid solution containing sodium without calcium, The XRF data also revealed that Bambu clay contains a small amount of sodium oxide (NaO_2) at 0.80%. The fifth peak was at 26.79, which was the highest intensity on the diffraction pattern and was characteristic of quartz. Other peaks were contained in the mixture of kaolinite versus quartz/kaolinite, illite versus kaolinite/quartz, and albite versus kaolinite/quartz.

The minor characteristic peaks of kaolinite are also assorted with other minerals found at different Bragg"s angles 20.06, 23.30, 25.10, 26.79, 35.00, 38.50, 55.50 and 63.20. However, the peak at 26.79 which was due to the presence of crystallite silica, referred to Quartz and the peak has the highest intensity of about 6000 counts, as shown in the figure. This highest intensity was also demonstrated by Ajayi *et al*. (2010).
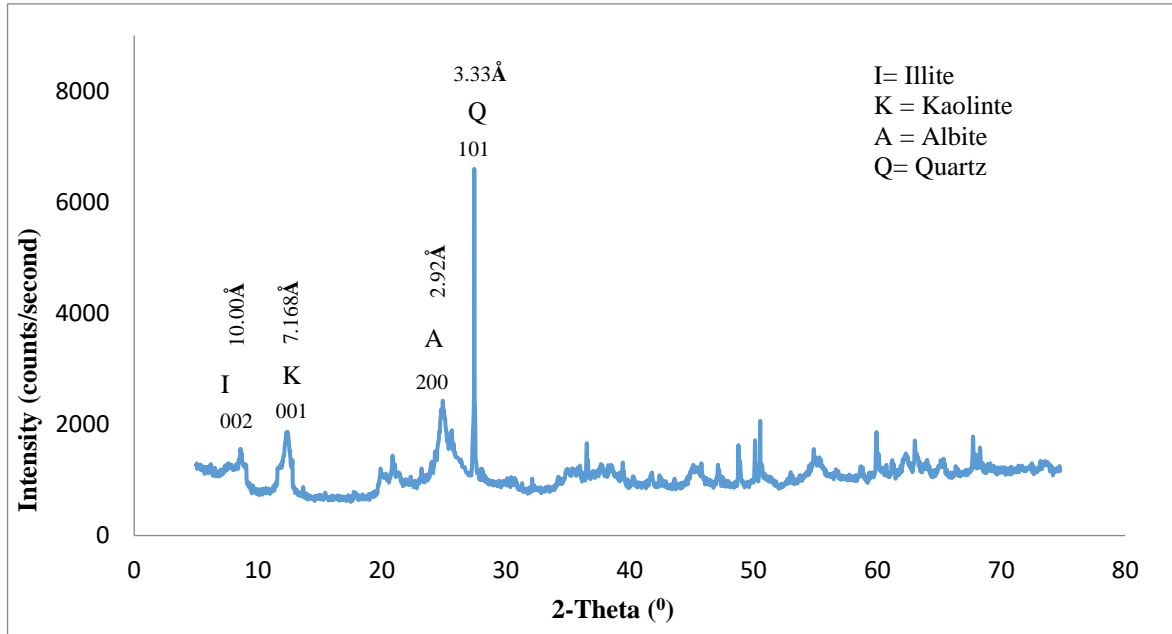
Figure 4.20: XRD pattern of Bambu clay

4.4.2.1 *Crystallite size of the Bambu clay generated from the XRD data*

The XRD data was further utilized to determine the crystalline size (D) of the Bambu clay, beneficiated clay, and meta-kaolin using Scherer's equation. The equation is

$$\tau = \frac{K\lambda}{\beta \cos \theta}$$

(4.10)

Where is the line broadening at half the maximum intensity (FWHM), is the Bragg angle, and K is a dimensionless shape factor (0.9), is the X-ray wavelength, and is the average size of the ordered (crystalline) domains.

Table 4.8 presents the crystallite size of the Bambu clay in the range of 8.04 - 85.52 nm, with an average crystallite size of 43.5 nm. Therefore, the overall average crystallite size of Bambu

clay has pores with diameters within the range of 2 and 50 nm and is referred to as

mesoporous clay

Table 4.8: Crystallite size of the Bambu clay generated from the XRD data

Diffraction angle 2Θ	Θ (radians)	d-spacing (nm)	FWHM (radians)	Crystallite size (nm)
7.845	0.06846054	11.2698	0.007144505	17.71511557
8.834	0.077091193	9.89837	0.006167994	21.07336324
12.3553	0.107820333	7.16641	0.005317146	8.039928525
23.3013	0.203342202	3.81759	0.005702863	23.41088838
24.9281	0.217538711	3.57201	0.008546005	16.62897919
25.7221	0.224467668	3.46352	0.005702863	23.51857313
28.0803	0.245046845	3.17778	0.005866924	16.85756203
30.613	0.267148822	2.92041	0.007144505	18.32360218
35.0066	0.305490215	2.92041	0.005909685	17.06018224
38.5496	0.336408723	2.56329	0.007141015	20.58559254
50.6011	0.4415779	1.8176	0.006604326	23.23999014
58.7474	0.512667778	1.57172	0.006604326	24.11043444
63.1081	0.550722065	1.472	0.008361872	85.51729819
73.7103	0.643243714	1.28427	0.007623598	10.6065098
Average crystallite size				**43.55840261**

4.4.3 Fourier Transform Infrared (FTIR) Spectroscopy of Bambu clay

To further characterize the raw Bambu clay, FTIR analyses were carried out on the clay at

an infrared wavelength of 4000-5000 cm^{-1} to ascertain the various functional groups present

in the Bambu clay. Figure 4.21 shows the result of the FTIR analysis of Bambu clay. The

clay has well resolved (-OH) absorption bands in the IR spectrum at 3695.30, 3626.20,

3402.98, 1620.26, 1443.66, 1350.22, 1111.03, 918, 799.48 and 678.97 cm^{-1}. The peaks at

3695.30, 3620.20, 3402.20, 1620.26, 799.48 and 678.78 cm^{-1} connected to the Bambu clay's

-OH- stretching vibrating bands. These bands indicated the presence of kaolinite, as revealed

by the research work of Frost, (1995).

Similarly, the -OH stretching at 3626.20 cm^{-1} was assigned to the inner layer Al-O--H. This stretching was closely similar to the peaks described by the research on Alkaleri clay in the 3626 cm^{-1} frequency band. The appearance of peaks 1018.45, 799.84 and 678.97cm^{-1}at low region indicates the presence of quartz. The Al-Al-OH was responsible for the peak at 918.15 cm^{-1}. From the FTIR spectrum in Figure (4-21) Bambu clay could be described as containing a predominant amount of kaolinite and quartz, which are also shown in the XRD analysis in Figure 4.20.
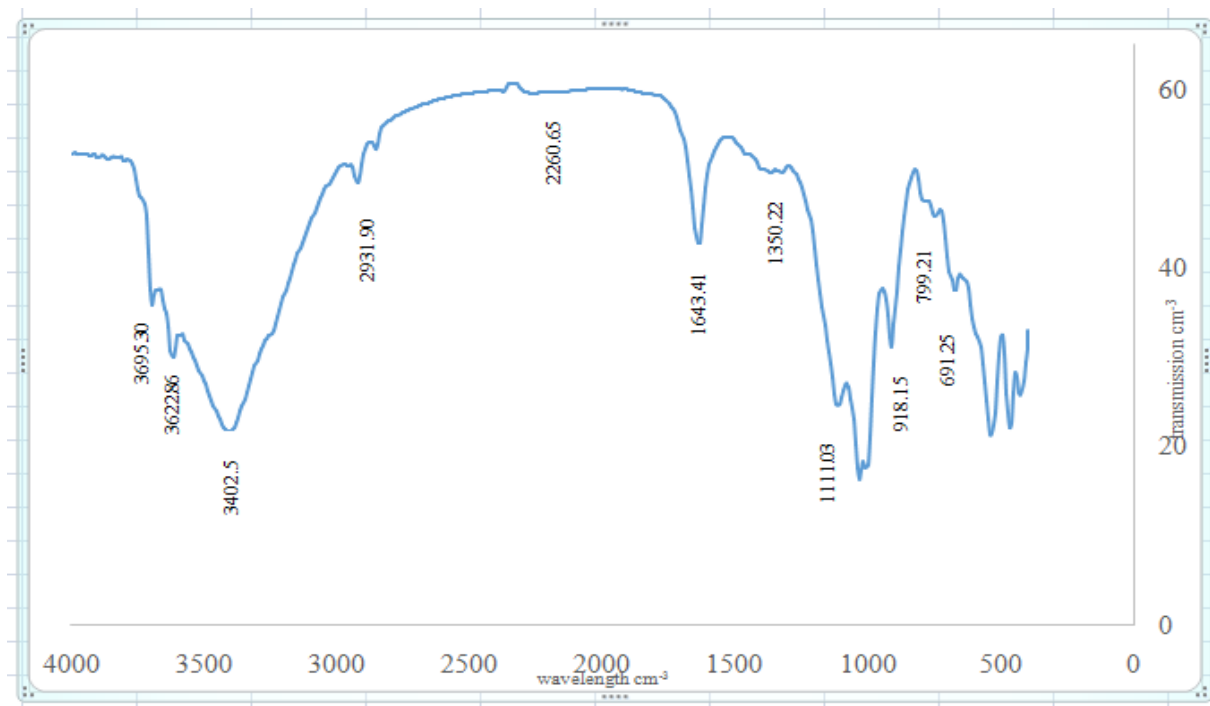
Figure 4.21: Fourier Transform Infrared spectra (FTIR) of Bambu clay

4.4.4 Brunauer-emmett-Teller analysis of Bambu clay

To ascertain the Bambu clay's pore radius, pore volume, and surface area, the Brunauer-Emmett-Teller (BET) study was conducted. Table 4.9 presents the BET analysis of Bambu clay and the literature values of other raw clay BETs.

The result of BET analysis as presented in Table 4.9 revealed that the clay has a good surface area up to 429.70 m^2g^{-1}, pore volume of 0.042 cm^3g^{-1} and a pore radius of 2.14 nm, which was higher than the surface area presented by the research work of Nuradden, (2015). Though the average crystallite size of Bambu clay was 43 nm as indicated in Table 4.9 which falls within the range of the IUPAC standard 2-50 nm, the clay is generally characterised as mesoporous. Therefore, combining the crystallite size of the clay and the BET as presented in Tables 4.8 and 4.9, Bambu clay is a promising material for absorption, diffusion, and cracking of oxygenated bio-oil. This is because catalyst activity, especially cracking, depends on the surface area and pore size. Bambu clay was characterized as a mesoporous, which could provide a lot of accessibility for the reactants such as volatile or vapor, so in a limited time, it could diffuse much more and meet more catalytic sites than microporous materials, which have low diffusion rates because of pore size as well as depend on the shape selectivity of small molecules.

Table 4.9: BET pore radius, pore volume, and surface area, of Bambu clay

Sample	BET Surface Area, (m^2/g)	Pore volume, (cm^3/g)	pore radius (nm)
Bambu clay	429.70	0.042	2.14
Literature value Nuradeen (2015)	12.95	0.0035	

4.4.5 Scanning electron microscope Bambu clay

The morphology of the Bambu clay was studied as a complementary characteristic method to the FTIR and XRD. The result of the Scanning Electron Microscope (SEM) on the Bambu clay was presented in Figure 4.22. There was a presence of hallyosite minerals scattered

within the clay structure, as shown in the scanning electron micrograph in the Figure. The halloysite mineral is in the form of a cylindrical tube spread within the Bambu clay structure, and it is represented by 'H' on the micrograph in the Figure. These structures of halloysite corroborate other research (Al-ani and Sarapaa, 2008).

In-fact, Bambu clay contains kaolinite crystals (pseudo-hexagonal crystals), represented by (K) in the Figure.
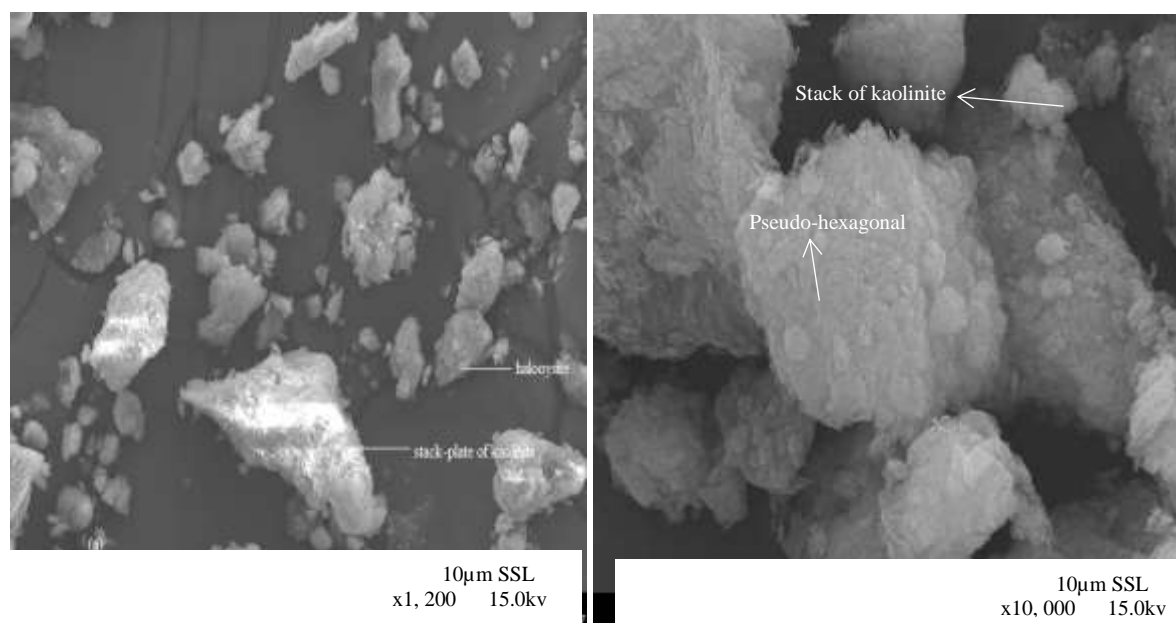
Figure 4.22: High Resolution Scanning Electron Microscopy of Bambu Clay (a) and (b) indicates the presence of stack-plate of kaolinite and pseudo-hexagonal.

4.4.6 X-ray photoelectron spectroscopy (XPS) to raw Bambu clay

The X-ray Photoelectron Spectroscopy (XPS) was used in the study to determine elemental composition binding energies of silicon, oxygen, and aluminum on the surface of raw clay as well as to reveal element that XRF and XRD could not reveal.

4.4.6.1 *XPS analysis of raw Bambu clay*

The XPS analysis of Bambu clay was done to study the binding energy and elemental composition. Table 4.10 presents the core-level electron binding energy (eV) of raw Bambu clay. The Table as presented consists of principal energy levels 1, 2 and 3 which consist of a number of sub-levels, S and P. It can be seen from the Table that the elemental composition was assigned to sub-energy levels that correspond to binding energy

Table 4.10: Core-level electron binding energy (eV) of Bambu clay

Element	$1S_1$	$2S_{1/2}$	$2P_{1/2}$	$2P$	$2P_{3/2}$	$3P_{1/2}$	$3P$	$3P_{1/2}$	$3P_{3/2}$
C	284								
O	532								
Na	1070	63	31						
Mg	1300	89	52						
Al		118	74	73	73				
Si		149	100	99	99				
K		377	297	294	294	34			
Ca		438	350	347	347	44			18
Ti		564		455	455	59		34	
Fe		846	723	710	710	95		57	
Mn		769	652	641	641	84	49	49	

Furthermore, the spectra of the clay were taken within the range of binding energy from 0 to 1400 eV. Figure (4.23) presents the intensity against the binding energy of raw clay. The BE values usually decrease from left to right, as shown in the Figure. The peaks in the figure show the presence of elements with sub-shells O_{1s}, C_{1s}, Si_{2p}, S_{2p}, Al_{2p}, Na_{1s}, Fe_{2p}, K_{2p}, Mn_{2s},

Ca_{2p}, Mg_{1s} and Ti_{2p}, photoelectron lines. These elements with sub-shells identified by the XPS analysis of clay corroborated the result of the XRF elemental composition analysis of Bambu clay presented in Table 4.10, except for the presence of carbon. However, this presence of carbon could be attributed from dried plants or insects, which mix in powder form with the earth.
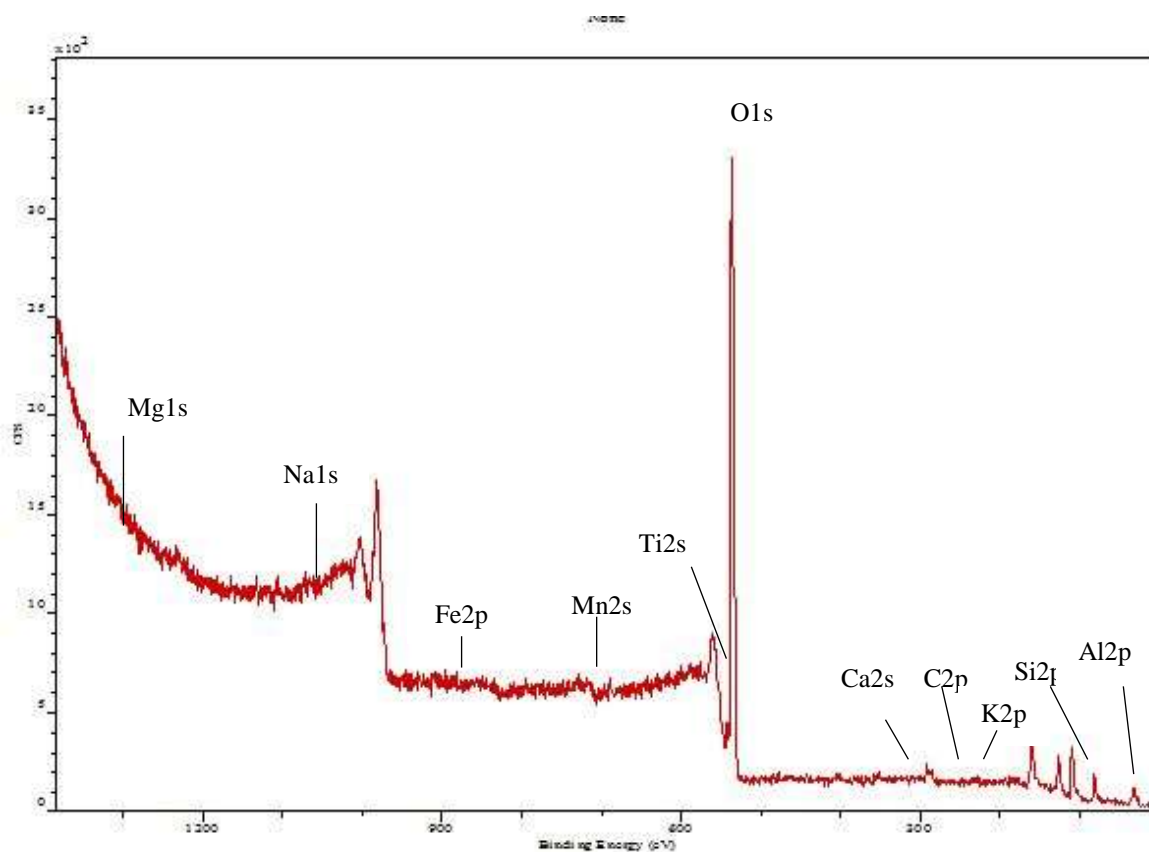
Figure 4.23: X-ray photoelectron spectroscopy analysis of Bambu clay

4.4.6.2 *Core level binding energy analysis of Bambu clay*

In the XPS analysis of Bambu clay, a spectrum in Figure 4.24 clearly shows the splitting of oxygen O_{1s} peaks at a binding energy of 532 eV. This reflects that O_{1s} signal could associate with Si-O and Al-OH groups, respectively. Figures 4.24 and 4.25 presented the high-

resolution curve fitting of Silicon Si_{2p} and Aluminum Al $_{2p}$. The high-resolution Si_{2p} curve fitting in Figure 4.26 for Bambu clay revealed that, at a binding energy of 99 eV, silicon could be assigned to the Si-O bond. While the high-resolution Al_{2p} spectra of Bambu clay also showed one peak at a binding energy of 73 eV. This binding energy could be assigned to Al in Al-OH. The pattern of high-resolution was demonstrated in the research of Xiaoyu *et al*., (2016).
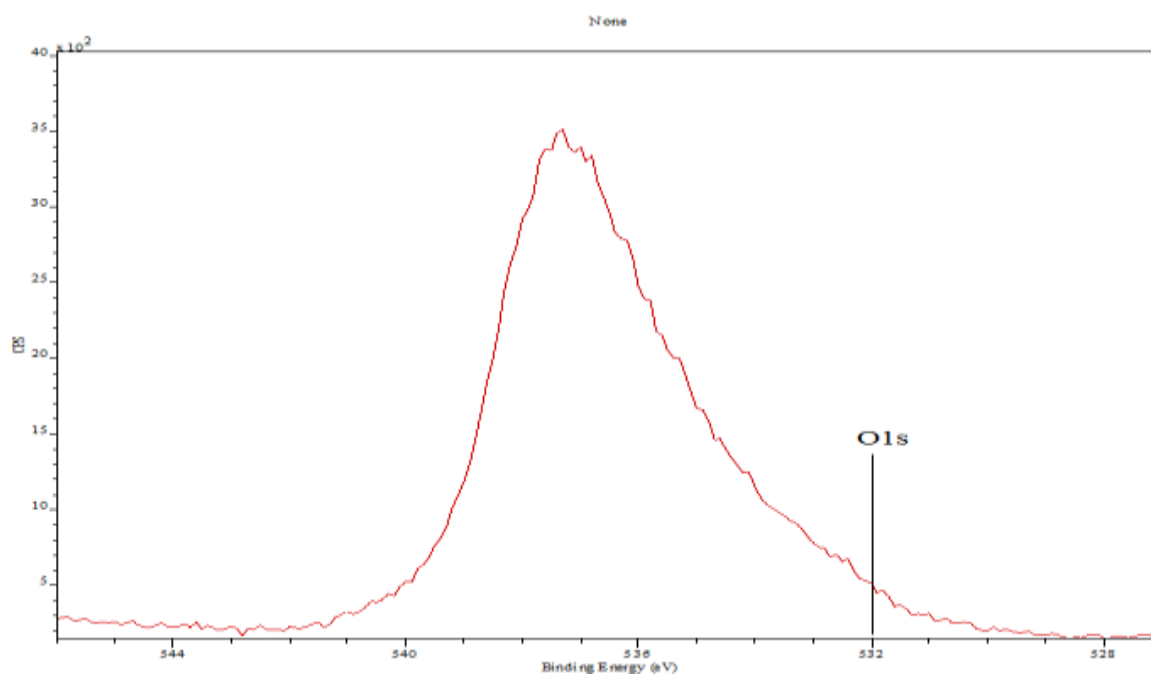
Figure 4.24: XPS binding energy of O_{1s} in Bambu clay
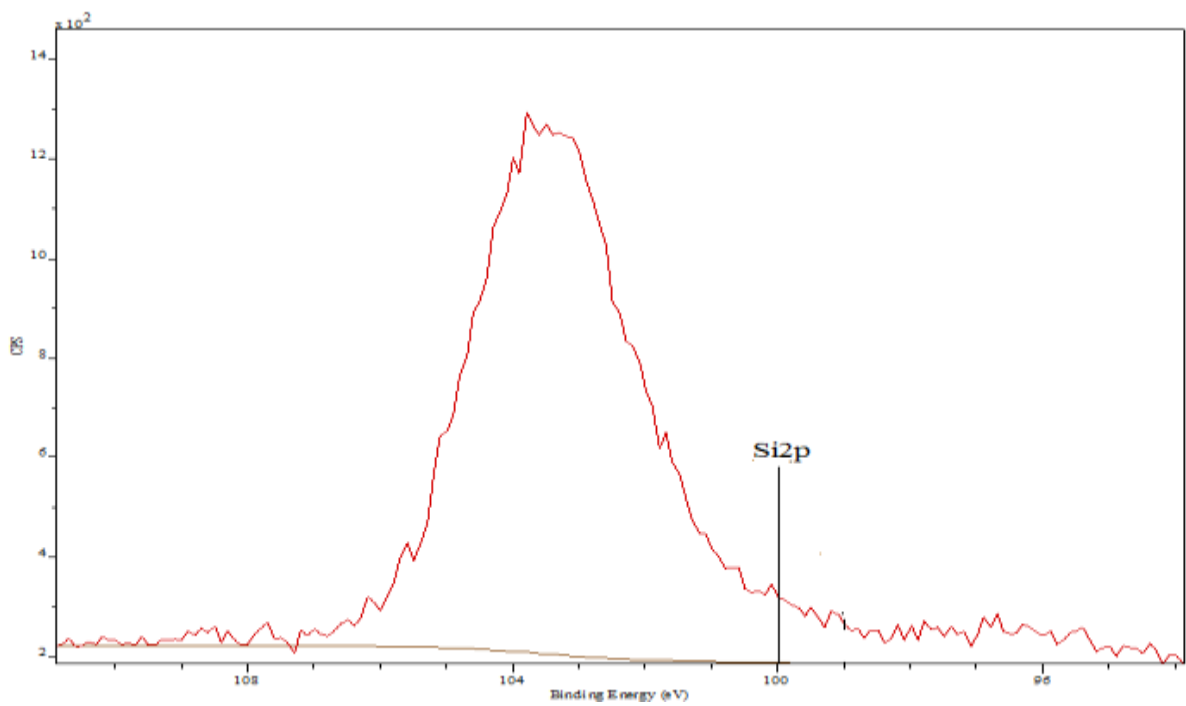
Figure 4.25: X-ray photoelectron spectroscopy of Bambu clay Si_{2p}
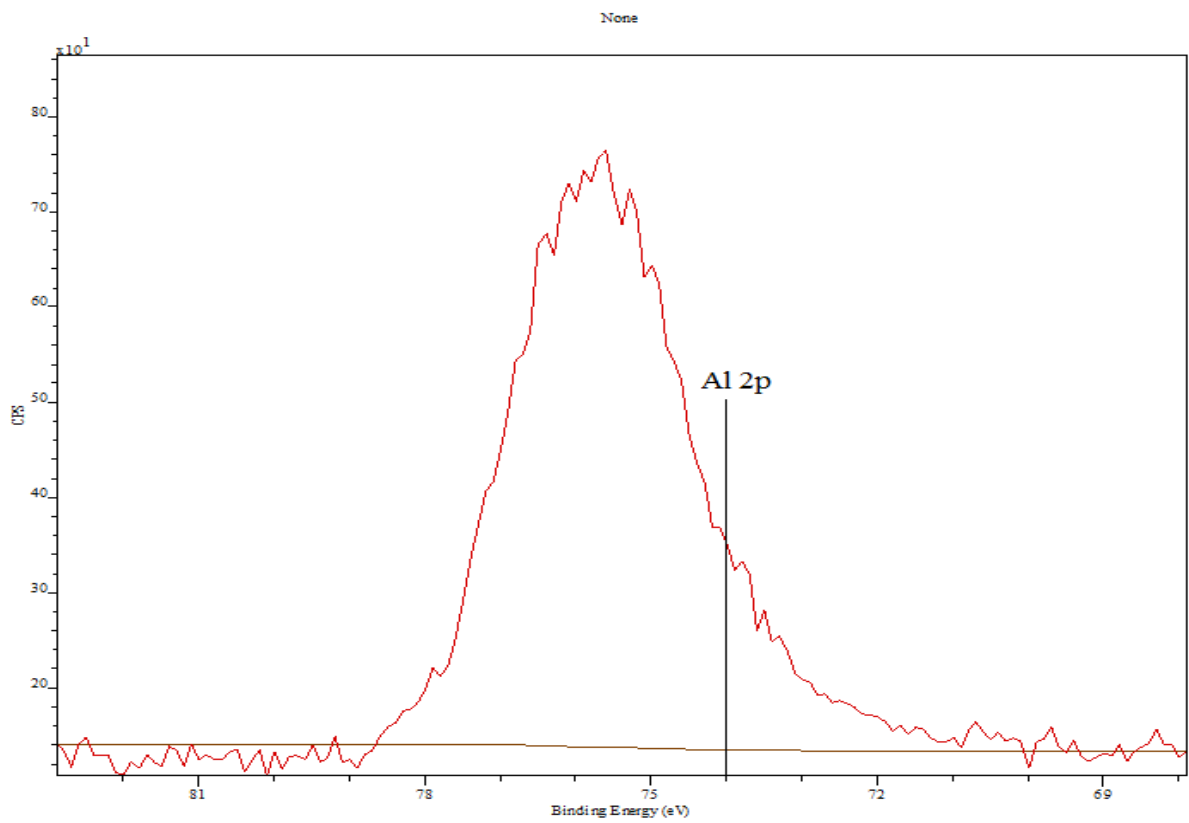
Figure 4.26: X-ray photoelectron spectroscopy of Bambu clay Al_{2p}

4.4.6.3 *Valency band spectra analysis of Bambu clay*

The valency band (VB) spectra analysis was conducted so as to understand the surface behavior of Bambu clay following its exposure to high-resolution analysis and was presented in Figure 4.27. The analysis shows the valence band of Bambu clay had a binding energy of 17 eV. At this binding energy, 17 eV, discrete tetrahedral (silicate) and octahedral (aluminate) layers are present.
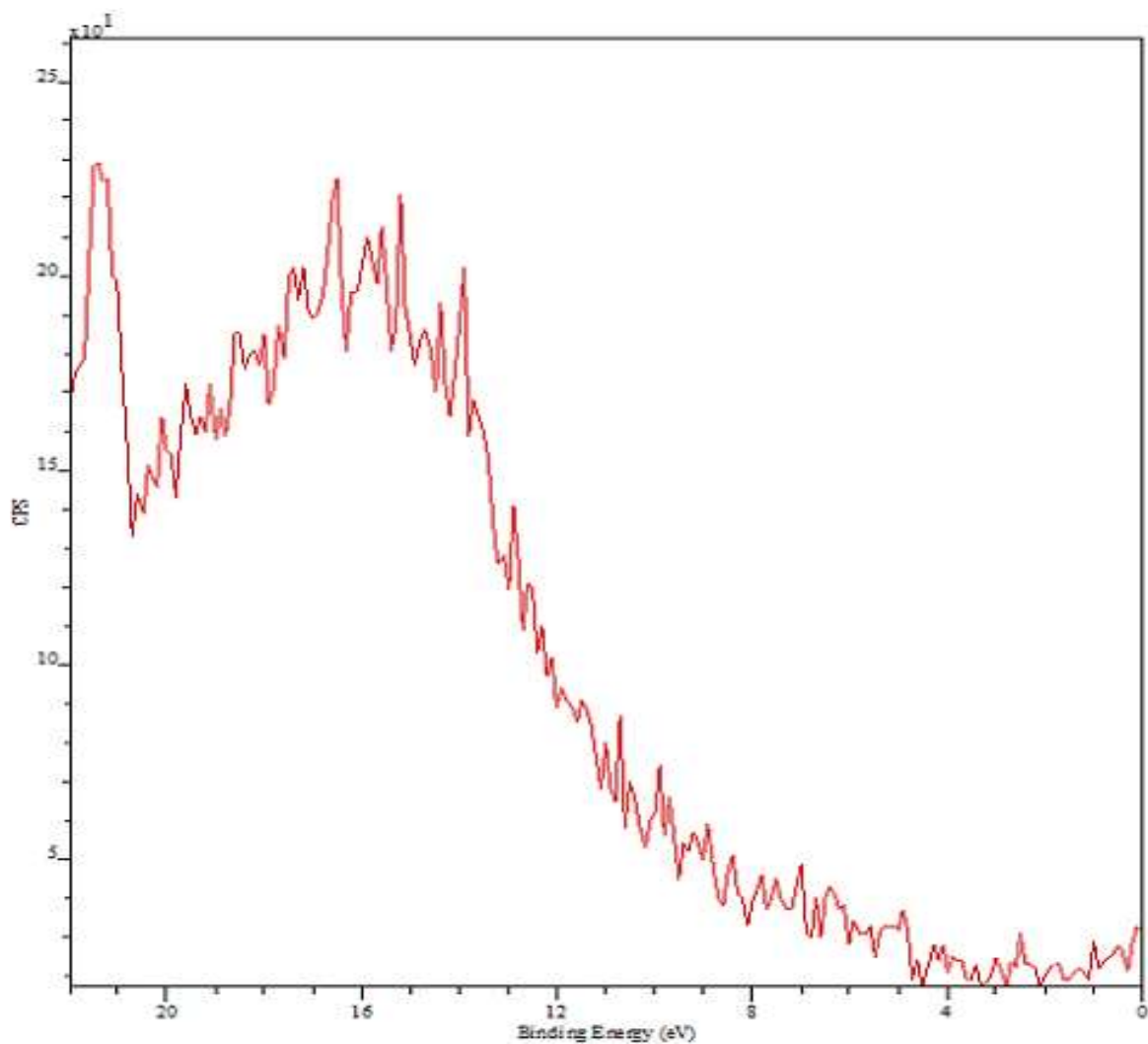
Figure 4.27: Valence band spectra analysis of Bambu clay

It can be established from the analyses conducted on Bambu clay that, the clay is kaolinite and possesses a suitable surface area for further processing as zeolite Y. The analysis of Bambu clay was compared to the result of research work of Nuradden (2015).

4.4.7 Beneficiation of Bambu clay

4.4.7.1 *XRF analysis of beneficiated Bambu clay*

The Bambu clay was beneficiated so as to extract fine and uniform particle sizes. The beneficiated clay was presented in Table 4.11.

Actually, the percentage of SiO_2 oxide has reduced from 52.30 % to 48.87 while the percentage of Al_2O_3 oxide has reduced from 29.20 % to 26.12 %, however, Fe_2O_3 has increased after the beneficiation. The increase of Fe_2O_3 could be as result of total dissolution of the clay in the distilled water, rather than the actual amount of Fe_2O_3. Though it was not clear what was responsible for the increment in the beneficiation process, Appreciable reductions were observed in CaO and K_2O after beneficiation. The reduction was likely to happen as a result of the washing off of soluble salts of calcium and potassium during the beneficiation process. The reduction in K_2O was an indication that Bambu clay could be a good material for the synthesis of zeolite catalysts. This was illustrated by Ajayi (2012) that K_2O was the most difficult impurity that inhibited the synthesis of zeolite Y. However, there was no appreciable reduction in MnO, Na_2O and TiO.

The silica to alumina ratio has slightly increased from 1.80 to 1.87; this increase could be due to washing off some silica higher than the alumina in the clay, furthermore, washing off also affected the loss on ignition (LoI) from 13.03 wt. % to 12.14 wt. %.

Table 4.11: XRF analysis of beneficiated clay

Oxides composition (%)	Beneficiated (%)
SiO_2	48.87
Al_2O_3	26.12
Fe_2O_3	5.14
CaO	0.51
K_2O	0.54
MnO	0.27
NaO_2	0.60
TiO_2	1.69
P_2O_5	Nd
SO_3	Nd
MgO	0.004
LOIwt% (1000^0C)	12.14
Si/Al ratio	**1.87**

Not display = Nd

4.4.8 XRD analysis of beneficiation Bambu clay

Figure 4.28 shows the XRD analysis of the beneficiated Bambu clay results. After beneficiation, the Bragg's angles have not been affected, that is the peaks remain at 12.50, 20.06, 23.30, 25.10, 28.10, 35.00, 38.50, 55.50 and 63.20. This implies that after beneficiation, the kaolinite minerals are more prominent because the peaks at 12.50° and 28.10° increase in intensity from 1800–3000 counts. It was also observed that the highest peak at 26.79° that was responsible for quartz became significantly lower by 66.7 % from its initial intensity counts after beneficiation, which was also indicated by XRF. The reduction

of intensity counts could also be attributed to the washing off of some oxide during the beneficiation process, which was confirmed by XRF in Table 4.11.
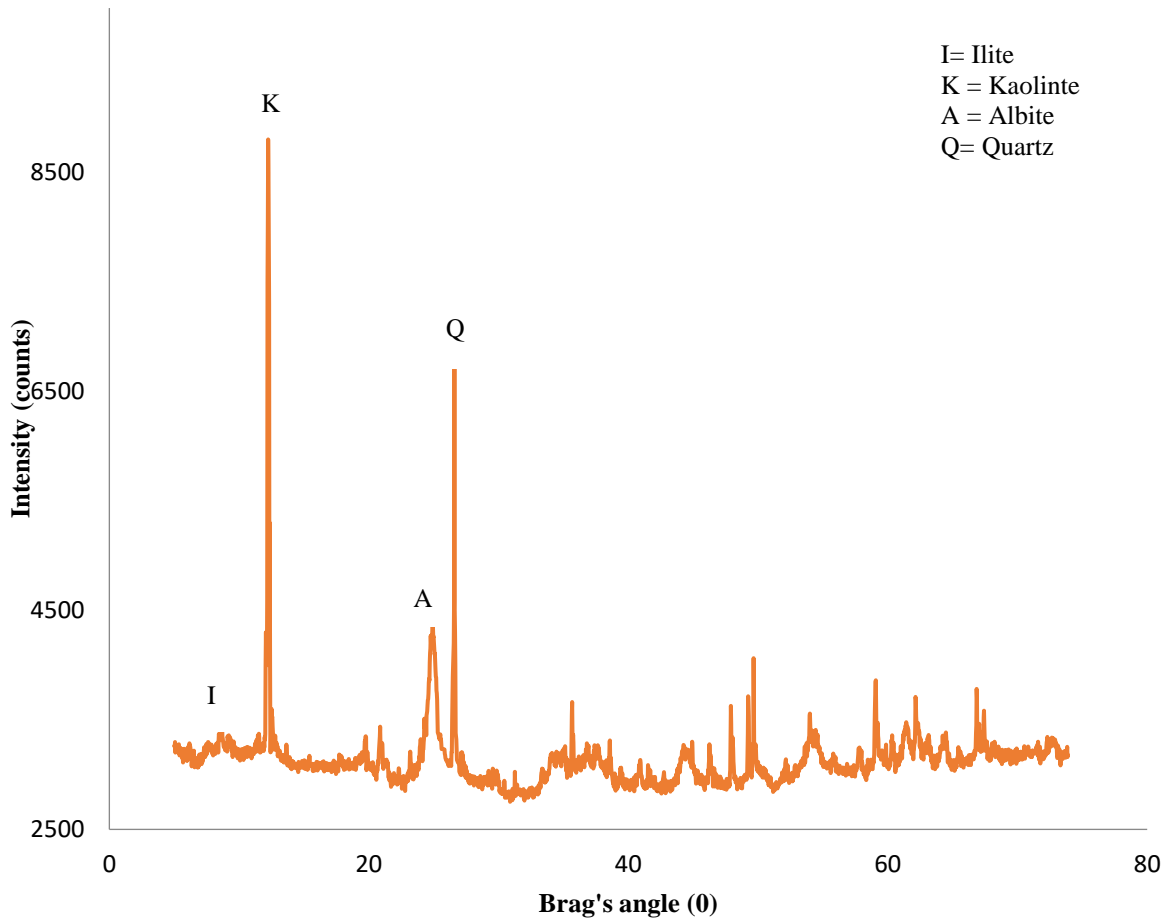
Figure 4.28: XRD pattern of beneficiated Bambu clay

4.4.8.1 *Crystallite size of the beneficiated clay generated from the XRD data*

The results presented showed that the crystallite size of the beneficiated clay was in the range of 8.6 - 35.92 nm as presented in Table 4.12. The overall average crystalline size was 34.27 nm. Therefore, the overall average crystallite size of beneficiated clay contains pores with diameters within the range of 2 and 50 nm which is a mesoporous.

Table 4.12: Crystallite size of the beneficiated clay generated from XRD data

Diffraction angle 2Θ	Θ (radians)	d-spacing (nm)	FWHM (radians)	Crystalline size (nm)
12.35	0.107774081	10.2698	0.008633271	16.16673381
19.92	0.173834793	8.89837	0.01637817	8.602018511
23.3	0.203330858	7.16641	0.005702863	24.84378442
25.72	0.224449342	4.81759	0.007812966	18.21742682
28.08	0.245044227	4.157201	0.009619382	14.8694519
35	0.305432619	3.46352	0.007598291	19.14851648
38.54	0.336324947	3.17778	0.00618981	23.74833912
40.39	0.352469242	2.92041	0.005702863	35.92582567
45.13	0.393833546	2.92041	0.00618981	24.27628794
47.24	0.412246769	2.26329	0.007812966	19.38444807
61.29	0.534856149	1.8176	0.016385151	9.843487566
62.41	0.544629993	1.57172	0.008363618	19.39761024
63.1	0.550651379	1.372	0.016524777	9.853751878
73.71	0.643241096	1.18427	0.007623598	22.74761649
Average crystalline size				**34.27003985**

4.4.9 Scanning electron microscope of beneficiated Bambu clay

The SEM of the beneficiated Bambu clay was presented in Figure 4.29. The Figure reflects the maintenance of kaolinite structure with a reduction in some amount of quartz compared to the amount present in raw clay, though; the Figure does not reflect the enrichment of other minerals after beneficiation other than kaolinite minerals, which are indicated as psedo-hexagonal. Hence, the scanning electronic micrograph is corroborated with both the XRD and XRF results of beneficiated Bambu clay. Therefore, the morphology of beneficiated Bambu clay is predominantly kaolinite.
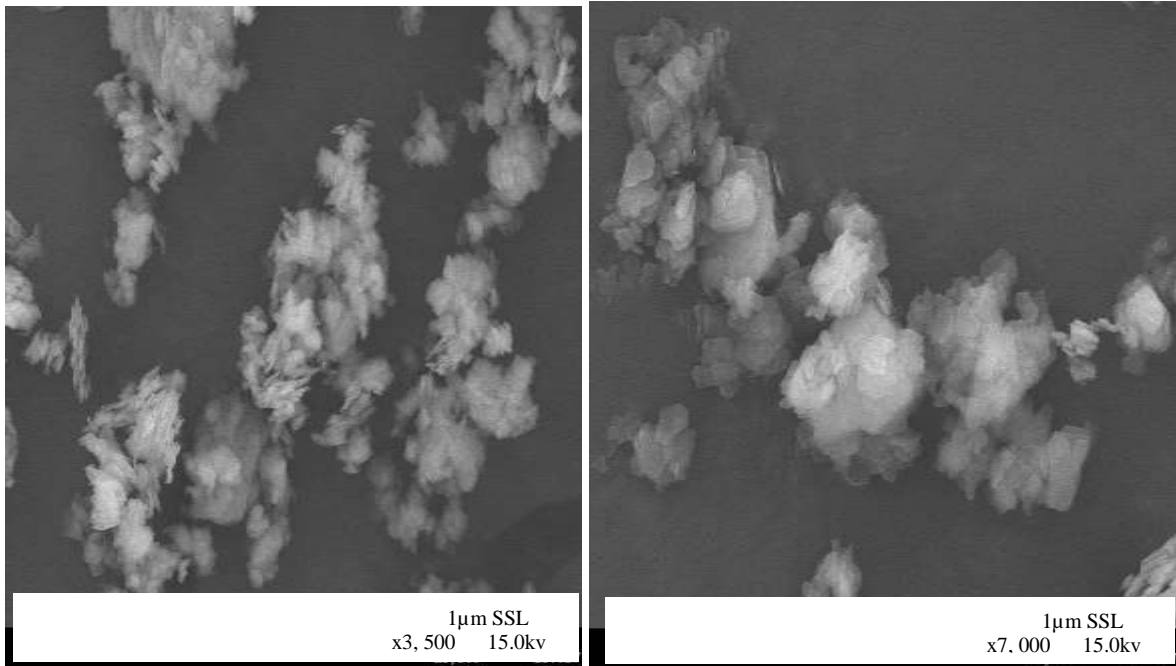
Figure 4.29: SEM of Beneficiated Bambu Clay, (a) at magnification of 3,500X, stack and pseudo-hexagonal (b) magnification of 7,000X, pseudo-hexagonal.

It can be deduced from the beneficiation that the Bambu clay was predominantly kaolinite.

4.5 Metakaolinisation

4.5.1 XRF analysis of metakaolin

The chemical analysis of metakaolin was conducted so as to study the structural changes in composition of SiO_2 to Al_2O_3 after subjecting the beneficiated clay to calcination at 750 ^{o}C in furnace. Table 4.13 presents the result of the chemical analysis of metakaolin, which shows that Al_2O_3 has decreased from 26.12 to 25.02. The decrease of Al_2O_3 illustrates the actual amount of alumina compound; in other words, small amounts of alumina ions have diffused out from the lattice structure of kaolinite, which resulted in the hampering of the octahedral structure. It was reported by Feng *et al*. (2009) that in the temperature range 600 – 800 ^{o}C Al_2O_3 octahedral does not maintain its octahedral shape.

In a similar perspective, during metakaolinization, the beneficiated clay has been subjected to dehydroxylation due to the effect of the heat inside the furnace, though the dehydroxylation begins between 420 °C to 450 °C. The water molecules diffuse out between the layers of the kaolinite structure, and the adjacent OH groups within the structure migrate through the crystal. Again, liberation of outer OH groups appear at temperatures above 450 °C in the kaolinite structure, which consequently, causes the kaolinite crystal structure to form microspores. Furthermore, as the temperature increases to 750 °C, the liberation of inner OH groups appear higher which leads to continuous disorder of the internal structure of kaolinite and, consequently, the porous size of kaolinite increased.

Table 4.13: Chemical analysis of meta-kaolinite

Compound	Raw clay (Bambu)
SiO_2	57.20
Al_2O_3	32.18
Fe_2O_3	5.32
CaO	0.24
V_2O_5	0.022
K_2O	0.41
MnO	0.28
NaO_2	0.50
TiO_2	1.7
P_2O_5	ND
SO_3	ND
CuO	0.034
MgO	0.004
NiO	-
CuO	-
ZnO	0.011
Ga_2O_3	0.021
Ta_2O_5	-
Cl	-
LOI (1000^0C)	2.08
Si/Al ratio	**2.11**

Not Display = ND

4.5.2 XRD analysis of metakaolinite

The XRD pattern of metakaolinite kaolin was presented in Figure 4.30. It was observed that Quartz appears to resist calcinations, but its component was suppressed. This resistance was evidence that quartz was still inert after calcinations at 750 °C, showing that the temperature was not high enough to deform the structure of quartz. The suppression was also noticed in Figure by the relatively short peak after beneficiation. Though, XRD pattern revealed that the metakaolinite became highly amorphous due to the collapse of the kaolin structure as a result of calcinations at 750 °C. As affirmed by XRF in Table 4.7, the illite and albite have been suppressed in the bambu clay; the peaks disappeared after being subjected to calcination at 750 °C but some phases were relatively passive to the calcination.

In order to appreciate the mechanism of metakaolinization, consider the chemical equation of dehydroxylation expressed in Equation 4.11. The crystallite structure of kaolin was completely transformed into a reactive amorphous structure known as meta-kaolin.

$$Al_2.2Si_2O_3.H_2O \xrightarrow{\quad 750\,^{\circ}C \quad} Al_2.2Si_2O_3 + 2H_2O \qquad (4.11)$$
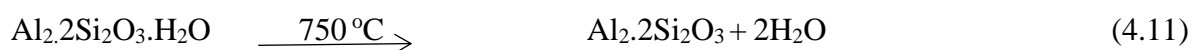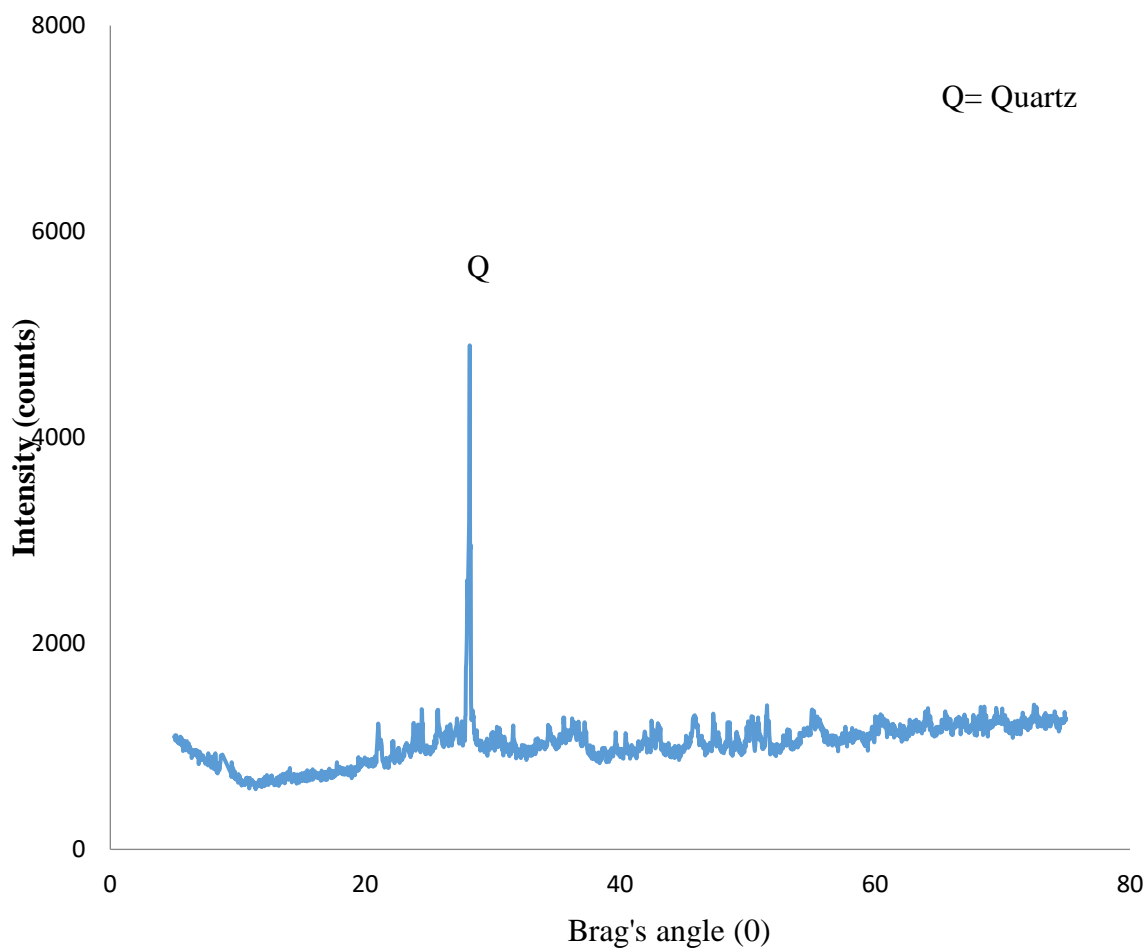
Figure 4.30: XRD pattern of metakaolinite

4.5.2.1 *Crystallite size of the metakaolin generated from the XRD data*

The result showed that the crystallite size of the mineral in raw Bambu clay was in the range of 8.6 - 60.20 nm while the overall average crystallite size was 24.94 nm as presented in Table 4.14.

Table 4.14: Crystallite size of the meta-kaolin generated from the XRD data

Diffraction angle 2Θ	Θ (radians)	d-spacing (nm)	FWHM (radians)	Crystalline size (nm)
9.845	0.085913832	9.71411	0.008320857	16.73814252
12.023	0.104920468	4.22586	0.006285803	22.19752663
21.7857	0.190116097	4.1875	0.017441948	8.101620679
23.1515	0.202034951	3.74092	0.005479461	25.84980086
25.6795	0.224095913	3.46917	0.004606797	30.89363014
27.109	0.236570653	3.32392	0.004127704	34.58039163
28.1755	0.245877622	3.16727	0.002376266	60.20572583
30.5323	0.266444582	2.92795	0.015871152	9.062831719
34.4856	0.300943632	2.60081	0.007042404	20.63099912
42.5295	0.371139902	2.23046	0.007894997	18.8600354
45.8229	0.399880239	1.98028	0.003571816	42.17655048
48.5042	0.423278996	1.87689	0.007894997	19.2772132
50.853	0.443776142	1.8144	0.006595599	23.2950018
53.2089	0.464335248	1.72008	0.005445427	28.49988076
63.0668	0.550361654	1.45226	0.006974336	23.34302633
69.7464	0.608652161	1.34724	0.015261159	11.0827391
72.523	0.632882567	1.30234	0.00588525	29.24118745
Average crystalline size				**24.94331198**

4.5.3 Scanning electronic microscope of metakaolinite

The Scanning Electron Microscope of the meta-kaolin is presented in Figure 4.31. It can be observed that the morphology presented earlier in the SEM image of the raw and beneficiated kaolin in Figures 4.22 and 4.29 has disappeared with the appearance of more platy plate lumps together. This relatively lump-like platy morphology observed in the material could be a result of the crystalline silica contained in the clay. The lump-like morphology could be attributed to the highly amorphous nature of the material as a result of the collapsing of the kaolinite structure, as was already identified by the analysis of the XRD results.
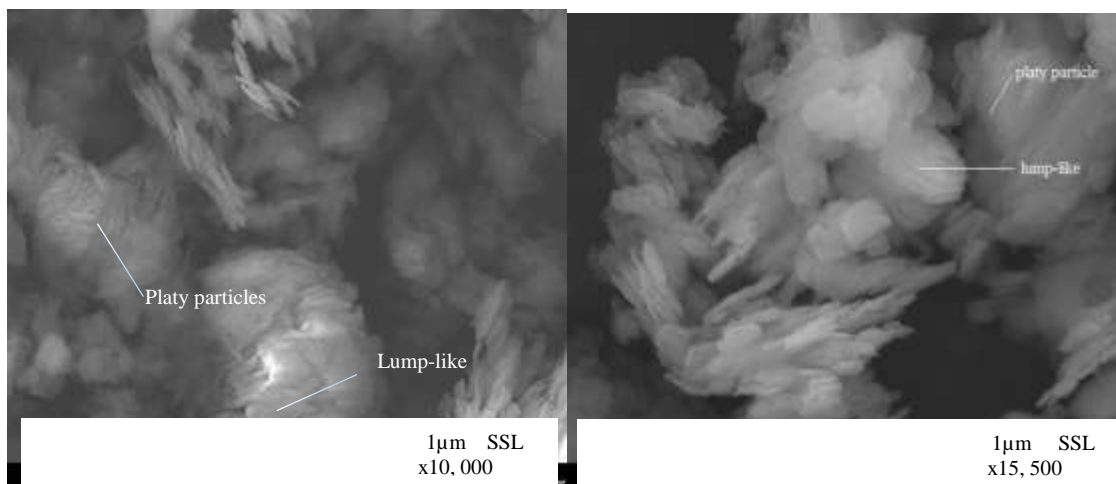
Figure 4.31: High Resolution Scanning Electron Microscopy of meta-kaolin (a) Platy particle indicated as lump-like at 15,000X magnification, and (b) lump-like particle at higher nano of 100 m magnification.

4.5.4 Brunauer-emmett-teller analysis of metakaolin

Table 4.15 presents the Brunauer-Emmett-Teller (BET) analysis of metakaolin and the literature values of other metakaolin BET. The result of BET analysis as presented in Table 4.15 shows that the metakaolin has a surface area of up to 530.40 m^2g^{-1}, pore volume of 0.120 cm^3g^{-1} and a pore radius of 2.128 nm. This result was compared to the results of BET presented in the research work of Khati *et al*. (2018).

Table 4.15: BET specific surface area and pore volume of metakaolin

Sample	BET surface (m^2/g)	Pore volume (cm^3/g)	Pore radius (nm)
Metakaolin	530.40	0.120	2.128

4.5.5 Comparison of chemical analysis of Bambu, beneficiated and metakaolin

Table 4.16 presents the comparison of chemical analyses of Bambu clay, beneficiated clay, and metakolin. The Si/Al ratio of the Bambu clay was 1:8, but after being subjected to beneficiation, it decreased by 3.8%. The decrease in Si/Al ratio could be attributed to the washing away of S^{4+} and Al^{3+} during the beneficiation process.

Similarly, the ratio also increased after metakolinization. The reduction was caused by the partial dissolution of Al^{3+} cations from the octahedral sheet of the Bambu clay structure and therefore resulted in a relative increment in the percentage of silica, reaching up from 48.8% to 57.20%, while that of alumina reduced from 26.20 to 32.12 % as shown in Table 4.16.

The LoI of the Bambu clay was 13.03 wt.%; after beneficiation, the clay decreased by 3%. The decrease could be a result of washing away some impurities. There was a sharp decrease after metakaolinization from 13.03 wt. % to 2.16 wt. %. This decrease could be assigned to the loss of the structural water, which takes place as an endothermic reaction from kaolin in the furnace during the calcination process; resulting in the driving off of the chemically combined water in the clay.

Table 4.16: Comparison of XRF analysis of raw, beneficiated, metakaolin and ideal kaolin

Compound	Bambu clay	Beneficiated clay	Meta-kaolin
SiO_2	54.40	48.87	57.20
Al_2O_3	29.30	26.12	32.18
Fe_2O_3	4.20	4.14	5.32
CaO	0.41	0.51	0.24
V_2O_5	0.029	-	0.022
K_2O	1.76	0.54	0.41
MnO	0.081	0.27	0.28
NaO_2	0.80	0.60	0.50
TiO_2	1.64	1.69	1.7
P_2O_5	ND	Nd	ND
SO_3	ND	Nd	ND
CuO	0.028	-	0.034
MgO	0.007	0.004	0.004
NiO	-	-	-
CuO	-	-	-
ZnO	0.019	-	0.011
Ga_2O_3	0.012	-	0.021
Ta_2O_5	-	-	-
Cl	-	-	-
LOI(1000^0C)	7.31	12.14	2.08
Si/Al ratio	**1.80**	**1.87**	**2.11**

LOI = Loss of Ignition

ND = Not Displace

The Comparison of the XRD patterns of Bambu clay, beneficiated clay, and metakaolin was presented in Figure 4.32. The three patterns showed further relative intensities of the various peaks so as to give a clearer understanding of the clay processes. The Figure shows that the highest peak was responsible for quartz, which became significantly lower by 66.7 % from its initial intensity after beneficiation.
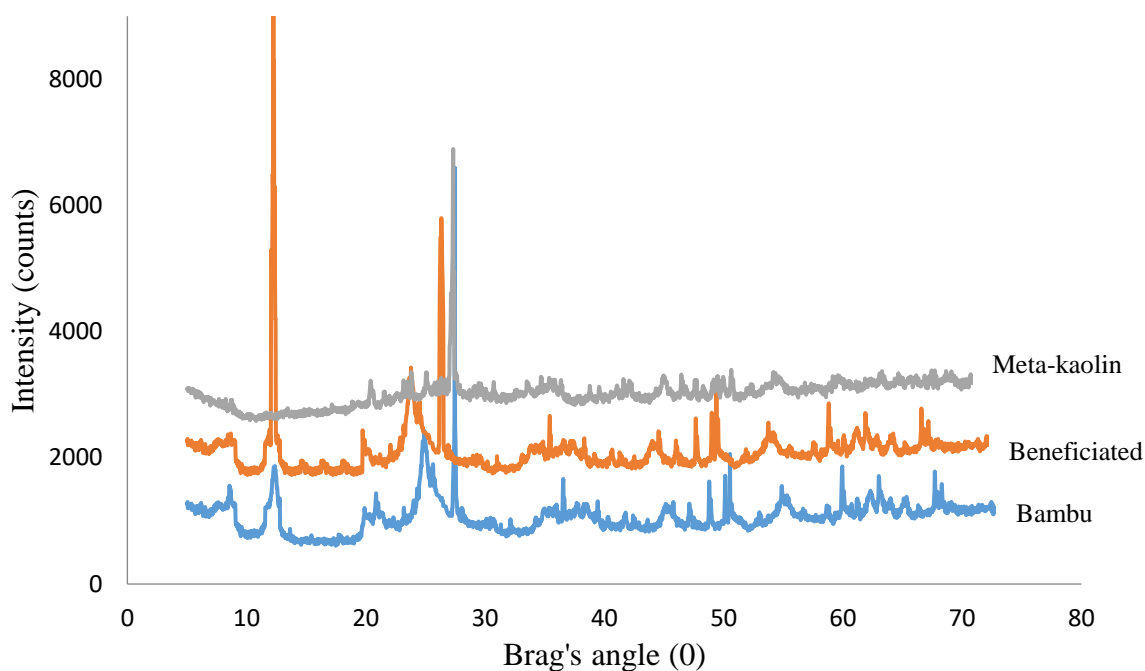
Figure 4.32: Comparison of the XRD pattern of Bambu clay, beneficiated clay and metakaolin

4.7 Characterization of the Synthesised Zeolite

The zeolite used in this study was locally sourced from Bambu clay for catalytic co-pyrolysis of *Sida Rhombifolia* with LDPE and HDPE.

Table 4.21 provides the X-ray Fluorescence (XRF) chemical analysis of synthetic zeolite. The analysis of the X-ray diffraction of the zeolite catalyst was presented in Figure 4.33. The BET result was presented in Table 4.22. A scanning electron microscope (SEM) was presented in Figure 4.34.

4.7.1 X-ray fluorescence of the synthesised zeolite

The X-Ray Fluorescence (XRF) analysis provides adequate information about the synthesized zeolite from Bambu clay. Table 4.21 provides the X-ray fluorescence analysis, where SiO_2 and AlO_3 predominate in a higher percentage than any oxides. From the Table, it was found that the synthetic zeolite was rich in silica (50.157%) and alumina (20.910%), which are regarded as the primary constituents. Other elements are in low proportion: Fe_2O_3 (1.4590%), Na_2O (2.2203%) and MgO (2.1600%) as well as traces of other elements as presented in Table 4.21. The synthetic zeolite has an approximately 2.4 Si/Al ratio; hence, the result obtained was in line with the chemical composition of a Y - type zeolites.

Table 4.21: XRF analysis of zeolite Y-type

Oxides composition	Zeolite Y-type
SiO_2	50.157
Al_2O_3	20.910
Fe_2O_3	2.3937
CaO	0.3399
V_2O_5	0.00987
K_2O	0.7319
MnO	0.01607
NaO_2	14.784
TiO_2	0.9508
P_2O_3	0.2624
SO_3	0.1208
CuO	0.00407
MgO	2.060
NiO	0.00509
Cr_2O_3	0.01352
ZnO	0.01003
Ga_2O_3	0.001649
PbO	0.01637
Ta_2O_5	0.000
Cl	1.920
LoI wt% (1000^0C)	4.47
Si/Al ratio (mass)	**2.42**

LoI = Loss of Ignition

4.7.2 X-ray diffraction of the synthesised zeolite

The X-Ray Diffraction (XRD) was also extensively used for the study of synthesized zeolite from Bambu clay. Figure (4.33) presents the XRD pattern of the zeolite. It was observed from the Figure that the diffraction peaks at 2θ angle 6.184°, 10.123°, 12.277°, 15.664°, 18.710°, 20,365°, 23.647°, 27.088°, 31.475°, 49.278°, 55.108°, 62.382° and 72.177° are similar to the diffraction peaks of zeolite Y. The Figure shows that each peak reveals the presence of a highly crystalline zeolite structure with well-defined diffraction peaks of a high structural order that are similar to the XRD pattern of standard zeolite Y. The intensity of the detected peaks was compared to information provided by JCPDS (Joint Committee on Powder Diffraction Standards) through the library of the International Center for Diffractional Data (ICDD, 2015). The presence of other non-zeolitic phases was not detected, and others were very minor, which indicated the purity level of the zeolite synthesized.
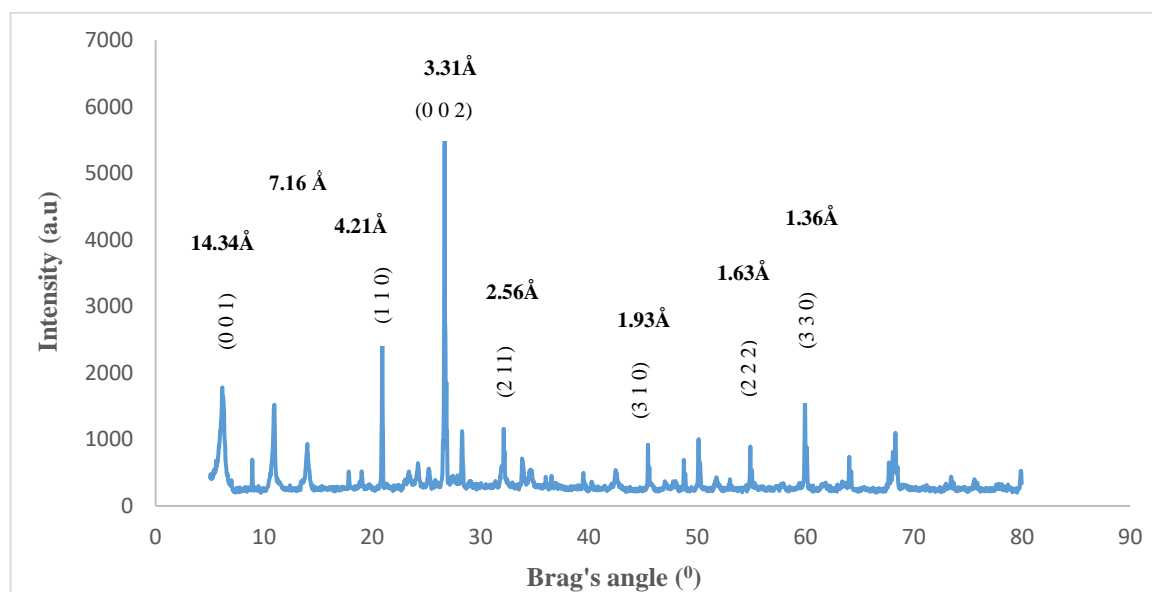
Figure 4.33: XRD analysis of synthesised zeolite

4.7.3 Scanning electron microscope of the synthesised zeolite

The Scanning Electron Microscope (SEM) of the synthesized zeolite was conducted at various magnifications from 3,500, to 40,000 so as to show the structural morphology of the zeolite. The result of the SEM was presented in Figure (4.34). It can be seen from the micrograph (a) that at lower magnification (3,500), the particles seemed to agglomerate closely. The micrograph (b) at higher magnification (40,000) shows the particles are closely flat. This implies that the micrograph shows individual particles having regular tetrahedral and bulky shapes. This explanation corroborated the micrograph of Ajayi (2012), where the individual particle appeared to be agglomerated at lower magnification.
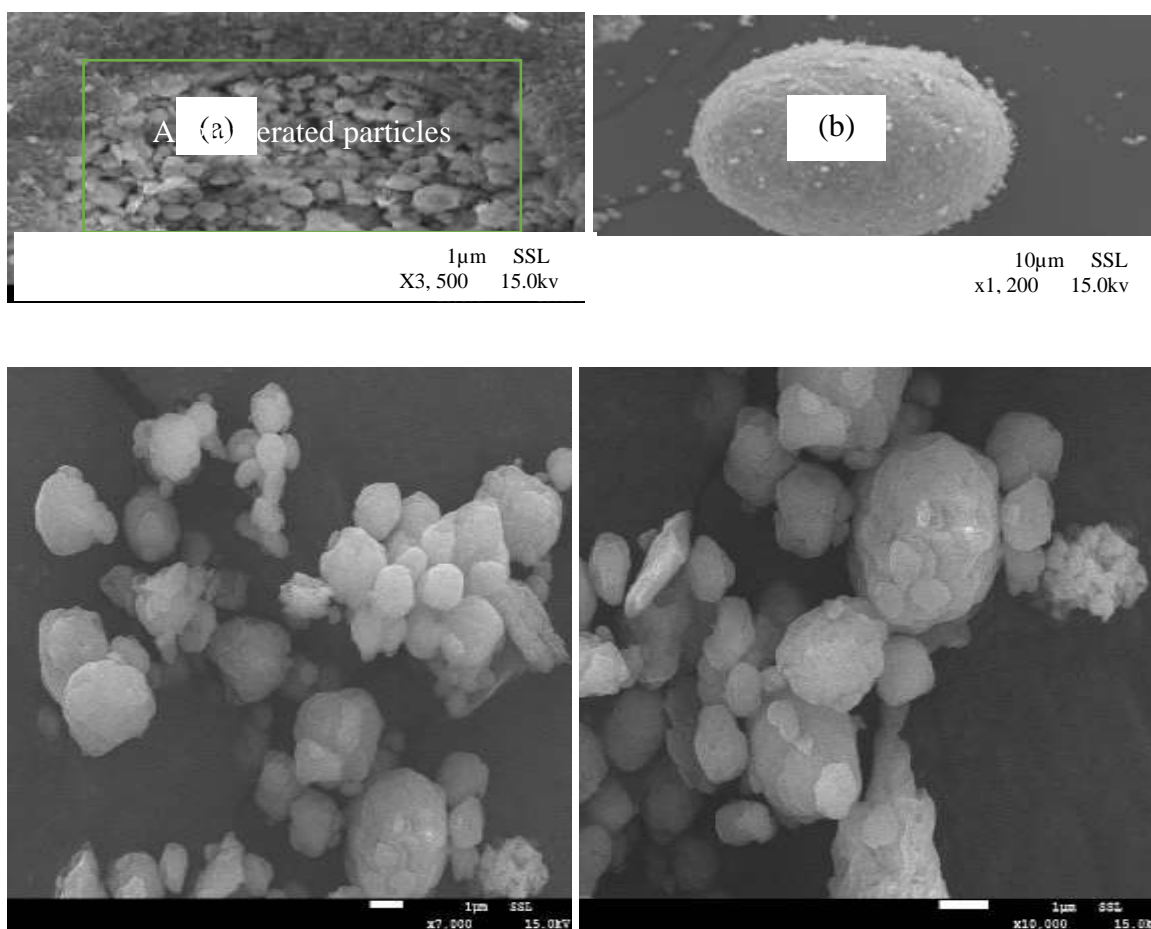
Figure 4.34: SEM of the synthesised zeolite

4.7.4 BET specific surface area and volume of the synthesised zeolite

The BET analysis was conducted to determine the surface area, pore volume, and pore radius of the synthesized zeolite. Table 4.22 presents the BET analysis of synthesis zeolite and the literature values of other zeolites BET.

The result of BET analysis as presented in the Table shows that the synthesized zeolite has a higher surface area of 549.092 m^2g^{-1}, pore volume of 0.270 cm^3g^{-1} and a lower pore radius of 2.111 nm. The surface area as presented in the Table was higher than the surface areas of Kankara and Elefun, at 462.0 and 493.0 m^2g^{-1}. The result of surface area as presented in Table 4.22 was higher compared to the result of BET presented by the research work of Ajayi (2012). This could be attributed to the higher number of silica available in the zeolite than the amount of alumina.

Table 4.22: BET of the synthesised zeolite catalyst

Sample	BET surface area (m^2/g)	Pore volume (cm^3/g)	Pore radius (nm)
Synthesis zeolite catalyst (from Bambu clay)	549.092	0.270	2.111
Synthesis zeolite catalyst (from kankara 2016)	462.00	-	-
Synthesis zeolite catalyst (from Elefun 2018)	493.00	-	-

4.7.5 X-ray photoelectron spectroscopy of the synthesised zeolite

The X-ray Photoelectron Spectroscopy (XPS) was used in the study to determine the elemental composition, binding energies of silicon, oxygen, and aluminum on the surface of the synthesized zeolite, as well as to reveal the elements that XRF and XRD could not detect. Table 4.23 presents the binding energy (eV) and atomic % of the synthesized zeolite.

4.7.5.1 *XPS analysis of the synthesized zeolite*

Table 4.23 presents the binding energy (eV) and atomic % of the synthesized zeolite. The Table as presented consists of the number of sub-level S and P orbitals of elemental composition with their associated binding energies. It can be seen from the Table that the elements O_{1s}, C_{1s}, Na_{1s}, Ca_{2p}, Si_{2p}, Al_{2p} and K_{2p} correspond with binding energies of 531.931, 283.604, 1070.595, 351.185, 296.684, 98.30, 72.10 eV. The Table also presents the Si/Al ratio of 2.45. This ratio is corroborated with XRF analysis as presented in Table 4.21 where the zeolite that developed has a Si/Al ratio of 2.4. Hence, XPS analysis reveals that the zeolite was Y - type.

Table 4.23: Binding energy (eV) and atomic % of the synthesized zeolite

S/n	Elemental	Binding energy	Atomic %	Atomic ratio Si/Al
1	O_{1s}	531.931	53.0	-
2	C_{1s}	283.604	11.0	-
3	Na_{1s}	1070.595	0.7	-
4	Ca_{2p}	351.185	0.9	-
5	K_{2p}	296.684	0.6	-
6	Si_{2p}	98.30	21.1	-
7	Al_{2p}	72.13	8.6	2.45

4.7.5.2 *Core level binding energy of the synthesized zeolite*

The core level binding energy of the synthesized zeolite was presented in Figure 4.35 (A to

B). Figure 4.35 (A) for Al_2p, (B) for Sip, (C) for O1s, and (D) for Ca_2p respectively. The

Figure as presented shows the results of the high-resolution scans for Al_{2p}, Si_{2p}, O_{1s}, and Ca_{2p}

of the zeolite. It can be seen from the Figure that the elements as presented have binding

energies of each Bridging Oxygen (BO) to the elements that formed the major structure of

the zeolite (Al_{2p}, Si_{2p} and O_{1s}). Al_{2p} has BO 72.13eV, Si_{2p} has BO 98.30eV, Ca has BO

351.185 and O_{1s} has BO 531.931 respectively. The shifting pattern in BO of the zeolite

analyzed by XPS could indicate the presence of covalent or ionic bonds within the

zeolite structure.

(A)

(B)

(B)

(D)
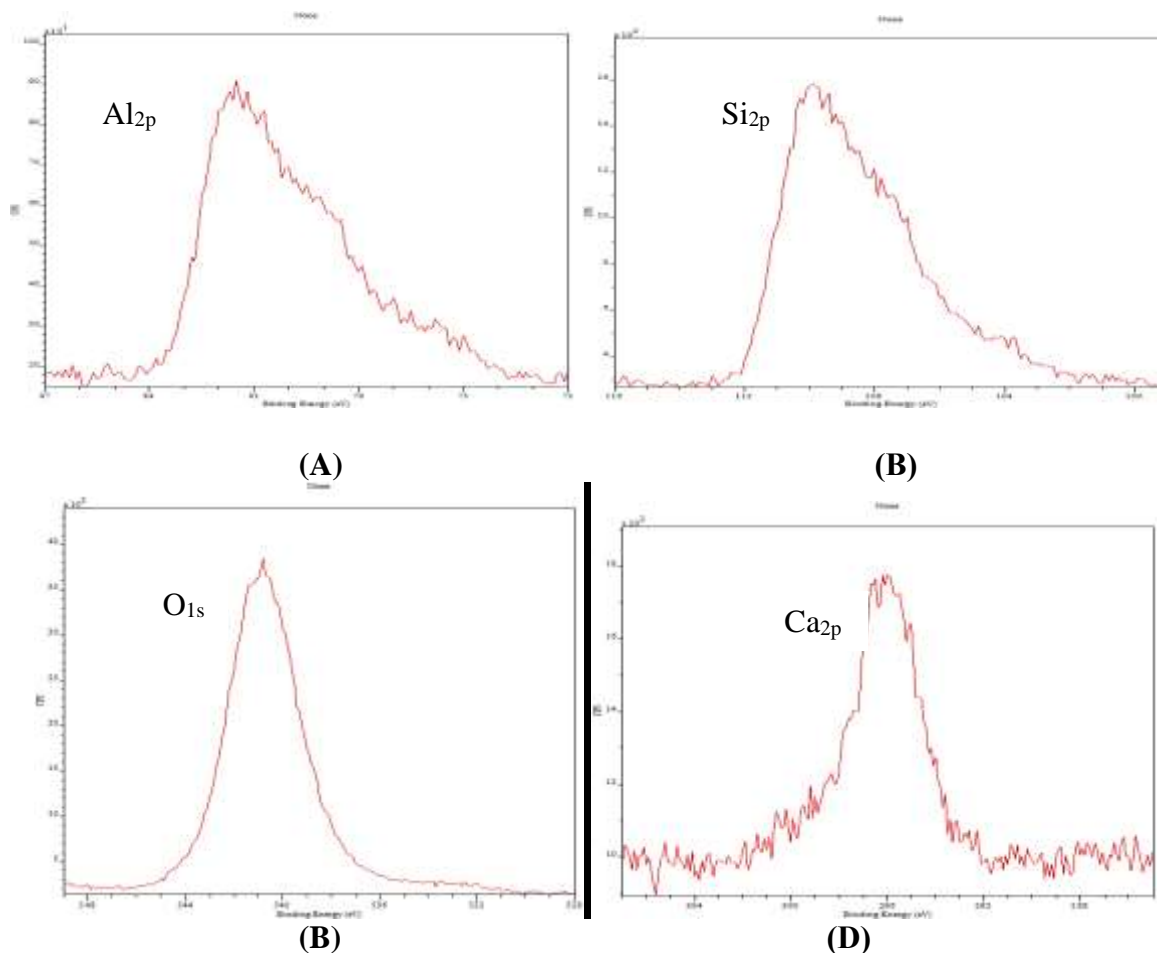
Figure 4.35: Results of Core level binding energy of the synthesized zeolite

4.7.5.3 *Valence band spectra analysis of the synthesized zeolite*

The valence band spectra of the synthesized zeolite were analysed so as to understand the inner and outer valence bands of the zeolite structure. Figure 4.36 presents the inner valence O_{2s} and outer valence band XPS spectra of the zeolite. It can be seen that the inner valence of O_{2s} peak was broad and asymmetric at binding energy 24.0347 eV as presented in the Figure. While the outer valence spectra have three peaks, peak one shows that Si_{2s} has 8.037 eV binding energy, peak two shows that Al_{2s} has 1.004 eV binding energy, and peak three shows Na_{2s} has 1.003 eV binding energy, respectively. It was observed from the outer valence spectra that peaks two and three slightly overlap between Al_{2s} and Na_{2s} respectively. This clearly indicated that Peaks 2 and 3 are closely associated as attachments to metals in the zeolite structure (Al, Na,), which implies that the synthesized zeolite could be more ionic than covalent.
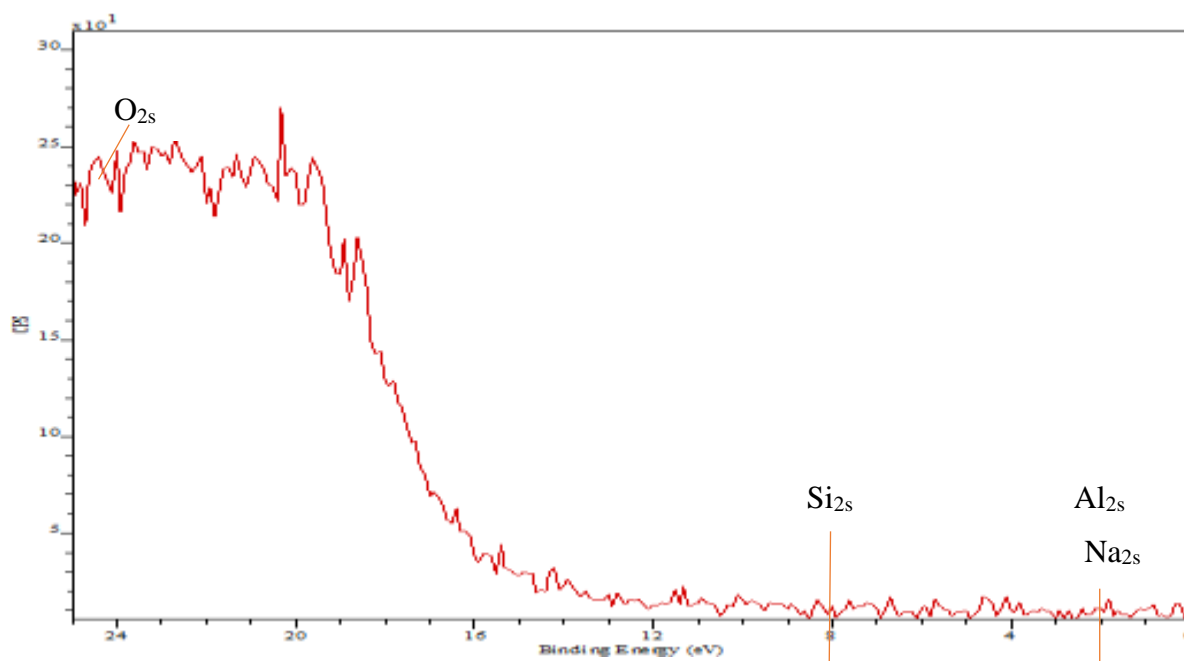
Figure 4.36: Inner valence (O_{2s}) and outer valence band XPS spectra of the synthesized zeolite

4.7.6 Acidity analysis of the clay, metakaolinite and zeolites

To determine the surface acidity of zeolites, pyridine was used as a probe molecule; bambu clay, meta-kaolin, synthesized zeolite Y-type, and commercial zeolite Y as presented in Table 4.24. The amount of adsorbed pyridine on the samples was analyzed in the 4500–500 cm^{-1} wavelength region. The Table presents the Lewis bond (cm^{-1}) and Bronsted bond (cm^{-1}), the integral areas (A$_L$ and A$_B$) covered by the Lewis and Bronsted spectra, the calculated concentrations of Lewis and Bronsted, and their ratio respectively.

Table 4.24: Acidity analysis of the samples

Samples of catalyst	Lewis broad (cm^{-1})	Lc Area (μmol)	Bronsted Bond (cm^{-1})	Bc Area (μmol)	Lc (μmol/g)	Bc (μmol/g)	Total (μ/mol/g)	Bc/Lc
Bambu clay	1483.66	5.374	1620.26	3.69	34.40	31.57	65.97	0.92
Meta-kaolin	1473.82	9.51	1633.69	3.70	60.92	24.12	85.04	0.39
SZY	1454.85	34.37	1650.90	10.85	220.18	93.44	313.62	0.42
CZY	1454.86	34.97	1652.91	11.87	224.02	102.20	326.22	0.46
Literature value (2015)	1450.00	20.36	1550	6.14	131.02	52.52	183.54	0.40

Table 4.42, as presented, indicated that the pyridine molecule interacted with the surface of the sample's acid sites. The interaction occurred when the protonated ion from the pyridine molecule interacted with the bronsted acid site of the catalysts at a specific absorption band at a wavenumber of 1620-1655 cm^{-1}. It was observed from the Table that the Bronsted acid

site of Bambu clay was at 1620.26 cm^{-1}, meta-kolin was at 1633.69 cm^{-1}, synthesize zeolite Y-type was at 1650.90 cm^{-1} and commercial zeolite Y was at 1652.91 cm^{-1} respectively. This specific wavenumber as presented differs from the wavenumbers revealed by the research work of Nuradden (2015), which show that their specific wavenumbers were at 1545 cm^{-1} and 1550 cm^{-1}.

Similarly, the Lewis acid site interaction with the pyridine molecule occurred when the free electron pairs of the pyridine molecule interact with an empty orbital of alumina in the zeolite. This interaction led to the appearance of the specific absorption at wavenumbers 1454 – 1485 cm^{-1}. Also, it was observed that the Lewis acid site of Bambu clay was at 1483.66 cm^{-1}, meta-kolin was at 1473.82 cm^{-1}, synthesised zeolite Y-type was at 1454.85 cm^{-1} and commercial zeolite Y was at 1454.86 cm^{-1} respectively. Though the specific wavenumber as presented was similar to the wavenumbers revealed by the research work of Nuradden (2015), which showed that their specific wavenumbers was at 1450 cm^{-1} and 1452 cm^{-1}.

Again, in the acidity analysis presented in the Table, it was observed that the integral areas covered by the Lewis spectra of the zeolite was higher than the Bronsted spectra of the zeolite, as well as the calculated concentration of the Lewis acidic site was higher than the Bronsted acidic site. Accordingly, the Bronsted/Lewis's acidity (BC/LC) ratio was very low. It was observed that the overall samples considered in the study possessed low values of Bronsted acidity and relatively high Lewis's acidity. This analysis corroborated the analysis of Nuradden (2015).

4.7.7 Effect of crystallization temperature for zeolite synthesis

The study also investigates the crystallization temperatures as one of the factors in the synthesis of zeolite Y. Figure 4.37 shows the Four diffractogram patterns of crystallization temperature at 80 °C, 90 °C, 100 °C and 110 °C respectively. The angle 2θ and d-spacing of the synthesized zeolite Y was compared with the similar 2θ and d-spacing of the reference zeolite Y (Ayodeji *et al*., 2018).

Figure 4.37 shows that the diffractograms show that the intensity of the first distinct peaks are not pronounced at the crystallization temperatures of 80 °C and 90 °C. This could be due to the amorphous materials associated with the precursor, which might require a higher temperature. It was observed that the intensity of the first distinct peaks appears at the pattern of temperatures 100 °C and 110 °C as shown in the Figure, though the intensity was more pronounced at pattern of temperatures 100 °C than 110 °C. Again, the second peak appears at the pattern of temperature 100 °C which was absent at the pattern of temperature 110 °C as presented in the Figure. This explanation corroborated the research work of Sumari *et al*. (2019), where at high temperatures the zeolite Y is transformed into another zeolite, such as zeolite P.
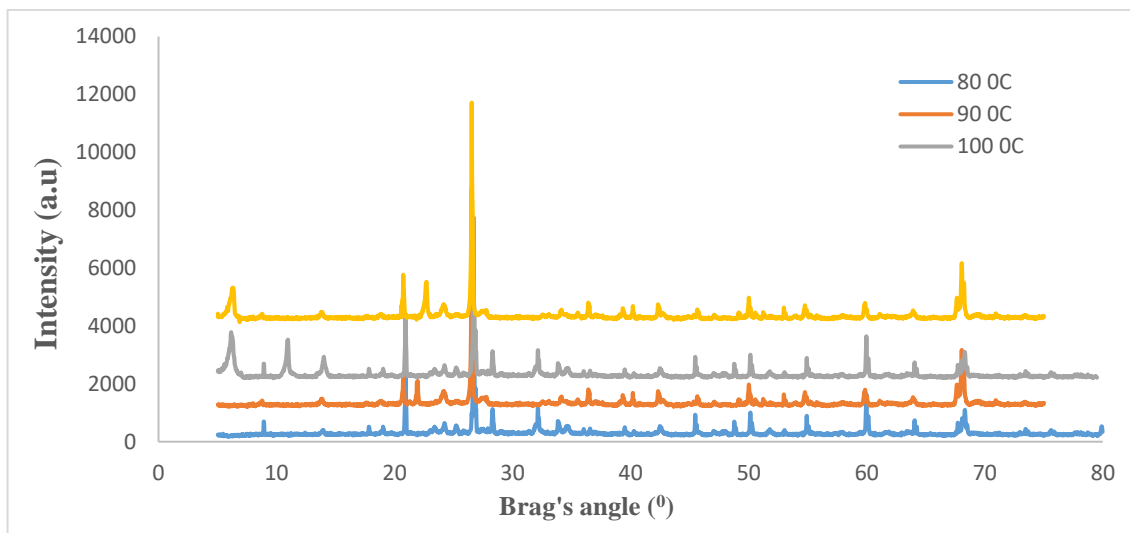
Figure 4.37: Crystallization temperature for zeolite synthesis

Therefore, it can be deduced that at a temperature of 100^0C, the synthesized zeolite Y was achieved by the sudden appearance of some sharp peaks with the intensity, position of angle 2θ and d-spacing as observed from the XRD diffractogram, hence, this zeolite is Y-type. This diffractogram was compared with the standard reference Zeolite Y in the research work of Ayodeji *et al*. (2018).

4.7.8   X-ray fluorescence of the synthesised zeolite Y catalyst

Table 4.25 shows that the X-Ray Fluorescence (XRF) analysis of the synthesized zeolite Y after ion exchange with ammonia chloride (protonation) As can be seen from the Table, the amount of Na_2O was 3.061 %. It was observed that after protonated, the amount of Na_2O in Table 4.25 was lower than the amount of Na_2O 14.784 % (at the molar ratio $15Na_2O$: Al_2O_3: $12SiO_2$: $173H_2O$ which was lower than the analysis) as presented in Table 4.21. This reduction was due to the ion exchange, that is, the Na was detached from the frame structure of the synthesis zeolite and replaced with proton H^+ from the NH_4Cl solution, which

122

consequently, became protonated zeolite (HY) and calcinated at 650 $^\circ$C for 2hr. The HZ produced contains active acid sites and is stable for application in catalytic reactions. This explanation corroborated the result of Ghandhi (2022) that there are active sites required for reaction.

Table 4.25: Chemical analysis of zeolite Y catalyst (HZY) meta-kaolinite

Oxides composition	Zeolite Y catalyst
SiO_2	48.760
Al_2O_3	20.125
Fe_2O_3	2.3937
CaO	1.4511
V_2O_5	0.0389
K_2O	0.0333
MnO	0.0000
NaO_2	3.0610
TiO_2	0.9247
P_2O_5	0.7076
SO_3	0.2693
CuO	0.0123
MgO	1.1300
NiO	0.0071
Cr_2O_3	0.0104
ZnO	0.0128
Ga_2O_3	0.0085
PbO	0.0098
Ta_2O_5	0.0029
Cl	0.7670
Si/Al ratio (mass)	**2.43**

4.7.9   X-ray diffraction of synthesised zeolite Y catalyst

The X-Ray Diffraction (XRD) diffraction was also extensively used for studying the protonated zeolite Y-type catalyst. Figure 4.39 presents the XRD pattern of the protonated zeolite Y-type catalyst. It was observed that the position of major diffraction peaks of 2θ angle in the Figure does not change, that is, there are minimal differences between the XRD pattern for the synthesized zeolite Y and the protonated synthesized zeolite Y, as shown in

Figure 4.39. Also, the Figure indicated the presence of a highly crystalline zeolite structure with well-defined diffraction peaks of a high structural order that are comparable with the XRD pattern of standard zeolite Y. The intensity of the detected peaks was compared to information provided by JCPDS (Joint Committee on Powder Diffraction Standards) through the library of the International Center for Diffractional Data (ICDD, 2015).

It can be seen from the Figure that the exact position of the first peak in the diffractogram appears at $2\theta = 6.21^0$ and the other five distinct peaks appear at $2\theta = 10.54^0$, 13.36^0, 26.11^0, 36.10^0 50.23^0 and 68.73^0. These distinct peaks confirm the presence of crystalline phases in the synthesized zeolite Y, though the few zigzag peaks in the diffractograms indicate the presence of amorphous materials. The positions of three distinct peaks $2\theta = 6.21^0$, 10.54^0 and 13.36^0 correspond to the XRD pattern for standard Zeolite Na-Y as presented in the research work of Ayodeji $et\ al$. (2018). Figure 4.38 has fewer peaks, and the intensities of the first peaks are not as pronounced as those of the commercial zeolite Y as presented in Figure 4.40. These could be due to the influence of the impurities associated with the alumina and silica emanating from the precursor (Bambu clay), such as Fe^{2+} and Mg^{2+}, which were not eliminated completely during beneficiations and metakaolinisation process.
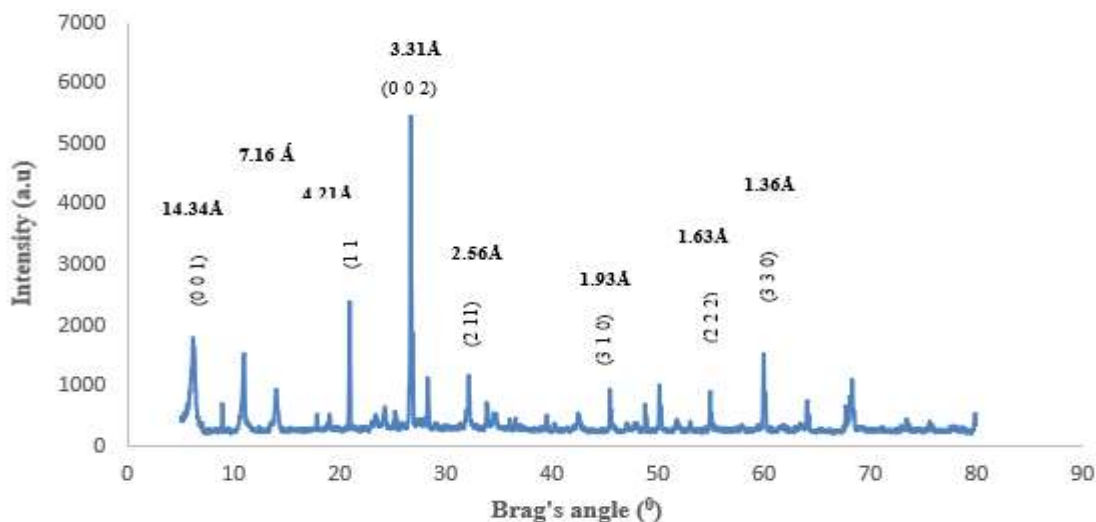
Figure 4.38: XRD analysis of synthesized zeolite Y-type catalyst

4.7.10 Scanning electron microscopy of the synthesised zeolite Y catalyst

The Scanning Electron Microscopy (SEM) of the protonated synthesis zeolite was scanned at various magnifications from 5000, to 15,000 so as to show the structural morphology of the protonation. The result of the SEM was presented in Figure 4.39. The Figure that the individuals agglomerate particles and bulky shapes appear to become bigger, flattened, and amorphous due to dealumination. This shape was due to ion exchange during protonation with ammonium chloride and calcination at a temperature of 650 $^{\circ}$C for 2 hours.
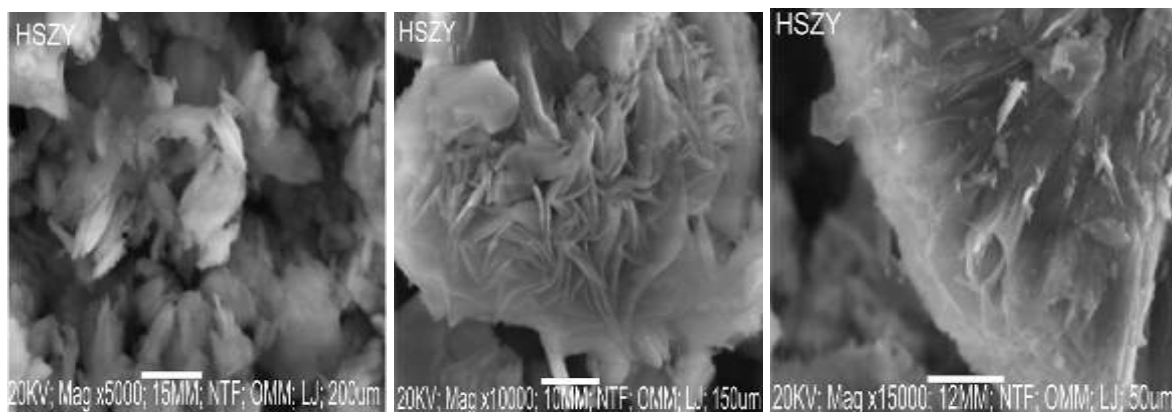
Figure 4.39: SEM of the protonated synthesised zeolite Y

125

4.7.11 X-ray fluorescence of commercial zeolite Y

The X-Ray Fluorescence (XRF) analysis of Commercial Zeolite Y (CZY) was presented in Table 4.26. The analysis also indicated that the oxides of SiO_2 and AlO_3 were predominately higher than any other oxides, as presented in the Table. The result as presented shows that the CZY has silica of 58.157% and alumina of 22.910% which were considered the main elements. Other elements are in low proportion. Fe_2O_3 was 1.4590%, Na_2O was 2.2203% and MgO was 2.1600% as well as traces of other elements as presented in Table 4.26. The synthesized zeolite's Si/Al ratio was approximately 4.26. It was observed that the CZY has a higher ratio of silica to alumina as presented in Table than the silica and alumina as presented in Table 4.26.

Table 2.26: X-ray fluorescence analysis of commercial zeolite Y

Compound	Commercial Zeolite Y
SiO_2	58.157
Al_2O_3	22.910
Fe_2O_3	1.4590
CaO	0.0131
V_2O_5	0.0248
K_2O	0.0305
MnO	0.0040
NaO_2	2.1310
TiO_2	0.8527
P_2O_5	0.5374
SO_3	0.2182
CuO	0.0025
MgO	2.1600
NiO	0.0071
CuO	0.0123
ZnO	0.0128
Ga_2O_3	0.0085
PbO	-
Ta_2O_5	0.0029
Cl	1.7670
LOI(1000^0C)	9.68
Si/Al ratio	**2.62**

4.7.12 X-ray diffraction of commercial zeolite Y

Figure 4.40 shows the Commercial zeolite Y's X-Ray Diffraction (XRD) pattern. The Figure shows that the position of the peaks in the chromatogram appears at $2\theta = 6.21^0$, 10.54^0, 11.36^0, 16.63^0, 20.86^0, 26.11^0 and 31.90^0. These distinct peaks correspond to the XRD pattern for standard Zeolite Na-Y as presented in the research work of Ayodeji *et al.*, (2018).
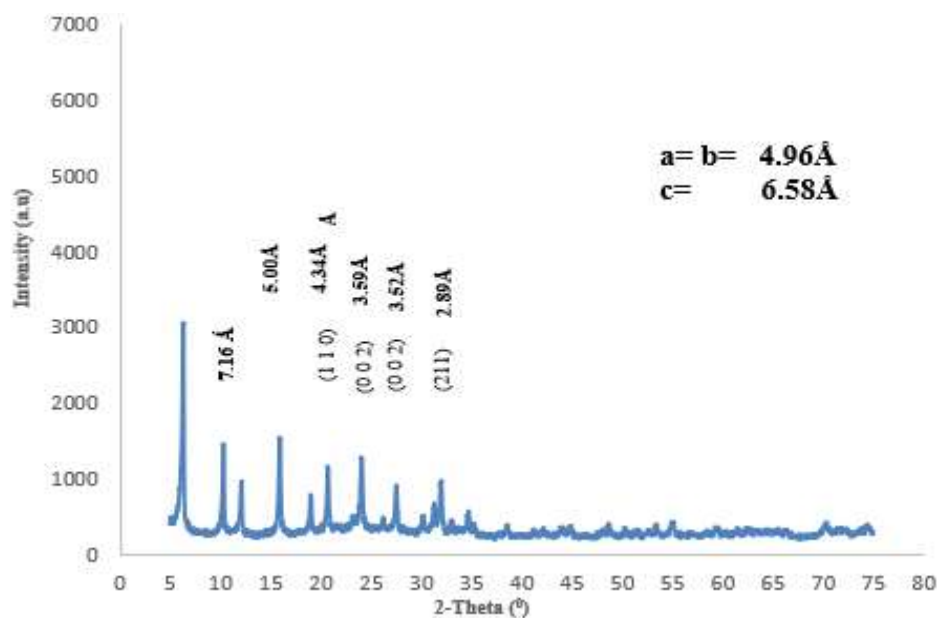
Figure 4.40: XRD analysis of commercial zeolite Y

4.7.13 Scanning electron microscope of commercial zeolite Y

The Scanning Electron Microscope (SEM) of CZY was conducted so as to study its structural morphology. The result of the SEM analysis of the CZY was presented in Figure 4.41. It can be seen from the micrograph (a) that at lower magnification, 7,500, the particles seemed to have densely agglomerate. The micrograph (b) at magnification 10,000 shows the particles are closely packed together with bulky shapes. The micrograph shows that the individual particles have regular tetrahedral shapes and are more hexagonal. This explanation

corroborated the micrograph of Ajayi (2012), where the individual particle appeared to be agglomerated at lower magnification.
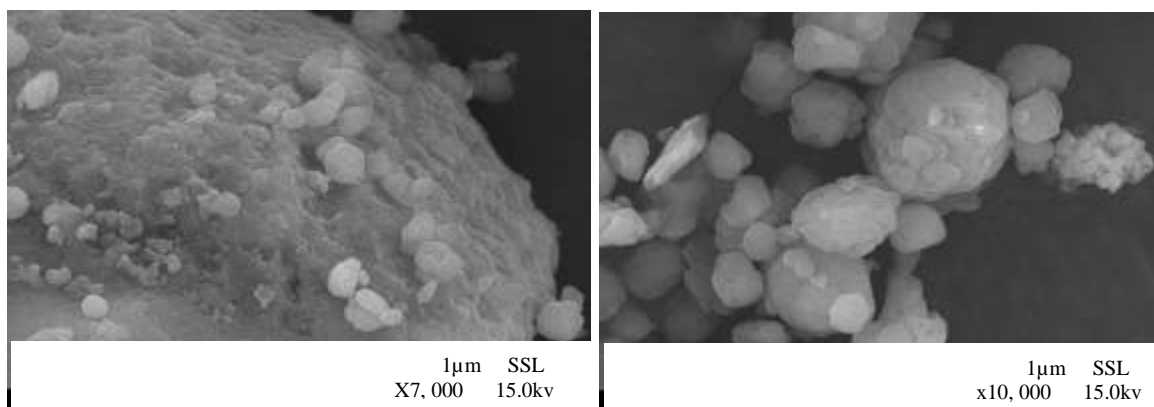
Figure 4.41: SEM of the commercial zeolite Y

4.8 Catalytic Co-pyrolysis of SR with LDPE and HDPE

A technique referred to as catalytic co-pyrolysis (CCP) of SR with LDPE and HDPE was used to test the performance of the synthesized Y-type zeolite. This was achieved by testing the performance of Bambu clay and meta-kaolin as zeolite, synthesized zeolite Y and HY, as well as commercial zeolite Y.

4.8.1 Catalytic (Bambu clay) co-pyrolysis of SR with LDPE and HDPE

Bambu clay was used to study the performance of clay as zeolite. Prior to this, the XRF result confirmed the abundance of silica and alumina in the clay, as presented in Table 4.7. Figure 4.42 shows that as the blending ratio of SR, LDPE and HDPE increases from 1:1:1 to 1:1:4, there are corresponding increase from 42.70 wt.% to 54.80 wt. % of the bio-oil, while the solid char decreases from 37.60 wt. % to 19.70 wt. %. This clearly shows that the cracking of volatile vapor occurred in the pore size of the Bambu clay, which implies the clay behaves as a zeolite. Though the clay has a good surface area of 429.70 m^2/g and a pore radius of 2.4

nm as presented in Table 4.9, which makes the clay accessible for volatile vapor to diffuse into the internal inner layers of the clay. In addition, most clays are thermally stable for application in terms of cracking. As the blending ratio increases from 1:1:4 to 1:1:6, the yield of bio-oil decreases slowly from 54.80 wt. % to 51.99 wt. % while the yield of solid char increases from 19.70 wt. % to 21.29 wt. %. The gas shows a linear increase throughout the co-pyrolysis from 19.70 wt. % to 26.81 wt. % as shown in the Figure. The linear increase of the gas could be attributed to impurities associated with the clay that hinder the bulk diffusion of volatile vapor onto the catalyst surface area.
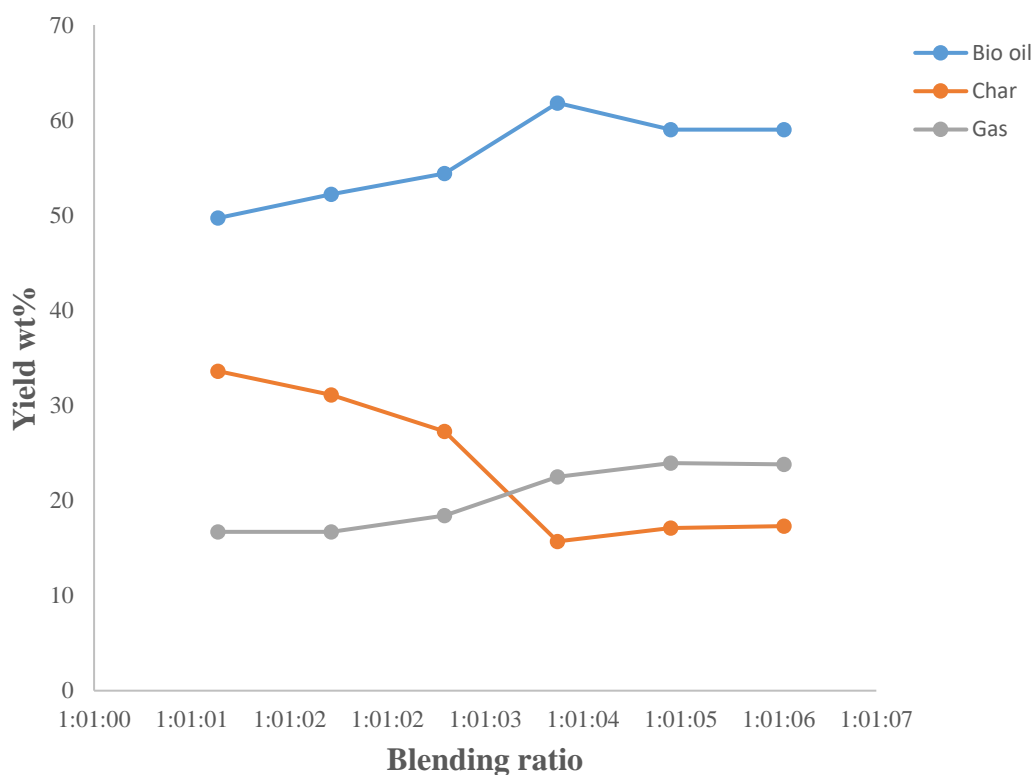
Figure 4.42: Catalytic (Bambu clay) co-pyrolysis of SR with LDPE and HDPE

4.8.2 Catalytic (metakaolin) pyrolysis of SR with LDPE and HDPE

Meta-kaolin was also tested as a zeolite, and the result was presented in Figure 4.43. The Figure shows that as the blending ratio increased from 1:1:1 to 1:1:3, there are corresponding increases from 52.20 wt. % to 61.30 wt. % of the bio-oil. The yield of the bio-oil from catalytic co-pyrolysis using metakaolin was higher than the bio-oil yield using clay, as presented in Figure 4.42. This higher yield from metakolin could be attributed to the higher surface area of meta-kaolin (530.40 m^2/g and pore radius 2.128 nm as presented in Table 4.15, where more volatiles diffuse into the internal structure of metakaolin for cracking than the clay. As the blending ratio increases from 1:1:3 to 1:1:5 the bio-oil decreases from 61.30 wt. % to 59.10 wt.%, the solid char decreases slowly from 27.15 wt. % to 24.9 wt. % the gas increases from 11.28 wt. % to 16.49 wt. %. This increase in gas was due to the vapor, which could not be absorbed at the surface of the metakaolin and therefore reduced the diffusion of lighter molecules that are more easily accessible to the surface structure.
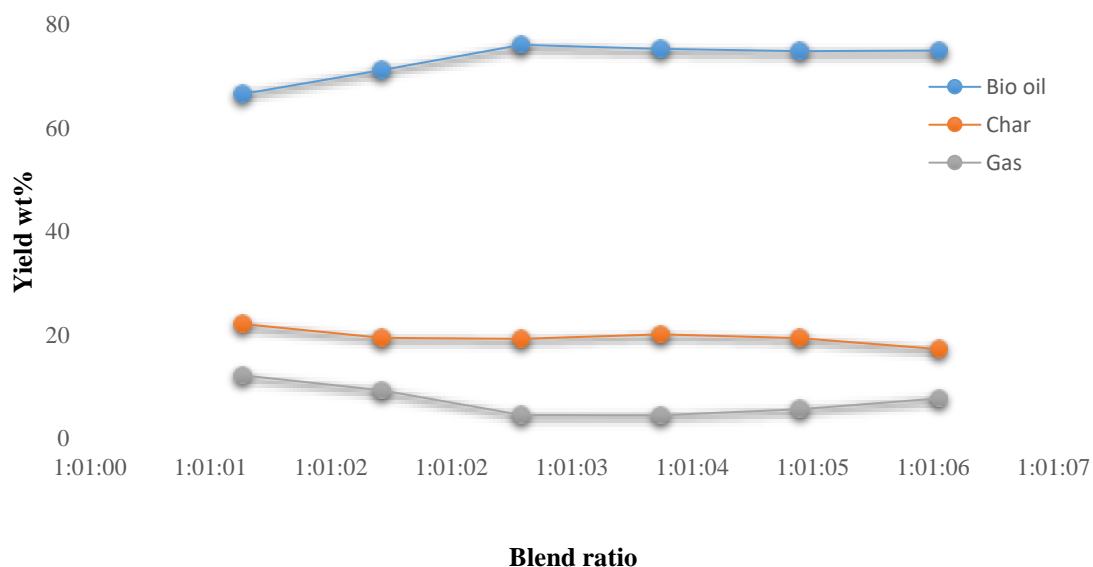
Figure 4.43: Catalytic (metakaoline) co-pyrolysis of SR with LDPE and HDPE

4.8.3 Catalytic (synthesised zeolite Y) co-pyrolysis of SR with LDPE and HDPE

The synthesised zeolite Y (SZY) was employed in the study so as to test the performance of the synthesized zeolite and is presented in Figure 4.44. The Figure shows that as the ratio increases from 1:1:1 to 1:1:5, there are corresponding increases from 61.21 wt. % to 72.53 wt. % while solid char decreases from 25.16 wt. % to 20.80 wt. % and the gas also decreases from 13.63 wt. % to 6.67 wt. %. The bio-oil obtained from the synthesized zeolite Y was higher than the bio-oil obtained from Bambu clay and meta-kaolin, as presented in Figures 4.42 and 4.44. This higher yield could be attributed to the characteristics possessed by the zeolite, which favour cracking of volatiles in the internal site structure of the zeolite. As the ratio increases from 1:1:5 to 1;1;9 the bio-oil yield decreases from 72.53 wt. % to 55.89 wt. % while solid char increases from 20.80 wt. % to 26.79 wt. % and the gas also increases from 6.67 wt. % to 17.32 wt. %.
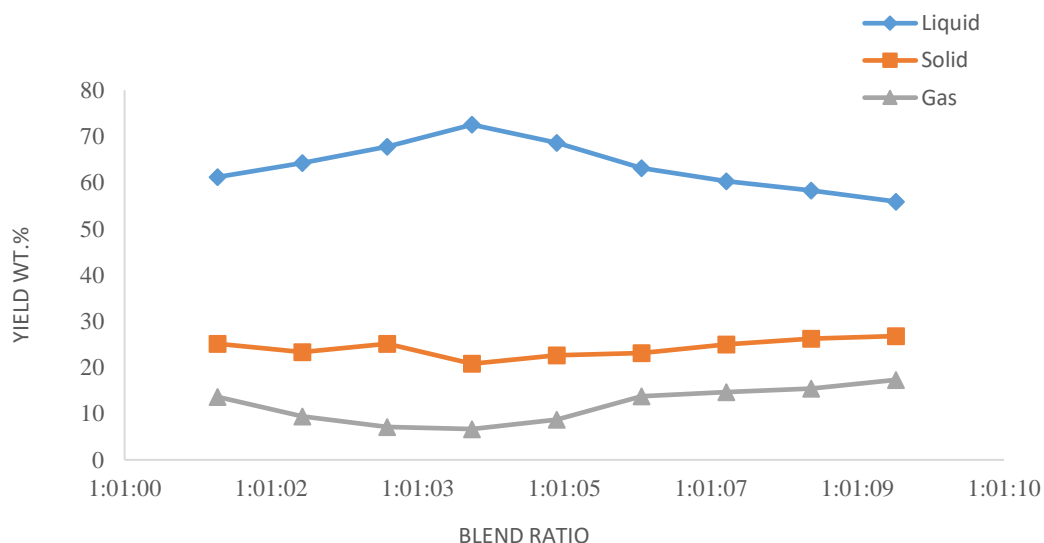
Figure 4.44: Catalytic (SZY) co-pyrolysis of SR with LDPE and HDPE

4.8.4 Catalytic (commercial zeolite Y) co-pyrolysis of SR with LDPE and HDPE

Commercial zeolite Y (CZY) was employed in the study so as to compare its effect with Bambu clay, meta-kaolin, and synthesized zeolite Y.

The result of catalytic (CZY) co-pyrolysis of SR with LDPE and HDPE was presented in Appendix D 4. The result was further presented in Figure 4.45. The result shows that as the blend ratio of SR with LDPE and HDPE increases from 1:3:1 to 1:3:3, there was corresponding increase in bio-oil obtained from 62.20 wt. % to 71.30 wt. %. The solid char decreases from 24.10 wt. % to 21.12 wt. and the gas decreases from 13.70 wt. % to 7.28 wt. %. However, as the ratio further increases from 1:3:3 to 1:3:6, the bio-oil yield decreases from 71.10 wt. % to 69.10 wt. %. Again, the solid char decreases slightly from 19.24 wt. % to 17.30 wt. % but the gas increases from 7.28 wt. % to 12.00 wt. %.
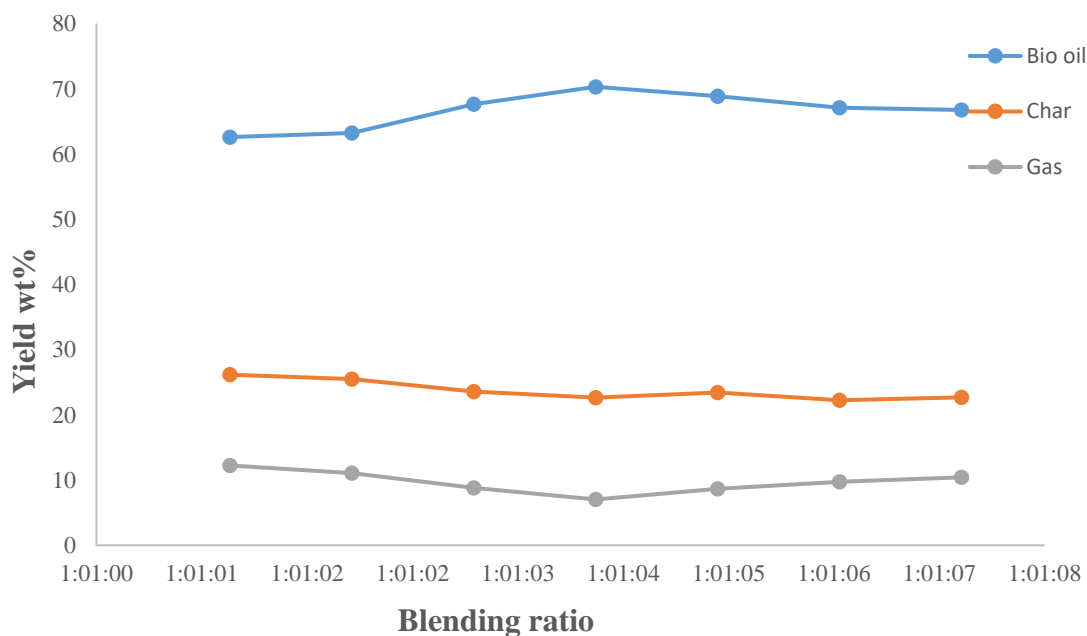
Figure 4.45: Catalytic (CZY) co-pyrolysis of SR with LDPE and HDPE

132

It can be inferred from the catalytic co-pyrolysis using four samples: Bambu clays, metakaolin synthesized and commercial zeolite Y, that a higher yield was obtained using synthesized zeolite Y, followed by commercial zeolite Y, metakaolin, and Bambu clay.

4.8.5 Physiochemical characterization of bio-oil obtained from catalytic co-pyrolysis of SR with LDPE and HDPE

The physiochemical characterization of bio-oil from catalytic co-pyrolysis of SR with LDPE and HDPE was conducted in order to study the performance of Banbu clay, metakaolin, synthesized zeolite and commercial zeolite Y.

4.8.5.1 *Physical properties of bio-oil obtained from catalytic co-pyrolysis*

The physical properties of bio-oil obtained from catalytic co-pyrolysis (CCP) of SR with LDPE and HDPE are presented in Table 4.27.

Table 4.27: Physical properties of bio-oil obtained from catalytic co-pyrolysis

Sample description	Calorific value MJ/kg	Viscosity (cst)@ 100°C	Density (g/cm^3)	Moisture Content	Flash point ^{0}C
CCP (raw clay)	27.23	5.81	0.8540	3.8	110.3
CCP (metakaolin)	29.95	5.70	0.8400	3.4	108.2
CCP (SZY)	34.60	3.99	0.822	3.3	104.4
CCP (CZY)	31.60	4.10	0.7397	3.2	101.2
Diesel (ASTM)	42.00 D975	2–3 D975	0.82-.845D975	0.05 max D975	60–80 D975
Gasoline (ASTM)	43.00D4814	0.006 D4814	0.7197D4814	-	-43 D4814

Table 4.27 presents the calorific values of the bio-oil using Bambu clay was 29.23 MJ/kg, 27.95 MJ/kg for meta-kaolin, 34.60 MJ/kg for SZY, and 31.60 MJ/kg for CZY. As presented in the Table, the calorific value of bio-oil using Bambu clay was less than that using metakaolin. Furthermore, the calorific value of bio-oil using SZY was 34.60 MJ/kg higher than the calorific value of bio-oil using CZY of 31.60 MJ/kg. This could be attributed to the fact that the surface area of SZY was higher than the calorific values of others considered zeolite. It was observed that the highest calorific value was close to the acceptable standard limits of the calorific values of diesel and gasoline set by the ASTM as presented in the Table. This could be attributed to the influence of LDPE and HDEP as well as zeolites. Also, all the calorific values in Table 4.25 as presented were higher than all the calorific values of bio-oil as presented in Table 4.5. This indicated that there was a significant reduction of oxygenated organics after employing the techniques of catalytic co-pyrolysis using zeolites.

The viscosity of bio-oil using Bambu clay was 5.81 cst, meta-kaolin was 5.70 cst, synthesis zeolite was 3.99 cst, and commercial zeolite Y was 4.10 cst, as shown in Table 4.27. It was observed from the Table that the viscosity of bio-oil from catalytic co-pyrolysis using synthesis zeolite catalyst was close to the acceptable standard limits of the viscosity of diesel but very far from the viscosity value of gasoline. The results as presented corroborate the result of Quesada *et al*. (2020) where catalyst decreases the waxy oil film from plastic and consequently reduces viscosity.

The result of the moisture content of bio-oil from CCP using raw clay was 3.8, meta-kolin was 3.4, synthesis zeolite catalyst was 3.3, and commercial zeolite Y was 3.2, as presented

in Table 4-27. The result as presented in the table shows that using commercial zeolite Y was lower than using synthesis zeolite catalyst, even though the moisture content of bio-oil using commercial zeolite Y was higher than the diesel standard limit of 0.005 max. This could be attributed to the amount of oxygen present in the volatiles that emanate from SR.

The flash point of bio-oil from CCP using raw clay was 110.3 $^{\circ}$C, meta-kolin was 108.2 $^{\circ}$C, synthesis zeolite catalyst was 104.4 $^{\circ}$C and commercial zeolite Y was 101.2 $^{\circ}$C as shown in Table 4.27. The flash point of the bio-oil from the zeolite Y was higher than the acceptable standard limit 60 – 80 $^{\circ}$C of flash point of diesel and by far higher than the acceptable standard limit of gasoline -43 $^{\circ}$C. This could be the result of highly volatile components associated with oxygen.

4.8.6 Full factorial analysis of bio-oil yield from catalytic co-pyrolysis

The 3-factor, 2-level complete factorial experimental design was implemented using the Design Expert ® 12 software tool.

Table (4.28) presents the results of catalytic co-pyrolysis of bio-oil yield for each experiment. The experimental run of the input parameters of three factors in actual form (temperature, catalyst ratio (zeolite: SR: LDPE/HDPE) and heating rate) and the experimental values for response.

Table 4.28: Experimental design and response factor of full factorial analysis of bio-oil yield

Run	Factor 1 A: Temperature ^{0}C	Factor 2 B: (C:SR:LDPE &HDPE) Ratio	Factor 3 C: Heating Rate ^{0}C/min	Response Bio-oil yield (wt. %) Actual	Predicted	Deviations
1	425.00	0.20	13.75	62.21	62.74	-2.19
2	500.00	0.07	20.00	64.50	64.40	0.1
3	600.00	0.33	7.50	65.87	65.77	0.1
4	350.00	0.33	7.50	61.72	61.38	0.34
5	500.00	0.33	20.00	72.43	72.09	0.34
6	425.00	0.20	13.75	61.53	62.74	-1.21
7	350.00	0.07	20.00	55.25	54.91	0.34
8	350.00	0.07	7.50	53.23	53.13	0.1
9	600.00	0.33	20.00	67.73	67.63	0.1
10	500.00	0.07	7.50	62.89	62.55	0.34

Equation 4.12, which represents the regression model of the bio-oil output from catalytic co-pyrolysis in terms of coded components, is shown in Table (4-29).

$$\text{Bio-oil yield} = 62.74 + 3.47A + 3.98B + 2.03C - 1.26AB + 0.0181AC + 1.12BC \qquad (4.12)$$

Table 4.29: Model coefficient in terms of coded factors for the bio-oil yield from catalytic co-pyrolysis

Factor	Coefficient Estimate	DF	Standard Error	95% CI Low	95% CI High	VIF
Interception	62.7400	1	0.2720	61.8700	63.6000	
A-Temperature	3.4700	1	0.3042	2.5000	4.4400	1
B-Blending Ratio	3.9800	1	0.3042	3.0200	4.9500	1
C-Heating Rate	2.0300	1	0.3042	1.0600	2.9900	1
AB	-1.2600	1	0.3042	-2.2300	-0.2902	1
AC	0.0181	1	0.3042	-0.9498	0.9861	1
BC	1.1200	1	0.3042	0.1502	2.0900	1
Ctr Pt 1	-0.351875	1	0.2982			
R²	0.9921					
Adjusted R²	0.9763					
Predicted R²	0.9148					

The regression model in terms of the actual factor for the catalytic co-pyrolysis bio-oil yield is represented by Equation 4.13.

$Y = 25.83195 + 7.0952 \times 10^{-2} *$ Temperature $+ 65.06673 *$ C: SR :(LDPE/HDPE) $+ 3.8644$

$\times 10^{-2} *$ Heating rate $- 0.126128 *$ Temperature $*$ Blending Ratio $+ 3.9 \times 10^{-5} *$ Temperature

$*$ Heating rate $+ 1.34511 *$ Blending Ratio $*$ Heating rate   (4.13)

Where Y is the yield of bio-oil.

Therefore, Equation 4.13 is suitable for predicting the response bio-oil yield for any given levels of each factor in its actual terms with the levels specified in the original units for individual factor.

Also from Table 4-29, the regression coefficients R^2, Adjusted R^2, and Predicted R^2 have values of 0.9921, 0.9763, and 0.9148, respectively. This implies that 99.21% of the experimental data were captured and explained by the model, which indicates the high significance of the model in predicting the response variable. This confirms that the accuracy and overall ability of the model were good, and the analysis of associated response trends was reasonable.

The plot of real against projected was also used to verify the model's validity. The plot of the actual or experimental reactions against the anticipated responses is shown in Figure 4.46. Figure 4.46 illustrates how closely the experimental and projected values are, with an R2 of 0.9921. Therefore, the developed models offer accurate predictions for these typical outcomes.
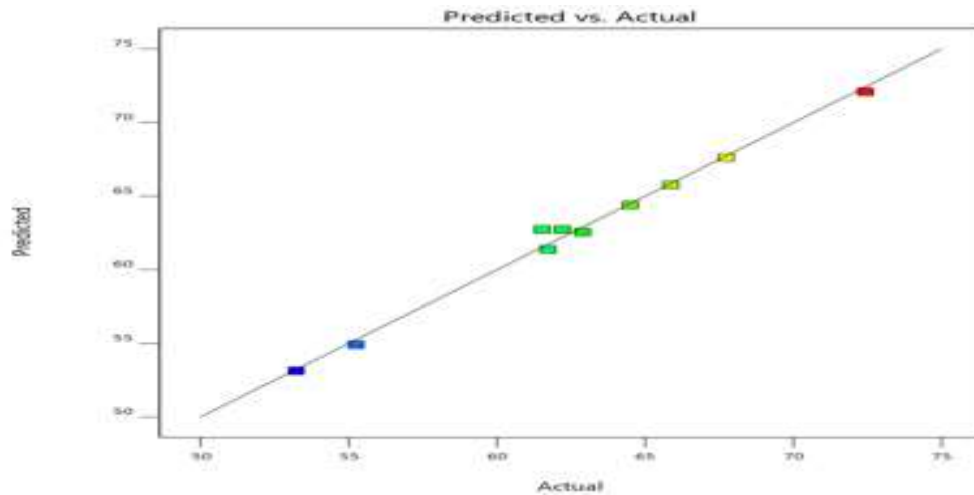
Figure 4.46: Plot of observed versus predicted values of bio-oil yield.

4.8.6.1 *Analysis of variance (ANOVA)*

To determine whether the empirical model was adequate, a statistical analysis of the model using ANOVA was carried out. Table 4.30 provides a summary of the ANOVA findings for the mean square approach to fitting the quadratic response model. Additionally, assessed were the full factorial method model's real factor coefficients. P-values, which also show the strength of each parameter's interaction, are used to determine the importance of each coefficient. The model's F-value and Lack of Fit F-value were also used to determine whether the model is valid.

Table 4.30: ANOVA of full factor model of bio-oil yield

Source	Sum of Squares	DF	Mean Square	F-value	P-value	
Model	278.7870	6	46.4645	62.7806	0.0030	Significant
A-Temperature	96.2925	1	96.2925	130.1057	0.0014	Significant
B-Blending Ratio	127.0020	1	127.0020	171.5988	0.0010	Significant
C-Heating Rate	32.8253	1	32.8253	44.3519	0.0069	Significant
AB	12.6630	1	12.6630	17.1097	0.0256	Significant
AC	0.0026	1	0.0026	0.0036	0.9562	Not Significant
BC	10.0016	1	10.0016	13.5137	0.0349	Significant
Residual	2.2203	3	0.7401			
Lack of Fit	1.9891	2	0.9946	4.3017	0.3227	Not significant
Pure Error	0.2312	1	0.2312			
C or Total	281.0073	9				

F-value and p-values were used to access the significance of the regression coefficients as well as the effects of each model variable. Table 4.30 as presented shows that the p-value is 0.003 which is less than 0.005. The model's p-value is 0.003 $p < 0.05$, indicating that the bio-oil yield model is significant. Additionally, it was noted that all of the model terms' p-values are significant ($p < 0.05$).

Additionally, Table 4.30 shows that the model The model is significant, and the F-value is 62.78, meaning that there is only a 0.03% chance that the high F-value resulted from experiment noise, the fitted model is significant when the probability value is 0.003 ($p < 0.05$).

4.8.6.2 *Factorial optimization of bio-oil yield from catalytic co-pyrolysis of SR with*

LDPE and HDPE

Figure 4.47 present the 3D surface plot that depicts the interaction among the factors and the

response bio-oil yield of catalytic co-pyrolysis. The Figure shows the influence of

temperature, ratio and heating rate for catalytic co-pyrolysis to obtained higher bio-oil yield.

Though, the Figure shows that catalytic co-pyrolysis is sensitive to temperature and heating

rate as presented in the Figure. Hence high bio-oil of 72.092% is obtained at temperature

500^0C. This maximum yield of liquid fuel yield could be attributed to the properties of the

catalyst, pore sizes and catalyst site (acidic site) available for cracking (Zhanjun *et al*., 2016).

| (a) | (b) |
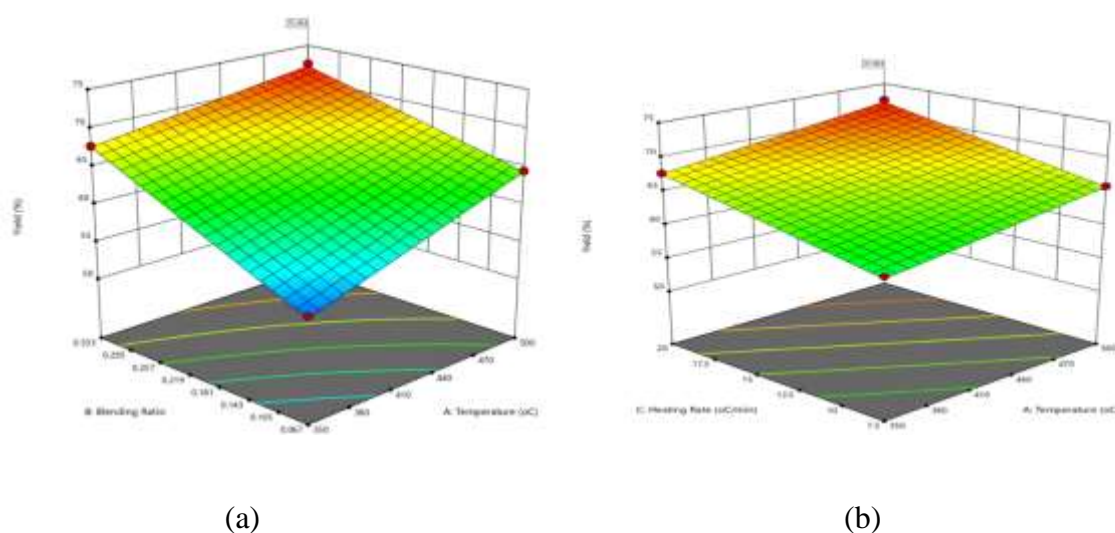
Figure 4.47: 3D surface plot (a) The effect of blending ratio and temperature (b) The effect

of heating rate and temperature.

 4.9 Catalytic Co-pyrolysis of Techniques Premix, Non-Premix and Bio-oil Upgradin

The performance of synthesized zeolite Y (SZY) was further tested by employing some

pyrolysis techniques such as Premix (P1), Non-Premix (NP1) and bio-oil Upgrading (BU1)

so as to determine the higher quality bio-oil for transportation. Samples P1 is the premix

pyrolysis where the synthesized zeolite Y, SR, LDPE, and HDPE were mixed together in the pyrolyser; NP1 is the non-premix where the synthesized zeolite Y was separated from SR, LDPE and HDPE and BU1 is upgrading of bio-oil.

4.9.1 Physical properties of bio-oil obtained from three techniques P1, NP1 and BU1

The Physical properties of bio-oil obtained from three techniques (P1, NP1 and BU1) are calorific value, viscosity, density, moisture content, flash point, pour point, cetane, and octane numbers, which are presented in Table 4.31. The Table presents the physical properties of bio-oil from premix (P), non-premix (NP) and Bio-oil upgrading (BU) as well as acceptable standard limits for diesel and gasoline.

Table 4.31: Physical properties of bio-oil obtained from Physical properties of the bio-oil obtained from P1, NP1 and BU1

Physical Properties of fuel	Premix (P1)	Non-premix (NP1)	Bio-oil upgrading (BU1)	Diesel (ASTM)	Gasoline (ASTM)
Calorific Value MJ/kg	34.60	36.26	39.10	42.00 D975	43.00D4814
Specific Gravity @ 30°C	0.840	0.7666	1.0169	0.85 D975	-
Density (g/cm^3) @ 30°C	0.822	0.7497	0.73946	0.82-.845D975	0.719D4814
Viscosity (cst) @100°C	3.99	2.23	1.098	2–3 D975	0.006D4814
Moisture Content (%)	3.3	2.3	1.6	0.05max D975	-
Flash Point (°C)	104.4	98	89.6	60–80 D975	-43 D4814
Cloud Point (°C)	-2.7	-3.6	-4.2	-15 to -5 D975	-
Pour Point (°C)	-20.4	-21.3	-24.6	-35 to -15	NA
Cetane Number (CN)	87.0	31.7	37.6	40–55 D613	-
Octane number MON (min)	105.4	101.0	89.0	NA	81-85
Octane number RO N (min)	95.4	91	99.0	NA	91-95

The calorific values of P1, NP1 and BU1 are 34.60 MJ/kg, 36.26 MJ/kg, and 39.10 MJ/kg, respectively, as shown in Table 4.31. The Table shows that the calorific value as presented for sample P_1 was 34.60 MJ/kg. This value was higher than the calorific value of oil obtained from SR 17.01 MJ/kg), as presented in Table 4.5, but a little lower than the average calorific value of oil from LDPE and HDPE of 37.03 MJ/kg.

The calorific value of technique NP_1 was 36.26 MJ/kg higher than the calorific value of technique P_1. This could be attributed to the influence of the zeolite Y, volatile vapor contact with the surface of the catalyst, and diffusion of volatile vapor into the mesoporous size of the catalyst for cracking of fuel. Consequently, there was a reduction in the amount of oxygen emanating from SR, which was indicated in the ultimate analysis in Table 4.2.

Furthermore, the calorific value of technique BU_1 was 39.10 MJ/kg, which has increased more than the calorific values of P_1 and NP_1.This increase could be attributed to the re-pyrolyzing of bio-oil, where bulk diffusion of volatile vapor into catalyst pore sizes caused cracking in the catalyst sites. This also indicated that a significant amount of oxygen has been reduced. It was observed that the calorific values of bio-oil obtained from three techniques are very close to the acceptable standard limits of the calorific values of diesel and gasoline set by the ASTM as presented in the Table.

From Table 4.31, the viscosity of P_1 was 3.99 cst. Though, the viscosity of P_1 was much higher than the viscosity value of diesel within acceptable standard limits, Furthermore, it can be seen that the viscosity value of technique NP_1 was 2.23 cst. Upon the upgrading technique being carried out, the viscosity value of the bio-oil obtained from technique BU_1

was 1.098 cst which was lower than the viscosity value obtained from techniques P_1 and NP_1. This low viscosity value obtained from BU_1 could be attributed to the re-pyrolyzing of the bio-oil using zeolite Y, which has a good surface area, pore volume, and zeolite site at which the de-waxing of the bio-oil was conducted. The viscosity of the three techniques was compared with the research work of Khan *et al.* (2016) which revealed that the viscosity value of bio-oil was higher than kerosene but lower than diesel. Again, the value of bio-oil from BU_1 has reached beyond the acceptable standard limits of diesel that is the minimum and maximum viscosity value of diesel but not close to viscosity value of gasoline.

The results of the moisture content of the three techniques P_1, NP_1 and BU_1 are 3.3, 2.3 and 1.6 respectively. It can be seen that the moisture content as presented in the Table for technique P_1 was 3.3, and this value was higher than the diesel standard limit of 0.005. This higher value of P_1 could be attributed to the amount of oxygen present in the volatiles emanating from SR. The moisture content of technique NP_1 has decreased to 2.3 as presented in Table 4.32. This reduction could be attributed to volatile hydrocarbons diffused into the zeolite pore size.

The analysis of the flash point of the bio-oil obtained from techniques P_1, NP_1, and BU_1 are also presented in Table 4.32. The analysis as presented corresponds to 104.4 ^oC, 98 ^oC and 89 ^oC respectively. The flash point of bio-oil from technique P_1 was 104.4^oC, by far, thi s value was higher than diesel and gasoline. The flash point of bio-oil obtained from the NP_1 technique has decreased from 104.4 ^oC to 98 ^oC as presented in Table 4.32. Though, the flash point of technique BU_1 reduces to 89.60 ^oC as presented, this value was close to the

acceptable standard limit of 60 – 80 °C but cannot be compared with the acceptable standard limit of gasoline at -43 °C.

The results of the pour points of the three techniques P_1, NP_1, and BU_1 are presented in Table 4.32. The results presented for bio-oil from the techniques P_1, NP_1 and BU_1 correspond to -20.4 °C, -21.3 °C and -24.6 °C respectively. It was observed from the Table that the pour point of bio-oil obtained from technique P_1 as -20.4 °C was within the range of acceptable standard limits for diesel. This value at technique P_1 could be attributed to the presence of hydrogen and carbon emanating from LDPE and HDPE. Though, the pour points of the bio-oil samples are not applicable to the limits of gasoline.

The cetane number (CN) of bio-oil was investigated in the research so as to understand the bio-oil's cetane rating. The result of CN of the bio-oil obtained from the techniques P_1, NP_1 and BU_1 are presented in Table 4.32. The results of CN as presented in the Table for the techniques P_1, NP_1 and BU_1 are 87.0 °C, 31.7 °C and 37.6 °C. The CN of technique P_1 was 87.0 °C and was higher than the acceptable standard limits of diesel fuel. This could be attributed to the higher amount of paraffin (C_{16}) available in the bio-oil. However, the CN of techniques NP_1 and BU_1 decreases sharply from 87.0 °C to 31.7 °C as presented in Table 4-26. The sudden decrease could be attributed to a reduction in the amount of paraffin (C_{16}).

The octane number (octane rating) was also investigated in the research so as to ascertain the ignition quality of the bio-oil. Two measurements were conducted, RON and MON are the Research and Motor octane numbers. The results of the octane of techniques P_1, NP_1 and BU_1 are presented in Table 4.30. The octane numbers of the three techniques P_1, NP_1 and

BU$_1$, for MON are 105.4 min, 101.0 min, and 89.0 min, and for RON they are 95.4 min, 91.0 min, and 99.0 min, respectively. The MON of bio-oil from technique P$_1$ was higher than the acceptable standard limits of oxygenate meant to be available in gasoline (oxygenate is commonly referred to as octane), but the RON of bio-oil from technique P$_1$ was close to the acceptable standard as presented in Table.

The MON and RON of bio-oil from technique NP$_1$ correspond to 101.0 min and 91.0 min, respectively. It was observed that there was a reduction in the small amount of oxygen in technique NP$_1$ and this could be attributed to the effect of zeolite Y, which allowed volatile hydrocarbons to have access to the internal structure for cracking. Though the MON value of NP$_1$ was still higher than the acceptable standard limits of oxygenate, the RON value of NP$_1$ was within the acceptable standard limits of oxygenate. The MON and RON of bio-oil sample BU$_1$ are 89.0 min and 99.0 min, as presented in Table 4.32. This shows that the MON of technique BU$_1$ was higher than the acceptable standard limits, while the RON of bio-oil from technique BU$_1$ was very close to the acceptable standard limits of oxygenate meant to be available in gasoline.

It can be deduced that the MON of the bio-oil from the techniques was higher in octane rating than gasoline, while the RON of the bio-oil from the techniques was within the acceptable standard limits of oxygenate meant to be available in gasoline.

4.9.2 Chemical properties of bio-oil obtained from techniques P$_1$, NP$_1$ and BU$_1$

The chemical properties of bio-oil from techniques P$_1$, NP$_1$ and BU$_1$ were conducted by using GC-MS.

4.9.2.1 *GC-MS analysis of bio-oil obtained from technique P₁*

Figure 4.48 presents the GC-MS analysis of bio-oil obtained from technique P_1. It was observed that the bio-oil obtained from P_1 appears to contain a slight waxiness. This waxy substance emanates from the LDPE and HDPE where some volatile vapor could not be cracked in the zeolite pore site. The Figure shows the hydrocarbon ranges C_9-C_{12}, C_{14}-C_{19} and C_{21}-C_{27} which correspond to 41.67%, 25.0% and 33.3% respectively.t means that the dominant condensable hydrocarbons in the bio-oil are alkane and alkene, which occupied 41.1% of the bio-oil; however, the majority of products obtained in 41.1% are branched chain hydrocarbons as naphtha-like fractions, which may have a good octane number. This bio-oil contains a heavy molecular weight of hydrocarbons, up to 58.33%. This analysis is contrary to the research work of Joppert *et al.* (2015), who explained in their result that the hydrocarbons in bio-oil start with the carbon number C_{10}.
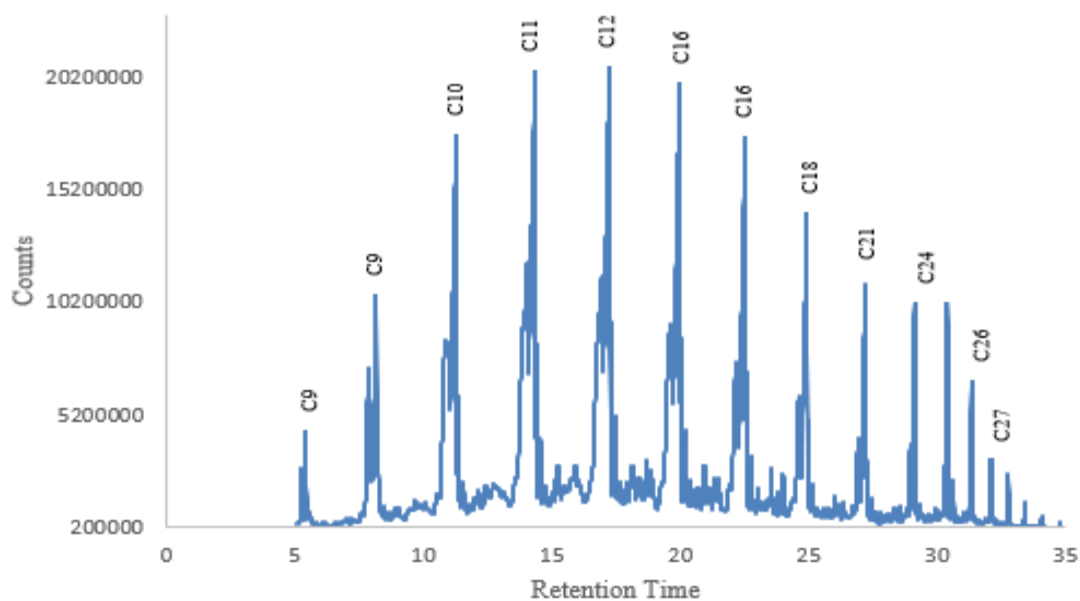
Figure 4.48: GC-MS analysis of bio-oil obtainesd from technique

4.9.2.2 GC-MS analysis of bio-oil obtained from technique NP₁

The bio-oil obtained from the technique of NP_1 from catalyst co-pyrolysis SR with LDPE and HDPE was presented in Figure 4.49.

Figure 4.49 presents the GC-MS analyses of the technique NP_1. The bio-oil from technique NP_1 contains no wax. This reduction of waxiness in NP_1 could be due to non-mixing, that is, a bed was created to separate zeolite with *SR*, LDPE, and HDPE. This separation enables volatile vapor to diffuse through the zeolite pore size and acidic sites where cracking of heavy volatiles occurs. The hydrocarbon compound range from C_9-C_{12} contains 40.0%, C_{14}-C_{19} contains 26.67% and C_{21}-C_{25} 33.33% respectively.
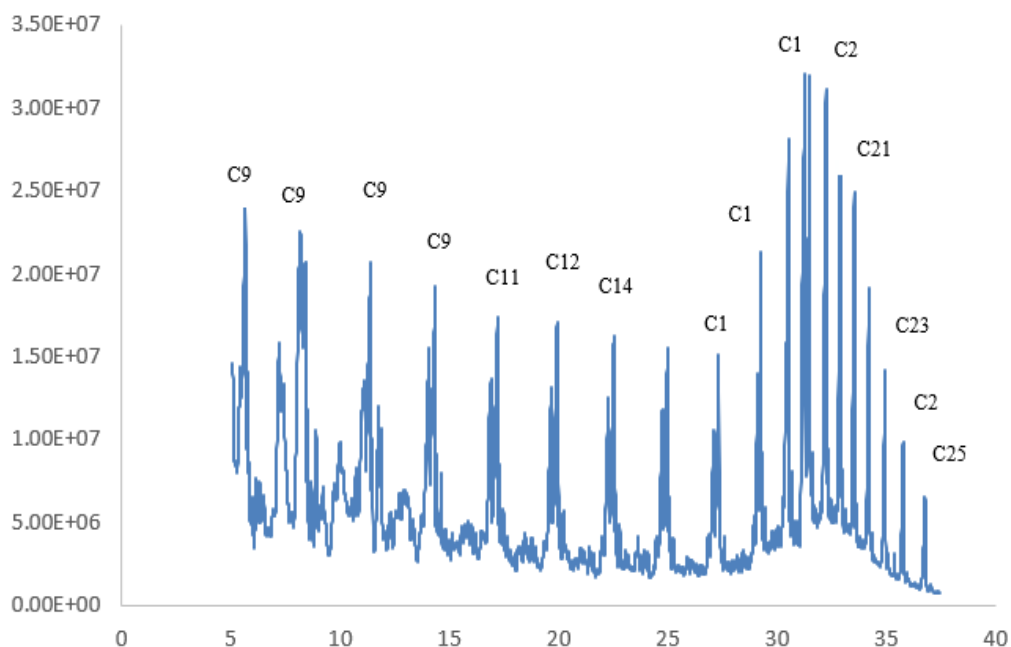
Figure 4.49: GC-MS analysis of bio-oil obtained from technique NP_1

4.9.2.3 *GC-MS analysis of bio-oil obtained from technique BU₁*

The GC-MS analysis of bio-oil obtained from technique BU_1 was presented in Figure 4.50. The analysis shows that all chemical components that exist in the bio-oil are of lower molecular weight with carbon numbers C_5-C_{14}. This lower molecular weight of hydrocarbons in the bio-oil sample from BU_1 indicated the presence of naphtha-like fraction compounds. In fact, the presence of naphtha-like fractions in the bio-oil could be due to the impact of secondary catalytic cracking, where volatile hydrocarbons from the bio-oil diffuse through the pore size of zeolite, resulting in lower hydrocarbons. It can be seen from the Figure that the dominant hydrocarbon compound ranges from C_5-C_{12} and C_{13}-C_{14} correspond to 77.78% and 22.22% respectively.
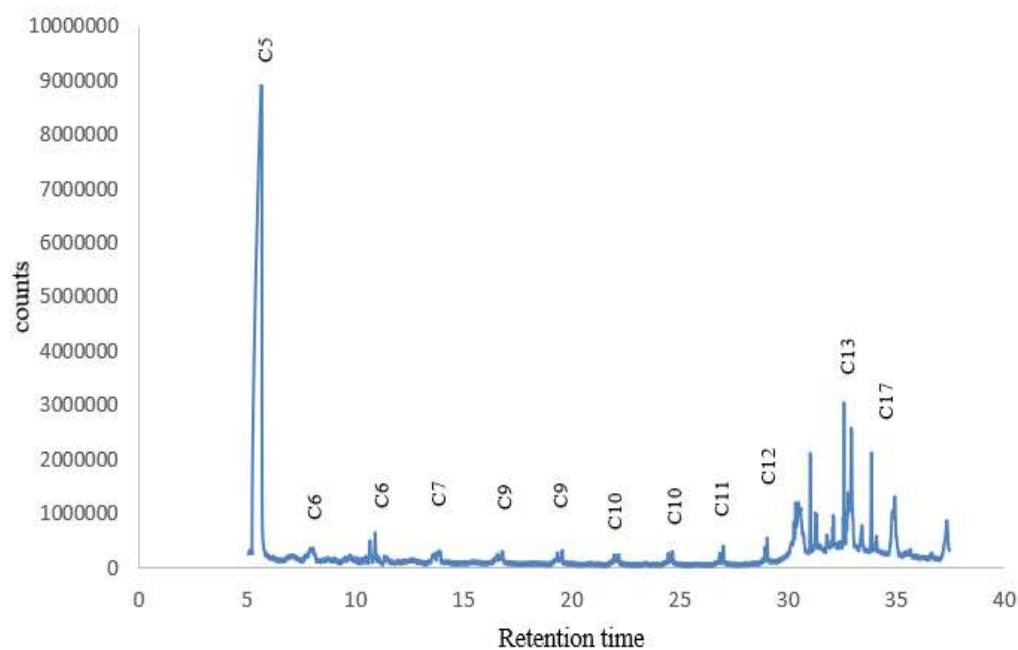
Figure 4.50: GC-MS analysis of bio-oil obtained from technique BU ₁

It can be deduced from the GC-MS analysis of bio-oil obtained from three techniques that the overall assessment of the bio-oil contains a lower molecular weight of hydrocarbons. The

portion of heavier hydrocarbon in the bio-oil was higher in technique from P_1 than sample NP_1. Upon being subjected to bio-oil upgrading, the portion of the heavier hydrocarbon was lower than both samples of P_1 and NP_1. The dominant hydrocarbons in the bio-oil sample from BU_1 contained light hydrocarbons, aromatics, alkanes, and alkene.

4.9.2.4 *FTIR analysis of bio-oil obtained from technique P_1*

The peaks as presented in Figure 4.51 of bio-oil obtained from the technique are assigned to corresponding absorption bands as 388.62 3765.17, 3649.44, 3572.29 3471.98, 3340.82, 3070.78, 2962.76, 2870.17, 2330.09, 1643.41, 1458.23, at 1266.35, 1141.90, 1033.88, 10388.88, 987.59, 645.71 and 779.27. The Figure shows that at 3765.17 and 1033.88 correspond to O-H stretching, at 3078.78 correspond to =C-H stretching, 2962.76, at 2871.17 correspond to C-H stretching, 2330.09, at 1643.41 correspond to C=C stretching, 1458.23, at 1266.35 correspond to C-O stretching, at 1141.90, 987.59 C=C stretching, 845.71 and at 773.27 correspond to C-H stretching, respectively. The most widely occupied region in the analysis of sample P_1 was single bonds of O-H and C-H, followed by triple bonds and double bonds, as shown in the Figure. From the analysis presented, it was observed that the absorption bands at 3765.17 and 1033.88 are related to O-H associated with the methyl group and aromatic ring (aryl). This presence of O-H was due to moisture emanating from SR, which was not a crack in the internal structure of zeolite. This was also manifest in the moisture content analysis described in Table 4.1, where oxygen was present in a small amount. The remaining other absorption bands indicated the presence of aromatic (benzene), saturated, and unsaturated aliphatic (alkane, alkene, and alkyl groups) hydrocarbons. These hydrocarbon compounds were formed as a result of the random scission or degradation of lignin from SR and the long chain of LDPE and HDPE.
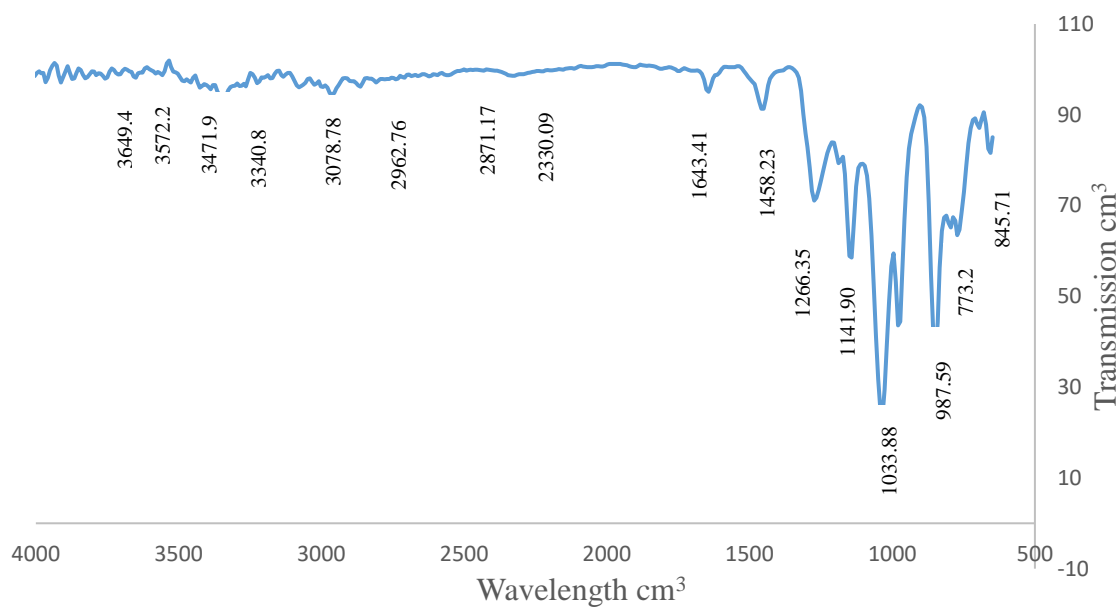
Figure 4.51: Presents FTIR analysis of bio-oil obtained from technique P$_1$

4.9.2.5 *FTIR analysis of bio-oil obtained from technique NP$_1$*

The peaks as presented in Figure 4.52 of bio-oil obtained from technique NP$_1$ are assigned to corresponding absorption bands as 3410.26, 2931.90, 2276.08, 1882.59, 1642.41, 1375.51, 812.41, 659.53 and 462.93. The Figure shows that the absorption bands at 3410.26 correspond to OH stretching, at 2931.90 correspond to C-H stretching, at 2276.08 correspond to -C=H stretching, at 1642.41 correspond to C=C stretching, at 1375.51 correspond to C-H bend, at 1133.32 correspond to C-O stretch, at 812.41 correspond to C-H bend and at 659 correspond to C-H stretching. The analysis indicated the presence of aromatic (benzene), saturated and unsaturated aliphatic (alkane and alkene) hydrocarbons in the fuel. These hydrocarbons were formed as a result of the degradation of lignin from SR as well as the long chains of LDPE and HDPE. It was observed in the analysis, one absorption band indicated the presence of oxygenate (ketone) in small fraction.
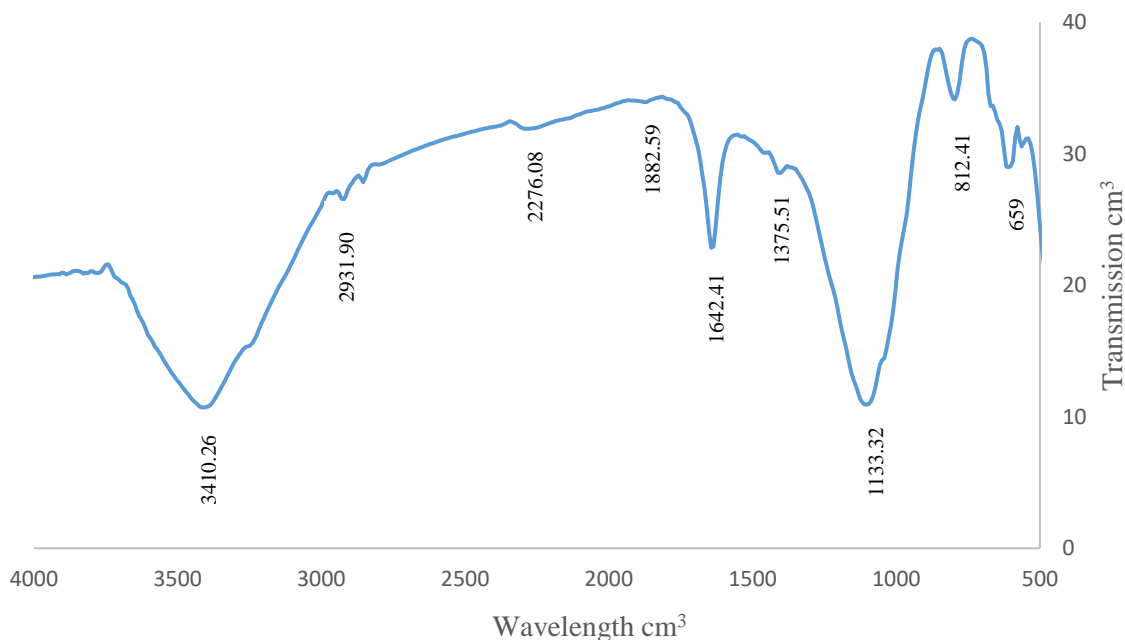
Figure 4.52 presents FTIR analysis of bio-oil obtained from technique NP$_1$

4.9.2.6 *FTIR analysis of bio-oil obtained from technique BU$_1$*

Figure 4.53 presents the FTIR analysis of bio-oil obtained from technique BU$_1$. The peaks as presented in the Figure were assigned to corresponding absorption bands as 3402.54, 2930.90, 2299.22, 1650.41, 1404.22, 1141.90, and 655.82. The Figure shows that the absorption bands at 3402.54 correspond to OH stretching, at 2930.90 correspond to C-H stretching, at 2299.22 correspond to -C=H with sharp and stretch, at 1650.41 and 1404.22 correspond to -C=C stretching, at 1140.90 correspond to C-H aromatic deformation ring, at 655.82 correspond to C-H stretch. The analysis indicated the presence of aromatic (benzene), aliphatic (alkane, alkene, and alkyl) hydrocarbons. The sample BU$_1$ shows the presence of an alkyl group, which was not indicated in the bio-oil samples P$_1$ and NP$_1$. This indicated the effective crack of volatile hydrocarbons in the internal structure of zeolite. It was observed

that the number of absorption bands has decreased compared to the number of absorption bands of bio-oil from samples P_1 and NP_1. This could be attributed to the fact that some oxygenated organics that appear in the FTIR of sample NP1 might have disappeared as a result of the zeolite catalyst application.
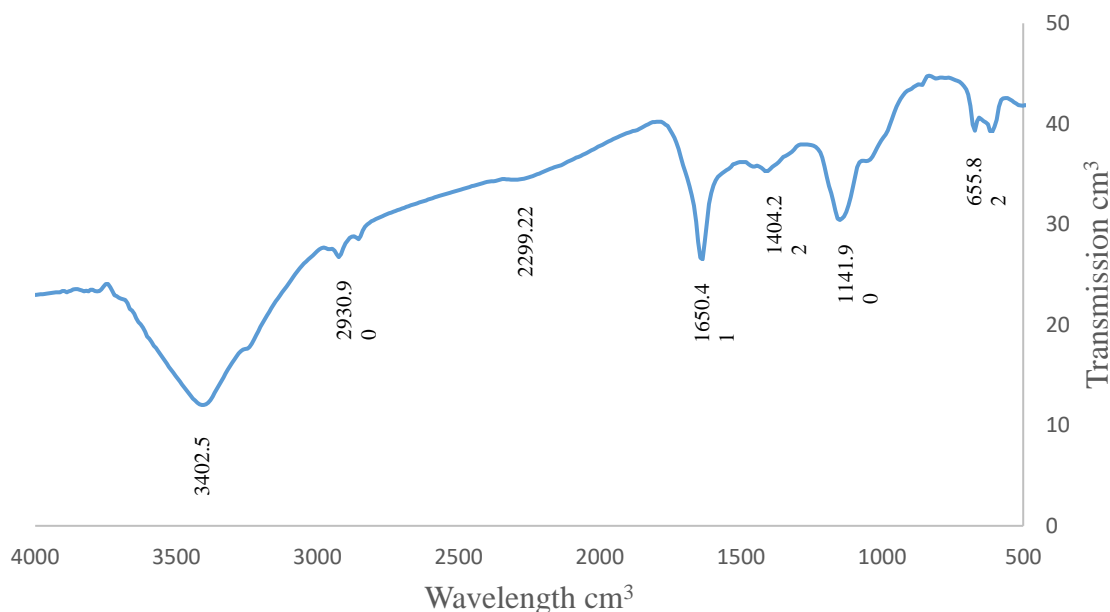
Figure 4.53: Presents FTIR analysis of bio-oil obtained from technique BU_1

4.9.3 Physical properties of bio-oil using HSZY and HCZY

The physical properties of bio-oil using synthesized zeolites as catalysts (HSZY) as well as commercial zeolite as catalysts (HCZY) are presented in Table 4.33. The bio-oil's properties, including calorific value, viscosity, density, moisture content, pH, flash and pour points, cetane number, and octane number, were reported in the table. Additionally, as shown in the Table, the AMST standards for diesel and gasoline were compared to the qualities of the bio-oil.

Table 4.33: Physical properties of bio-oil using HSZY and HCZY

Physical Properties of bio-oil	SZY	HSZY	HCZY	Diesel (ASTM)	Gasoline (ASTM)
Calorific Value MJ/kg	32.26	36.97	36.20	42.00D975	43.00D4814
pH	6.87	6.58	6.73	-	-
Density(g/cm^3)@30°C	0.7617	0.7482	0.7497	0.82-.845D975	0.7197D4814
Viscosity(cst)@100°C	2.13	1.02	1.12	2–3 D975	0.006 D4814
Moisture Content (%)	2.3	1.21	1.01	0.05max D975	-
Flash Point (^{0}C)	48	24.32	50.45	60 – 80 D975	-43 D4814
Cloud Point (^{0}C)	-3.6	-8.50	-8.50	-15 - 5 D975	-
Pour Point (^{0}C)	-21.3	-7.10	-5.01	-35 -15 D975	-
Cetane Number (CN)	31.70	30.75	31.50	40–65 D975	-
Octane number	55.72	65.70	69.10	-	81-87 D4814

The calorific values obtained using HSZY and HCZY as zeolite catalysts are 36.97 and 36.20 MJ/kg, respectively. The bio-oil obtained using these two catalysts has the same calorific value. This implies that there is substantial decrease in oxygenated organic hydrocarbons. This reduction could be attributed to the excellent catalytic activity site of the protonated synthesized zeolite of HSZY as well as the protonated commercial zeolite of HCZY. The catalysts converted the oxygenated organics that emanated from *Sida Rhombifolia* into aliphatic hydrocarbons and aromatic compounds. The conversion of the organic hydrocarbon occurred through reactions such as dehydration, decarboxylation, decarbonylation, and cracking. Therefore, it was observed that the influence of the synthesized zeolite Y catalyst has the same effect as the commercial zeolite Y catalyst, which produced bio-oil with almost the same calorific value as presented in the Table.

Table 4.33 shows the result of the viscosity analysis of the bio-oil at a temperature of 100^{0}C, though the result of the viscosity was compared with the viscosity of diesel and gasoline at

the ASTM standard as presented in the Table. The Table shows that the viscosity of the bio-oil obtained from SZY was 2.13 cst, which is higher than the viscosities obtained using HSZY and HCZY of 1.02 and 1.12 cst, respectively. This implies that the viscosity of the bio-oil significantly reduces as a result of the synergic effect of the catalyst. It can be deduced that the HSZY from Bambu clay reduces the viscosity as well as the waxiness of the bio-oil (Quesada *et al*., 2020).

Table 4.33 also presents the moisture content of the bio-oil under the influence of protonated zeolites HSZY and HCZY, which are 1.21 % and 1.01% respectively. It was observed that the moisture content obtained under the influence of the catalyst was lower than the moisture content obtained from SZY at 2.3%. This implies that with the use of a catalyst, the moisture content decreases as a result of the dehydration reaction that occurs between oxygenated organic and hydrogen from the protonated catalyst (Mishra and Mohanty, 2021). However, the bio-oil obtained from protonated zeolites was lower than the moisture content of diesel oil at 0.05, though the moisture content is not applicable to gasoline as presented in the Table.

The flash points of the bio-oil obtained under the influence of protonated zeolites HSZY and HCZY are 24.72 ºC and 50.45 ºC as presented in Table 4.33. The flash points obtained using HSZY were lower than the flash points of diesel oil (60–80). Similarly, Table 4.33 presents the pour points of the bio-oil obtained under the influence of protonated zeolites of HSZY and HCZY, which are -7.10 ºC and -5.01 ºC respectively. It was observed that the pour point is lower than the pour point of diesel oil, ranging from -35 ºC to -15 ºC.

Table 4.33 also presents the cetane numbers of bio-oil under the influence of protonated zeolites HSZY and HCZY, which are 30.75 and 31.50, respectively. It can be seen that the

cetane number under the influence of protonated zeolites was lower than the cetane number of diesel oil (40–55), though the cetane number is not applicable to gasoline as presented in the Table. The octane number (octane rating) of the bio-oil obtained under the influence of protonated zeolites HSZY and HCZY are 65.70 and 69.10, respectively. The octane number of the bio-oil under the influence of the HSZY was lower than the octane number of the acceptable ASTM standard for gasoline, 81–85 D4818, as presented in the Table 4.33.

4.9.4 Chemical properties of bio-oil obtained using HSZY and HCZY

4.9.4.1 *GC-MS analysis of bio-oil obtained using HSZY and HCZY*

The GC-MS analysis of bio-oil using HSZY was presented in Figure 4.54. The chromatograph presented in the Figure shows the major peaks contain hydrocarbons from hexane (C_8) to Eicosane (C_{20}). The analysis shows that the bio-oil contains straight-chain and branched chain alkanes, alkenes, cycloalkanes, aromatics, and organic hydrocarbons. There was a chromatogram showing the presence of organic hydrocarbons detected by mass spectrometry. The peak of the organic was at retention time 14.76 min, and peak number 10 contains Benzeneacetic acid, 4-tetradecyl ester. Further calculations were made using the spectrum library to determine the proportion of various hydrocarbon types in the bio-oil. The analysis indicated that the bio-oil contains 11.76% organic hydrocarbons (esters and aldehydes), 58.81% aliphatic hydrocarbons (straight and branched chain alkane was 7.65%, cycloalkane was 5.87%, and alkene was 35.29%), and 23.53% aromatic hydrocarbons.

The bio-oil obtained using HSZY has hydrocarbons of lower molecular weight with carbon numbers ranging from octane (C_8) to Eicosane (C20) than diesel oil, whose molecular weight of hydrocarbons ranges from nonane (C_9) to dotriacontane (C_{30}). However, the molecular

weight of the bio-oil produced using HSZY was slightly higher than the molecular weight of kerosene, whose carbon number ranges from heptane (C_9) to hexadecane (C_{16}) as well as higher than the molecular weight of gasoline, whose carbon number ranges from pentane (C_5) to dodecane (C_{12}). Therefore, the bio-oil produced using HSZY has a molecular weight lower than diesel oil but close to kerosene; hence, the bio-oil can be used for domestic cooking.
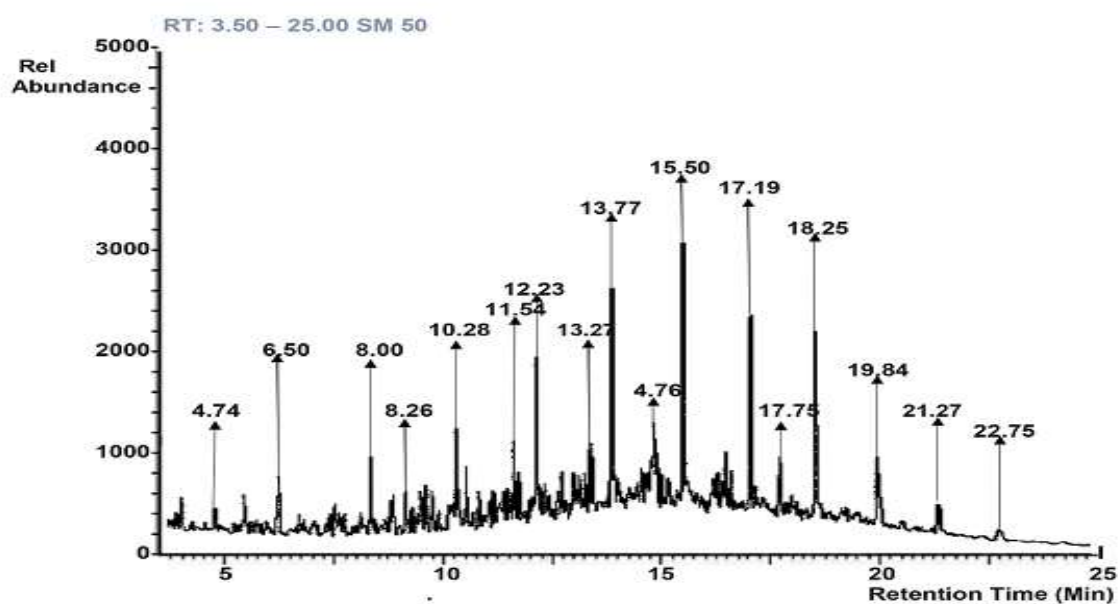
Figure 4.44: GC-MS analysis of bio-oil obtained using HSZY

4.9.4.2 *GC-MS analysis of bio-oil obtained using HCZY*

The GC-MS analysis of bio-oil obtained using HCZY was presented in Figure 4.45. The chromatogram of the bio-oil as presented shows the major peaks contain hydrocarbons from hexane (C_8) to Heneicosane (C_{21}). Also, the analysis shows that the bio-oil contains straight chain and branched-chain alkane, alkene, cycloalkane, aromatic, and organic hydrocarbons. There are chromatograms showing the availability of organic hydrocarbons, specifically

ester, in the bio-oil. Further calculations were made using the spectrum library to determine the proportion of various hydrocarbon types in the bio-oil.

The analysis indicated that the bio-oil contains 11.76% organic hydrocarbons (esters), 70.58% aliphatic hydrocarbons, and 17.27% aromatic hydrocarbons. The bio-oil obtained using HCZY has the same hydrocarbons of lower molecular weight, whose carbon numbers range from octane (C_8) to Heneicosane (C_{21}). Therefore, the bio-oil produced using HCZY could be used for domestic cooking. The molecular weight of the bio-oil was close to kerosene.
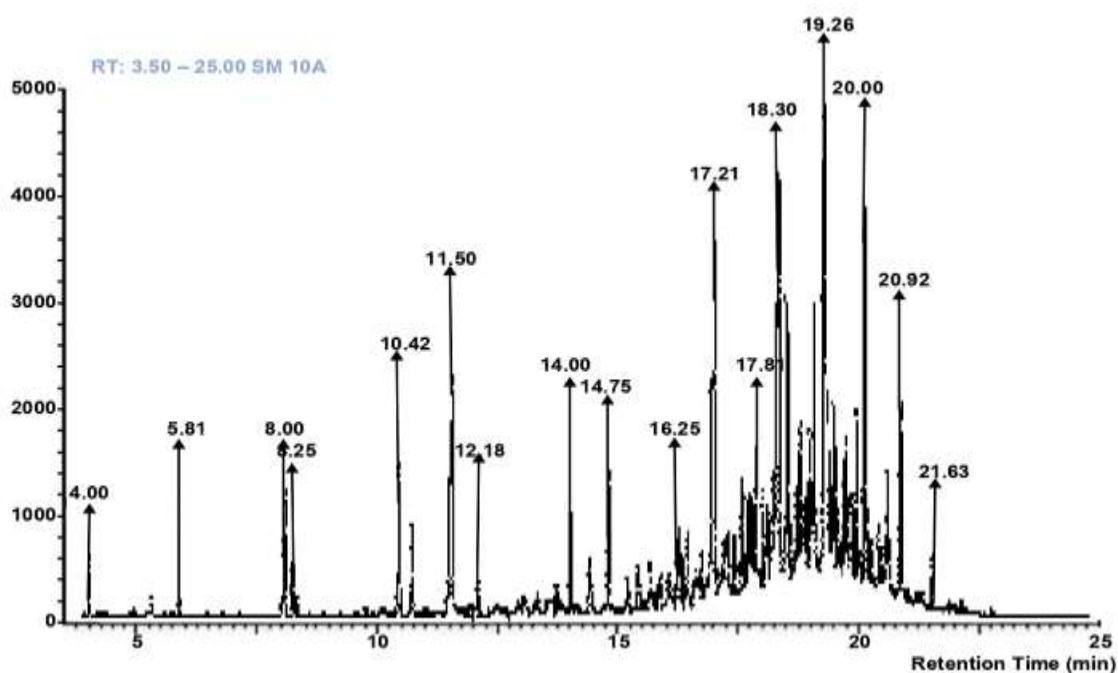
Figure 4.55: GC-MS analysis of bio-oil obtained using HCZY

4.9.5 Mechanism of catalytic co-pyrolysis of *Sida Rhombifolia* with LDPE and HDPE

The catalytic co-pyrolysis of *Sida Rhombifolia* (SR) with LDPE (Low-Density Polyethylene) and HDPE (High-Density Polyethylene) involves the simultaneous thermal decomposition

of SR with LDPE and HDPE in the presence of the synthesis zeolite Y catalyst, as presented in Figure 4.56. The reaction mechanism: started where the co-pyrolysis reaction starts with the thermal decomposition of the mixed feedstock (SR with LDPE and HDPE) at a temperature of $550\,^0C$ where there was breaking down of the chemical bonds in the feedstock, leading to the formation of smaller molecules. During this thermal decomposition, SR undergoes depolymerization of cellulose, hemicellulose, and lignin, producing various volatile compounds such as sugars, phenols, and aromatics. While the LDPE and HDPE break down into smaller hydrocarbon fragments due to the cleavage of their polymer chains, generating waxes, alkenes, and other hydrocarbons as presented in the Figure. Though the smaller fragments as a primary product from SR facilitate cracking of LDPE and HDPE at a temperature lower than the decomposition temperature of LDPE and HDPE so as to produce the primary product.

The influence of the zeolite Y catalyst enhances the overall reaction, yielding and selectively releasing desired products. The catalyst facilitated the secondary reactions of the primary pyrolysis products with SR and with LDPE and HDPE. The secondary reactions include deoxygenation, decarboxylation, dehydrogenation, and polymerization, as presented in the Figure. The cracked vapors from both SR and LDEP/HDPE condensed to form a bio-oil phase. The overall products obtained from the catalytic pyrolysis contain bio-oil (less oxygenated organics and high aliphatic aromatic hydrocarbon compounds of varying chain lengths), gaseous products (carbon dioxide, carbon monoxide, and hydrogen are generated during the pyrolysis process), and the remaining non-volatile components that do not undergo complete pyrolysis, along with any unreacted catalyst, form a solid char residue.
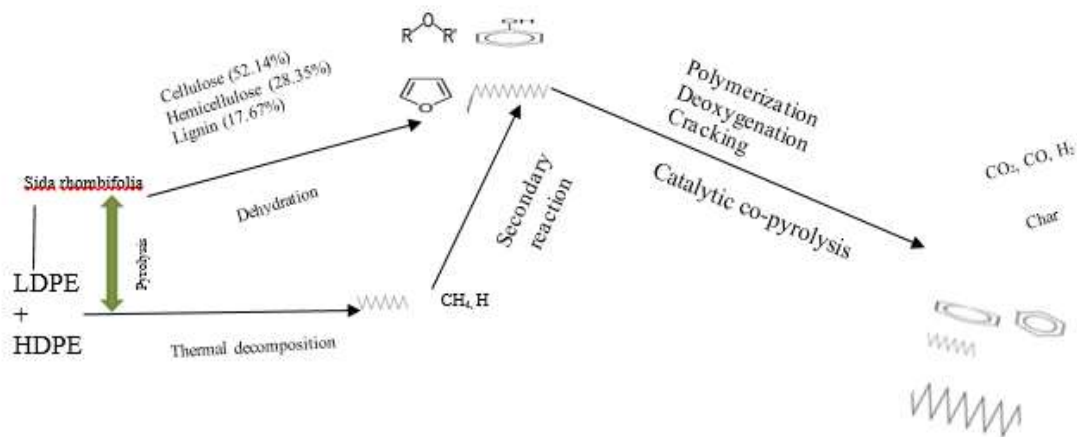
Figure 4.56: Mechanism of catalytic co-pyrolysis of SR with LDPE and HDPE

CHAPTER FIVE

5.1   CONCLUSION AND RECOMMENDATIONS

5.1   Conclusion

In this study, the production of higher quality bio-oil obtained from catalytic co-pyrolysis of SR with LDPE and HDPE with synthetic zeolite Y catalyst was investigated. From the preliminary study, the proximate analysis shows that the SR has volatile matter of 76.42 wt. %, LDPE of 97.89 wt. % and HDPE of 92.86 wt. %. The result shows the maximum bio-oil yield was 48.10 wt. % at pyrolysis temperature of 500 ºC, reaction time of 60 minutes, and an average range of particle sizes of 2-4 mm. The physical characteristics of the bio-oil produced by the pyrolysis of SR included a low calorific value of 17.01 MJ/kg, a high viscosity of 13.23 cst, a high density of 1.0460 kg/m^3, and flash and pour points of 36 ºC and -32 ºC. The GC-MS analysis reveals that the bio-oil has a high level of oxygenated organics (esters, aldehyde, ketone, amine, carboxylic acid, ether, and phenol) hydrocarbons (77.77%) and aliphatic (alkane and alkene) hydrocarbons (22.23%).

The oils produced from the pyrolysis of LDPE and HDPE are 78.6 wt. % and 75.20 wt. % at temperatures of 550 ºC and a reaction time of 60 minutes, respectively. The oil obtained from pyrolysis of LDPE and HDPE shows calorific values of 35.04 MJ/kg and 34.02 MJ/kg, viscosities of 5.06 and 5.73 cst, moisture contents of 2.01 and 2.14 %, pH of 6.96 and 6.89, flash points of 54 ºC and 53 ºC and pour points of -23 and -21 ºC respectively. While the GC-MS shows the majority of compounds are aliphatic hydrocarbon.

Additionally, bio-oil was produced by co-pyrolyzing SR with LDPE as well as HDPE. The bio-oil's calorific values after being co-pyrolyzed are 27.90 and 26.17 MI/kg, though these

values are higher than the individual pyrolysis of SR alone, which has a calorific value of 17.01 MJ/kg. The increase was attributed to the effective interaction between free radicals in SR with LDPE and HDPE. Similarly, the viscosities of the products produced from the co-pyrolysis are 5.06 and 5.73 cst, the moisture content are 2.01 and 2.14 %, the density are 0.7801 and 0.7806 kg/m^3, the pH are 6.01 and 6.95, the flash points are 54 ^{o}C and 53 ^{o}C, the pour points are -23 and -21 ^{o}C respectively. However, it was observed that the co-pyrolysis improves other physico-chemical parameters such as calorific value, pH, density, and the oxygenated organics that emanate from SR. In fact, the 77.77 % of oxygenated organics contained in the bio-oil produced from pyrolysis of SR alone reduces to 5.32 % while the 22.23 % of aliphatic increases to 88.48%, with the appearance of aromatic hydrocarbons at 6.20%. Also, the influence of HDPE showed that the 77.77 % of oxygenated compound produced from pyrolysis of SR alone reduces to 21.05 % while the 22.23 % of aliphatic increases to 73.535 %, with an appearance of aromatic hydrocarbons of 5.42 %. Therefore, it can be deduced that the co-pyrolysis shows an effective synergy between SR with LDPE and HDPE though, the bio-oil contains viscous and waxy.

This study discussed the feasibility of synthesizing a zeolite Y-type catalyst from Bambu clay, with comparable characteristics to the commercial zeolite Y catalyst for catalytic cracking of volatile hydrocarbons during co-pyrolysis of SR with LDPE and HDPE. Two-step preparation of zeolite catalyst: Seed gel and feed gel were prepared from locally sourced aluminium hydroxide and sodium silicate.

The XRF analysis indicated that Bambu clay was considered to be kaolinite with a Si/Al ratio of approximately 1:85; hence, Bambu clay could be a potential source for zeolite Y synthesis.

The clay was thereafter dehydroxylated, and the ratio slightly increased to 2:11. The Si/Al ratio of SZY and CZY was 2:40 and 2.62, respectively. From the SEM, the individual particles of SZY and CZY have regular tetrahedral and bulky shapes with average crystallite sizes of 24.77nm and 24.04 nm, respectively. The BET analysis reveals that the surface area of SZY was 549.10 m2g-1 higher than that of the commercial zeolite, CZY (426.20 m2g-1. The analysis shows that the SZY has more Lewis acid sites, though the overall acidities of Lewis and Bronsted are SZY 220.18 and 93.44 µmol/g which are lower than the acidities of CZY 224.02 and 102.20µmol/g.

The SZY from the Bambu clay was further underwent ion exchange with ammonia chloride to form protonated zeolite catalyst, HSZY. The HSZY contains active acid sites for application in catalytic reactions. The HSZY was tested for catalytic application in order to reduce the oxygenated organic, increase the aliphatic and aromatic hydrocarbons, increase the calorific value, reduce the viscosity, and eliminate the waxiness contained in the bio-oil.

The SZY's performance test shows that the calorific value of the bio-oil produced by catalytic co-pyrolysis was 36.26 MJ/kg, its viscosity was 2.23 cst, and its moisture content was 2.3%. In a similar performance test, the HSZY demonstrated a significant improvement with calorific value increases from 36.26 to 36.97 MJ/kg, a decrease in viscosity from 2.23 to 1.02 cst, moisture content from 2.3% to 1.21% and density from 0.8220 to 0.7842 g/cm3, aromatic hydrocarbon increases from 16.44% to 35.00%.

Similarly, the GC-MS shows that the bio-oil contains carbon in the range from octane (C_8) to Eicosane (C_{20}) which are lower than the carbon contained in diesel oil in the range from

nonane (C_9) - dotriacontane (C_{30}) but closer to the carbon contained in kerosene in the range from heptane (C_9) to hexadecane (C_{16}) as well as higher than the carbon contained in gasoline in the range from pentane (C_5) to dodecane (C_{12}). Therefore, the bio-oil obtained using HSZY has a carbon range close to that of kerosene; hence, the bio-oil can be used for domestic cooking.

5.2 Recommendations

The following recommendations are hereby made from the research work:

i. To synthesis a Zeolite Y catalyst for the production of bio-oil, other clay sources across Nigeria should be studied.

ii. The bio-oil produced in this research work can be further investigated for utilization in the Aviation industry.

iii. The regeneration of the used catalyst in the pyrolyser bed needs to be studied

5.3 Contribution to knowledge

The research work has been able to contribute to knowledge in the following ways:

1. The surface area of 129.60 m^2g^{-1} and acidic sites of 34.40 µmol/g of Bambu clay were improved to 530.40 m^2g^{-1} and 60.92 µmol/g. Synthesized Zeolite Y catalyst (HSZY) has been successfully developed for the first time.

2. The developed catalyst, which possessed a high surface area of 549.092 m^2/g^{-1} and Lewis's acidic site of 220.18 µmol/g, compared favorably with the commercial zeolite Y catalyst (HCZY) in terms of activity characterization.

3. The synthesized HSZY, catalyzed low- and high-density polyethylene bio-oil comprised of heavier molecular hydrocarbons in the carbon, range from C_{12}-C_{34} to bio-kerosene of carbon, range from C_8-C_{20}.

4. The research has successfully produced bio-kerosene (C_8-C_{20}), which was used as a domestic fuel and can be applied in the aviation industry. Summarily, local content, environmental issues, and transportation industries have been addressed in the research.

REFERENCES

Abnisa, F., Daud, W. M. A.W., & Saliu, J.N. (2014). Pyrolysis of Mixtures of Palm Shell and Polystyrene: an Optional Method to Produce a High Grade Pyrolysis Oil. Environmental Progress and Sustainable Energy, 33, 1026 33.

Agrawal, T., Quraishi, A., Jadhav, K., (2019). Bioethnaol production from Madhucalatifolia L. flowers by a newly isolated strain of Pichia kudriavzevii. Energy Environ.30, 1477–1490.

Ajayi, A. O., Atta, A. Y., Aderemi, B. O. and Adefila, S. s. (2010). Novel Method of Metakaolin Dealumination Preliminary Investigation. Journal of Applied Sciences Research. 6(10).

Ajayi, O., A. (2012). Development of large pore zeolite from kaolinite clays. Advances in chemical Engineering and Science, Vol.10. 04. 226

Aktar, J., Amin, N., S. (2012). A review on operating parameters for optimum liquid oil yield in biomass pyrolysis. Renewable and Sustainable Energy. Vol. 16, 7, - 5101-5109.

Al-Ani, T., Sarapaa, O. (2008). Clay and clay mineralogy: physical-chemical properties and industrial uses. Geological Survey of Finland. 94.

Ali, O. (2011). Polymer/clay nanocomposites, advances in diverse industrial applications of nano-composites. Retrieved from http://www.intechopen.com/books/advances-in-diverse-industrial-applications-of-nanocomposites/polymer/polymer-clay-nanocomposite

Andrej-kovicova, S. (2012). Air Lime Mortars with Incorporation of Sepiolite and Synthetic of a Zeolite Pellets. *Acta Geodynamica et Geomaterialia,* 9: 79–91.

Anderson, J. R., Foger, K., Mole, T., Rajadhyaksha, R. A. and Saunders, J. V. (1979). Reactions on ZSM5-Type Zeolite Catalysts. Journal of Catalysis. 58: 114-130.

Asadullah M., Rahman, M.A., Ali, M.M., Rahman, M.S., Motin, M.A. (2007). Production of bio-oil from fixed bed pyrolysis of bagasse. *fuel*, 86(16): 2514-2520.

Ayodeji, A., A., Kofi, H., F., Modupe, O., E., Osayomwanbo, U., J. (2018). Effects of Sodium Hydroxide Concentration on Zeolite Y Synthesized from Elefun Kaolinite Clay in Nigeria. International Journal of Applied Engineering. Vol 13. 3: 1536-1542.

Bardalai M. (2015). A review of physical properties of biomass pyrolysis oil. International Journal of Renewable *Energy Research (IJRER)*, 5(1): 277-286.

Bardalai M., Mahanta D. K., (2015). A Review of Physical Properties of Biomass Pyrolysis Oil. Renewable Energy Research. Vol.5, No.1, page 282.

Bridgwater A., V. (2012). Review of fast pyrolysis of biomass and product upgrading. Biomass and Bioenergy. Vol. 38, pp. 68-94.

Bu, Q., Lei, H., Wang, L., Wei, Y., Zhu, L., Zhang, X., Liu, Y., Yadavalli, G., Tang, J. (2014). Bio-based phenols and fuel production from catalytic microwave pyrolysis of lignin by activated carbons. Bioresour. Technol., 162, 142-7.

Cejka, J., Zone, S. (2010). Zeolites and Catalysis, Synthesis, Reactions and Applications. WILEY-VCH Verlag GmbH & Co. KGaA, Weinheim.

Conti, R., Pezzolesi, L., Pistocchi, I., R., Torri, C., M., Fabbri, D., (2016). Photobioreactor cultivation and catalytic pyrolysis of the microalga Desmodesmus communis (Chlorophyceae) for hydrocarbons production by HZSM-5 zeolite cracking. Bioresour. Technol. 222, 148–155.

Chen, Y., Dong, Qin, W., Xiao, D., (2010). Xylose and cellulose fractionation from corncob with three different strategies and separate fermentation of them to bioethanol. Bioresour. Technol. 101, 6994–6999.

Ciolkosz, D. (2014). Introduction to biomass combustion, wood-biomass Energy in the North forest Retrieved on February 2, 2018 from https://link.springer.com/chapter/10.1007/978-1-4614-9478-2_8. pp. 135–151.

David, T. W. (2007). Zeolites- Earliest Solid State Acids. *AU Journal of Tchnology,* 11(1): 36- 41.

Dewangan, A. (2014). Co-pyrolysis of lignocellulose biomass and synthetic polymer. Unpublished project report, Department of Chemical Engineering, National Institute of Technology, Rourkela, India.

Dewangan, A., Pradhan, D., Singh, R. S., K. (2016). Co-pyrolysis of Sugarcane Bagasse and Low-Density-Polyethylene: Influence of Plastic on Pyrolysis Product Yield. Fuel, 185, 508-516.

Dyer, A. (1988). Introduction to Zeolite Molecular Sieves. England, John Wile Y & Sons. 1: 65-80,

Edomwonyi-Otu, L. (2013). Influence of Thermal Treatment on Kankara Kaolinite. Opticon 1826 15: 5, pp. 1-5, DOI: http://dx.doi.org/10.5334/opt.bc.

Enweremadu, C., Ojediran, J., Oladeji, J., T., d., Afolabi, I. O. (2004). Evaluation of Energy Potential of Husks from Soy-beans and Cowpea. Science Focus. 8:18-23.

Feng, P., Bu, X., Stucky, D. (1997). Hydrothermal syntheses and structural characterization of zeolite analogue compounds based on cobalt phosphate. *Nature*, 388, 735-741

Foong, S.Y., Liew, R.K., Yang, Y., Cheng, Y.W., Yek, P.N.Y., Peng, W., Lam, S.S., (2020). Valorization of biomass waste to engineered activated biochar by microwave pyrolysis: Progress, challenges, and future directions. Chem. Eng. J. 389, 124401.

Freel, B., G. (1996). Bio-Oil Production and Utilization. Proceedings of the 2nd EU/Canada Workshop on Thermal Biomass Processing, 23.

Frost, R. (1995). Fourier Transform Infrad Spectroscopy of kaolinite, dickite and halloysite. Clay and Clay Minerals. 43(2), 191-195.

Fukushima, Y. (1980). Effect of Zeolite Additives in Feed on the Physiological Condition of Cows. Chikusan no Kenkyu, 33: 1393-1395.

Garba, M. U., Inalegwu A., Musa, U. (2017). Thermogravimetric Characteristic and Kinetic of catalytic co-pyrolysis of biomass with low- and high-density polyethylenes. *Biomass Conv. Bioref*, 1, 4.8.

Garcia-Perez, M. (2002). Vacuum pyrolysis of sugarcane bagasse. Analytical and applied pyrolysis65(2): 111-136.

George, W.. H., Avelino C. (2015). Synergies between bio-oil refineries for the production of fuel from Biomass. Biorefineries. Journal German Chemist Society. Vol. 46, 7184-7201.

Hwang, Y., Farooq, A., Park, S., H., Kim, K., H., M., H., Choi, S., C., Kim, M., Y., Park, R., Park, Y.K., (2019). J., NH3-induced removal of NOx from a flue gas stream by silent discharge ozone generation in a double reactor system. Korean J. Chem. Eng. 36, 1291–1297.

Huber, G., Iborra, S., Corma, C., A. (2006). Synthesis of transportation fuels from biomass: chemistry, catalysts, and engineering. Chem. Rev. 106, 4044–4098.

Holtz, R, D., Kovacs, W., D. (2010). An introduction to geotechnical engineering. New York. Prentice-Hall Civil Engineering and Engineering Mechanics Series.

ICDD. (2015). International Centre for Diffraction Data software.

Isikgor, F., H., Becer, B., R., (2015). Lignocellulosic Biomass: a Sustainable Platform for the production of bio-based chemicals and polymers. Journal of Polymer Chemistry. 6, 4497–4559.

Iftikhar, H., Zeeshan, M., I., S., Muneer, B., Razzaq, M., (2019). Co-pyrolysis of sugarcane bagasse and polystyrene with ex-situ catalytic bed of metal oxides/HZSM-5 with focus on liquid yield. Journal of Bioresources Technology. Vol. 289, 121647.

Johansson, A., C., Sandström, L., Ohrman, O., W., Jilvero, H. (2018). Co-pyrolysis of woody biomass and plastic waste in both analytical and pilot scale. J. Anal. Appl. Pyrol. 134, 102–113.

Khan, M., H., M. Sultana, M. R. Al-Mamun, Hasan, M. (2016). Pyrolytic Waste Plastic Oil and Its Diesel Blend: Fuel Characterization. Journal of Environmental and Public Health Volume 2016, Article ID 7869080, 6 pages.

Kumar, G. P. (2010). Optimization of process for the production of bio-oil from eucalyptus wood. Journal of Fuel Chemistry and Technology, 38(2): 162-167.

Kumar, M., Patel, S., Hamid, F. (2011). Characteristics of some forestry nonwoody biomass species and estimation of their power generation potentials. Energy sources, part a: recovery, utilization, and environmental effects. Pp.1650

Lercher, J. A., & Jentys, A. (2002). Handbook of Porous Solids. Vol.12. 111.

Lu, Q., Li. (2009). Overview of fuel properties of biomass fast pyrolysis oils. *Energy conver. and Management*, 50(5): 1376-1383.

Martinez, J., D., Vesses, A., Mastral, A., M., Murillo, R., Navarro, M., Puy, N. (2014). Co-pyrolysis of Biomass with Waste Tyres: Upgrading of Liquid Biofuel. Fuel Process Technology, 119, 263-71.

Mishra, R, Mohanty, K. (2021). Bio-oil and Biochar Production Using Thermal and Catalytic pyrolysis of low-value waste neem seeds over low-cost catalysts: effects of operating conditions on product yields and studies of physicochemical characteristics of bio-oil and biochar. Biochar-springer. **3**, 641–656.

Mohanty T., P. (2011). Fuel production from biomass. Indian perspective for pyrolysis oil. Journal of Scientific & Industrial Research. 70, 668-674.

Moinuddin S., Mohammad M. R., Mohammed M. (2011). Waste Plastic Conversion into Chemical Product like Naphtha. Journal of Renewable Energy and Applications. 1, 3.

Muggen, G. (2015). Bio liquids fuel. *Biomass conference*, 1. Retrieved from July, 2018.

Mravec, D., Hudec, J., Janotka, H. (2005). Some Possibilities of Catalytic and Noncatalytic Utilization of Zeolites. Chemistry Paper, 59(1): 62 – 69.

New York Times; Asia Pacific, (2011). Level of Radioactive Materials RISE Near Japanese Plant. By the Associated Press. New York.

Nuradden, S. (2015). Development of zeolite Y and ZSM5 composite catalyst from Kankara Kaolin. Journal for Applied Science Technology. 11, 2. 127-135.

Onal, E., Uzun, B., Putin, A., E. (2014). Bio-oil Production via Co-pyrolysis of Almond Shell as Biomass and High Density Polyethylene. Journal of Energy Conversion and Management, 78, 704-10

Park, Y., J. (2004). Bio-oil from rice straw by pyrolysis using fluidised bed and char removal system. *Prepr. Pap.-Am. Chem. Soc., Div. Fuel Chem*, 49(2): 800.

Ralph, P., Overend. A. (2002). Thermochemical Conversion of Biomass. *National Renewable Energy Laboratory, Golden, Colorado, USA*, 1-5.

Reed, T., Graboski, M., Markson, M. (1982). The SERI High Pressure Oxygen Gasifier. *Solar Energy Research Institute, Golden, Colorado*, 234-1455.

Quesada, L., M., C., Hoces, M., A., Martínlara, G., Luzon, Blazquez, G. (2020). Performance of Dierent Catalysts for the In Situ Cracking of the Oil-Waxes Obtained by the Pyrolysis of Polyethylene FilmWaste. Sustainability. 12(13), 5482.

Ruren, X., Gao, Z.Chen, J., Wenfu, Y. (2007). Zeolites to Porous MOF Materials. Journal of material science. 2: 168-414.

Sachin K., Sing K., (2011). Recovery of hydrocarbon liquid from waste high-density Polyethylene by thermal pyrolysis. Journal of Chemical Engineering. Vol. 28, pp. 665.

Sharuddin, D., A., Abnisa, F., Wandaud, D., W., Aroua, M., A., M., K. (2016). A review on pyrolysis of plastic wastes. Energy Conversion and Management. 115, 308-326.

Simone, M., Barontini, F., Nicolel C., Tognotti, L., (2012). Gasification of pelletized biomass in a pilot scale downdraft gasifier. Bio-resource Technology. 116, 403–412

Shah, A., Y., Zeeshan, M., Farooq, Z., Ahmed, N., Iqbal, N., (2019). Co-pyrolysis of cotton stalk and waste tire with a focus on liquid yield quantity and quality. Renewable Energy 130, 238–244.

Tumuluru, J., Wright, T., Boardman, R., D., Yancey, N., A., Sokhansan S. (2011). A review on biomass classification and composition, co-firing issues and pre-treatment methods. America Society of Agricultural and Biological Engineering. 10, 110458.

Uzoejinwa, B., He, X., Wang, S., El-Fatah Abomohra, A., B., Hu, Y., W., Wang, Q., (2018). Copyrolysis of biomass and waste plastics as a thermochemical conversion technology for high-grade biofuel production: recent progress and future directions elsewhere worldwide. Energy Conversion. Management. 163, 468–492.

Wilaipon, P. (2008). Density Equation of Bio-Coal Briquette and Quantity of Maize Cob in Phitsanulok, Thailand. Journal of Applied Sciences. 5(2):1808-1811.

Xu, R., Pang, W., Yu, J., Huo, Q., Chen, J. (2007). Chemistry of Zeolites and Related Porous

Materials: Synthesis and Structure. John Wiley & Sons (Asia) PTE Ltd, Singapore. Journal of chemistry. 978; 82233-3

Yin, R., Liu, I. (2013). Characterization of bio-oil and bio-char obtained from sweet sorghum bagasse fast pyrolysis with fractional condensers. l. *Fuel*, 112: 96-104.

Zanzi, R., Sjotom, K. Bjornbom, E. (2002). Rapid pyrolysis of Agricultural Residues at High Temperature, Biomass and Bioenergy. Vol. 23,357-366.

Zhang Y., Chen D., Zhang D., Zhu X. (2016). TG-FTIR analysis of bio-oil and its pyrolysis and gasification property. Journal of Fuel Chemistry and Technology. Vol. 40: 1196.

Zheng, Y., Yang, X., Huang, Y., Liu, C., Zheng, Z., (2018). Study of the thermal behavior, kinetics, and product characterization of biomass and low-density polyethylene co-pyrolysis by thermogravimetric analysis and pyrolysis-GC/MS. Journal of Analytic Applied. Pyrolysis. 133, 185–197.

Zhao C., Yun, l., Angeliki, A. (2009). Highly Selective Catalytic Conversion of Phenolic Bio-Oil to Alkanes. Journal of Chemistry. 121, 4047.

Zhu, X., Mallinson, R., G., Resasco, R., E. (2010). Role of Trans-alkylation Reactions in the Conversion of Anisole over HZSM-5. *Applied Catalysis A: General*. 379(1–2): p172-181.

APPENDIX A

EFFECT OF TEMPERATURE ON PYROLYSIS OF SR

Table A-1 pyrolysis data generated from laboratory experiment for effect of temperature

s/n	Temperature ^0C	Time	Liquid (w/v)	Solid char (g)
1	350	75	16.69	24.85
2	400	75	20.75	18.75
3	450	75	25.52	15.15
4	500	75	26.68	14.95
5	550	75	25.68	15.25
6	600	75	25.35	14.75

Calculations of bio-oil from *Sida Rhombifolia* (SR)

Results of Pyrolysis

The product of the pyrolysis are bio-oil, char, and gas. They are calculated in terms of weight percent as follows:

$$\text{Yield of Bio-oil} = \frac{Volume\ of\ bio\ oil\ (ml)}{Starting\ weight\ of\ SR\ (g)} \quad\quad\quad \text{(A-1)}$$

$$\text{Yield of Bio-Char} = \frac{Weight\ of\ bio\ char\ (g)}{Starting\ weight\ of\ SR\ (g)} \quad\quad\quad \text{(A-2)}$$

Yield of gas = 100 – (%bio oil + % Char) $\quad\quad\quad$ (A-3)

Given that:

Starting weight of SR = 50g

Density of bio from SR = 1.1046

The Volume of bio-oil obtained using the mass-density relation as follows:

Vol of bio-oil from pyrolysis of SR$= \frac{Liquid\ w/v}{Density}$

Step 1

1st run

Volume of bio-oil = $\dfrac{Liquid\ w/v}{Density}$ = $\dfrac{16.59}{1.1046}$ = 15.02

Therefore % yield of Bio-oil = $\dfrac{Volume\ of\ bio\ oil\ (ml)}{Starting\ weight\ of\ SR\ (g)}$ = $\dfrac{15.02}{50}$ = 30.04

% yield of Bio-Char = $\dfrac{24.85}{50}$ = 49.7

% yield of gas = 100 – (30.04 + 49.7) = 20.26

2nd run

Volume of bio-oil = $\dfrac{Liquid\ w/v}{Density}$ $\dfrac{20.71}{1.1046}$ = 18.75

% yield of Bio-oil = $\dfrac{Volume\ of\ bio\ oil\ (ml)}{Starting\ weight\ of\ SR\ (g)}$ $\dfrac{18.75}{50}$ = 35.70

% yield of Bio-Char = $\dfrac{18.75}{50}$ = 37.50

% yield of gas = 100 – (35.7 + 37.50) = 26.8

3rd run

Vol of bio-oil = $\dfrac{Liquid\ w/v}{Density}$ $\dfrac{25.52}{1.1046}$ = 23.10

% yield of Bio-oil = $\dfrac{Volume\ of\ bio\ oil\ (ml)}{Starting\ weight\ of\ SR\ (g)}$ = $\dfrac{23.10}{50}$ = 46.2

% yield of Bio-Char = $\dfrac{15.15}{50}$ = 30.30

% yield of gas = 100 – (46.2 + 30.30) = 23.50

4th run

Vol of bio-oil = $\dfrac{Liquid\ w/v}{Density}$ = $\dfrac{26.57}{1.1046}$ = 24.05

% yield of Bio-oil = $\dfrac{Volume\ of\ bio\ oil\ (ml)}{Starting\ weight\ of\ SR\ (g)}$ = $\dfrac{24.05}{50}$ = 48.10

% yield of Bio-Char = $\dfrac{14.95}{50}$ = 29.9

% yield of gas = 100 – (48.10 + 29.9) = 22.00

5th run

Vol of bio-oil = $\dfrac{\text{Liquid w/v}}{\text{Density}} = \dfrac{25.682}{1.1046} = 23.25$

% yield of Bio-oil = $\dfrac{\text{Volume of bio oil (ml)}}{\text{Starting weight of SR (g)}} = \dfrac{23.23}{50} = 46.5$

% yield of Bio-Char = $\dfrac{15.25}{50} = 30.50$

% yield of gas = 100 – (46.5 + 30.50) = 23.00

6th run

Vol of bio-oil = $\dfrac{\text{Liquid w/v}}{\text{Density}} = \dfrac{25.35}{1.1046} = 22.95$

% yield of Bio-oil = $\dfrac{\text{Volume of bio oil (ml)}}{\text{Starting weight of SR (g)}} = \dfrac{22.95}{50} = 45.90$

% yield of Bio-Char = $\dfrac{14.25}{50} = 28.50$

% yield of gas = 100 – (45.90 + 28.5) = 25.60

Step 11

The generated data were calculated and presented in Table (A-2)

Table A-2: Effect of temperature on pyrolysis of SR

S/n	Temp (^{0}C)	Time (min)	Yield		
			Liquid	**Solid**	**Gas**
1	350	75	30.04	49.7	20.26
2	400	75	35.7	37.5	26.8
3	450	75	46.2	30.3	23.5
4	500	75	48.1	29.9	22
5	550	75	46.5	30.2	23.3
6	600	75	45.9	28.5	25.6

EFFECT OF REACTION TIME ON PYROLYSIS OF SR

Table A-3 pyrolysis data generated from laboratory experiment for effect of reaction time

s/n	Temperature ^{0}C	Time	Liquid (w/v)	Solid char (g)
1	500	30	18.28	21.70
2	500	40	21.76	19.10
3	500	45	24.91	16.45
4	500	60	26.67	14.90
5	500	90	25.30	14.65
6	500	120	21.76	14.10

1st run

Volume of bio-oil = $\frac{Liquid\ w/v}{Density}$ = $\frac{18.28}{1.1046}$ = 16.55

Therefore % yield of Bio-oil = $\frac{Volume\ of\ bio\ oil\ (ml)}{Starting\ weight\ of\ SR\ (g)}$ = $\frac{16.55}{50}$ = 33.1

% yield of Bio-Char = $\frac{21.70}{50}$ = 43.4

% yield of gas = $100 - (33.1 + 43.4) = 23.5$

2nd run

Volume of bio-oil = $\frac{Liquid\ w/v}{Density}$ = $\frac{21.76}{1.1046}$ = 19.70

Therefore % yield of Bio-oil = $\frac{Volume\ of\ bio\ oil\ (ml)}{Starting\ weight\ of\ SR\ (g)}$ = $\frac{19.70}{50}$ = 39.4

% yield of Bio-Char = $\frac{19.10}{50}$ = 38.2

% yield of gas = $100 - (39.4 + 38.2) = 22.4$

3rd run

Volume of bio-oil = $\frac{Liquid\ w/v}{Density}$ = $\frac{24.91}{1.1046}$ = 22.50

Therefore % yield of Bio-oil = $\frac{Volume\ of\ bio\ oil\ (ml)}{Starting\ weight\ of\ SR\ (g)}$ = $\frac{22.50}{50}$ = 45.1

% yield of Bio-Char = $\frac{16.45}{50}$ = 32.9

% yield of gas = $100 - (45.1 + 32.9) = 22.00$

4th run

Volume of bio-oil = $\frac{Liquid\ w/v}{Density}$ = $\frac{26.67}{1.1046}$ = 24.15

Therefore % yield of Bio-oil = $\frac{Volume\ of\ bio\ oil\ (ml)}{Starting\ weight\ of\ SR\ (g)}$ = $\frac{24.15}{50}$ = 48.3

% yield of Bio-Char = $\frac{14.90}{50}$ = 29.8

% yield of gas = 100 − (48.3 + 29.8) = 21.9

5ᵗʰ run

Volume of bio-oil = $\dfrac{Liquid\ w/v}{Density}$ = $\dfrac{25.30}{1.1046}$ = 22.90

Therefore % yield of Bio-oil = $\dfrac{Volume\ of\ bio\ oil\ (ml)}{Starting\ weight\ of\ SR\ (g\ )}$ = $\dfrac{22.90}{50}$ = 46.7

% yield of Bio-Char = $\dfrac{14.65}{50}$ = 29.3

% yield of gas = 100 − (46.7 + 29.3) = 24.0

6ᵗʰ run

Volume of bio-oil = $\dfrac{Liquid\ w/v}{Density}$ = $\dfrac{21.76}{1.1046}$ = 19.70

Therefore % yield of Bio-oil = $\dfrac{Volume\ of\ bio\ oil\ (ml)}{Starting\ weight\ of\ SR\ (g\ )}$ = $\dfrac{19.70}{50}$ = 45.8

% yield of Bio-Char = $\dfrac{19.10}{50}$ = 38.2

The generated data were calculated and presented in Table (A-4)

Table A-4 Effect of reaction time on pyrolysis of sida rhombifolia

S/n	Temp (^{0}C)	Time (min)	Yield		
			Liquid	Solid	Gas
1	500	30	33.1	43.4	23.5
2	500	40	39.4	38.2	22.4
3	500	45	45.1	32.9	22
4	500	60	48.3	29.8	21.9
5	500	90	46.7	30.1	23.2
6	500	120	45.8	29.3	24.9

EFFECT OF PARTCLES SIZE ON PYROLYSIS OF SR

Table A-5 pyrolysis data generated from laboratory experiment for effect of particle size

s/n	Temperature ^{0}C	Reaction time	Particle sizes	Liquid (w/v)	Solid char (g)
1	500	60	0.1-0.5	19.44	25.70

175

2	500	60	0.5-.1.0	22.04	26.79
3	500	60	1.0-2.0	25.02	27.98
4	500	60	2.0-4.0	27.92	28.95
5	500	60	4.0-6.0	27.39	30.70
6	500	60	6.0-8.0	26.67	32.90

1st run

Volume of bio-oil = $\dfrac{Liquid\ w/v}{Density} = \dfrac{19.44}{1.1046} = 17.60$

Therefore % yield of Bio-oil = $\dfrac{Volume\ of\ bio\ oil\ (ml)}{Starting\ weight\ of\ SR\ (g)} = \dfrac{17.60}{50} = 35.2$

% yield of Bio-Char = $\dfrac{12.85}{50} = 25.70$

% yield of gas = $100 - (35.2 + 25.70) = 39.10$

2nd run

Volume of bio-oil = $\dfrac{Liquid\ w/v}{Density} = \dfrac{22.04}{1.1046} = 19.99$

Therefore % yield of Bio-oil = $\dfrac{Volume\ of\ bio\ oil\ (ml)}{Starting\ weight\ of\ SR\ (g)} = \dfrac{19.99}{50} = 39.92$

% yield of Bio-Char = $\dfrac{13.40}{50} = 26.79$

% yield of gas = $100 - (39.92 + 26.79) = 33.29$

3rd run

Volume of bio-oil = $\dfrac{Liquid\ w/v}{Density} = \dfrac{25.02}{1.1046} = 22.65$

Therefore % yield of Bio-oil = $\dfrac{Volume\ of\ bio\ oil\ (ml)}{Starting\ weight\ of\ SR\ (g)} = \dfrac{22.65}{50} = 45.30$

% yield of Bio-Char = $\dfrac{13.99}{50} = 27.98$

% yield of gas = $100 - (45.30 + 27.98) = 26.72$

4th run

Volume of bio-oil = $\dfrac{Liquid\ w/v}{Density} = \dfrac{27.92}{1.1046} = 25.28$

Therefore % yield of Bio-oil = $\dfrac{Volume\ of\ bio\ oil\ (ml)}{Starting\ weight\ of\ SR\ (g)} = \dfrac{25.28}{50} = 50.55$

% yield of Bio-Char = $\dfrac{14.47}{50} = 28.95$

% yield of gas = 100 − (50.55 + 28.95) = 30.50

5th run

Volume of bio-oil = $\dfrac{Liquid\ w/v}{Density} = \dfrac{27.39}{1.1046} = 24.80$

Therefore % yield of Bio-oil = $\dfrac{Volume\ of\ bio\ oil\ (ml)}{Starting\ weight\ of\ SR\ (g)} = \dfrac{24.80}{50} = 49.60$

% yield of Bio-Char = $\dfrac{13.40}{50} = 30.70$

% yield of gas = 100 − (49.60 + 30.70) = 19.70

6th run

Volume of bio-oil = $\dfrac{Liquid\ w/v}{Density} = \dfrac{26.67}{1.1046} = 24.15$

Therefore % yield of Bio-oil = $\dfrac{Volume\ of\ bio\ oil\ (ml)}{Starting\ weight\ of\ SR\ (g)} = \dfrac{24.15}{50} = 48.30$

% yield of Bio-Char = $\dfrac{16.45}{50} = 32.90$

% yield of gas = 100 − (48.30 + 32.90) = 18.80

The generated data were calculated and presented in Table (A-6)

Table A-6 Effect of particle size on pyrolysis of SR

S/n	Temperature	Particle sizes	Yield

	(⁰C)	(mm)	Liquid	Solid	Gas
1	500	0.1-0.5	35.2	25.7	39.1
2	500	0.5-.1.0	39.92	26.79	33.29
3	500	1.0-2.0	45.3	27.98	26.72
4	500	2.0-4.0	50.55	28.95	20.5
5	500	4.0-6.0	49.6	30.7	19.7
6	500	6.0-8.0	48.3	32.9	18.8

EFFECT OF TEMPERATURE ON PYROLYSIS OF LDPE

Table B-1 pyrolysis data generated from laboratory experiment for effect of temperature on LDPE

s/n	Temperature ^0C	Liquid (w/v)	Solid char (g)
1	350	40.70	6.81
2	400	41.97	6.61
3	450	42.58	6.40
4	500	43.24	6.00
5	550	43.41	5.90
6	600	43.18	5.55

1st run

Volume of bio-oil = $\frac{Liquid\ w/v}{Density}$ = $\frac{40.70}{1.1046} = 36.85$

Therefore % yield of Bio-oil = $\frac{Volume\ of\ bio\ oil\ (ml)}{Starting\ weight\ of\ SR\ (g)}$ = $\frac{36.85}{50} = 73.7$

% yield of Bio-Char = $\frac{6.81}{50} = 13.62$

% yield of gas = $100 - (73.70 + 13.62) = 12.68$

2nd run

Volume of bio-oil = $\frac{Liquid\ w/v}{Density}$ = $\frac{41.97}{1.1046} = 38.00$

Therefore % yield of Bio-oil = $\frac{Volume\ of\ bio\ oil\ (ml)}{Starting\ weight\ of\ SR\ (g)}$ = $\frac{38.00}{50} = 76.0$

% yield of Bio-Char = $\frac{6.61}{50} = 13.21$

% yield of gas = $100 - (76.0 + 13.21) = 10.79$

3rd run

Volume of bio-oil = $\frac{Liquid\ w/v}{Density}$ = $\frac{42.58}{1.1046} = 38.55$

Therefore % yield of Bio-oil = $\dfrac{Volume\ of\ bio\ oil\ (ml)}{Starting\ weight\ of\ SR\ (g)} = \dfrac{38.55}{50} = 77.1$

% yield of Bio-Char = $\dfrac{6.40}{50} = 12.8$

% yield of gas = 100 – (77.1 + 12.8) = 10.1

4th run

Volume of bio-oil = $\dfrac{Liquid\ w/v}{Density} = \dfrac{43.24}{1.1046} = 39.15$

Therefore % yield of Bio-oil = $\dfrac{Volume\ of\ bio\ oil\ (ml)}{Starting\ weight\ of\ SR\ (g)} = \dfrac{39.15}{50} = 78.30$

% yield of Bio-Char = $\dfrac{6.00}{50} = 12.0$

% yield of gas = 100 – (78.30 + 12) = 9.70

5th run

Volume of bio-oil = $\dfrac{Liquid\ w/v}{Density} = \dfrac{43.41}{1.1046} = 39.30$

Therefore % yield of Bio-oil = $\dfrac{Volume\ of\ bio\ oil\ (ml)}{Starting\ weight\ of\ SR\ (g)} = \dfrac{39.30}{50} = 78.60$

% yield of Bio-Char = $\dfrac{5.90}{50} = 11.80$

% yield of gas = 100 – (78.60 + 11.80) = 9.6

6th run

Volume of bi-oil = $\dfrac{Liquid\ w/v}{Density} = \dfrac{43.08}{1.1046} = 39.00$

Therefore % yield of Bio-oil = $\dfrac{Volume\ of\ bio\ oil\ (ml)}{Starting\ weight\ of\ SR\ (g)} = \dfrac{39.00}{50} = 78.0$

% yield of Bio-Char = $\dfrac{5.55}{50} = 11.10$

% yield of gas = 100 – (78.0 + 11.10) = 10.9

The generated data were calculated and presented in Table (A-10)

Table B-2 Effect of temperature on pyrolysis of LDPE

S/no	Temp ^{0}C	Yield wt%		
		Liquid	**Char**	**Gas**
1	350	73.7	13.62	12.68
2	400	76.0	13.21	10.79
3	450	77.1	12.8	10.1
4	500	78.3	12.0	9.7
5	550	78.6	11.8	9.6
6	600	78.0	11.1	8.9

EFFECT OF TEMPERATURE ON PYROLYSIS OF HDPE

Table B-3 pyrolysis data generated from laboratory experiment for effect of temperature on HDPE

s/n	Temperature ^{0}C	Liquid (w/v)	Solid char (g)
1	350	38.85	6.85
2	400	39.77	5.50
3	450	40.10	5.20
4	500	40.59	4.25
5	550	41.53	2.90
6	600	41.25	2.22

1st run

Volume of bio-oil = $\frac{Liquid\ w/v}{Density} = \frac{38.85}{1.1046} = 35.18$

Therefore % yield of Bio-oil = $\frac{Volume\ of\ bio\ oil\ (ml)}{Starting\ weight\ of\ SR\ (g)} = \frac{35.18}{50} = 70.35$

% yield of Bio-Char = $\frac{6.85}{50} = 13.70$

% yield of gas = 100 – (70.35 + 13.70) = 15.95

2nd run

Volume of bio-oil = $\frac{Liquid\ w/v}{Density} = \frac{39.77}{1.1046} = 36.00$

Therefore % yield of Bio-oil = $\frac{Volume\ of\ bio\ oil\ (ml)}{Starting\ weight\ of\ SR\ (g)} = \frac{36.00}{50} = 72.00$

% yield of Bio-Char = $\frac{5.50}{50} = 11.0$

% yield of gas = 100 – (72.0 + 11.0) = 17.00

3ʳᵈ run

Volume of bio-oil = $\dfrac{Liquid\ w/v}{Density}$ = $\dfrac{40.10}{1.1046}$ = 36.30

Therefore % yield of Bio-oil = $\dfrac{Volume\ of\ bio\ oil\ (ml)}{Starting\ weight\ of\ SR\ (g)}$ = $\dfrac{36.30}{50}$ = 72.60

% yield of Bio-Char = $\dfrac{5.20}{50}$ = 10.40

% yield of gas = 100 – (72.60 + 10.40) = 17.1

4ᵗʰ run

Volume of bio-oil = $\dfrac{Liquid\ w/v}{Density}$ = $\dfrac{40.59}{1.1046}$ = 36.75

Therefore % yield of Bio-oil = $\dfrac{Volume\ of\ bio\ oil\ (ml)}{Starting\ weight\ of\ SR\ (g)}$ = $\dfrac{36.75}{50}$ = 73.50

% yield of Bio-Char = $\dfrac{4.25}{50}$ = 8.50

% yield of gas = 100 – (73.50 + 8.5) = 18.00

5ᵗʰ run

Volume of bio-oil = $\dfrac{Liquid\ w/v}{Density}$ = $\dfrac{41.53}{1.1046}$ = 37.60

Therefore % yield of Bio-oil = $\dfrac{Volume\ of\ bio\ oil\ (ml)}{Starting\ weight\ of\ SR\ (g)}$ = $\dfrac{37.60}{50}$ = 75.20

% yield of Bio-Char = $\dfrac{2.90}{50}$ = 5.80

% yield of gas = 100 – (75.20 + 5.80) = 19.00

6ᵗʰ run

Volume of bio-oil = $\dfrac{Liquid\ w/v}{Density}$ = $\dfrac{41.25}{1.1046}$ = 37.35

Therefore % yield of Bio-oil = $\dfrac{Volume\ of\ bio\ oil\ (ml)}{Starting\ weight\ of\ SR\ (g)}$ = $\dfrac{37.35}{50}$ = 74.69

% yield of Bio-Char = $\dfrac{2.22}{50} = 4.44$

% yield of gas = 100 – (74.69 + 4.44) = 20.87

The generated data were calculated and presented in Table (A-12)

Table B-3 Pyrolysis of High-Density Polyethylene (HDPE)

S/no	Temp ^{0}C	Yield wt%		
		Liquid	**Char**	**Gas**
1	350	70.35	13.7	15.95
2	400	72.00	11.0	17.0
3	450	72.60	10.4	17.0
4	500	73.50	8.50	18.0
5	550	75.20	5.80	19.0
6	600	74.69	4.44	20.87

EFFECT OF BLENDING SR WITH LDPE ON PYROLYSIS

Table B-4 pyrolysis data generated from laboratory experiment for effect of blending SR with LDPE

s/n	Temperature ^{0}C	Liquid (w/v)	Solid char (g)
1	350	31.59	14.55
2	400	30.21	15.80
3	450	37.83	5.30
4	500	37.77	5.05

1ˢᵗ run

Volume of bio-oil = $\dfrac{Liquid\ w/v}{Density} = \dfrac{31.59}{1.1046} = 28.60$

Therefore % yield of Bio-oil = $\dfrac{Volume\ of\ bio\ oil\ (ml)}{Starting\ weight\ of\ SR\ (g)} = \dfrac{28.60}{50} = 57.2$

% yield of Bio-Char = $\dfrac{14.55}{50} = 29.10$

% yield of gas = 100 – (57.2 + 29.10) = 13.7

2ⁿᵈ run

Volume of bio-oil = $\dfrac{Liquid\ w/v}{Density} = \dfrac{30.21}{1.1046} = 27.35$

Therefore % yield of Bio-oil = $\dfrac{Volume\ of\ bio\ oil\ (ml)}{Starting\ weight\ of\ SR\ (g)} = \dfrac{27.35}{50} = 54.70$

% yield of Bio-Char = $\dfrac{15.80}{50} = 31.60$

% yield of gas = 100 – (54.70 + 31.60) = 13.70

3rd run

Volume of bio-oil = $\dfrac{Liquid\ w/v}{Density} = \dfrac{37.83}{1.1046} = 34.25$

Therefore % yield of Bio-oil = $\dfrac{Volume\ of\ bio\ oil\ (ml)}{Starting\ weight\ of\ SR\ (g)} = \dfrac{34.25}{50} = 68.50$

% yield of Bio-Char = $\dfrac{5.30}{50} = 10.70$

% yield of gas = 100 – (68.5 + 10.70) = 20.8

4th run

Volume of bio-oil = $\dfrac{Liquid\ w/v}{Density} = \dfrac{37.77}{1.1046} = 34.20$

Therefore % yield of Bio-oil = $\dfrac{Volume\ of\ bio\ oil\ (ml)}{Starting\ weight\ of\ SR\ (g)} = \dfrac{34.20}{50} = 68.4$

% yield of Bio-Char = $\dfrac{5.05}{50} = 10.1$

% yield of gas = 100 – (68.4 + 10.10) = 21.60

The generated data were calculated and presented in Table (A-14)

Table 0-14 Effect of blending SR with LDPE

S/no	Blending ratio	Yield wt%		
		Liquid	Char	Gas
1	1:1	57.2	29.1	13.7
2	1:2	54.7	31.6	13.7
3	1:3	68.5	10.7	20.8
4	1:4	68.4	10.1	21.6

EFFECT OF BLENDING SR WITH HDPE ON PYROLYSIS

Table B pyrolysis data generated from laboratory experiment for effect of blending SR with HDPE

s/n	Temperature ^0C	Liquid (w/v)	Solid char (g)
1	350	27.44	17.30
2	400	28.83	15.55
3	450	35.07	7.85
4	500	35.73	8.35

1st run

Volume of bio-oil = $\dfrac{Liquid\ w/v}{Density} = \dfrac{27.44}{1.1046} = 24.85$

Therefore % yield of Bio-oil = $\dfrac{Volume\ of\ bio\ oil\ (ml)}{Starting\ weight\ of\ SR\ (g)} = \dfrac{24.85}{50} = 49.7$

% yield of Bio-Char = $\dfrac{17.30}{50} = 34.60$

% yield of gas = 100 – (49.7 + 34.60) = 15.7

2nd run

Volume of bio-oil = $\dfrac{Liquid\ w/v}{Density} = \dfrac{28.83}{1.1046} = 26.10$

Therefore % yield of Bio-oil = $\dfrac{Volume\ of\ bio\ oil\ (ml)}{Starting\ weight\ of\ SR\ (g)} = \dfrac{27.35}{50} = 52.2$

% yield of Bio-Char = $\dfrac{15.55}{50} = 31.1$

% yield of gas = 100 – (52.20+ 31.1) = 16.70

3rd run

Volume of bio-oil = $\dfrac{Liquid\ w/v}{Density} = \dfrac{35.07}{1.1046} = 31.75$

Therefore % yield of Bio-oil = $\dfrac{Volume\ of\ bio\ oil\ (ml)}{Starting\ weight\ of\ SR\ (g)} = \dfrac{31.75}{50} = 63.50$

% yield of Bio-Char = $\dfrac{7.85}{50} = 15.7$

% yield of gas = 100 – (63.50 + 15.70) = 20.8

4th run

Volume of bio-oil = $\dfrac{Liquid\ w/v}{Density} = \dfrac{35.73}{1.1046} = 32.35$

Therefore % yield of Bio-oil = $\dfrac{Volume\ of\ bio\ oil\ (ml)}{Starting\ weight\ of\ SR\ (g)} = \dfrac{32.35}{50} = 64.7$

% yield of Bio-Char = $\dfrac{8.35}{50} = 16.7$

% yield of gas = 100 – (64.70 + 16.70) = 18.60

The generated data were calculated and presented in Table (A-16)

Table B Effect of blending ratio of SR with HDPE

S/no	Blending ratio	Yield wt%		
		Liquid	**Char**	**Gas**
1	1:1	49.7	34.6	15.7
2	1:2	52.2	31.1	16.7
3	1:3	63.5	15.7	20.8
4	1:4	64.7	16.7	18.6

Table C-1: GC-MS analysis of bio-oil from pyrolysis of *sida rhombifolia*

Compounds	Formula	R.T	Area %
1-Nonene	C9H18	6.8096	0.704
Nonane	C9H20	7.1027	0.5257
5-Hepten-2-one, 6-methyl-	C8H14O	7.6889	0.6159
D-Limonene	C10H16	9.9236	0.548
1-Decene	C10H20	10.6563	1.821
Decane	C10H22	11.0227	0.8974
4-Nonanone	C9H18O	12.7079	0.4474
Linalool	C10H18O	14.503	0.5661
5-Undecene	C11H22	14.8327	0.483
Cyclopropane, 1-methyl-2-pentyl-	C9H18	15.2723	2.2547
P-Cresol	C7H8O	16.1882	0.519
6-Octenal, 3,7-dimethyl-, (R)-	C10H18O	17.214	0.3369
Isoneral	C10H16O	17.8734	0.6105
Isogeranial	C10H18O	18.8992	0.8035
1,11-Dodecadiene	C12H22	19.6685	0.7059
3-Dodecene, (Z)-	C12H24	20.7676	0.4661
2,6-Octadienal, 3,7-dimethyl-, (Z)-	C10H16O	22.7825	13.8389
2,6-Octadienal, 3,7-dimethyl-, (E)-	C10H16O	24.6142	18.7976
Z,Z-6,13-Octadecadien-1-ol acetate	C20H36O2	27.9114	0.3584
Geranyl acetate	C12H20O2	29.0837	2.6499
Tetradecane	C14H30	29.853	2.5573
Caryophyllene	C15H24	30.5491	0.8713
Phenol, 2-methoxy-4-(1-propenyl)-	C11H12O3	32.0511	0.529
1,12-Tridecadiene	C13H24	33.37	0.48
1-Pentadecene	C15H30	33.8462	2.7371

Pentadecane	C15H32	34.2126	2.7752
Naphthalene, 1,2,3,4,4a,5,6,8a-octahydro-7-methyl-4-methylene-1-	C15H24	34.7255	0.5715
pentadecen-1-ol, acetate	C17H32O2	37.583	0.6185
Hexadecane	C16H34	38.2791	1.9251
Benzene, 1,1'-(1,3-propanediyl)bis-	C18H22	40.3672	1.0209
8-Heptadecene	C17H34	41.4663	0.5979
Benzene, (3-nitropropyl)-	C9H11NO2	43.005	0.3039
1-Nonadecene	C19H38	49.3062	0.4285
Nonadecane	C19H40	49.5993	0.7547
1-Octadecene	C18H36	52.8231	1.7372

Table C-2 FTIR analysis of bio-oil from SR

s/n	Absorption band cm^{-1}	Functional group	Compounds name	Types of vibration	Intensity
1	725.25	C-H	Mono alkyl	Bending	Weak
2	923.86	CH-CH$_2$	Alkane	Bending	Strong
3	1103.32	C=O	Ketones,	Stretch	Medium
4	1282.49	C-O-C	Esters, ethers,	Stretch	
5	1410.80	C=O	aldehyde	Bending	Weak
6	1603.82	C=C	Alkyl associated with aromatic	Stretch	Medium
7	1705.12	COO	Carboxylic acids	Stretch	
8	2847.62	CH-CH	Alkane	Stretch	Strong
9	3063.06	OH	Alcohol	Bending	Weak
	3345.25	N-H	Amines	Stretch	Strong
10	3456.55	O-H	Water	Stretch	Weak
11	3842.04	O-H	Water	Stretch	Medium

Table C-3 GC-MS analysis of liquid oil from pyrolysis of LDPE

Peaks	R.T	Compounds	Formula	Area %
1	7.10	Cylcopropene 1,2	C$_5$H$_{10}$	1.91

2	6.80	1-Nonene	C_9H_{18}	0.93
3	7.10	Nonane	C_9H_{20}	0.5257
4	15.27	Cyclopropane, 1-methyl-2-pentyl-	C_9H_{18}	2.2547
5	7.68	5-Hepten-2-one, 6-methyl-	$C_8H_{14}O$	0.6159
6	10.65	Hexane	$C_{10}H_{20}$	1.821
7	11.02	Butane, 2,3-di methyl	$C_{10}H_{22}$	0.8974
8	5.97	1- Undecane	$C_{11}H_{24}$	3.02
9	6.10	Undecane	$C_{11}H_{24}$	1.74
10	7.51	1-Dodecene	$C_{12}H_{24}$	3.34
11	7.62	Dodecene	$C_{12}H_{24}$	2.27
12	19.66	1,11-Dodecadiene	$C_{12}H_{22}$	0.7059
13	33.37	1,12-Tridecadiene	$C_{13}H_{24}$	0.48
14	9.07	Tridecane	$C_{13}H_{28}$	2.51
15	29.85	Tetradecane	$C_{14}H_{30}$	2.5573
16	30.54	Caryophyllene	$C_{15}H_{24}$	0.8713
17	17.32	Hexadecane	$C_{16}H_{34}$	1.9251
18	18.48	8-Heptadecene	$C_{17}H_{34}$	0.5979
19	19.823	1-Octadecene	$C_{18}H_{36}$	1.7372
20	49.30	1-Nonadecene	$C_{19}H_{38}$	0.4285
21	49.59	Nonadecane	$C_{19}H_{40}$	0.7547
22	21.65	Eicosane	$C_{20}H_{42}$	3.21
23	24.42	Heneicosane	$C_{21}H_{44}$	0.37
24	25.26	Tetracosane	$C_{24}H_{50}$	2.09

Table C-4 FTIR of liquid oil obtained from LDPE

Peak Serial Number	Wave Number (cm^{-1})	Functional Group
1	725.25	CH=CH (cis)
2	964.44	-CH=CH (trans)
3	902.72	

4	1473.44	-CH$_3$
5	1604.20	
6	2731.29	-C-CH$_3$
7	2729.30	-C-CH$_3$
8	2939.61	-C-CH$_3$
9		

Table C-5 GC-MS analysis of liquid oil from pyrolysis of HDPE

Peaks	R.T	Compounds	Formula	Area %
1	3.062	Nonene	C$_9$H$_{18}$	0.93
2	3.152	1-Nonane	C$_9$H$_{20}$	0.5257
3	3.270	Cyclopropane, 1-methyl-2-pentyl-	C$_9$H$_{18}$	2.2547
4	4..465	Decane	C$_{10}$H$_{22}$	1.23
5	4.435	1-Undecene	C$_{10}$H$_{20}$	2.63
6	5.97	1- Undecane	C$_{11}$H$_{24}$	3.02
7	6.10	Undecane	C$_{11}$H$_{24}$	1.74
8	7.51	1-Dodecene	C$_{12}$H$_{24}$	3.34
9	7.62	Dodecene	C$_{12}$H$_{24}$	2.27
10	7.629	1,11-Dodecadiene	C$_{12}$H$_{22}$	0.7059
11	7.537	1,12-Tridecadiene	C$_{13}$H$_{24}$	0.48
12	9.07	Tridecane	C$_{13}$H$_{28}$	2.51
13	11.856	Tetradecane	C$_{14}$H$_{30}$	2.5573
14	11.724	Caryophyllene	C$_{15}$H$_{24}$	0.8713
15	12.32	Hexadecane	C$_{16}$H$_{34}$	1.9251
16	18.48	8-Heptadecene	C$_{17}$H$_{34}$	0.5979
17	19.823	1-Octadecene	C$_{18}$H$_{36}$	1.7372
18	49.30	1-Nonadecene	C$_{19}$H$_{38}$	0.4285
19	49.59	Nonadecane	C$_{19}$H$_{40}$	0.7547
20	21.65	Eicosane	C$_{20}$H$_{42}$	3.21
21	24.42	Heneicosane	C$_{21}$H$_{44}$	0.37

22	25.26	Tetracosane	$C_{24}H_{50}$	2.09
23	29.21	Heptacosane	$C_{27}H_{56}$	
24	29.99	Heptacosane	$C_{27}H_{56}$	
25	28.45	Octacosane	$C_{28}H_{58}$	

Table C-6 FTIR of liquid oil obtained from HDPE

Peak Serial Number	Wave Number (cm^{-1})	Functional Group
1	887.28	CH=CH (cis)
2	991.23	-CH=CH (trans)
3	1226.77	
4	1465.94	$-CH_3$
5	1604.26	
6	2731.29	$-C-CH_3$
7	2729.30	$-C-CH_3$
8	2939.61	$-C-CH_3$
9	3616.58	

Table C-7 GC-MS analysis of liquid oil from pyrolysis of SR with LDPE and HDPE

Retention time	Compound name	Molecular formula	Area%
15.6753	Undecane	C11H24	0.2292
20.1814	1-Dodecene	C12H24	1.006
20.621	Dodecane	C12H26	0.665
25.0538	1-Tridecene	C13H26	2.3286
25.3836	Tridecane	C13H28	1.7715
29.4867	2-Tetradecene, (E)-	C14H28	10.2524
37.986	Cetene	C16H32	1.1957
41.9426	1-Heptadecene	C17H34	10.0987
42.2723	Heptadecane	C17H36	4.3349
50.2221	1-Heptadecene	C17H34	8.95
45.7159	1-Octadecene	C18H36	0.6219
45.9724	Octadecane	C18H36	9.2829
53.0429	Eicosane	C20H42	7.0222
11.0227	Phenol	C6H5OH	0.1646
15.0892	Cyclopropane, 1-methyl-2-pentyl-	C9H18	0.1646
18.6061	Phenol, 2,3-dimethyl-	C8H10O	0.1316
19.522	Phenol, 4-ethyl-	C8H10O	0.2749
20.1448	Creosol	C8H10O2	0.1357
20.5844	6-Dodecene, (Z)-	C12H24	0.129
20.9507	Cyclododecane	C12H24	0.1651

22.1597	Cyclododecane	C12H24	0.2558
24.2845	Cis-4a-Methyl-decahydronaphthalene C11H20	C11H20	0.7118
25.7499	Pentanoic acid, 10-undecenyl ester	C16H30O2	0.2372
27.6916	Phenol, 2,6-dimethoxy-	C8H10O3	0.3187
29.7798	1-Tetradecene	C14H28	5.502
30.4758	7-Tetradecene	C14H28	0.4586
30.8422	Cyclotetradecane	C14H28	0.4569
31.465	9-Tetradecenal, (Z)-	C14H26O	0.3298
31.7581	Cyclotetradecane	C14H28	0.8199
32.6007	Dodeca-1,6-dien-12-ol, 6,10-dimethyl-	C14H26O	0.7806
36.3008	Methyl 7,9-tridecadienyl ether	C14H26O	0.4079
36.5572	Cyclohexene, 1-nonyl-	C15H28	0.3666
37.0701	endo-2-Methylbicyclo[3.3.1]nonane	C10H18	0.5947
38.6088	2-Tetradecene, (E)-	C14H28	10.2524
39.1949	Cyclotetradecane	C14H28	1.049
40.0009	cis-2-Methyl-4-n-pentylthiane	C11H22O2S	0.4694
40.2574	cis-9-Hexadecenal	C16H30O	0.4017
43.1515	2-Methyl-E-7-hexadecene	C17H34	0.3398
43.7377	E-14-Hexadecenal	C16H30O	0.3398
44.2872	1,12-Tridecadiene	C13H24	0.3398
	9-Octadecene, (E)-	C18H36	0.9889
	E-15-Heptadecenal	C17H32O	0.8949
	Heneicosane	C21H44	6.0777
	Tetracosane	C24H50	1.9527
	Tetracosane	C24H50	1.2002
	1-Hexacosene	C26H52	0.6128

Table C-8 GC-MS analysis of bio-oil at blending ratio 4:1 *sida rhombifolia* with LDPE/HDPE.

Pk	Retention time	Name of the compound	Compound formula	Quantity
1	12.568	2-Heptene, 4-methyl-, (E)-	C8H16	38
		4-Methyl-2-heptene-,	C8H16	
2	15.952	3,4-dimethyl-	C8H16	

Peak	R.T	Compounds	Formula	
3	27.706	Cyclopentane, propyl-	C_8H_{16}	
4	14.282	2,3-Dimethyl-3-heptene, (Z)-	C_9H_{16}	53
25	28.219	Cyclohexane, 1,2,4-trimethyl-	C_9H_{18}	58
11	19.949	2,4,6-Trimethyl-3-heptene	$C_{10}H_{20}$	59
16	21.207	2-Acetylcyclopentanone	$C_{10}H_7O_2$	43
18	22.808	3-Hexene, 2,2,5,5-tetramethyl-,	$C_{10}H_{20}$	53
29	29.451	3-Octene, 2,2-dimethyl-	$C_{10}H_{20}$	43
8	16.809	Benzoic acid	C_6H_5COOH	94
5	15.139	1,7-Nonadiene, 4,8-dimethyl- Citral	$C_{11}H_{20}$	52
15	20.925	3-Ethyl-6-heptafluorobutyryloxyoct	$C_{11}H_{24}$	47
35	33.711	Cyclohexane, 1-ethyl-2-propyl-	$C_{11}H_{22}$	43
61	38.703	Cyclohexane, 1-ethyl-2-propyl-	$C_{11}H_{22}$	41
2	12.399	1-Undecene, 7-methyl-	$C_{12}H_{24}$	52
28	28.932	Dodecanoic acid	$C_{12}H_{24}O_2$	91
		3-Hexene, 2,5-dimethyl-3,4-bis(1-methyl	$C_{14}H_{28}$	50
30	29.626	Ethanol, 2-(dodecyloxy)-	$C_{14}H_{30}O_2$	72
20	25.617	Hexadecane	$C_{16}H_{34}$	80
59	38.421	Methyl stearate	$C_{19}H_{38}$	94
	36.614	3-Eicosene, (E)-	$C_{20}H_{40}$	
57	38.252	Heptadecane, 2,6,10,15-tetramethyl	$C_{21}H_{44}$	89
55	37.952	2-Methyl-2-docosene	$C_{23}H_{46}$	58
10	19.718	Oxalic acid, cyclohexyl tetradecyl	$C_{22}H_{40}O_4$	59
60	38.553	Cyclohexane, (1-exyltetradecyl)-	$C_{26}H_{52}$	46
48	36.689	Tritetracontane	$C_{43}H_{88}$	76
32	32.385	Tetratetracontane	$C_{44}H_{90}$	90

Table C-9 GC-MS analysis of bio-oil at blending ratio 1:1 *sida rhombifolia* with LDPE/HDPE.

Peak	Compounds	Formula	R.T	Area %
1	1-Nonene	C_9H_{18}	6.8096	0.704
2	Nonane	C_9H_{20}	7.1027	0.5257
3	5-Hepten-2-one, 6-methyl-	$C_8H_{14}O$	7.6889	0.6159
4	D-Limonene	$C_{10}H_{16}$	9.9236	0.548

5	1-Decene	$C_{10}H_{20}$	10.6563	1.821
6	Decane	$C_{10}H_{22}$	11.0227	0.8974
7	4-Nonanone	$C_9H_{18}O$	12.7079	0.4474
8	Linalool	$C_{10}H_{18}O$	14.503	0.5661
9	5-Undecene	$C_{11}H_{22}$	14.8327	0.483
10	Cyclopropane, 1-methyl-2-pentyl-	C_9H_{18}	15.2723	2.2547
11	P-Cresol	C_7H_8O	16.1882	0.519
12	6-Octenal, 3,7-dimethyl-, (R)-	$C_{10}H_{18}O$	17.214	0.3369
13	Isoneral	$C_{10}H_{16}O$	17.8734	0.6105
14	Isogeranial	$C_{10}H_{18}O$	18.8992	0.8035
15	1,11-Dodecadiene	$C_{12}H_{22}$	19.6685	0.7059
16	3-Dodecene, (Z)-	$C_{12}H_{24}$	20.7676	0.4661
17	2,6-Octadienal, 3,7-dimethyl-, (Z)-	$C_{10}H_{16}O$	22.7825	13.8389
18	2,6-Octadienal, 3,7-dimethyl-, (E)-	$C_{10}H_{16}O$	24.6142	18.7976
19	Tetradecane	$C_{14}H_30$	29.853	2.5573
20	Caryophyllene	$C_{15}H_{24}$	30.5491	0.8713
21	Hexadecane	$C_{16}H_{34}$	38.2791	1.9251
22	Benzene, 1,1'-(1,3-propanediyl)bis-	$C_{18}H_{22}$	40.3672	1.0209
23	8-Heptadecene	$C_{17}H_{34}$	41.4663	0.5979
24	1-Nonadecene	$C_{19}H_{38}$	49.3062	0.4285
25	Nonadecane	$C_{19}H_{40}$	49.5993	0.7547

Table C-10 GC-MS analysis of bio-oil at blending ratio 1:4 *sida rhombifolia* with LDPE/HDPE.

Pk	Return time	Name of the compound	Compound formula	Quantity
1	11.776	3-Methyl-2-butenoic acid, 6-ethyl-	$C_{13}H_{16}O_2$	72
2	12.399	1-Undecene, 7-methyl-	$C_{12}H_{24}$	52
3	12.568	2-Heptene, 4-methyl-, (E)-	C_8H_{16}	38
		4-Methyl-2-heptene-,	C_8H_{16}	

		3-Heptene, 2-methyl-, (E)-	C_8H_{16}	
4	14.282	2,3-Dimethyl-3-heptene, (Z)-	C_9H_{16}	53
5		1,7-Nonadiene, 4,8-dimethyl-	$C_{11}H_{20}$	52
	15.139	Citral		
6		1-Isopropyl-1,4,5-	$C_{12}H_{24}$	53
	15.252	trimethylcyclohe		
7	15.952	3,4-dimethyl-	C_8H_{16}	64
		2,3-dimethyl-		
		3,4-dimethyl-	C_8H_{16}	
8	16.809	Benzoic acid	C_6H_5COOH	94
9	18.267	Nonane, 2,6-dimethyl-	C_8H_{16}	59
10		Oxalic acid, cyclohexyl		59
	19.718	tetradecyl		
11	19.949	2,4,6-Trimethyl-3-heptene	$C_{10}H_{20}$	59
12		Cyclohexane, 1-ethyl-2,3-	$C_{10}H_{20}$	38
	20.125	dimethyl-		
13		3-Hexene, 2,5-dimethyl-3,4-	$C_{14}H_{28}$	50
	20.487	bis(1-methyl		
14		Cyclohexane, 1,2,4-trimethyl-,	C_9H_{18}	35
	20.663	(1. alpha.,2.beta.,4.beta.)-		
		1-Dodecyn-4-ol	$C_{12}H_{24}$	
		Cyclooctane, (1-methylpropyl)-	$C_{12}H_{24}$	
15		3-Ethyl-6-	$C_{11}H_{24}$	47
	20.925	heptafluorobutyryloxyoct		
16	21.207	2-Acetylcyclopentanone	$C_{10}H_7O_2$	43
17		3-Hexene, 2,2,5,5-tetramethyl-,	$C_{10}H_{20}$	47
	22.108	(Z)-		
18	22.808	3-Hexene, 2,2,5,5-tetramethyl-,	$C_{10}H_{20}$	53
19		6,11-Dimethyl-2,6,10-	$C_{14}H_{24}O$	30
	22.927	dodecatrien-1-ol		
20	25.617	Hexadecane	$C_{16}H_{34}$	80
21		Cyclohexane carboxylic acid, 3-	$C_{22}H_{42}O_2$	43
	26.536	pentadecyl ester		
22	27.431	Cyclohexane, 1,2,4-trimethyl-	C_9H_{18}	46
23		1-Undecene, 7-methyl-	$C_{12}H_{24}$	43
		Cyclopentane, propyl-	C_8H_{16}	
	27.706	Cyclopentane, propyl-	C_8H_{16}	
24			C_9H_{18}	46
	27.912	Cyclohexane, 1,2,4-trimethyl-		
25	28.219	Cyclohexane, 1,2,4-trimethyl-	C_9H_{18}	58
26	28.513	Cyclopentane, 1-butyl-2-propyl-	$C_{12}H_{24}$	64
27	28.676	Bacchotricuneatin c	$C_{20}H_{22}O_5$	50
28	28.932	Dodecanoic acid	$C_{12}H_{24}O_2$	91
29	29.451	3-Octene, 2,2-dimethyl-	$C_{10}H_{20}$	43
30	29.626	Ethanol, 2-(dodecyloxy)-	$C_{14}H_{30}O_2$	72
31		Trichloroacetic acid, tetradecyl	$C_{29}H_{16}cl_3O_2$	91
	32.166	esther		

32	32.385	Tetratetracontane	$C_{44}H_{90}$	90
33		3-Decen-5-one	$C_{10}H_{20}$	43
	32.560	2,4,6-Trimethyl-3-heptene		
34	33.417	Cyclohexane, 1-ethyl-2-propyl-	$C_{11}H_{22}$	43
35	33.711	Cyclohexane, 1-ethyl-2-propyl-	$C_{11}H_{22}$	43
36	33.961	Tetracosyl heptafluorobutyrate	$C_{28}H_{49}F_3O_2$	46
37	34.355	Cyclohexane, 1-ethyl-2-propyl-	$C_{11}H_{22}$	43
38	34.593	Cyclopentane, 1-butyl-2-propyl-	$C_{11}H_{22}$	43
39		3-Hexene, 2,2,5,5-tetramethyl-,	$C_{10}H_{20}$	58
	34.787	(Z)-		
40	34.987	1,2-Tetradecanediol	$C_{14}H_{30}O_2$	53
41		3-Eicosene, (E)-Bromoacetic acid, pentadecyl ester Behenic	$C_4H_7BrO_2$	91
	35.112	alcohol		
42	35.256	1-Dodecanol, 2-hexyl-	$C_{18}H_{38}O_2$	52
43		1-Cyclohexyl-2-methyl-prop-2-	$C_{16}H_{10}O$	72
	35.438	en-1-one		
44	35.544	Triallylsilane	$C_9H_{15}Si$	46
45		Cyclohexane, 1,2,4,5-tetraethyl-,(1.alpha.,2.alpha.,4.alpha.,5.alpha.)-8-Chloro-1-octanol, tert-	$C_9H_{20}O_2Si$	38
	35.913	butyldimethylsilyl ether		
46	36.076	Triallylsilane	$C_9H_{15}Si$	46
47		Dichloroacetic acid, heptadecyl ester	$C_{19}H_{36}cl_3O_2$	91
			$C_{19}H_{38}$	
		1-Nonadecene	$C_{20}H_{40}$	
	36.614	3-Eicosene, (E)-		
48	36.689	Tritetracontane	$C_{43}H_{88}$	76
49		Sulfurous acid, pentadecyl 2-	$C_{21}H_{44}O_3S$	38
	36.901	propyl ester 2-Bromo dodecane		
50	37.252	Hexacosyl heptafluorobutyrate	$C_{30}H_{53}F_7O_2$	52
51	37.320	Cyclopentane, 1-butyl-2-propyl-	$C_{12}H_{24}$	58
52		Cyclohexane, 1-ethyl-2-propyl-	$C_{22}H_{22}$	46
	37.477	Octacosyl trifluoroacetate		
53	37.533	Octacosyl trifluoroacetate	$C_{30}H_{57}F_3O_2$	50
54	37.771	Triallylsilane	$C_9H_{15}Si$	49
55	37.952	2-Methyl-2-docosene	$C_{23}H_{46}$	58
56	38.102	Cyclopentane, 1-butyl-2-propyl-	$C_{12}H_{24}$	55
57		Heptadecane, 2,6,10,15-	$C_{21}H_{44}$	89
	38.252	tetramethyl		
58		2- Chloropropionic acid,	$C_{19}H_{37}clO_2$	74
	38.284	hexadecyl ester		
59	38.421	Methyl stearate	$C_{19}H_{38}$	94
60	38.553	Cyclohexane, (1-exyltetradecyl)-	$C_{26}H_{52}$	46

APPENDIX D

Catalytic (raw clay) co-pyrolysis of SR with LDPE and HDPE

Table A-17 pyrolysis data generated from laboratory experiment for catalyst (raw clay)

s/n	Blending ratio (Catalyst:SR:LDEP&HDPE)	Liquid (w/v)	Solid char (g)
1	1:3:1	27.44	6.85
2	1:3:2	28.83	5.50
3	1:3:3	30.04	5.20
4	1:3:4	34.13	4.25
5	1:3:5	32.58	2.90

1st run

Volume of bio-oil = $\dfrac{Liquid\ w/v}{Density}$ = $\dfrac{27.44}{1.1046}$ = 24.85

Therefore % yield of Bio-oil = $\dfrac{Volume\ of\ bio\ oil\ (ml)}{Starting\ weight\ of\ SR\ (g)}$ = $\dfrac{24.85}{50}$ = 49.70

% yield of Bio-Char = $\dfrac{16.80}{50}$ = 33.60

% yield of gas = 100 – (49.70 + 33.60) = 16.70

2nd run

Volume of bio-oil = $\dfrac{Liquid\ w/v}{Density}$ = $\dfrac{28.83}{1.1046}$ = 26.10

Therefore % yield of Bio-oil = $\dfrac{Volume\ of\ bio\ oil\ (ml)}{Starting\ weight\ of\ SR\ (g)}$ = $\dfrac{26.10}{50}$ = 52.2

% yield of Bio-Char = $\dfrac{15.55}{50}$ = 31.1

% yield of gas = 100 – (52.2+ 31.1) = 16.70

3rd run

Volume of bio-oil = $\dfrac{Liquid\ w/v}{Density}$ = $\dfrac{30.04}{1.1046}$ = 27.72

Therefore % yield of Bio-oil = $\dfrac{Volume\ of\ bio\ oil\ (ml)}{Starting\ weight\ of\ SR\ (g)}$ = $\dfrac{27.72}{50}$ = 54.4

% yield of Bio-Char $= \dfrac{13.64}{50} = 27.28$

% yield of gas $= 100 - (54.4 + 27.28) = 18.32$

4th run

Volume of bio-oil $= \dfrac{Liquid\ w/v}{Density} = \dfrac{34.13}{1.1046} = 30.90$

Therefore % yield of Bio-oil $= \dfrac{Volume\ of\ bio\ oil\ (ml)}{Starting\ weight\ of\ SR\ (g\ )} = \dfrac{30.90}{50} = 61.8$

% yield of Bio-Char $= \dfrac{7.85}{50} = 15.70$

% yield of gas $= 100 - (61.80 + 15.7) = 22.50$

5th run

Volume of bio-oil $= \dfrac{Liquid\ w/v}{Density} = \dfrac{32.58}{1.1046} = 29.49$

Therefore % yield of Bio-oil $= \dfrac{Volume\ of\ bio\ oil\ (ml)}{Starting\ weight\ of\ SR\ (g\ )} = \dfrac{29.49}{50} = 58.99$

% yield of Bio-Char $= \dfrac{8.55}{50} = 17.11$

% yield of gas $= 100 - (58.99 + 17.11) = 23.90$

Table A-18 Catalytic (raw clay) pyrolysis of sida rhombifolia with LDPE and HDPE

S/no	Blending ratio	Yield wt%		
		Liquid	Char	Gas
1	1:3:1	49.7	33.6	16.7
2	1:3:2	52.2	31.1	16.7
3	1:3:3	54.4	27.28	18.42
4	1:3:4	61.8	15.7	22.5
5	1:3:5	58.99	17.11	23.93

Catalytic (metakaolin) co-pyrolysis of SR with LDPE and HDPE

Table A-19 pyrolysis data generated from laboratory experiment for catalyst (metakaolin)

s/n	Blending ratio (Catalyst:SR:LDEP&HDPE)	Liquid (w/v)	Solid char (g)
1	1:3:1	34.35	12.05
2	1:3:2	36.78	11.04
3	1:3:3	39.37	10.96
4	1:3:4	38.16	10.10
5	1:3:5	38.11	9.15

1st run

Volume of bio-oil = $\frac{Liquid\ w/v}{Density} = \frac{34.35}{1.1046} = 31.10$

Therefore % yield of Bio-oil = $\frac{Volume\ of\ bio\ oil\ (ml)}{Starting\ weight\ of\ SR\ (g)} = \frac{31.10}{50} = 62.2$

% yield of Bio-Char = $\frac{12.05}{50} = 24.1$

% yield of gas = 100 – (62.2 + 24.1) = 16.70

2nd run

Volume of bio-oil = $\frac{Liquid\ w/v}{Density} = \frac{36.78}{1.1046} = 33.30$

Therefore % yield of Bio-oil = $\frac{Volume\ of\ bio\ oil\ (ml)}{Starting\ weight\ of\ SR\ (g)} = \frac{33.30}{50} = 66.60$

% yield of Bio-Char = $\frac{11.04}{50} = 22.09$

% yield of gas = 100 – (66.60+ 22.09) = 11.35

3rd run

Volume of bio-oil = $\frac{Liquid\ w/v}{Density} = \frac{39.37}{1.1046} = 35.65$

Therefore % yield of Bio-oil = $\frac{Volume\ of\ bio\ oil\ (ml)}{Starting\ weight\ of\ SR\ (g)} = \frac{35.65}{50} = 71.30$

% yield of Bio-Char = $\frac{10.96}{50} = 21.92$

% yield of gas = 100 – (71.30 +21.92) = 6.78

4th run

Volume of bio-oil = $\dfrac{Liquid\ w/v}{Density} = \dfrac{38.16}{1.1046} = 34.55$

Therefore % yield of Bio-oil = $\dfrac{Volume\ of\ bio\ oil\ (ml)}{Starting\ weight\ of\ SR\ (g)} = \dfrac{34.55}{50} = 69.10$

% yield of Bio-Char = $\dfrac{10.10}{50} = 20.20$

% yield of gas = 100 – (69.10 + 20.20) = 10.70

5th run

Volume of bio-oil = $\dfrac{Liquid\ w/v}{Density} = \dfrac{38.11}{1.1046} = 34.50$

Therefore % yield of Bio-oil = $\dfrac{Volume\ of\ bio\ oil\ (ml)}{Starting\ weight\ of\ SR\ (g)} = \dfrac{34.50}{50} = 69.0$

% yield of Bio-Char = $\dfrac{9.15}{50} = 18.31$

% yield of gas = 100 – (69.0 + 18.31) = 12.69

Table A-20 Catalytic (metakaolin) co-pyrolysis of SR with LDPE and HDPE

S/no	Blendig ratio	Yield wt%		
		Liquid	**Char**	**Gas**
1	1:3:1	62.2	24.1	13.7
2	1:3:2	66.6	22.09	11.31
3	1:3:3	71.3	21.12	7.28
4	1:3:4	69.1	20	11.9
5	1:3:5	69.2	18.31	12.49

Table A-21 pyrolysis data generated from laboratory experiment for catalyst (metakaolin)

s/n	Blending ratio (Catalyst:SR:LDEP&HDPE)	Liquid (w/v)	Solid char (g)
1	1:3:1	36.78	11.08
2	1:3:2	39.33	9.74
3	1:3:3	42.03	9.66
4	1:3:4	41.60	10.10
5	1:3:5	41.36	9.72

1st run

Volume of bio-oil = $\dfrac{Liquid\ w/v}{Density}$ = $\dfrac{36.78}{1.1046} = 33.30$

Therefore % yield of Bio-oil = $\dfrac{Volume\ of\ bio\ oil\ (ml)}{Starting\ weight\ of\ SR\ (g)}$ = $\dfrac{33.30}{50} = 66.60$

% yield of Bio-Char = $\dfrac{11.08}{50} = 22.16$

% yield of gas = $100 - (66.60 + 22.16) = 11.24$

2nd run

Volume of bio-oil = $\dfrac{Liquid\ w/v}{Density}$ = $\dfrac{39.33}{1.1046} = 35.61$

Therefore % yield of Bio-oil = $\dfrac{Volume\ of\ bio\ oil\ (ml)}{Starting\ weight\ of\ SR\ (g)}$ = $\dfrac{35.61}{50} = 71.22$

% yield of Bio-Char = $\dfrac{9.74}{50} = 19.47$

% yield of gas = $100 - (71.22 + 19.47) = 9.31$

3rd run

Volume of bio-oil = $\dfrac{Liquid\ w/v}{Density}$ = $\dfrac{42.03}{1.1046} = 38.05$

Therefore % yield of Bio-oil = $\dfrac{Volume\ of\ bio\ oil\ (ml)}{Starting\ weight\ of\ SR\ (g)}$ = $\dfrac{38.05}{50} = 76.10$

% yield of Bio-Char = $\dfrac{9.66}{50} = 19.32$

% yield of gas = $100 - (76.10 + 19.32) = 4.58$

4th run

Volume of bio-oil = $\dfrac{Liquid\ w/v}{Density}$ = $\dfrac{41.60}{1.1046} = 37.66$

Therefore % yield of Bio-oil = $\dfrac{Volume\ of\ bio\ oil\ (ml)}{Starting\ weight\ of\ SR\ (g)}$ = $\dfrac{37.66}{50} = 75.31$

% yield of Bio-Char = $\dfrac{10.10}{50} = 20.16$

% yield of gas = $100 - (75.31 + 20.16) = 4.53$

5th run

Volume of bio-oil = $\dfrac{Liquid\ w/v}{Density}$ = $\dfrac{41.36}{1.1046}$ = 37.44

Therefore % yield of Bio-oil = $\dfrac{Volume\ of\ bio\ oil\ (ml)}{Starting\ weight\ of\ SR\ (g)}$ = $\dfrac{37.44}{50}$ = 74.89

% yield of Bio-Char = $\dfrac{9.72}{50}$ = 19.44

% yield of gas = 100 – (74.89 + 19.44) = 5.67

Table A-22   Catalytic (commercial zeolite Y) co-pyrolysis of SR with LDPE and HDPE

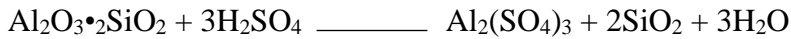| S/no	Blending ratio	Yield wt%		
		Liquid	**Char**	**Gas**
1	1:1:3	66.6	22.16	12.24
2	1:2:3	71.22	19.47	9.31
3	1:3:3	76.1	19.32	4.58
4	1:3:4	75.31	20.16	4.53
5	1:3:5	74.89	19.44	5.67

APPENDIX E

Calculations for the Dealumination of Metakaolin

Step 1

Calculation of de-alumination reaction for metakaolin using sulphuric acid can be
expressed as in Equation

$$Al_2O_3 \cdot 2SiO_2 + 3H_2SO_4 \longrightarrow Al_2(SO_4)_3 + 2SiO_2 + 3H_2O$$

The alumina was the only component of the metakaolin that takes place in the reaction with
the sulphuric acid during the dealumination while silica component was inert. Therefore
equation above

$$Al_2O_3 + 3H_2SO_4 \longrightarrow Al_2(SO_4)_3 + 2SiO_2 + 3H_2O$$
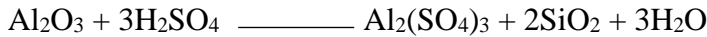
In-order to calculate stoichiometric ratio of alumina to acid ratio for dealumination process,
the stoichiometric Mass of Al_2O_3 and $3H_2SO_4$ are given as102g and 294g respectively. The
source of aluminium for dealumination was from metakaolin, hence the XRF analysis of
metakaolin was considered for the calculations and is given as 26.26 wt% of Al_2O_3.

Step 11

Calculations of volume of acid needed for dealumination

50g of meta-kaolin was considered as the basis for each batch of dealumination.

Amount of Al_2O_3 from the 50 g of metakaolin = 0.2502 x 50 = 13.51g Al_2O_3.

The weight of acid needed for dealumination (assuming 100% concentration H_2SO_4) =

12.51g x 294/102 = 36.06g

Actually, the concentration of the H_2SO_4 used for dealumination was 98%. Therefore the weight of 98% Conc acid needed = 100/98 x 36.06g = 36.06g

To calculate the volume of acid needed for the dealumination,

Let considered $V = \dfrac{M}{\rho}$

Density of the acid was given as 1.83 g/cm^3. Hence, the volume of acid needed for each batch of dealumination V, was calculated using equation ();

$V = \dfrac{36.796}{1.83} = 20.12$cm^3

Therefore, the volume of acid required for the dealumination was 20.12cm^3.

Step 111

Calculations of the volume of water needed to prepare for dilution

Mmix = Mw + Macid (98%)

Where Mmix was the mass of mixture of acid-water at concentration C_1 and C_2 respectively, Mw was the mass of water and Macid (98%) was the mass of the acid at 98%.

Therefore: Mw = Mmix - Macid (98%)

This implies that M= ρv

Vw ρw = Vmix ρmix – Vacid (98%) ρacid (98%)

To prepare the acids at concentration C_1 and C_2,

Let the dealumination was carried out using 60wt% concentration of acid as reported by Edomwonyi-Otu, (2008).

$M_1C_1 = M_2C_2$

$M_{(98\%)}C_{(98\%)} = M_{(60\%)}C_{(60\%)}$

$V_{(98\%)}\rho_{(98\%)}C_{(98\%)} = V_{(60\%)}\rho_{(60\%)}C_{(60\%)}$

$\rho_{(98\%)} = 1.83$ g/cm^3 and $\rho_{(60\%)} = 1.51$ g/cm^3 (Edomwonyi-Otu, 2008) and $\rho_{(w)} = 1$g/cm^3

$V_{(60\%)} = 20.12$ x 1.83 x $98/1.51$ x $60 = 39.83$cm^3

The volume of acid-water mixture was 39.83cm^3.

Mw = Mmix - Macid (98%)

Vw ρw = Vmix ρmix – Vacid (98%) ρacid (98%)

Vw = (39.83 x 1.51 – 20.12 x 1.83)/1 = 23.32cm^3

The de-alumination process parameters was found as follows;

Amount of mnetakaolin per batch = 50g

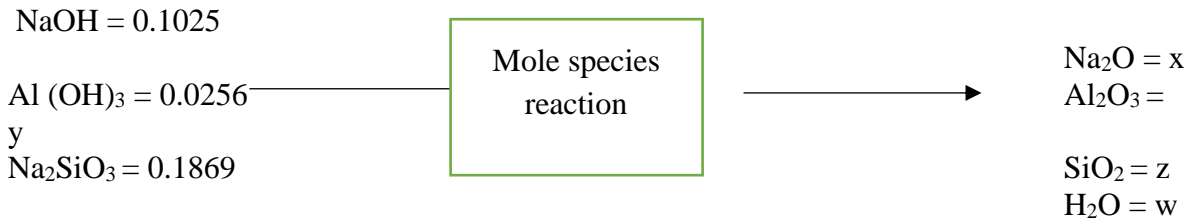Volume of acid (98% Concentrated sulphuric acid) = 20.12cm^3

Volume of distilled water = 23.32cm^3

Therefore, the general formula considered in synthesis of the catalyst in the work was considered to be in ratio of metakaolin to volume of acid and water was 1:2:3.

The balanced equation of the reaction is presented below:

$$2NaOH + 2Al(OH)_3 + Na_2SiO_3 \longrightarrow 2Na_2O + Al_2O_3 + SiO_2 + 4H_2O$$

Reactant	Mass (g)	Molar mass (g/mol)	$Moles = \dfrac{mass}{molar\ mass}$
NaOH	4.1	40	0.1025
Al(OH)$_3$	2	78	0.0256
Na$_2$SiO$_3$	22.8	122	0.1869
H$_2$O	20	18	1.1111

NaOH = 0.1025

Al (OH)$_3$ = 0.0256

y

Na$_2$SiO$_3$ = 0.1869

| Mole species reaction |

Na$_2$O = x

Al$_2$O$_3$ =

SiO$_2$ = z

H$_2$O = w

Si Balance

1 mol of Na$_2$SiO$_3$ contains 1 mol of Si
0.1869 Na$_2$SiO$_3$ contains 0.1869 mol Si
Atomic Si specie Balance

$$\frac{0.1869\ mol\ Si}{} \frac{1\ mol\ SiO2}{1\ mol\ Si} = 0.1869 \text{ mol } SiO_2$$

Al Balance

1 mol Al (OH)$_3$ contains 1 mol Al
0.0256 Al (OH)$_3$ contains 0.0256
Atomic Al species Balance

$$\frac{0.0256\ mol\ Al}{} \frac{1\ mol\ Al2O3}{2\ mol\ Al} = 0.0128 \text{ mol } Al_2O_3$$

Na Balance

1 mol NaOH contains 1 mol Na
0.1025 NaOH contains 0.1025 Na
1 mol Na$_2$SiO$_3$ contains 2 mol Na

0.1869 Na_2SiO_3 contains 0.3738 mol Na
Total Na = 0.4763

Atomic Na Balance
$$\frac{0.4763\ mol\ Na}{}\frac{1\ mol\ Na2O}{2\ mol\ Na} = 0.23815\ mol\ Na_2O$$

<u>H balance</u>

1 mol NaOH contains 1 mol H
0.1025 NaOH contains 0.1025 mol H
1 mol $Al(OH)_3$ contains 3 mol H
0.0256 $Al(OH)_3$ contains 0.0768 mol H
1 mol H_2O contains 2 mol H
1.1111 H_2O contains 2.2222 mol H
Total H = 2.4015

Atomic H Balance

$$\frac{2.4014\ mol\ H}{}\frac{1\ mol\ H2O}{2\ mol\ H} = 1.20075\ mol\ H_2O$$

Ratio 0.23815 : 0.0128 : 0.1869 : 1.20075
= 19 : 1 : 15 : 94

For the feed:
Na_2O = 1.1698
Al_2O_3 = 0.0808
SiO_2 = 1.1680
H_2O = 7.5218
Ratio 1.1698 : 0.0808 : 1.1680 : 7.5218
=   14 : 1 : 14 : 93
Overall 1.4080: 0.0936: 1.3549: 8.72255
15 : 1 : 12 : 173

APPENDIX F

1. Journals Publications

i. **Abdullahi, A., M., Garba, M., U., Eterigho E., J., Alhassan, M., Adeniyi. O., D.** (2022). Physico-Chemical Analysis of Bio-Oil produce From Co-Pyrolysis of *Sida Rhombifolia* with Low- and High-Density Polyethylene. Nigerian Journal of Engineering and Applied Science (NJEAS). Volume 7-9. ISSN 2465-1425.

ii. **Abdullahi, A., M., Garba, M., U., Eterigho E., J., Alhassan, M.** Characterization Bambu clay as a precursor for the synthesis of zeolite for catalytic application. Nigerian Journal of Science and Engineering Infrastructure (NJSEI). Volume 1.

2. Conference proceeding

Abdullahi, A., M., Garba, M., U., Eterigho E., J., Alhassan, M., (2022). Characterization of Bambu clay: As a potential source for zeolite Y synthesis. Nigerian Society of Chemical Engineering (NSChE) Conference. 52 AIC: page 40.